This electronic thesis or dissertation has been downloaded from the King's Research Portal at https://kclpure.kcl.ac.uk/portal/

The role of strong gravity in the early universe

Aurrekoetxea, Josu C.

Awarding institution:
King's College London

The copyright of this thesis rests with the author and no quotation from it or information derived from it may be published without proper acknowledgement.

END USER LICENCE AGREEMENT

Unless another licence is stated on the immediately following page this work is licensed under a Creative Commons Attribution-NonCommercial-NoDerivatives 4.0 International licence. https://creativecommons.org/licenses/by-nc-nd/4.0/

You are free to copy, distribute and transmit the work

Under the following conditions:

- Attribution: You must attribute the work in the manner specified by the author (but not in any way that suggests that they endorse you or your use of the work).
- Non Commercial: You may not use this work for commercial purposes.
- No Derivative Works - You may not alter, transform, or build upon this work.

Any of these conditions can be waived if you receive permission from the author. Your fair dealings and other rights are in no way affected by the above.

Take down policy

If you believe that this document breaches copyright please contact librarypure@kcl.ac.uk providing details, and we will remove access to the work immediately and investigate your claim.

Download date: 09. Jan. 2025

The role of strong gravity in the early universe

Josu C. Aurrekoetxea

Supervisor: Prof Eugene Lim

Department of Physics
King's College London

This dissertation is submitted for the degree of
Doctor of Philosophy

September 2021

Nire familia eta lagunei,
nigan jarritako konfidantza eta etengabeko babesagatik

Acknowledgements

I am extremely grateful to my supervisor Eugene Lim for his relentless support and guidance throughout my PhD. His impact on my career goes beyond his major contributions to the work presented in this thesis.

I am also deeply indebted to Thomas Helfer and Katy Clough for their training and being an endless source of advice. I am grateful to Eloy de Jong and Bo-Xuan Ge for their patience and insightful discussions. Many thanks to senior colleagues for sharing their knowledge and advice, in particular José Juan Blanco-Pillado, Diego Blas, Malcolm Fairbairn, Pedro Ferreira, Pau Figueras, Helvi Witek and Masahide Yamaguchi. Special thanks to my high school teacher Olga Estrada.

Thanks to my friends in the physics department at King's College London for making the PhD journey a fantastic experience, Adrian, Alessandro, Alex, Ali, Bo-Xuan, David, Eloy, Emilie, Fani, Francesco, Giuseppe, James, Katarina, Laia, Louis, Marciano, Matt, Miguel C., Miguel E., Nashwan, Patrick, Sree, Stephanie, Tarso, Thomas, Ville, Yurema. Many thanks also to Alberto, Carlos, Sharan, Valentini and Yannis. I would like to thank the GRChombo team for providing the friendliest research atmosphere one could ask for, in particular Jamie Bamber, Katy Clough, Robin Croft, Daniel Cutting, Eloy de Jong, Amelia Drew, Tiago França, Bo-Xuan Ge, Thomas Helfer, Cristian Joana, Francesco Muia, Zainab Nazari, Miren Radia, Justin Ripley and Dina Traykova.

I had the great pleasure of working with amazing collaborators Katy Clough, Pedro Ferreira, Raphael Flauger, Thomas Helfer, Eloy de Jong and Eugene Lim, who have made invaluable contributions to the work presented in this thesis. I also acknowledge helpful conversations with Ana Achucarro, Daniel Baumann, José Juan Blanco-Pillado, Bernard Carr, Ed Copeland, Tim Dietrich, Amelia Drew, William East, Kieran Finn, Tiago França, Mark Hannam, Tanja Hinderer, Mark Hindmarsh, Alex Jenkins, Cristian Joana, Sotirios Karamitsos, Sebastian Khan, David Marsh, Yolanda Murillo, Samaya Nissanke, Levon Pogosian, Miren Radia, Mairi Sakellariadou, Paul Shellard, Kepa Sousa, Ulrich Sperhake, Oliver Tattersall, James Widdicombe, Andrew Williamson and Helvi Witek.

I would also like to extend my deepest gratitude to the cosmology group at the Tokyo Institute of Technology for inviting me to visit in March 2020. Special thanks to Luca Buoninfante, Fabio Chibana, Teruaki Suyama and Masahide Yamaguchi. Thanks to the Universities of Barcelona, Cambridge, Oxford, the Basque Country, JILA Boulder

Colorado, Perimeter Institute, SISSA and TITECH for inviting me to talk about my work.

I would like to acknowledge the support of the ARCHER UK National Supercomputing Service and the Argonne Leadership Computing Facility, which provided substantial training throughout my PhD. In particular thanks to Marta Garcia Martinez from the Argonne Training Program on Extreme-Scale Computing (ATPESC) in 2019. I would also like to thank the COSMOS team at DAMTP, Cambridge University for their ongoing technical support and in particular Kacper Kornet and Miren Radia. The work presented in this thesis was performed using the following computational resources: The Leibnitz Supercomputing Centre SuperMUC-NG under PRACE grant Tier-0 Proposal 2018194669, on the Jülich Supercomputing Center JUWELS HPC under PRACE grant Tier-0 Proposal 2020225359, the BSC Marenostrum IV via PRACE grant Tier-0 PPFPWG, the Supercomputing Centre of Galicia, La Palma Astrophysics Centre via BSC/RES grants AECT-2017-2-0011 and AECT-2017-3-0009, on SurfSara Cartesius under Tier-1 PRACE grant DECI-14 14DECI0017, COSMA7 in Durham, Leicester DiAL HPC under DiRAC RAC13 Grant ACTP238, the Cambridge Service for Data Driven Discovery (CSD3), part of which is operated by the University of Cambridge Research Computing on behalf of the STFC DiRAC HPC Facility. The DiRAC component of CSD3 was funded by BEIS capital funding via STFC capital grants ST/P002307/1 and ST/R002452/1 and STFC operations grant ST/R00689X/1.

Abstract

The Nobel-Prize-winning detection of gravitational waves (GWs) in 2015 opened up a brand new window into observational cosmology, paving the way for the use of GWs to search directly for signatures of new physics. Moreover, recent computational developments in numerical relativity (NR) allow us to investigate Einstein's equations in regimes where the gravitational force is strong – a very promising area to test and search for physics beyond the standard model of cosmology. In this thesis we will focus in the use of numerical relativity to investigate the strong-field regime of the early universe.

We will start by studying inflation, the current paradigmatic theory of the Big Bang that assumes a period of accelerated expansion to explain why the current universe is homogeneous and isotropic at the largest cosmological scales. The prevalent mechanism is to use a scalar field that is assumed to homogeneously roll-down a model-dependent potential, extracting the energy that drives the accelerated expansion. However, if such a process can only begin in cases where the universe is already smooth, it becomes, to some extent, redundant. In this thesis we will derive and test a simple analytical criterion to predict if inflation can begin from inhomogeneous initial conditions. We will show that convex and concave potentials that vary on super-Planckian scales are significantly more robust than those that vary on sub-Planckian scales.

Then, we will pioneer the use of gravitational waves to detect cosmic strings, relics that are expected to have been formed after a phase transition in the early universe, and one of the key targets of the current LIGO/Virgo/KAGRA (LVK) detector searches. We will present the first fully general relativistic dynamical simulations of abelian Higgs circular cosmic strings loops that collapse and can either (i) unwind and disperse or (ii) form a black hole. To maximise the discovery potential of such events – often obscured by background noise in the detectors – we will construct their time-domain gravitational-wave strain waveform, which features a low-frequency infall followed by a characteristic merger and ringdown, with a large contribution of GW memory.

Lastly, we will simulate the formation of primordial black holes (PBHs) from sub and superhorizon perturbations in a matter dominated universe with numerical relativity. We will discuss the two primary mechanisms of formation that depend on the initial perturbation mass and its geometry – via direct collapse of the initial overdensity and via post-collapse accretion of the ambient dark matter. In both cases, we will confirm that the process occurs around a Hubble time, and the initial mass of the black hole is $M_{\rm BH} \sim 10^{-2} H^{-1} M_{\rm Pl}^2$. We will also discuss how post formation, the PBH undergoes rapid mass growth beyond the self-similar limit $M \propto H^{-1}$, showing that most its final mass is accreted from the ambient dark matter.

Table of contents

List of figures

List of tables

Part I

Background material

Chapter 1

Introduction

This thesis is split in three main parts: background, research and extra material.

The first part of the thesis comprises Chapters 1 and 2 and provides an overview[1] of the key background to the presented research work. In Chapter 1 we review the modern understanding of the universe, introducing general relativity, black holes and gravitational waves. We also discuss the Friedmann-Lemaître-Robertson-Walker (FLRW) universe and the shortcomings that led to the development of new physical theories and phenomena beyond the standard model of cosmology, such as inflation, cosmic strings and primordial black holes (PBHs). Chapter 2 introduces the key techniques of numerical relativity (NR), where we explain the approaches to solve Einstein's equations in a computer. This chapter will lay the groundwork for the main technical concepts that will be used in the research part of the thesis.

The research material in Chapters 3, 4 and 5 constitutes the core of the thesis, where we study several early universe phenomena using numerical relativity[2]. In particular, in Chapter 3 we will study the robustness of inflation to inhomogeneities in the initial scalar field profile. Using 3+1 non-linear numerical simulations, we will test a simple analytical criterion to predict when a given inflationary model will fail when starting from inhomogeneous initial conditions. We will show that small-field concave models are particularly sensitive to inhomogeneities in the scalar field. In Chapter 4, we will focus on the study of cosmic strings, where we will present their first-ever general relativistic dynamical simulations. Motivated by current detector searches by the LIGO/Virgo/KAGRA (LVK) collaboration, we will construct the gravitational-wave

---

[1] Mostly based on well-known literature Refs. [321, 454, 40, 77].

[2] We will use the numerical relativity code GRCHOMBO [55, 154], which has been applied to study a wide range of astrophysical and cosmological phenomena [203, 156, 157, 266, 437, 202, 150, 155, 265, 45, 465, 179, 152, 264, 324, 153, 355, 69, 464, 61, 186, 463, 263, 64, 200, 371, 56, 68, 293, 399, 151, 435, 187, 176, 400, 201, 461, 292, 63, 171].

chirp waveform of a collapsing circular cosmic string loop. In Chapter 5, we will use numerical relativity to simulate the formation of PBHs through the collapse of superhorizon-sized scalar perturbations in a matter dominated era. We will describe the two primary formation mechanisms – via direct collapse of the initial overdensity, and via post-collapse accretion of the ambient dark matter.

Lastly, detailed calculations that have been omitted throughout the text and additional material such as numerical methodologies and convergence tests are included in Appendix A, B, C and D, which make up the extra material part of the thesis.

1.1 The universe today

After the successful tests of the theory of special relativity proposed by Albert Einstein in 1906 [194], it was clear that the theory of gravity at that time, Newtonian gravity, could not be complete. Special relativity is based on the postulate that nothing can travel faster than light, which would not allow the instantaneous forces that Newtonian theory needs to explain gravitational interactions. It was not until 1916 that Einstein published one of his most revolutionary works, completely changing the understanding of gravity and introducing a totally new formalism to think about space and time, the theory of general relativity [195] – the modern theory of gravitation. Although there are reasons to believe that it cannot be the ultimate theory of gravity, it has been proven to be very successful in explaining the universe that is observed today.

General relativity is based on (i) the principle of general covariance: laws of physics must take the same form for all observers, and (ii) the principle of equivalence: all masses fall with the same acceleration regardless of their mass. Following these principles, the theory of general relativity is written in tensor language that describes gravity from a geometrical viewpoint of spacetime, fixed by the distribution of energy. It turned out to be incredibly successful and more than a hundred years after its publication, it is still passing with flying colours all the tests of the predictions that had been made, such as the observation of gravitational waves [8] or the observation by the Event Horizon Telescope of the shadow of the supermassive black hole candidate in the center of the giant elliptical galaxy M87 [25–30].

General relativity is a geometric theory that relates the gravitational effects with the curvature of spacetime, so differential geometry plays a crucial role. The most fundamental object is a differentiable manifold $\mathcal{M}$, which is a continuous and smooth space that can be one-to-one mapped from $\mathcal{R}^n$ to $\mathcal{M}$. One of the most important objects is the metric tensor $g_{\mu\nu}$ which contains information about the "shape" of the spacetime and allows to define the notion of line element in a manifold

$$ds^2 = g_{\mu\nu} dx^\mu dx^\nu \, . \tag{1.1}$$

In three dimensional *Euclidean* geometry (in Cartesian coordinates), the metric takes the usual form: $g_{ij} = \mathrm{diag}(1,1,1)$ so that distances are $ds^2 = dx^2 + dy^2 + dz^2$. On the other hand, the spacetime metric is *Lorentzian* (has one negative and three positive eigenvalues) and takes more complex forms that can depend on the position x^μ. Vectors in the manifold are classified depending the sign of their magnitude $V^2 = g_{\mu\nu} V^\mu V^\nu$: $V^2 < 0$ timelike, $V^2 = 0$ null, and $V^2 > 0$ spacelike. For example, massive and massless particles travel along timelike and null geodesics, respectively.

For later use, it will be useful to introduce two types of derivatives of tensors. The first one is called Lie derivative. Having a vector field $\vec{V}$ on a manifold, integral curves can be defined integrating $V^\mu(x^\mu(\lambda)) = dx^\mu(\lambda)/d\lambda$. A family of these curves is called a congruence with affine parameter λ. The Lie derivative of a tensor T^α_β with respect to $\vec{V}$ measures how much the tensor changes when moving along the congruence. Mathematically,

$$\pounds_{\vec{V}} T^\alpha_\beta = V^\sigma \partial_\sigma T^\alpha_\beta - T^\sigma_\beta \partial_\sigma V^\alpha + T^\alpha_\sigma \partial_\beta V^\sigma \, . \tag{1.2}$$

The other interesting derivative of a tensor is called covariant derivative. A partial derivative of a tensor does not transform as a tensor under coordinate transformations, whereas the covariant derivative does

$$\nabla_\alpha V^\beta = \partial_\alpha V^\beta + \Gamma^\beta_{\alpha\sigma} V^\sigma \, , \tag{1.3}$$

where $\Gamma^\beta_{\alpha\sigma}$ are the Christoffel symbols, defined using the metric tensor as

$$\Gamma^\alpha_{\mu\nu} = \frac{1}{2} g^{\alpha\beta} \left(\partial_\mu g_{\beta\nu} + \partial_\nu g_{\mu\beta} - \partial_\beta g_{\mu\nu} \right) \, . \tag{1.4}$$

The easiest way to measure the curvature of a spacetime and distinguish between flat or curved manifolds is by considering what happens to a vector V^α when it is parallelly transported in a closed loop. For a flat manifold it will not change, whereas for a curved manifold it will. The value of this change is quantified in the Riemann curvature tensor, defined as

$$\left[\nabla_\mu, \nabla_\nu \right] V^\alpha \equiv R^\alpha_{\beta\mu\nu} V^\beta \, , \tag{1.5}$$

or in terms of the Christoffel symbols,

$$R^{\alpha}_{\beta\mu\nu} = \partial_\mu \Gamma^{\alpha}_{\beta\nu} - \partial_\nu \Gamma^{\alpha}_{\mu\beta} + \Gamma^{\alpha}_{\lambda\mu}\Gamma^{\lambda}_{\beta\nu} - \Gamma^{\alpha}_{\lambda\nu}\Gamma^{\lambda}_{\beta\mu} \,. \tag{1.6}$$

By definition, it is antisymmetric on the first and second pair of indices, and symmetric with respect to exchange of these two pairs

$$R_{\alpha\beta\mu\nu} = -R_{\beta\alpha\mu\nu} = -R_{\alpha\beta\nu\mu} = R_{\mu\nu\alpha\beta} \,, \tag{1.7}$$

in addition to satisfy

$$R^{\alpha}_{\beta\mu\nu} + R^{\alpha}_{\mu\nu\beta} + R^{\alpha}_{\nu\beta\mu} = 0 \,. \tag{1.8}$$

We also define the Ricci curvature tensor as

$$R_{\alpha\mu} = g^{\beta\nu} R_{\alpha\beta\mu\nu} \,, \tag{1.9}$$

and the Ricci scalar

$$R = g^{\mu\nu} R_{\mu\nu} \,. \tag{1.10}$$

Einstein's equations tell spacetime how to curve given the matter distribution and, at the same time, the spacetime tells the matter how to move through it. Mathematically, the equations can be elegantly obtained applying the principle of least action to the Einstein-Hilbert action[3]

$$S_{EH} = \int d^4x \frac{M_{\rm Pl}^2}{16\pi} \sqrt{-g} R + S_M \,, \tag{1.11}$$

where $M_{\rm Pl}^2 \equiv G^{-1}$ is the non-reduced Planck mass with G the gravitational constant, S_M is the matter content action and $g = \det g_{\mu\nu}$. The equations of motion obtained are known as the Einstein's field equations

$$R_{\mu\nu} - \frac{1}{2} R g_{\mu\nu} = 8\pi G T_{\mu\nu} \,, \tag{1.12}$$

where the cosmological constant has been neglected, and $T_{\mu\nu}$ is the stress-energy-momentum tensor given by

$$T_{\mu\nu} \equiv -\frac{2}{\sqrt{-g}} \frac{\delta S_M}{\delta g^{\mu\nu}} \,, \tag{1.13}$$

where T^{00}, T^{0i} and T^{ij} are the energy density, momentum density and flux of momentum i in the j direction, respectively. It obeys the energy-momentum conservation laws,

---

[3] In this thesis we will use the $(-,+,+,+)$ convention.

written in covariant language as

$$\nabla_\mu T^{\mu\nu} = 0\,. \tag{1.14}$$

Although the covariant formulation introduces Einstein's equations in a very simplified and elegant form, they consist of a complex system of 16 non-linear second order differential equations, which only in particular cases with high degrees of symmetry or weak-field limit can analytically be solved. We briefly review some of their most important solutions below.

Black holes

The Schwarzschild spacetime [416] is one of the first and most fundamental solutions, describing the exterior of stars and showing the existence of dense objects known as black holes. It is a spherically symmetric spacetime with line element given by

$$ds^2 = -\left(1 - \frac{2GM}{r}\right) dt^2 + \left(1 - \frac{2GM}{r}\right)^{-1} dr^2 + r^2\left(d\theta^2 + \sin^2\theta d\phi^2\right)\,, \tag{1.15}$$

where M is a positive constant – usually the mass of the system. The metric is static and describes the curvature of empty spacetime outside some central mass distribution with total mass M, with $r = 2GM$ being a coordinate singularity, the *Schwarzschild radius*. In the limit of large $r \to \infty$, $2GM/r \to 0$ and the metric asymptotically approaches Minkowski. For $M = 0$, Minkowski spacetime is recovered.

Gravitational waves

Another interesting solution to Einstein's equations are gravitational waves. In the weak-field limit – where the gravitational force is negligible – one can decompose the metric into

$$g_{\mu\nu} \approx \eta_{\mu\nu} + h_{\mu\nu}\,, \tag{1.16}$$

where $\eta_{\mu\nu} = \mathrm{diag}(-1, 1, 1, 1)$ is the flat space metric (called background metric) and the metric perturbation $h_{\mu\nu}$. We will skip the details here, but in the limit in which only linear terms in $h_{\mu\nu}$ are kept, the linearized version of Einstein's equations can be reduced to a wave equation for $h_{\mu\nu}$, corresponding to what we call gravitational waves, *ripples in the fabric of space and time*

$$\Box \bar{h}_{\mu\nu} = 0\,, \tag{1.17}$$

where $\bar{h}_{\mu\nu} \equiv h_{\mu\nu} - \frac{1}{2}h\eta_{\mu\nu}$ is the trace-reversed metric perturbation and $h = \eta_{\mu\nu}h^{\mu\nu}$.

These waves are produced in some of the most catastrophic events in the universe, such as in compact binary coalescences of black holes (BH) or neutron stars (NS), and then propagate through space. It was in fact the detection of these perturbations in the gravitational field with the LIGO/Virgo interferometers that allowed for the first direct observation of black holes in 2015. After upgrades, the current LVK network of detectors has since then observed more than 50 events, including NS-NS and NS-BH mixed binary mergers [7, 11, 19, 20].

The Friedmann-Lemaître-Robertson-Walker metric

Einstein's field equations have been very successful in describing the dynamics of objects in the universe and they are an incredibly powerful tool that can be applied to the universe as a whole to learn about its past and future evolution. Our universe contains a wide range of objects: stars, galaxy clusters, black holes... it is highly inhomogeneous. However, when we look at different directions, the same density of these objects is observed. In addition, observations of the Cosmic Microwave Background (CMB) demonstrate that the universe is highly homogeneous – no special places – and isotropic – no special directions – in large scales. This is known as the *cosmological principle* and the appropriate metric tensor to describe such a universe is the so-called Friedmann-Lemaître-Robertson-Walker (FLRW) spacetime, with line element

$$ds^2 = -dt^2 + a^2(t)dl^2\,, \tag{1.18}$$

where t is the cosmic time, $a(t)$ is the scale factor of the universe and dl^2 represents the line element on a three-dimensional space of constant curvature k

$$dl^2 = \frac{dr^2}{1-kr^2} + r^2(d\theta^2 + \sin^2 d\phi^2)\,. \tag{1.19}$$

The constant curvature k is determined by the spatial topology and geometry of the universe: (i) $k=+1$ closed, (ii) $k=0$ flat, and (iii) $k=-1$ open universe, respectively.

Sometimes it is conventient to write the metric using an alternative time coordinate called conformal time τ defined as $dt = a(t)d\tau$, where the metric takes the simpler form

$$ds^2 = a^2(\tau)\left[-d\tau^2 + dl^2\right]\,, \tag{1.20}$$

and null-rays travel along 45° trajectories in a spacetime diagram.

The energy-momentum tensor of the matter content $T^{\mu\nu}$ must respect the same symmetries as the homogeneous and isotropic spacetime. Modeling it as a perfect fluid with energy density ρ and presssure P

$$T^{\mu\nu} = (\rho + P)u^\mu u^\nu + P g^{\mu\nu} \,, \tag{1.21}$$

where u^μ is the four-velocity of a comoving observer[4]. The local conservation of energy (1.14) provides an equation for the evolution of the energy density

$$\dot{\rho} + 3\left(\frac{\dot{a}}{a}\right)(\rho + P) = 0 \,. \tag{1.22}$$

For a complete description of the evolution of the matter components, we must also specify its equation of state, $P = P(\rho)$. It is useful to describe the universe by the simple equation of state $P = w\rho$, which has been proven to be very accurate with the observational evidence and allows us to explore a variety of types of matter with a single parameter w. Integrating (1.22), we get the evolution of the energy density

$$\rho = \rho_0 a^{-3(1+w)} \,. \tag{1.23}$$

The scale factor $a(t)$ is constrained to obey Einstein's equations, so applying Eqn. (1.12) to the FLRW metric (1.18) we derive the so-called Friedmann equation

$$H^2 = \frac{8\pi}{3M_{\rm Pl}^2}\rho - \frac{k}{a^2} \,, \tag{1.24}$$

where the Hubble parameter is defined as $H \equiv \dot{a}/a$. The evolution of the scale factor is related to the matter content of the universe by a third field equation,

$$\frac{\ddot{a}}{a} = -\frac{4\pi}{3M_{\rm Pl}^2}\left(\rho + 3P\right) \,, \tag{1.25}$$

which is not independent of Eqns. (1.22), (1.24) and can be obtained using the Bianchi identities. The Eqn. (1.24) can be integrated and in the flat case ($k = 0$) lies

$$a(t) = \left(\sqrt{\frac{8\pi}{3M_{\rm Pl}^2}\rho_0}\,\frac{3(1+w)}{2}t\right)^{\frac{2}{3(1+w)}} \,. \tag{1.26}$$

If the universe is filled with non-relativistic matter with negligible pressure, such as dust $w \approx 0$, and then (1.23) implies $\rho \propto a^{-3}$ and $a(t) \propto t^{2/3}$. If the dominant contribution to matter content of the universe is relativistic, such as radiation $w = 1/3$, and the energy density evolves as $\rho \propto a^{-4}$ and $a(t) \propto t^{1/3}$. So if the universe is

---

[4] The comoving observer is the one that stays at fixed spatial coordinates.

expanding and is filled by both dust and radiation, the non-relativistic matter will inevitably dominate.

The critical density for a zero spatial curvature universe is defined as

$$\rho_{\rm crit} \equiv \frac{3H^2 M_{\rm Pl}^2}{8\pi}\,, \tag{1.27}$$

so that for both dust and radiation dominated universes $\rho_{\rm crit} \propto t^{-2}$. We define a dimensionless density parameter

$$\Omega \equiv \frac{\rho}{\rho_{\rm crit}}\,, \tag{1.28}$$

which distinguishes between a closed $\Omega > 1$, flat $\Omega = 1$ and open $\Omega < 1$ universe. We can rewrite the Friedmann equation (1.24) in terms of this new quantity as

$$\Omega = 1 + \frac{k}{a^2H^2}\,. \tag{1.29}$$

This expression clearly indicates that for a dust or radiation dominated universe, where $(aH)^{-1}$ increases with time, the $\Omega = 1$ flat solution is a repeller. Cosmological observations measuring the Hubble parameter today estimate $H_0 \approx 70$ km s^{-1} Mpc^{-1}, consistent with a flat universe $\Omega \approx 1$. Most of this model's predictions have shown very accurate agreement with observational data. However, several problems have remained open, and we briefly list them below as the most important shortcomings of the standard cosmological model.

Homogeneity problem: A horizon is the region that separates the spacetime into its causal and non-causal parts. In this way the comoving radius of a photon in causal contact can be calculated to be $\sim (a(t)H(t))^{-1}$, which grows with time for a dust or radiation dominated universe. In fact, the last scattering surface[5] is made of small disconnected regions of approximately 1° on the sky. However, the data of the CMB proves that the microwave radiation reaching us from opposite directions has approximately the same temperature – the universe is homogeneous and isotropic. How is this possible if the photons had not had enough time to interact and thus establish thermal equilibrium? Why did the universe start with such homogeneous initial conditions?

Flatness problem: As we have discussed, the critical density $\Omega = 1$ is a point of unstable equilibrium, so that deviations from that value grow in time (see Eqn. (1.29)). However, cosmological observations evidences that the density of the universe is very

---

[5] When photons stopped scattering with matter and started to freely propagate.

close to the critical density today. For this to be possible, Ω had to be finely tuned to be closer to one in the early universe. How?

Small scale inhomogeneity: Although the universe is apparently very smooth on large scales, there is a plethora of structure on smaller scales such as stars and galaxies. The standard cosmological model provides a nice successful framework for understanding the origin of such a rich abundance of small-scale structure through the growth of primordial density inhomogeneities. However, this poses another puzzle for standard cosmology, what is the origin of these primeval fluctuations?

Exotic relics: As we will see later, local symmetries in Grand Unified Theories (GUTs) are spontaneously broken at some energy around 10^{16} GeV to the symmetry of the standard model $SU(3) \times SU(2) \times U(1)$. These phase transitions are expected to create relics that would radically change the evolution of the universe and the standard cosmological model has no mechanism to get rid of this exotic matter.

Dark matter: Cosmological observations strongly indicate the existence of *invisible* matter, only interacting through gravity and making up about $\sim 25\%$ of the content of the universe today. Though many candidates have been suggested, the exact nature of dark matter remains unknown.

The first three issues are closely related to the very special initial conditions of the FLRW metric. In the next section we will introduce cosmic inflation, based upon classical gravitational theory and ideas in modern quantum field theory, as a possible solution. The last two relate to outstanding problems in cosmology and particle physics, and as we will see later, both cosmic strings and primordial black holes have been considered as candidate solutions for such puzzles.

1.2 Beyond the standard cosmological model

1.2.1 The inflationary universe

As we have seen in the previous section, several of the standard cosmological model puzzles have their origin in the increasing Hubble radius

$$\frac{d}{dt}\left(\frac{1}{aH}\right) > 0\,. \tag{1.30}$$

What happens during a period where the Hubble radius decreases?

$$\frac{d}{dt}\left(\frac{1}{aH}\right) < 0\,, \qquad \Longrightarrow \qquad -\frac{\ddot{a}}{\dot{a}^2} < 0\,. \tag{1.31}$$

And thus, the universe expands with positive acceleration. From Eqn. (1.25) positive acceleration requires an equation of state where

$$\rho + 3P < 0\,, \qquad \Longrightarrow \qquad w < -\frac{1}{3}\,. \tag{1.32}$$

In addition to the already discussed dust ($w = 0$) and radiation ($w = 1/3$) solutions, vacuum energy (exotic matter with negative pressure, $w = -1$) allows for such an accelerated expansion. This universe is very special because its energy density remains constant as it evolves, via Eqn. (1.22).

One can also show that for a vacuum dominated universe the scale factor increases exponentially

$$a(t) \propto e^{Ht}\,, \tag{1.33}$$

where H is the Hubble parameter given by Eqn. (1.24), and the comoving Hubble radius decreases as

$$\frac{1}{aH} \propto e^{-2Ht}\,, \tag{1.34}$$

possessing the ideal properties to resolve the homogeneity, flatness and unwanted relics problems. This is what we call the inflationary universe and below we briefly describe the ways in which such an accelerated expansion resolves some of the standard cosmological puzzles.

Homogeneity problem: A decreasing Hubble radius during the inflationary period allows for regions in the sky that seem to be out of causal contact today to have been within the horizon at some point in the past, and hence providing the universe with a smoothing mechanism.

Spatial flatness problem: Is also solved by growing the curvature radius exponentially while keeping the energy density of the universe constant. In other words, the accelerated expansion drives the energy density exponentially close to its critical value at the end of inflation $\Omega \propto 1 + ke^{-2Ht}$, thus predicting its $\Omega \approx 1$ value today.

Unwanted relics: Inflation erases any unwanted relics that were produced before the accelerated expansion had started – their energy density is exponentially diluted away. However, it will not get rid of exotica formed during a phase transition at a lower energy scale, leaving an open observational window for these objects. In fact, we will later focus on cosmic strings and the use of gravitational waves to detect them.

Small-scale inhomogeneity: As we will see below, the inflationary mechanism can be included within a framework at the classical level by the dynamics of a homogeneous scalar field ϕ. We will not go into details, but measurements from the CMB are compatible with density perturbations responsible for the formation of small-scale structure having the origin on quantum fluctuations of this field, which grow as the universe inflates.

Single scalar field inflation

We have already discussed vacuum energy, a type of matter that would provide the properties of such an accelerated expansion with $w = -1$ (a cosmological constant). However, the inflationary period must at some point end giving rise to the standard cosmology we observe today. A successful model for "turning off" such a mechanism is the use of a scalar field ϕ – which we call the *inflaton*, together with a model dependent potential $V(\phi)$. The action of this new fundamental field minimally coupled to gravity is written as

$$S_M = \int d^4x\sqrt{-g}\left(\frac{1}{2}\nabla_\mu\phi\nabla^\mu\phi + V(\phi)\right) . \tag{1.35}$$

The derived equation of motion for the scalar field is the famously known Klein-Gordon equation

$$\nabla^2\phi = -\frac{dV(\phi)}{d\phi} . \tag{1.36}$$

We can also derive the energy-momentum tensor of a single real scalar field via Eqn. (1.13)

$$T_{\mu\nu} = \partial_\mu\phi\partial_\nu\phi - g_{\mu\nu}\left(\frac{1}{2}\partial_\alpha\phi\partial^\alpha\phi + V(\phi)\right) , \tag{1.37}$$

where the components can be identified with the energy density and pressure from (1.21). In an FLRW spacetime,

$$\rho = \frac{1}{2}\dot{\phi}^2 + \frac{1}{2}\frac{(\nabla\phi)^2}{a^2} + V(\phi) , \tag{1.38}$$

$$P = \frac{1}{2}\dot{\phi}^2 - \frac{1}{6}\frac{(\nabla\phi)^2}{a^2} - V(\phi) , \tag{1.39}$$

and the Klein-Gordon equation of motion for the field ϕ also reduces to

$$\ddot{\phi} + 3H\dot{\phi} - \frac{1}{a^2}\nabla^2\phi + \frac{dV(\phi)}{d\phi} = 0 . \tag{1.40}$$

A key ingredient to make this mechanism successful is the assumption that the field is homogeneous – it does not depend on spatial coordinates x – and thus $\phi = \phi(t)$. In this limit, the gradient terms in Eqn. (1.38) vanish, giving as final quantities

$$\rho = \frac{1}{2}\dot{\phi}^2 + V(\phi)\,, \tag{1.41}$$

$$P = \frac{1}{2}\dot{\phi}^2 - V(\phi)\,. \tag{1.42}$$

Then, $w = P/\rho \approx -1$ if the kinetic term is subdominant when compared to the potential $\dot{\phi}^2 \ll V(\phi)$, meaning that the field should "slow-roll". This condition will constrain the shape and properties of the potential $V(\phi)$. In the slow-roll regime, the equations of motion for the field $\phi(t)$ and scale factor $a(t)$ take the simpler form

$$\ddot{\phi} + 3H\dot{\phi} + \frac{dV(\phi)}{d\phi} = 0\,, \tag{1.43}$$

$$H^2 = \frac{8\pi}{3M_{\mathrm{Pl}}^2}\left(\frac{1}{2}\dot{\phi}^2 + V(\phi)\right)\,. \tag{1.44}$$

We can quantify by how much the universe has expanded during the inflationary period defining the number of e-folds

$$N = \ln\left(\frac{a_f}{a_i}\right)\,, \tag{1.45}$$

which can be rewritten as $dN = d\ln a$ so that

$$N = \int_{a_i}^{a_f} \frac{da}{a} = \int_{t_i}^{t_f} H dt = \int_{\phi_0}^{\phi_f} \frac{H}{\dot{\phi}} d\phi\,, \tag{1.46}$$

where $\phi_0 = \phi(t_i)$.

We define a slow-roll parameter ϵ to check that the comoving Hubble horizon is decreasing

$$\frac{d}{dt}\left(\frac{1}{aH}\right) < 0\,, \qquad \Longrightarrow \qquad \epsilon \equiv -\frac{\dot{H}}{H^2} < 1\,. \tag{1.47}$$

Not only we want this instantaneous behaviour to take place, but we also want it to last enough in order to solve the homogeneity and flatness problems. A second slow-roll parameter to track such a condition is defined as

$$|\eta| \equiv \frac{|\dot{\epsilon}|}{H\epsilon} \ll 1\,. \tag{1.48}$$

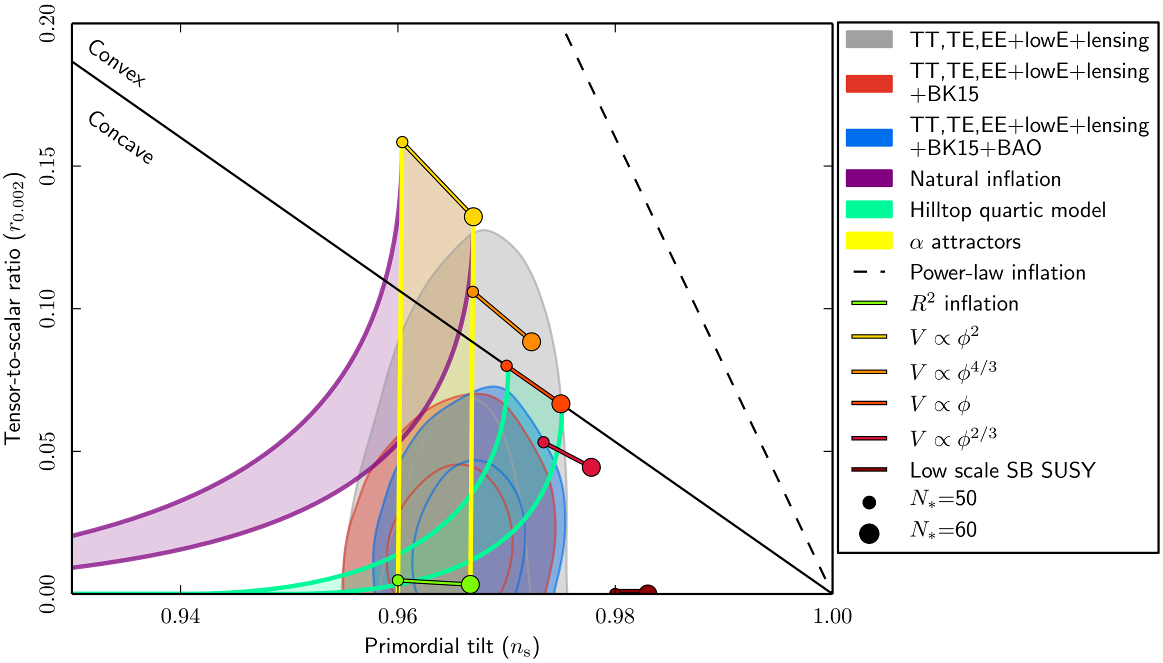

Fig. 1.1 Predictions vs observations for different popular inflationary models. The axes correspond to the scalar index n_s and the tensor-to-scalar ratio r. Observational data favours concave models with an almost scale invariant power spectrum $n_s \approx 1$ and a negligible amount of tensor perturbations $r \approx 0$. Figure from [31].

We can reformulate these conditions as constraints on the shape of the scalar field potential using (1.43) and (1.44)

$$\epsilon(\phi) \equiv \frac{M_{\rm Pl}^2}{16\pi}\left(\frac{V'}{V}\right)^2 , \tag{1.49}$$

$$\eta(\phi) \equiv \frac{M_{\rm Pl}^2}{8\pi}\left(\frac{V''}{V}\right) . \tag{1.50}$$

Therefore, the universe will inflate while $\epsilon \ll 1$ and $\eta \ll 1$. A common classification of inflationary models is given by the shape of the scalar potential $V(\phi)$,

- Convex models where $V'' > 0$.
- Concave models where $V'' < 0$.

It is also common to classify them depending on their *characteristic scale* – the field-range in which the scalar field transverses along

- Large field models: The field slow-rolls over a region $\Delta\phi \gg M_{\rm Pl}$.

- Small field models: The field slow-rolls over a region $\Delta\phi \ll M_{\mathrm{Pl}}$.

Figure 1.1 illustrates how several inflationary models perform when compared to observational constraints from the CMB by the Planck Collaboration [31]. The data is consistent with a nearly scale invariant power spectrum where $n_s \approx 1$ and a negligible tensor-to-scalar ratio, heavily disfavouring convex models. When inflation ends a period known as reheating starts, when the inflaton couples to other fields, transferring its energy to produce particles and starting the standard Hot Big Bang era.

What is next?

However, throughout the derivation of this mechanism, a key ingredient has been enforced in order for inflation to succeed, the assumption that the pre-inflationary state of the scalar field ϕ is homogeneous. However, if such a process can only begin in cases where the universe is already smooth, it becomes, to some extent, redundant. It is then crucial to study whether the homogeneous end-state is an attractor solution of (any) inflationary model, regardless of its initial conditions [224, 257, 459, 430, 73, 33, 74, 225, 291, 260, 386, 359, 313, 314, 117, 341, 226, 103, 118, 358, 72, 86, 125, 441, 71, 70, 395, 342, 436, 113, 223, 343, 116, 142, 164, 415, 402, 165, 357, 403, 82, 316, 344, 205, 98, 34, 35, 326, 199, 115, 228, 227, 114, 327, 229, 325, 193, 190, 107, 46, 47, 110, 157, 155, 61, 204, 293]. To do so, we must introduce a space dependent field $\phi(x)$, recovering all the terms in Eqn. 1.40. Moreover, large variations of the scalar field along the plateau of the inflationary potential can lead to gradients where strong-field gravitational effects become important, and thus a description with Einstein's field equations is essential. In Chapter 3, we will use numerical relativity to study the robustness of inflation to such inhomogeneous initial conditions for popular inflationary models.

1.2.2 Cosmic strings

Cosmic strings were the rivals to inflationary theories in the structure formation debate until they were ruled out after disagreement with the power spectrum observed by the BOOMERanG experiment [175, 449, 438, 439, 112, 444, 385, 384, 32, 188, 160, 104, 391, 469]. They still remain a popular and active field of research because they are a source of gravitational waves that could probe the high-energy physics regime of the universe, beyond the capabilities of any current or planned particle accelerator.

Cosmic strings are an example of topological defects that form through one of the most important concepts in modern particle theory, spontaneous symmetry breaking.

The idea that there are underlying symmetries of nature that are not manifest in the structure of the vacuum plays a crucial role in the unification of the forces – such as in the standard model of particle phyiscs – and the construction of a theory of everything. Of particular interest for cosmology is the theoretical expectation that symmetries that are spontaneously broken today, were restored in the early universe provided that the temperatures exceeded the energy scale of such a broken symmetry. Cosmic strings are relics of the early universe that are expected to be produced in one of such phase transitions, where the topology of the vacuum manifold is not simply connected, and the forces that govern our universe today (weak, strong and electromagnetic forces) were broken from a unified whole (known as Grand Unified Theory). After the process of spontaneous symmetry breaking, the ground state of the theory is characterised by a non-zero expectation value of the field and does not exhibit all the symmetries of the Lagrangian. To illustrate this, we can look at the Lagrangian density of a complex scalar field ϕ

$$\mathcal{L} = (\partial_\mu \bar{\phi})(\partial^\mu \phi) + V(\phi)\,, \tag{1.51}$$

with potential

$$V(\phi) = \frac{\lambda}{4}\left(\bar{\phi}\phi - \eta^2\right)^2\,, \tag{1.52}$$

where λ and η are the dimensionless coupling constant and the symmetry breaking scale, respectively. This model is invariant under the *global U(1)* group of phase transformations

$$\phi(x) \to e^{i\alpha}\phi(x), \tag{1.53}$$

where “global” indicates that α is independent of the spacetime location x. As we will see shortly, there is also a similar proccess for “local gauge” transformations with space dependent $\alpha(x)$.

As Fig. 1.2 shows, the minimum of the potential lies on a circle at the symmetry breaking scale $|\phi| = \eta$, and the vacuum of the theory is characterized by a non-zero expectation value

$$\langle 0|\phi|0\rangle = \eta e^{i\theta}\,, \tag{1.54}$$

with an arbitrary phase θ. It is clear then that the vacuum state is not invariant under the phase transformation (1.53),

$$\langle 0|\phi|0\rangle \to \eta e^{i(\theta+\alpha)}\,, \tag{1.55}$$

so it does not respect the symmetry of the Lagrangian and we say that the symmetry is spontaneously broken. The state in which the symmetry remains unbroken $\langle 0|\phi|0\rangle = 0$

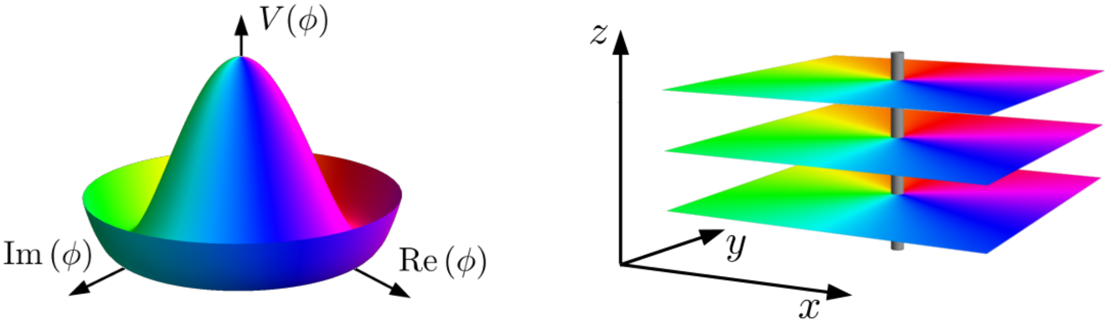

Fig. 1.2 Higgs potential and a straight string with colours illustrating the non-trivial mapping of the field configuration from the degenerate circle of minima of the potential in Eqn. (1.52) (left) into the physical space (right). The grey tube illustrates the location of the infinite straight string along the z direction, where the field rests at the local maximum of the potential.

corresponds to the local maximum of the potential and thus is not the lowest energy configuration.

We can study the vacua in which the symmetry is broken by expanding around the ground state and rewriting the complex scalar field in terms of two real fields φ and ϑ,

$$\phi(x) = \left(\eta + \frac{1}{\sqrt{2}}\varphi(x)\right) e^{i\vartheta(x)}\,, \tag{1.56}$$

The Lagrangian then becomes

$$\mathcal{L} = \frac{1}{2}\left(\partial_\mu\varphi\right)^2 + \eta^2\left(\partial_\mu\vartheta\right) + \frac{1}{2}\lambda\eta^2\varphi^2 + \mathcal{L}_{\mathrm{int}}\,, \tag{1.57}$$

where $\mathcal{L}_{\mathrm{int}}$ includes cubic and higher order interaction terms in φ and ϑ. We see that φ represents a particle with a positive mass $m_\varphi = \sqrt{\lambda}\eta$, corresponding to radial oscillations about a point on the circle of minima $|\phi| = \eta$. On the other hand, the real field ϑ features in the Lagrangian without a mass term, so that $m_\vartheta = 0$, corresponding to a massless scalar particle – also called Goldstone boson.

However, most of particle physics is described by gauge theories, such as the abelian Higgs model

$$\mathcal{L} = (\bar{D}_\mu\bar{\phi})(D^\mu\phi) + \frac{\lambda}{4}\left(\bar{\phi}\phi - \eta^2\right)^2 + \frac{1}{4}F_{\mu\nu}F^{\mu\nu}\,, \tag{1.58}$$

where the covariant derivative is given by $D_\mu = \partial_\mu - ieA_\mu$, with A_μ a gauge vector field, e the gauge coupling and the antisymmetric tensor $F_{\mu\nu} = \partial_\mu A_\nu - \partial_\nu A_\mu$. This model is invariant under the *local gauge U(1)* group of transformations

$$\phi(x) \to e^{i\alpha(x)}\phi(x) \ , \qquad A_\mu(x) \to A_\mu(x) + \frac{1}{e}\partial_\mu \alpha(x) \, . \tag{1.59}$$

Similar to the global case, the symmetry at the vacuum $|\phi| = \eta$ is spontaneously broken, and the field ϕ acquires a non-zero vacuum expectation value. We again study its properties representing the field as $\phi = \eta + \varphi/\sqrt{2}$, so that in the unitary gauge

$$\mathcal{L} = \frac{1}{2}\left(\partial_\mu \varphi\right)^2 + \frac{1}{2}m_\varphi^2\varphi^2 + \frac{1}{4}F_{\mu\nu}F^{\mu\nu} + \frac{1}{2}m_A^2 A_\mu A^\mu + \mathcal{L}_{\text{int}} \, , \tag{1.60}$$

where

$$m_\varphi = \sqrt{\lambda}\eta \, , \qquad m_A = \sqrt{2}e\eta \, . \tag{1.61}$$

We see that in this case the breaking of a gauge symmetry is not accompanied by a massless Goldstone boson, and instead, its corresponding degree of freedom is absorbed into the vector field, which becomes massive – the massless Goldstone boson is "eaten" by the vector field A^μ.

Cosmic strings [308, 448, 453, 442, 37, 38, 65, 271, 454] are one-dimensional structures that arise in models where a continuous symmetry is broken, such as the $U(1)$ gauge symmetry breaking that we have discussed. One possibility is that the symmetry-breaking transition is not "perfect" and false vacuum remnants are left behind when different regions of space decay to different ground states, see Fig. 1.2. As we traverse a closed path in physical space it is possible for ϕ to wrap once around the circle of minima, so that it develops a non-trivial winding, $\Delta\theta = 2\pi$. Then, the field far from the string centre takes the form

$$\phi \approx \eta e^{in\theta} \, , \tag{1.62}$$

where n is an integer known as the string winding number. We can keep measuring the winding on smaller loops as the path is shrunk to a point, up to the point in which reach the string centre. There, the phase of ϕ is not well-defined and $\Delta\theta$ cannot continuously change from $\Delta\theta = 2\pi$ to $\Delta\theta = 0$. There must then be one point contained within the path where the phase is undefined, which is when the field ϕ rises to the top of the potential, having a non-zero energy density, $V(0) = \lambda\eta^4/4$. The width of the string is determined by the Compton wavelengths of the Higgs and gauge bosons: $\delta_\varphi = m_\varphi^{-1}$ and $\delta_A = m_A^{-1}$, and in general the characteristic transverse dimension is far smaller than their length, so the can be treated as one-dimensional objects called strings. In this work we will restrict the parameter space to strings where $m_\varphi = m_A$, which happens in the so-called critical coupling limit when $\lambda = 2e^2 = 1$. Then, the total string mass per unit length can be computed to be [101, 285]

$$\mu = 2\pi\eta^2 \,. \tag{1.63}$$

Their coupling to gravity – and thus their gravitational effects – depend upon the dimensionless quantity

$$G\mu = 2\pi \left(\frac{\eta}{M_{\mathrm{Pl}}}\right)^2 \,, \tag{1.64}$$

known as the *string tension*. For GUT scale strings with $\eta \sim 10^{16}$ GeV, this corresponds to an enormous mass density $\mu \sim 10^{22}\ \mathrm{g\,cm^{-1}}$ and extremely small width $\delta \sim 10^{-30}$ cm.

Given that the width is much smaller than any cosmological scale, strings are often studied in the zero-width limit, or Nambu–Goto approximation. The metric of a zero-width static straight string lying along the z-axis in the linear approximation of general relativity is given by [450]

$$ds^2 = -dt^2 + dr^2 + (1 - 4G\mu)^2\, r^2 d\theta^2 + dz^2 \,. \tag{1.65}$$

Transforming the polar angle, $\theta \to (1 - 4G\mu)\,\theta$, the metric takes a flat-space Minkowskian form. However, the polar angle varies in the range $0 \leq \theta \leq 2\pi\,(1 - 4G\mu)$, introducing an azimuthal "deficit angle" of $8\pi G\mu$. This is referred to as a conical singularity and has interesting observational effects such as lensing, fluctuations in the cosmic microwave background and the formation of wakes that were thought to play an important role in structure formation. The network consisting of both infinite strings and closed loops is conformally stretched by the expansion of the universe and strings straighten themselves out due to their tension. Intercommutation of intersecting string segments [310] leads to the continual chopping up of long strings into smaller loops.

In the Nambu-Goto limit, when the radius of curvature of a string is much greater that its width, we can regard the string as a one-dimensional object, represented by a two-dimensional surface in spacetime – the string worldsheet

$$x^\mu = x^\mu(\sigma^0,\ \sigma^1)\,, \tag{1.66}$$

obeying the Nambu–Goto action [370, 230]

$$S = -\mu \int d^2\sigma \sqrt{-\gamma}\,, \tag{1.67}$$

where γ is the determinant of the worldsheet metric $\gamma_{ab} = g_{\mu\nu}x^{\mu}_{,a}x^{\nu}_{,b}$ and $g_{\mu\nu}$ is the four-dimensional metric that sets the spacetime interval between two nearby points in the worldsheet

$$ds^2 = g_{\mu\nu}x^{\mu}_{,a}x^{\nu}_{,b}d\sigma^a d\sigma^b \,. \tag{1.68}$$

In the limit in which gravitational effects are negligible and the strings are taken to be in flat spacetime neglecting any possible backreaction so that $g_{\mu\nu} = \eta_{\mu\nu}$, the string equations of motion take the simpler form

$$\partial_a\left(\sqrt{-\gamma}\gamma^{ab}x^{\mu}_{,b}\right) = 0 \,. \tag{1.69}$$

After clever parametrisations of the worldsheet, it can be shown that the equation of motion for the string reduces to a simple two-dimensional wave equation

$$\ddot{x}^{\mu} - x^{\mu\prime\prime} = 0 \,. \tag{1.70}$$

Setting $t \equiv x^0 = \sigma^0$ allows us to write the string trajectory as the three-vector $\mathbf{x}(t,\sigma)$, where $\sigma \equiv \sigma^1$ is the spacelike parameter on the string, and the contraints and equations of motion take the form

$$\dot{\mathbf{x}}\cdot\mathbf{x}' = 0 \,, \qquad \dot{\mathbf{x}}^2 + \mathbf{x}'^2 = 1 \,, \qquad \ddot{\mathbf{x}} - \mathbf{x}'' = 0 \,. \tag{1.71}$$

The physical meaning of the first equation is that the vector $\dot{x}$ representing the physically observable velocity is perpendicular to the string. The second constraint is the conservation of energy that can be written as $d\sigma = (1-\dot{\mathbf{x}}^2)^{-1/2}|d\mathbf{x}| = d\epsilon/\mu$, where

$$\epsilon = \mu\int(1-\dot{\mathbf{x}}^2)^{-1/2}dl = \mu\int d\sigma \,, \tag{1.72}$$

is the energy of the string and $dl = |d\mathbf{x}|$. Finally, the last equation implies that the acceleration of a string element in its local rest frame ($\dot{\mathbf{x}} = 0$) is inversely proportional to the local curvature radius, $|d^2\mathbf{x}/dl^2|$, so that the direction of $\ddot{\mathbf{x}}$ is such that a curved string tends to straighten.

A general solution of Eqn. (1.70) is

$$\mathbf{x}(\sigma,t) = \frac{1}{2}\left[\mathbf{a}(\sigma-t) + \mathbf{b}(\sigma+t)\right] \,, \tag{1.73}$$

with constraints $\mathbf{a}'^2 = \mathbf{b}'^2 = 1$. The geometric interpretation of these is that σ is the length parameter along the three-dimensional curves $\mathbf{a}(\sigma)$ and $\mathbf{b}(\sigma)$. Some of the most popular simulations are based on the study of networks of Nambu-Goto strings [389, 91, 96, 92, 93, 90, 405, 337, 347, 348, 309, 406, 456, 446, 380, 390].

As we will study cosmic string loops in Chapter 4, it is convenient to introduce the solution of a closed loop in the Nambu-Goto limit. Its motion is described by the previous equations, with $0 \leq \sigma \leq L$, where $L = M_0/\mu$ is the invariant length of the loop. For a circular loop of radius R_0, the energy is then

$$M_0 = \mu L = 2\pi\eta^2 L = 4\pi^2\eta^2 R_0\,. \tag{1.74}$$

Given the periodicity of a closed loop, we require $\mathbf{x}(\sigma + L,\ t) = \mathbf{x}(\sigma,\ t)$, which implies

$$\mathbf{b}(\sigma_+ + L) - \mathbf{b}(\sigma_+) = -\mathbf{a}(\sigma_- + L) + \mathbf{a}(\sigma_-)\,, \tag{1.75}$$

where we have defined $\sigma_\pm = \sigma \pm t$. In the centre-of-mass frame of the loop, $\mathbf{a}$ and $\mathbf{b}$ are periodic functions

$$\mathbf{a}(\sigma + L) = \mathbf{a}(\sigma)\,, \qquad \mathbf{b}(\sigma + L) = \mathbf{b}(\sigma)\,, \tag{1.76}$$

Then it is clear from Eqn. (1.73) that the motion of the loop must also be periodic in time, with period $T = L/2$, since

$$\mathbf{x}(\sigma + L/2, t + L/2) = \mathbf{x}(\sigma, t)\,, \tag{1.77}$$

and the fact that the timescale of the oscillation is comparable to the loop length indicates that the motion must be relativistic. More precisely, if we think about a string loop of initial radius R_0 in the $z = 0$ plane, the $\mathbf{a}(\sigma)$ and $\mathbf{b}(\sigma)$ curves in polar coordinates

$$\mathbf{a}(\sigma) = \left\{R_0 \cos\left(\sigma/R_0\right),\ R_0 \sin\left(\sigma/R_0\right),\ 0\right\}\ , \tag{1.78}$$

$$\mathbf{b}(\sigma) = \left\{R_0 \cos\left(\sigma/R_0\right),\ R_0 \sin\left(\sigma/R_0\right),\ 0\right\}\ . \tag{1.79}$$

satisfy the constraints. After using simple trigonometric identities, the solution via Eqn. (1.73) is then

$$\mathbf{x}(\sigma, t) = R_0 \cos\left(t/R_0\right)\left\{\cos\left(\sigma/R_0\right),\ \sin\left(\sigma/R_0\right),\ 0\right\}\ , \tag{1.80}$$

so that the radial trajectory and velocity of the loop is given by

$$R(t) = R_0 \cos\left(t/R_0\right) \;, \qquad v(t) = \sin\left(t/R_0\right) \;, \tag{1.81}$$

precisely showing the ultrarelativistic nature of the collapse.

From the Nambu-Goto perspective the loop would forever oscillate under its tension. However, the string width $\delta = (\sqrt{\lambda}\eta)^{-1}$ introduces a cutoff scale for the oscillation, where its Nambu-Goto description breaks down. In this regime, field theory simulations must evolve the equations of motion derived from the Lagrangian to understand the dynamics of individual strings [418, 330, 350, 328, 52, 329, 419, 22, 206, 378, 379, 349, 414], or the whole network [455, 353, 85, 336, 270]. Most of these studies are based on the traditional "fixed grid" approach, where a single mesh containing a constant number of grid points resolves the evolution of the system. There exists computational limitations to this approach given the dynamical nature of interesting scales that can evolve and differ by orders of magnitude, such as the string width and size of the network. An attempt to fix this and resolve the string core throughout the simulations is adopting the so-called "fat-string" approach, where the string width artificially grows to match the comoving grid resolution. However, the extracted radiation rate predictions differ from results of Nambu-Goto network simulations [455, 379, 405, 423, 337, 91, 92, 96, 336]. A promising approach to accurately resolve these differences is the use of Adaptive Mesh Refinement (AMR), which allows to dynamically adapt and concentrate the computational power near the string core, to study the massless and massive radiative modes of strings (see promising work in [186, 187]).

What is next?

When the Nambu-Goto limit is not valid, we need to solve the field theory equations of motion for the strings. Moreover, even for light strings with $G\mu \ll 1$, the system can evolve into a configuration where gravitational effects dominate and need to be taken into account in the dynamics – such as the endpoint of a collapsing loop. There has recently been interesting progress in incorporating the linearized gravitational backreaction of Nambu-Goto strings and estimate its effect on the smoothing of these structures [457, 458, 95, 145, 97, 407], but most of previous work is based on numerical simulations that neglect their full gravitational description. In this thesis, we will present the first general relativistic simulations of cosmic strings using numerical relativity. We will make use of the AMR capabilities of GRCHOMBO [55, 154, 400] to accurately resolve the string core as the system evolves. Moreover, motivated by recent gravitational-wave detections by the LVK network of interferometers and their particular interest in cosmic strings [6, 1, 4, 15, 13, 18], in Chapter 4 we will construct the first-ever gravitational chirp waveform of a collapsing circular cosmic string loop.

1.2.3 Primordial black holes

As we have discussed, the early universe had inhomogeneities that led to the formation of the galaxies we observe today. These local fluctuations in the density could have also underwent gravitational collapse to produce black holes, which would then grow by accreting nearby matter [474, 252, 136]. These are known as primordial black holes (PBHs) and due to their very unique properties, they are often invoked to resolve various cosmological puzzles.

Unlike stellar black holes that form from the collapse of massive stars and can only present masses above $\sim 3M_\odot$, primordial black holes can widely vary in mass range. For example, they can be small enough for Hawking radiation to take place – where particles are emitted as the black holes evaporate. This phenomena brings together general relativity, thermodynamics and quantum mechanics, opening up an intriguing avenue for hints of a theory of quantum gravity.

More importantly, PBHs could alleviate some problems associated with the standard cold dark matter scenario [144, 129, 128], which comprises $\sim 25\%$ of the energy density in the universe today. This is often characterised in the parameter $f_{\rm PBH}$, conveying the energy fraction of dark matter that is in PBHs

$$f_{\rm PBH} \equiv \frac{\Omega_{\rm PBH}}{\Omega_{\rm DM}} \,, \tag{1.82}$$

where Ω corresponds to the energy density and critical density fractions today. In the case in which PBHs make up all the dark matter in the universe, $f_{\rm PBH} = 1$.

There exists several channels to detect PBHs, estimating what fraction of the dark matter they comprise ($f_{\rm PBH}$), and providing stringent constraints on models of the early universe, see Fig. 1.3. For example, black holes smaller than $10^{15} g$ would have evaporated by today, placing strong bounds on galactic and extra-galactic γ-ray backgrounds, short bursts and cosmic rays [382, 133, 467, 332, 311, 339, 149]. PBHs with masses larger than $10^{15} g$ would still be present today having important astrophysical consequences. For example, lensing effects [261, 39] constrain masses around $10^{22} - 10^{34} g$, dynamical effects such as the heating of the stars or the thermal history of the universe $10^3 - 10^{13} M_\odot$ [24, 404], gravitational waves solar mass PBHs

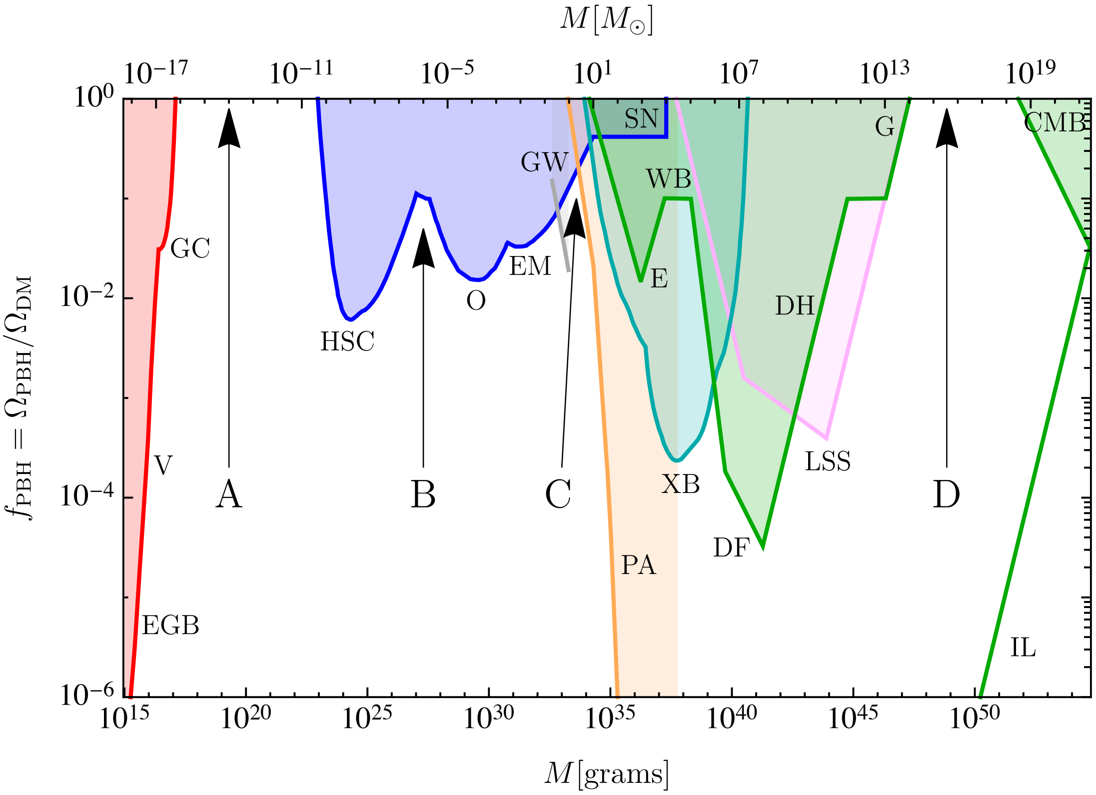

Fig. 1.3 Fraction of PBH dark matter and observational constraints for a monochromatic mass function, from evaporation (red), lensing (blue), GWs (gray), dynamical effects (green), accretion (light blue), CMB distortions (orange), and large-scale structure (purple). The four mass windows A, B, C and D correspond to PBHs that could account for a relevant fraction of the dark matter density. Figure from [128].

$1 - 10^2 M_\odot$ [5, 11, 19, 20] and the generation of large-scale structure [139, 80, 351] the intermediate and supermassive range $10^2 - 10^{13} M_\odot$. Figure 1.3 shows the existence of four main mass windows where PBHs could account for a relevant fraction of all of the dark matter in the universe.

Even though the precise origin of these black holes is still unknown, the most popular mechanism for PBH formation is through the collapse of superhorizon-sized inhomogeneities that were generated and enhanced during cosmic inflation. When inflation ends and the standard Hot Big Bang era starts, these primordial fluctuations re-enter the horizon and can collapse to form black holes [131, 241, 394, 412, 248, 368, 360, 222, 362]. Another possible channel to produce PBHs of a wide mass range is via the collapse of cosmic strings [273, 253, 393, 220, 120, 99, 338, 462, 245, 366, 137, 109, 84, 286].

What is next?

Numerical relativity provides the techniques to study PBH formation channels without the need of making any assumptions. The study of alternative mechanisms could lead to the formation of PBHs with distinct properties, such as low-mass but highly spinning PBHs. In this thesis, we will study the collapse of sub and superhorizon-sized scalar perturbations in a matter dominated era with full numerical relativity. Our main goal is to quantitatively investigate (i) what parameters control the formation of the PBHs (ii) what is the fraction of energy that goes into the PBH mass compared to the Hubble horizon.

Chapter 2

Numerical relativity

In this chapter we will introduce the techniques to solve Einstein's equations numerically [77, 40]. We will start by presenting the 3+1 decomposition of general relativity (or ADM formalism [58]), which consists in splitting the space and time coordinates in order to formulate the system of equations as an initial value problem. This decomposition results in four constraints and a set of evolution equations that are known to be numerically problematic due to their weak-hyperbolic properties. Then, we will devise several approaches to solve the constraint equations, including a novel prescription for initial data consisting of fundamental fields [62]. Lastly, we will introduce the BSSN formalism [421, 79], a reformulation with strongly-hyperbolic properties and also mention about useful dynamical gauge conditions that allow for long-term stable simulations of black hole spacetimes.

2.1 3+1 decomposition

2.1.1 Foliation of spacetime

As seen in Chapter 1, the covariant formulation of Einstein's equations makes them incredibly elegant. However, it also entails a challenge to solve them as an initial value problem[1]. We would like to recast them in a 3+1 form where the roles of space and time are split. To do this, we foliate the full spacetime into a family of non-intersecting three-dimensional spacelike surfaces Σ, where each surface is identified by a different value of a scalar parameter t interpreted as a global time function, Fig. (2.1).

---

[1] Also called Cauchy problem, in which the solution is obtained evolving the data from a given time t to a later time $t + dt$.

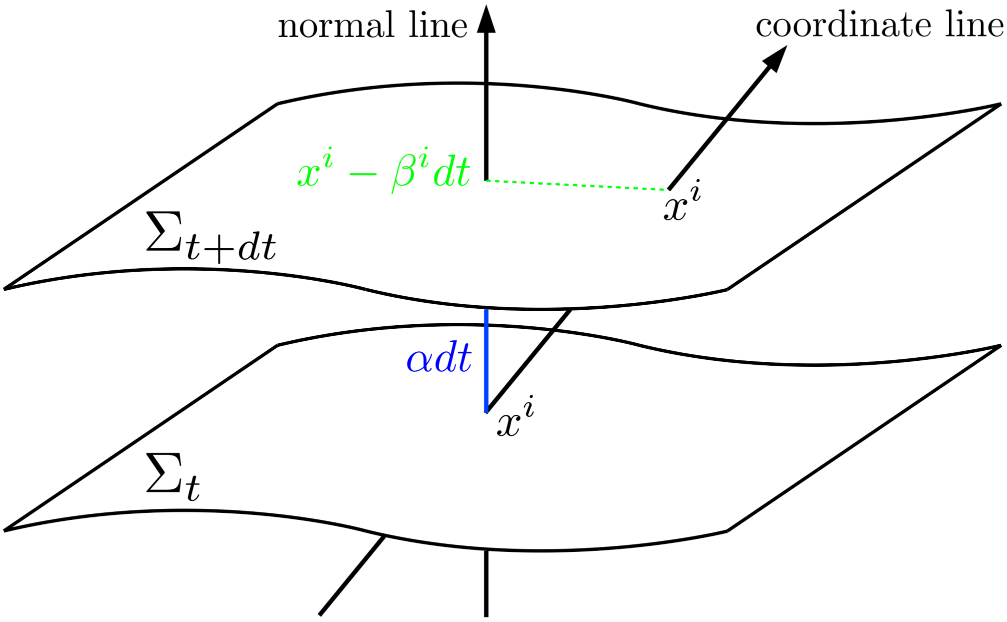

Fig. 2.1 Foliation of spacetime by three-dimensional spacelike surfaces Σ. The lapse function α measures how much proper time elapses between neighboring hyperslices along the normal vector. The shift functions β^i measure the amount by which the spatial coordinates are shifted within a slice with respect to the normal vector.

Focusing on two of these slices at different times, we introduce the following key definitions

• $dl^2 = \gamma_{ij} dx^i dx^j\,,$	spatial line element on the surface.
• $d\tau = \alpha(t, x^i) dt\,,$	$\alpha(t, x^i)$ lapse function.
• $x^i_{t+dt} = x^i_t - \beta^i(t, x^i) dt\,,$	$\beta^i(t, x^i)$ shift function.

The functions α and β^i measure how much proper time elapses between neighboring time slices along the normal vector to the slice and the amount by which the spatial coordinates are shifted within a slice with respect to the normal vector, respectively. Given the coordinate freedom, both α and β^i are non-unique gauge functions that will determine how the coordinates evolve in time. As we will see later, their choice is crucial to obtain long-term stable numerical simulations.

Following a geometric argument in Fig. (2.1), it can be shown that the spacetime line element is expressed in terms of these quantities as

$$ds^2 = -\alpha^2 dt^2 + \gamma_{ij}(dx^i + \beta^i dt)(dx^j + \beta^j dt)\,, \tag{2.1}$$

and the four-dimensional metric and its inverse are identified as

$$g_{\mu\nu} = \begin{pmatrix} -\alpha^2 + \beta_k\beta^k & \beta_i \\ \beta_j & \gamma_{ij} \end{pmatrix} , \qquad g^{\mu\nu} = \begin{pmatrix} -1/\alpha^2 & \beta^i/\alpha^2 \\ \beta^j/\alpha^2 & \gamma^{ij} - \beta^i\beta^j/\alpha^2 \end{pmatrix} . \tag{2.2}$$

We define the unit vector normal to the 3-surfaces as

$$n_\mu = (-\alpha, 0) \qquad n^\mu = (1/\alpha, -\beta^i/\alpha) . \tag{2.3}$$

In addition, the spatial metric induced by $g_{\mu\nu}$ on each 3-surface Σ is

$$\gamma_{\mu\nu} = g_{\mu\nu} + n_\mu n_\nu , \tag{2.4}$$

which is nothing but the projection operator onto spatial surfaces

$$P^\mu_\nu \equiv \gamma^\mu_\nu = \delta^\mu_\nu + n^\mu n_\nu . \tag{2.5}$$

The unit normal vector can then be rewritten in terms of α and $\nabla_\mu t$

$$n^\mu = -\alpha \nabla^\mu t , \tag{2.6}$$

with

$$g^{\mu\nu}\nabla_\mu t \nabla_\nu t \equiv \frac{-1}{\alpha^2} . \tag{2.7}$$

The minus sign in (2.6) is chosen such that n^μ points in the direction of increasing t as shown in figure (2.1). It is easy to show that n^μ is timelike

$$n^\mu n_\mu = g_{\mu\nu} n^\mu n^\nu = \alpha^2 g_{\mu\nu} \nabla^\mu t \nabla^\nu t = \alpha^2 \left(\frac{-1}{\alpha^2} \right) = -1 . \tag{2.8}$$

A key ingredient is to define the time vector using n^μ and β^μ:

$$t^\mu = \alpha n^\mu + \beta^\mu , \tag{2.9}$$

which is tangent to time lines. It is useful to choose t^μ to be the congruence along which the spatial coordinate grid is propagated from one time slice to the next one. In other words, t^μ connects points with the same spatial coordinates on neighbouring time slices.

When the spacetime is foliated, a clear distinction between intrinsic and extrinsic curvatures is often done:

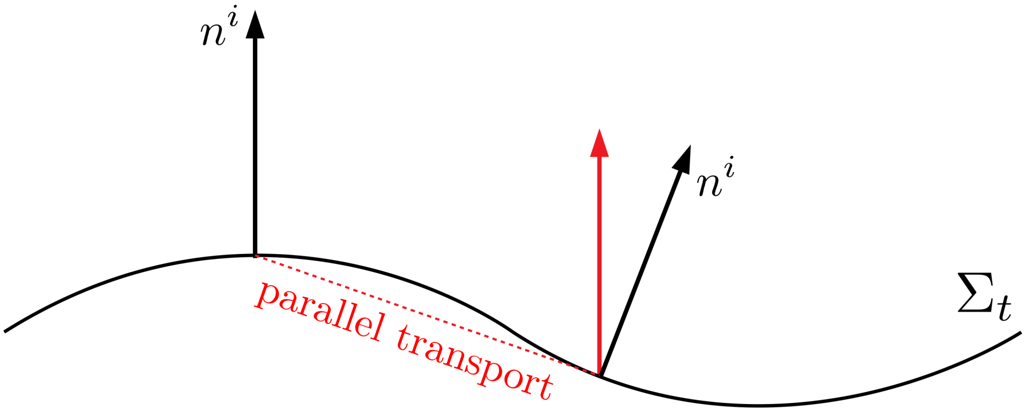

Fig. 2.2 The extrinsic curvature is defined as the change of the normal vector under parallel transport on a curved hypersurface. It measures the rate at which the slice deforms as it is carried forward along a normal.

- The intrinsic curvature is the curvature of the hypersurfaces. It is given by the three-dimensional Riemann tensor ${}^{(3)}R$ defined as usual by (1.6) but using the metric of the 3-surface γ_{ij}.
- The extrinsic curvature is related to how the 3-surfaces are immersed within the full spacetime. It is defined in terms of how much the direction of the normal vector changes as it is parallelly transported from one point in the hypersurface to another. The extrinsic curvature measures the rate at which the hypersurface deforms as it is carried forward along a normal, Fig. (2.2).

The extrinsic curvature can be found by projecting gradients of the normal vector into the slice Σ

$$K_{\mu\nu} = -P^{\alpha}_{\mu} P^{\beta}_{\nu} \nabla_{\alpha} n_{\beta} = -(\nabla_{\mu} n_{\nu} + n_{\mu} n^{\alpha} \nabla_{\alpha} n_{\nu}) \,, \tag{2.10}$$

where $n^{\beta} n_{\beta} = -1 \Longrightarrow n^{\beta} \nabla_{\alpha} n_{\beta} = 0$. Given the definition of $K_{\mu\nu}$, it is clear that it is symmetric and purely spatial

$$n^{\mu} K_{\mu\nu} = -(n^{\mu} \nabla_{\mu} n_{\nu} + n^{\mu} n_{\mu} n^{\alpha} \nabla_{\alpha} n_{\nu}) = -(n^{\mu} \nabla_{\mu} n_{\nu} - n^{\alpha} \nabla_{\alpha} n_{\nu}) = 0 \,. \tag{2.11}$$

so that it is possible to only consider spatial components of the extrinsic curvature tensor K_{ij}, where $(i,\, j)$ take values from one to three.

Using the definition of the Lie derivative we can relate the definition of $K_{\mu\nu}$ to the first time derivative of the spatial metric γ_{ij}

$$\begin{aligned}
\pounds_{\vec{n}}\gamma_{\mu\nu} &= n^\alpha\nabla_\alpha\gamma_{\mu\nu} + \gamma_{\mu\alpha}\nabla_\nu n^\alpha + \gamma_{\nu\alpha}\nabla_\mu n^\alpha \\
&= n^\alpha\nabla_\alpha(g_{\mu\nu} + n_\mu n_\nu) + (g_{\mu\alpha} + n_\mu n_\alpha)\nabla_\nu n^\alpha + (g_{\nu\alpha} + n_\nu n_\alpha)\nabla_\mu n^\alpha \\
&= n^\alpha\nabla_\alpha(n_\mu n_\nu) + g_{\mu\alpha}\nabla_\nu n^\alpha + g_{\nu\alpha}\nabla_\mu n^\alpha \\
&= n^\alpha n_\nu\nabla_\alpha n_\mu + n^\alpha n_\mu\nabla_\alpha n_\nu + \nabla_\nu n_\mu + \nabla_\mu n_\nu = -K_{\mu\nu} - K_{\nu\mu} = -2K_{\mu\nu}\,,
\end{aligned}$$

where the symmetry properties of $K_{\mu\nu}$, $\nabla_\alpha g_{\mu\nu} = 0$ and again $n^\alpha\nabla_\mu n_\alpha = 0$ have been used. Therefore, the extrinsic curvature tensor can be rewritten in a very compact form

$$K_{\mu\nu} = -\frac{1}{2}\pounds_{\vec{n}}\gamma_{\mu\nu}\,. \tag{2.12}$$

The trace of the extrinsic curvature, often called the mean curvature or expansion

$$K = g^{\mu\nu}K_{\mu\nu} = -\pounds_{\vec{n}}\gamma^{1/2}\,, \tag{2.13}$$

measures the fractional change in the proper 3-volume along n^μ. Following the definition of the time vector (2.9) and properties of the Lie derivatives[2], the definition can be split into a time vector $\vec{t}$ and a shift vector $\vec{\beta}$ parts

$$K_{\mu\nu} = -\frac{1}{2\alpha}\pounds_{\alpha\vec{n}}\gamma_{\mu\nu} = -\frac{1}{2\alpha}\left(\pounds_{\vec{t}} - \pounds_{\vec{\beta}}\right)\gamma_{\mu\nu}\,, \tag{2.14}$$

so that $\pounds_{\vec{t}}\gamma_{\mu\nu} = -2\alpha K_{\mu\nu} + \pounds_{\vec{\beta}}\gamma_{\mu\nu}$, and in an adapted coordinate system where $\pounds_{\vec{t}} = \partial_t$,

$$\partial_t\gamma_{ij} = -2\alpha K_{ij} + \pounds_{\vec{\beta}}\gamma_{ij}\,. \tag{2.15}$$

The metric and the extrinsic curvature (γ_{ij}, K_{ij}) are the fundamental variables of our initial value formulation and can be considered as the equivalent of positions and velocities in classical mechanics, measuring the instantaneous state of the gravitational field.

2.1.2 Foliation of Einstein's equations

As we have described in the first chapter, the dynamics of the gravitational field is contained in Einstein's field equations. However, so far we have only introduced the tools to foliate the spacetime into three-dimensional hypersurfaces. In this section, we

---

[2] It can be shown that $\pounds_{\vec{v}} = (1/k)\pounds_{k\vec{v}}$.

will apply such techniques in order to recast Einstein equations in a 3+1 form. The way to procceed is to contract their covariant form with the normal vector n^μ and the spatial projector P^μ_ν different number of times. This is not a difficult but tedious process and in this chapter we will only present the final results, but an extensive and detailed derivation can be found in Appendix A.

If all the indices of the four-dimensional Riemannian tensor are projected onto spatial hypersurfaces, the *Gauss-Codazzi* equations are obtained

$$P^\delta_\alpha P^\kappa_\beta P^\lambda_\mu P^\sigma_\nu R_{\delta\kappa\lambda\sigma} = {}^{(3)}R_{\alpha\beta\mu\nu} + K_{\alpha\mu}K_{\beta\nu} - K_{\alpha\nu}K_{\beta\mu}. \tag{2.16}$$

If instead, only three indices are projected and one is contracted with the normal unit vector, the obtained equations are the *Codazzi-Mainardi* equations

$$P^\delta_\alpha P^\kappa_\beta P^\lambda_\mu n^\nu R_{\delta\kappa\lambda\nu} = D_\beta K_{\alpha\mu} - D_\alpha K_{\beta\mu}, \tag{2.17}$$

where D_μ is the projected covariant derivative $D_\mu \equiv P^\alpha_\mu \nabla_\alpha$.

On the other hand, note that if only two indices (not the trivial antisymmetric indices of the Riemannian tensor) are contracted with the spatial projection operator

$$\begin{aligned} P^{\alpha\mu}P^{\beta\nu}R_{\alpha\beta\mu\nu} &= (g^{\alpha\mu} + n^\alpha n^\mu)(g^{\beta\nu} + n^\beta n^\nu)R_{\alpha\beta\mu\nu} \\ &= R + 2n^\mu n^\nu R_{\mu\nu} = 2n^\mu n^\nu G_{\mu\nu}, \end{aligned} \tag{2.18}$$

since the term with $n^\alpha n^\mu n^\beta n^\nu R_{\alpha\beta\mu\nu}$ vanishes due to the antisymmetry properties of $R_{\alpha\beta\mu\nu}$, and $G_{\mu\nu} = R_{\mu\nu} - Rg_{\mu\nu}/2$.

Therefore, from Eqns. (2.16), (2.18) and $G_{\mu\nu} = 8\pi T_{\mu\nu}$, with $G = c = 1$, we obtain the first important result, the *Hamiltonian constraint*

$$\boxed{{}^{(3)}R + K^2 - K_{\mu\nu}K^{\mu\nu} = 16\pi\rho\,,} \tag{2.19}$$

where $\rho \equiv n^\mu n^\nu T_{\mu\nu}$ is the local energy density measured by Eulerian observers[3]. Considering now

$$\begin{aligned} P^{\alpha\mu}n^\nu G_{\mu\nu} &= (g^{\alpha\mu} + n^\alpha n^\mu)n^\nu \left(R_{\mu\nu} - \frac{1}{2}Rg_{\mu\nu}\right) \\ &= P^{\alpha\mu}n^\nu R_{\mu\nu} - \frac{1}{2}n^\alpha R + \frac{1}{2}n^\alpha R = P^{\alpha\mu}n^\nu R_{\mu\nu}, \end{aligned} \tag{2.20}$$

---

[3] It is the observer with four-velocity n^μ.

and together with the contraction of the Codazzi-Mainardi equations (2.17)

$$g^{\alpha\mu} P^{\delta}_{\alpha} P^{\kappa}_{\beta} P^{\lambda}_{\mu} n^{\nu} R_{\delta\kappa\lambda\nu} = P^{\kappa}_{\beta} n^{\nu} R_{\kappa\nu} = g^{\alpha\mu} \left(D_\beta K_{\alpha\mu} - D_\alpha K_{\beta\mu} \right), \tag{2.21}$$

Defining the momentum density measured by Eulerian observers as $S^\alpha \equiv -P^{\alpha\mu} n^\nu T_{\mu\nu}$, the second important result is obtained, the *momentum constraints*.

$$\boxed{D_\mu \left(K^{\alpha\mu} - \gamma^{\alpha\mu} K \right) = 8\pi S^\alpha \,.} \tag{2.22}$$

Equations (2.19) and (2.22) show that in order to be consistent with Einstein's equations, the metric γ_{ij} and the extrinsic curvature K_{ij} cannot be chosen arbitrarily and instead, they need to satisfy the Hamiltonian and momentum constraints at all times. In addition, they do not depend on the gauge functions, so they have to be satisfied regardless of the choice of coordinates.

However, we are interested not only in finding the initial data for a gravitational system but also the evolution at later times. Hence, it is inevitable to derive equations that involve time derivatives of spacetime quantities. Although when introducing the definition of the extrinsic curvature tensor Einstein's equations were not discussed, an evolution equation for the spatial metric had already been introduced in (2.15).

$$\boxed{\pounds_{\vec{t}} \gamma_{\mu\nu} = -2\alpha K_{\mu\nu} + \pounds_{\vec{\beta}} \gamma_{\mu\nu} \,.} \tag{2.23}$$

The evolution equation for the extrinsic curvature tensor $K_{\mu\nu}$ is more subtle so the result is presented here and its derivation is in Appendix A

$$\boxed{\begin{aligned} \pounds_{\vec{t}} K_{\mu\nu} = & - D_\mu D_\nu \alpha + \alpha \left[{}^{(3)}R_{\mu\nu} + K K_{\mu\nu} - 2 K_{\mu\lambda} K^{\lambda}_{\nu} \right] \\ & + 4\pi\alpha \left[\gamma_{\mu\nu} \left(S - \rho \right) - 2 S_{\mu\nu} \right] + \pounds_{\vec{\beta}} K_{\mu\nu} \,, \end{aligned}} \tag{2.24}$$

where $S_{\mu\nu} \equiv P^{\alpha}_{\mu} P^{\beta}_{\nu} T_{\alpha\beta}$ is the spatial stress tensor measured by Eulerian observers and S is its trace. The Eqns. (2.19), (2.22), (2.23) and (2.24) are equivalent to Einstein's equations and are usually referred to as the ADM decomposition [58].

2.2 Initial data and the constraint equations

One of the most important (and often hardest) steps in numerical relativity simulations is the construction of constraint satisfying initial data. As we have seen, there is no complete freedom in choosing of such data, and the spatial metric γ_{ij}, the extrinsic curvature K_{ij} and any matter fields need to satisfy the Hamiltonian and momentum constraints. If the provided “starting values” are not compatible, results from their dynamical evolution lack of any relevant physical interest.

The Hamiltonian constraint (Eqn. (2.19)) and the three momentum constraints (Eqn. (2.22)) can only determine 4 of the 12 independent components of the gravitational fields (γ_{ij}, K_{ij}) – symmetric and 3-dimensional tensors – leaving 8 undetermined. Four of these eight undetermined functions are related to coordinate choices: three specify the spatial coordinates within the slice, and one associated with the time coordinate, chooses the hypersurface. Hence, there are four undetermined functions that represent the two dynamical degrees of freedom characterizing a gravitational field in general relativity – two independent sets of values for the conjugate pair (γ_{ij}, K_{ij}) – corresponding to the two polarization modes of a gravitational wave in GR. Ideally one would like to separate unambiguously the longitudinal from the transverse parts of the gravitational fields at some initial time – so that we specify the latter and then solve the constraints for the former. However, this is not possible given the non-linear nature of general relativity.

The approach to the solution of Einstein’s initial value equations is: We first decide which field variables we want to determine by solving the constraint equation – we choose a particular decomposition of the constraint equations. Then, we make choices for the remaining freely specifiable variables. These choices will in general reflect the physical problem that we are trying to solve, but may also be guided by any resulting simplifications that they induce in the constraint equations, or even numerical advantages such as improvements in convergence, as we will see later.

2.2.1 Conformal transverse-traceless decomposition

Given the hyperbolic nature of the wave equation, its solution at any time depends on its past history. Constraint equations, on the other hand, are elliptic equations and constrain the fields in space at every instant of time, independently of their past history. So if constraints are satisfied at the initial hyperslice, they should remain under control throughout the numerical simulation[4].

We start by writing the spatial metric γ_{ij} as a product of a conformal factor ψ and a background metric $\bar{\gamma}_{ij}$. To solve the constraint equations it is convenient to decompose it as

$$\gamma_{ij} = \psi^4 \bar{\gamma}_{ij} \,, \tag{2.25}$$

---

[4] This is in fact one of the most robust tests to check whether evolution equations are correctly implemented and results can be trusted.

with $\bar{\gamma} = \det\bar{\gamma}_{ij} = 1$. The conformal factor absorbs the overall scale of the metric and leaves five degrees of freedom in the conformally related metric $\bar{\gamma}_{ij}$. One can show that given this choice, the Hamiltonian constraint reduces to

$$8\bar{D}^2\psi - \psi\bar{R} - \psi^5 K^2 + \psi^5 K_{ij}K^{ij} = -16\pi\psi^5\rho\,, \tag{2.26}$$

where $\bar{D}^2 = \bar{\gamma}^{ij}\bar{D}_i\bar{D}_j$ is the covariant Laplace operator associated with $\bar{\gamma}_{ij}$. Given a choice of the conformal metric $\bar{\gamma}_{ij}$, the Hamiltonian constraint provides a differential equation for the conformal factor ψ.

We split the extrinsic curvature tensor into its trace and traceless part

$$K_{ij} = A_{ij} + \frac{1}{3}\gamma_{ij}K\,, \tag{2.27}$$

which we then conformally transform[5]. A choice that brings constraint equations into a simpler form is taking

$$A_{ij} = \psi^{-2}\bar{A}_{ij}\,, \tag{2.28}$$

$$K = \bar{K}\,, \tag{2.29}$$

so that $D_jA^{ij} = \psi^{-10}\bar{D}_j\left(\bar{A}^{ij}\right)$ and the constraints become

$$8\bar{D}^2\psi - \psi\bar{R} - \frac{2}{3}\psi^5K^2 + \psi^{-7}\bar{A}_{ij}\bar{A}^{ij} = -16\pi\psi^5\rho, \tag{2.30}$$

$$\bar{D}_j\bar{A}^{ij} - \frac{2}{3}\psi^6\bar{\gamma}^{ij}\bar{D}_jK = 8\pi\psi^{10}S^i\,. \tag{2.31}$$

Any symmetric, traceless tensor such as $\bar{A}^{ij}$ can be split into a transverse-traceless part that is divergenceless and a longitudinal part that can be written as a symmetric, traceless gradient of a vector. So we can decompose $\bar{A}^{ij}$ as

$$\bar{A}^{ij} = \bar{A}^{ij}_{\mathrm{TT}} + \bar{A}^{ij}_{\mathrm{L}}\,, \tag{2.32}$$

where the transverse part is divergenceless $\bar{D}_j\bar{A}^{ij}_{\mathrm{TT}} = 0$ and the longitudinal part satisfies

$$\bar{A}^{ij}_{\mathrm{L}} = \bar{D}^iW^j + \bar{D}^jW^i - \frac{2}{3}\bar{\gamma}^{ij}\bar{D}_kW^k\,. \tag{2.33}$$

---

[5] Note that this is a different conformal rescaling for $\bar{A}_{ij}$ than the one we will introduce in the next section for $\tilde{A}_{ij}$.

We can now write the divergence of $\bar{A}^{ij}$ as

$$\bar{D}_j \bar{A}^{ij} = \bar{D}_j \bar{A}^{ij}_{\mathrm{L}} = \bar{D}^2 W^i + \frac{1}{3}\bar{D}^i \left(\bar{D}_j W^j\right) + \bar{R}^i{}_j \equiv \left(\bar{\Delta}_{\mathrm{L}} W\right)^i , \tag{2.34}$$

where $\bar{\Delta}_{\mathrm{L}}$ is the vector Laplacian. Hence, the momentum constraints are rewritten as

$$\left(\bar{\Delta}_{\mathrm{L}} W\right)^i - \frac{2}{3}\psi^6 \bar{\gamma}^{ij} \bar{D}_j K = 8\pi \psi^{10} S^i , \tag{2.35}$$

while the Hamiltonian constraint remains unchanged.

We can freely choose the conformally related metric $\bar{\gamma}_{ij}$, the mean curvature K and the transverse-traceless part of the conformally related extrinsic curvature, $\bar{A}^{ij}_{\mathrm{TT}}$. Given these choices, we will solve the Hamiltonian and momentum constraints for ψ and the vector potential W^i, and then we can construct the physical solutions γ_{ij} and K_{ij}.

Counting degrees of freedom: We started with 6 in γ_{ij} and 6 in K_{ij}. Now 1 in ψ, 5 in $\bar{\gamma}_{ij}$, 1 in K, 2 in $\bar{A}^{ij}_{\mathrm{TT}}$ and 3 in $\bar{A}^{ij}_{\mathrm{L}}$. So if we specify the 8 degrees of freedom in $\bar{\gamma}_{ij}$, K and $\bar{A}^{ij}_{\mathrm{TT}}$, the four constraint equations will fix the remaining 4 degrees of freedom in ψ and $\bar{A}^{ij}_{\mathrm{L}}$.

Solving the vector Laplacian

In the rest of this section we will restrict to conformally flat spacetimes ($\bar{\gamma}_{ij} = \delta_{ij}$, $\bar{R} = 0$) where the vector Laplacian $(\bar{\Delta}_{\mathrm{L}} W)^i$ in Cartesian coordinates reduces to

$$\left(\bar{\Delta}_{\mathrm{L}} W\right)^i = \partial^j \partial_j W^i + \frac{1}{3}\partial^i \partial_j W^j . \tag{2.36}$$

Below we present two methods that can lead to different numerical convergence properties, depending on the physical system studied.

- One approach [105, 106] to solve this equation is based on writing the vector field W_i as a sum of another vector field V_i and the gradient of a scalar field U,

  $$W_i = V_i + \partial_i U , \tag{2.37}$$

  so that the vector Laplacian is expressed as

  $$\left(\bar{\Delta}_{\mathrm{L}} W\right)_i = \partial^j \partial_j V_i + \frac{1}{3}\partial_i \partial^j V_j + \partial^j \partial_j \partial_i U + \frac{1}{3}\partial_i \partial^j \partial_j U . \tag{2.38}$$

We have the freedom to choose U in such a way that it cancels the second term in the equation above,

$$\boxed{\partial^j\partial_j U = -\frac{1}{4}\partial_j V^j \ .} \tag{2.39}$$

The vector Laplacian reduces to a very simple form of three flat-space Poisson equations for V_i and the momentum constraints are

$$\boxed{\partial^j\partial_j V_i - \frac{2}{3}\psi^6\partial_i K = 8\pi\psi^6 S_i \ .} \tag{2.40}$$

- A second approach [420, 369] chooses

  $$W_i = \frac{7}{8}V_i - \frac{1}{8}\left(\partial_i U + x^k\partial_i V_k\right) \ , \tag{2.41}$$

  so that the momentum constraint yields

  $$\frac{5}{6}\partial^j\partial_j V_i - \frac{1}{6}\partial_i\partial^j\partial_j U - \frac{1}{6}x^k\partial_i\partial^j\partial_j V_k - \frac{2}{3}\psi^6\partial_i K = 8\pi\psi^6 S_i \, . \tag{2.42}$$

  If we choose U such that

  $$\boxed{\partial^j\partial_j U = -8\pi\psi^6 x^j S_j + \frac{2}{3}\psi^6\partial_j K \, ,} \tag{2.43}$$

  then

  $$\frac{5}{6}\partial^j\partial_j V_i - \frac{1}{6}\partial_i\partial^j\partial_j U - \frac{1}{6}x^k\partial_i\partial^j\partial_j V_k - \frac{2}{3}\psi^6\partial_i K = 8\pi\psi^{10} S_i \, , \tag{2.44}$$

  which is solved by

  $$\boxed{\partial^j\partial_j V_i = 8\pi\psi^6 S_i + \frac{2}{3}\psi^6\partial_i K \, .} \tag{2.45}$$

We can solve the (*non-linear*) Hamiltonian constraint by expanding around a "guess" solution $\psi = \psi_0 + \delta\psi$ and solving for $\delta\psi$ as a *linear* differential equation iteratively. Note that in general, the matter sources will also depend on the conformal factor ψ and thus they should be linearised accordingly too. In the next subsections, we will solve these equations for different physical systems. We will start by reviewing solutions in vacuum, the so-called Bowen-York solutions of the momentum constraint, where we will find the initial data for boosted and rotating black holes. Then, we will introduce a novel approach to solve the constraints when matter terms are present, avoiding a uniqueness problem that the Hamiltonian constraint possesses. To conclude, we will describe the most general case to obtain constraint satisfying initial data for a mixed system containing both black holes and matter fields.

2.2.2 Solutions with black holes

We begin by looking at vacuum solutions for which the matter source terms vanish, $\rho = S^i = 0$. At a moment of time symmetry, momentum constraints are trivially satisfied by choosing $K_{ij} = K = 0$. The Hamiltonian constraint then reduces to

$$\bar{D}^2\psi = \frac{1}{8}\psi\bar{R}\,, \tag{2.46}$$

where $\bar{R}$ is the Ricci scalar associated to the conformal metric $\bar{\gamma}_{ij}$. Choosing the conformally related metric to be flat $\bar{\gamma}_{ij} = \eta_{ij}$ makes $\bar{D}_i$ reduce to the standard flat covariant derivative so that $\bar{D}^2 = \partial^i\partial_i$ and the Ricci scalar vanishes $\bar{R} = 0$. The Hamiltonian constraint then becomes

$$\partial^i\partial_i\psi = 0\,. \tag{2.47}$$

Asymptotically flat solutions with spherical symmetry are given by

$$\psi = 1 + \frac{M}{2r}\,, \tag{2.48}$$

where the constant M is the mass of the black hole. In addition, the solution is linear so if we want to construct multiple black hole initial data we can just superpose the single solution

$$\psi = 1 + \sum_i \frac{M_i}{2r_i}\,. \tag{2.49}$$

Equation (2.48) is just the Schwarzschild solution in isotropic coordinates

$$dl^2 = \left(1 + \frac{M}{2r}\right)^4 \left(dr^2 + r^2\left(d\theta^2 + \sin^2\theta d\phi^2\right)\right)\,, \tag{2.50}$$

which can be transformed to the solution in Schwarzschild coordinates

$$dl^2 = \left(1 - \frac{2M}{R}\right)^{-1} dR^2 + R^2\left(d\theta^2 + \sin^2\theta d\phi^2\right)\,, \tag{2.51}$$

by relating the Schwarzschild and isotropic radial coordinates as

$$R = r\left(1+\frac{M}{2r}\right)^2 \,, \tag{2.52}$$

where the location of the horizon for a M mass black hole is at $R = 2M$ (or $r = M/2$ in isotropic coordinates).

If we want to generalise the previous solution to boosted or rotating black holes solving the momentum constraints becomes unavoidable, which in vacuum reduce to

$$\partial^j\partial_j W^i + \frac{1}{3}\partial^i\partial_j W^i = 0\,. \tag{2.53}$$

- *A boosted black hole* solution is given by

$$W^i = -\frac{1}{4r}\left(7\mathcal{P}^i + n^i n_j \mathcal{P}^j\right) \,, \tag{2.54}$$

  where $n^i = x^i/r$ is the outward-pointing unit radial vector and $\mathcal{P}^i$ is the linear momentum of the black hole.

- *A spinning black hole*, on the other hand,

$$W^i = \frac{1}{r^2}\epsilon^{ijk} n_j \mathcal{S}_k \,, \tag{2.55}$$

  where ϵ_{ijk} is the completely antisymmetric Levi-Civita tensor in three dimensions and $\mathcal{S}^i$ is the spin of the black hole.

Given the linearity of the momentum constraints, we can obtain the boosted and rotating black hole solution by adding Eqns. (2.54) and (2.55). Then, reconstructing the longitudinal part of the traceless extrinsic curvature tensor via Eqn. (2.33),

$$\bar{A}^{ij}_{\mathrm{L}} = \frac{3}{2r^2}\left[n^i\mathcal{P}^j + n^j\mathcal{P}^i + n_k\mathcal{P}^k\left(n^i n^j - \delta^{ij}\right)\right] - \frac{3}{r^3}\left(\epsilon_{ilk}n_j + \epsilon_{jlk}n_i\right) n^l \mathcal{S}^k \,. \tag{2.56}$$

Note that for boosted or rotating black holes, the analytical conformal factor in Eqn. (2.48) does not solve the Hamiltonian constraint anymore and one needs to find its numerical solution sourced by

$$\bar{D}^2\psi + \frac{1}{8}\psi^{-7}\bar{A}_{ij}\bar{A}^{ij} = 0\,. \tag{2.57}$$

So far we have focused on vacuum solutions, but what happens if one includes non-trivial matter fields? One of the first problems that arises is that the use of the maximum principle for the Hamiltonian constraint is not applicable to prove local uniqueness of solutions because the matter term $-16\pi\psi^5\rho$ features with the "wrong sign" – a negative coefficient combined with a positive exponent [473, 425, 387, 78, 460]. The fact that there exists no unique solutions entails a big problem for the convergence of the used numerical algorithm. A method to partially cure this defect is to introduce a rescaled energy density $\rho = \psi^s\bar{\rho}$ with $s < -5$, so that $-16\pi\psi^{5-s}\bar{\rho}$ recovers the "right sign" and the maximum principle is applicable [78, 460]. In this case, $\bar{\rho}$ becomes the freely specifiable quantity and once the solution for ψ is found, one would need to reconstruct the usual energy density ρ. An obstacle to this approach is the loss of control over the initially specified energy density. In particular, if the energy density is derived from other fundamental quantities such as scalar fields, it might not even be possible to do such a reconstruction. In the next section we present a novel approach to solve the Hamiltonian constraint that restores the uniqueness of its solutions in the presence of matter fields.

2.2.3 Solutions with fundamental fields

When dealing with fundamental fields, the sources ρ and S_i are often derived from other quantities such as the field gradients and momenta (and can depend on the conformal factor ψ per se). For example, for a theory with a real scalar field ϕ, non-trivial momentum Π, and scalar potential $V(\phi)$, the energy and momentum flux densities are given by

$$\rho(\psi) = \frac{1}{2}\psi^{-4}(\partial_i\phi)^2 + \frac{1}{2}\Pi^2 + V(\phi)\,, \qquad S_i = -\Pi\partial_i\phi\,. \tag{2.58}$$

Choosing a rescaled energy density $\bar{\rho}$ would also entail reconstructing the fundamental quantities ϕ, Π, and $V(\phi)$. This process has the disadvantage of losing control over the initially specified field configurations, in addition to changing the physical dynamics of the system by modifying the scalar potential $V(\phi)$.

As we have seen throughout this section, given a particular decomposition, the construction of the initial data demands making well-motivated choices for the freely-specifiable independent background data and then solving the constraint equations for the constrained variables. As we will see below, for cases in which fundamental fields are the freely-specifiable quantities, it is preferable to choose $\psi = \psi_0$ and solve for the trace of the extrinsic curvature tensor K using the Hamiltonian constraint. The fixed value ψ_0 plays the role of the initial scale factor in FLRW spacetime $\psi_0 \sim a_0^{1/2}$. This approach avoids the non-uniqueness problem while keeping under control the specified initial field configuration.

For this particular choice, the Hamiltonian constraint reduces from a differential equation for ψ to an algebraic equation for K

$$\boxed{K^2 = 12\psi_0^{-5}\bar{D}^2\psi_0 + \frac{3}{2}\psi_0^{-12}\bar{A}_{ij}\bar{A}^{ij} + 24\pi\rho\,,} \tag{2.59}$$

with the freedom to choose between an overall collapsing or expanding $K = \pm\sqrt{K^2}$ spacetime[6]. The price to pay by pursuing this method is that even in the case of absent momentum flux densities $S^i = 0$, a space-dependent K will induce a source in the momentum constraints, so that they always need to be solved

$$\boxed{\left(\bar{\Delta}_{\mathrm{L}}W\right)^i - \frac{2}{3}\psi_0^6\partial_i K = 8\pi\psi_0^6 S_i\,,} \tag{2.60}$$

using any of the vector Laplacian decompositions that have been described before[7].

2.2.4 Solutions with black holes and fundamental fields

If we want to study a mixed system where black holes and fundamental fields are present, we rewrite the conformal factor as $\psi = \psi_{\mathrm{BH}} + \psi_*$, and the traceless extrinsic curvature tensor as $\bar{A}^{ij} = \bar{A}^{ij}_{\mathrm{BH}} + \bar{A}^{ij}_*$, where ψ_{BH} and $\bar{A}^{ij}_{\mathrm{BH}}$ are approximate[8] Bowen-York initial data [105, 106] for a black hole with linear and angular momentum $\mathcal{P}$ and $\mathcal{S}$ respectively[9]

$$\psi_{\mathrm{BH}} = 1 + \frac{M}{2r}\,, \tag{2.61}$$

$$\bar{A}^{ij}_{\mathrm{BH}} = \frac{3}{2r^2}\left[n_i\mathcal{P}_j + n_j\mathcal{P}_i + n_k\mathcal{P}^k\left(n_i n_j - \delta_{ij}\right)\right] - \frac{3}{r^3}\left(\epsilon_{ilk}n_j + \epsilon_{jlk}n_i\right)n^l\mathcal{S}^k\,, \tag{2.62}$$

---

[6] The second and last terms are always positives, but $\bar{D}^2\psi$ should not take negative values such that $K^2 < 0$.

[7] See also [216] for an interesting approach for inhomogeneous cosmologies.

[8] Note that while $\bar{A}^{ij}_{\mathrm{BH}}$ is an exact solution to the momentum constraints, $\psi_{\mathrm{BH}} = 1 + M/2r$ becomes only an approximate solution when $\bar{A}^{ij} \neq 0$.

[9] We are focusing on a single black hole but the extension to multiple boosted and rotating black holes is trivial given the linearity of the momentum constraints.

The Hamiltonian and momentum constraints reduce to

$$\begin{gathered}
\partial^j\partial_j\psi_* - \frac{1}{12}\left(\psi_{\mathrm{BH}}+\psi_*\right)^5 K^2 + \frac{1}{8}\left(\psi_{\mathrm{BH}}+\psi_*\right)^{-7}\left(\bar{A}^{ij}_{\mathrm{BH}}+\bar{A}^{ij}_*\right)^2 = -2\pi\left(\psi_{\mathrm{BH}}+\psi_*\right)^5\rho\,,\\
\left(\bar{\Delta}_{\mathrm{L}}W_*\right)_i - \frac{2}{3}\left(\psi_{\mathrm{BH}}+\psi_*\right)^6\partial_i K = 8\pi\left(\psi_{\mathrm{BH}}+\psi_*\right)^6 S_i\,,
\end{gathered}$$

where the solutions $\partial^j\partial_j\psi_{\mathrm{BH}}=0$ and $\partial_j\bar{A}^{ij}_{\mathrm{BH}}=0$ have been used. The vector W^i_* is associated to the vector decomposition of $\bar{A}^{ij}_*$

$$\bar{A}^{ij}_* = \left(\partial^i W^j_* + \partial^j W^i_* - \frac{2}{3}\eta^{ij}\partial_k W^k_*\right)\,. \tag{2.63}$$

Analogously to the case with fundamental fields, we will make a clever choice of the trace of the extrinsic curvature tensor so that it includes the matter source terms, ensuring the maximum principle applies for the Hamiltonian constraint. The remaining $\bar{A}_{ij}\bar{A}^{ij}$ term sources the right-hand-side of the elliptic equation for ψ_*, which can be solved using standard integration methods

$$\boxed{\begin{gathered}
K^2 = 24\pi\rho\,,\\
\partial^j\partial_j\psi_* + \frac{1}{8}\left(\psi_{\mathrm{BH}}+\psi_*\right)^{-7}\left(\bar{A}^{ij}_{\mathrm{BH}}+\bar{A}^{ij}_*\right)^2 = 0\,,\\
\left(\bar{\Delta}_{\mathrm{L}}W_*\right)_i - \frac{2}{3}\left(\psi_{\mathrm{BH}}+\psi_*\right)^6\partial_i K = 8\pi\left(\psi_{\mathrm{BH}}+\psi_*\right)^6 S_i\,.
\end{gathered}}\qquad\begin{gathered}(2.64)\\(2.65)\\(2.66)\end{gathered}$$

We want to re-emphasise that the choice of decomposition for the vector Laplacian $(\bar{\Delta}_{\mathrm{L}}W_*)_i$ should be guided by the physical system studied, which can lead to an important impact in the convergence of the numerical algorithm used.

2.3 Long-term stable numerical simulations

Assuming we had initial data that satisfies the constraint equations (2.19), (2.22), we could in principle integrate the Eqns. (2.23) and (2.24) to evolve the system to a later time. However, even in the simplest scenarios such as a perturbation around flat spacetime, our 3+1 code would most likely crash after a short time. So the ADM evolution equations that we have derived are not yet in a suitable form for stable numerical integration, and their failure can be understood in terms of their mathematical properties, they have been proven to be only weakly hyperbolic. In this case, the evolution problem is not well-posed, and there is no reason to expect the numerical implementations to be well-behaved.

In the first part of this section we will recast these equations in a form that is suitable for numerical evolution. To do so, we will add multiples of the constraints to the evolution equations and thus affecting the mathematical properties of the system. In particular, we will discuss a strongly hyperbolic reformulation known as the BSSN reformulation of the evolution equations, which has proven more robust and successful [421, 79].

The second part of this section will focus on suitable choices of the lapse and the shift for long-term stable numerical simulations. As we have discussed, the decomposed Einstein equations do not provide any equations for α or β^i. These are arbitrary functions that represent the coordinate freedom of general relativity, and thus must be determined by imposing gauge conditions. We will discuss and compare a few canonical gauge conditions that form the basis of choices frequently adopted in numerical relativity schemes.

2.3.1 BSSN reformulation

The key idea is the non-uniqueness of the 3+1 evolution equations by adding arbitrary multiples of the constraints, to obtain new equations which have the same physical solution. However, rewriting the equations will inevitably change the mathematical properties, with the possibility of finding a reformulation which is better behaved numerically.

To derive the BSSN reformulation we begin by doing again a conformal transformation of the spatial metric $\gamma_{ij} = \bar{\gamma}_{ij}/\chi$. The conformal factor is usually chosen such that the background metric $\bar{\gamma}_{ij}$ has unit determinant, implying $\chi = \gamma^{-1/3}$ with $\gamma = \det \gamma_{ij}$. It has been suggested that this choice deals better with spacetimes which contain black hole singularities [124]. Other conventions often choose $\chi \to \chi^2$, $\chi = e^{4\phi}$ or $\chi = \psi^{-4}$, as we have seen in the previous section. We will also make a new conformal rescaling of the traceless extrinsic curvature[10] $A_{ij} \equiv \tilde{A}_{ij}/\chi$. We will apply a first-order reduction of the equations by writing all second derivatives in terms of first derivatives of a new set of auxiliary functions that contain first derivatives of the original variables. The conformal connection functions are defined in terms of the Christoffel symbols of the conformal metric as

$$\bar{\Gamma}^i \equiv \bar{\gamma}^{jk}\bar{\Gamma}^i_{jk} = -\partial_j \bar{\gamma}^{ij} \,. \tag{2.67}$$

---

[10] Note that this is different to the rescaling of the traceless extrinsic curvature tensor denoted by $\bar{A}_{ij}$, which is more convenient for solving the constraint equations.

The number of dynamical variables have been increased from 12: (γ_{ij}, K_{ij}); to 17: ($\bar{\gamma}_{ij}$, $\tilde{A}_{ij}$, K, χ, $\bar{\Gamma}^i$), so the system of equations must also increase to fix the new degrees of freedom that have been introduced. The detailed derivation can be found in Appendix A and here only the final results are presented.

$$\frac{d}{dt}\chi = \frac{2}{3}\chi\alpha K\,, \tag{2.68}$$

$$\frac{d}{dt}\bar{\gamma}_{ij} = -2\alpha\tilde{A}_{ij}\,, \tag{2.69}$$

$$\begin{aligned}\frac{d}{dt}\tilde{A}_{ij} =& \chi\left\{-D_iD_j\alpha + \alpha\left({}^{(3)}R_{ij} - 8\pi\alpha S_{ij}\right)\right\}^{\text{TF}} \\ &+ \alpha\left(\tilde{A}_{ij}K - 2\tilde{A}_{ik}\tilde{A}^k_j\right)\,,\end{aligned} \tag{2.70}$$

$$\frac{d}{dt}K = -\gamma^{ij}D_iD_j\alpha + \alpha\left(\tilde{A}_{ij}\tilde{A}^{ij} + \frac{1}{3}K^2\right) + 4\pi\alpha(\rho + S)\,, \tag{2.71}$$

where $d/dt \equiv \partial_t - \pounds_{\vec{\beta}}$ and TF denotes the trace-free part. The extra evolution equations for the conformal connection functions can be obtained using (2.67) and (2.69)

$$\partial_t\bar{\Gamma}^i = -\partial_j\left(\pounds_{\vec{\beta}}\bar{\gamma}^{ij}\right) - 2\left(\alpha\partial_j\tilde{A}^{ij} + \tilde{A}^{ij}\partial_j\alpha\right)\,. \tag{2.72}$$

We can expand the Lie derivatives using the rule for tensor densities $\tilde{T} = \gamma^{w/2}T$

$$\pounds_{\vec{v}}\tilde{T} = \left[\pounds_{\vec{v}}\tilde{T}\right]_{w=0} + w\tilde{T}\partial_i v^i\,, \tag{2.73}$$

which in the convention that is being used $w = -2/3$ for $\bar{\gamma}^{ij}$ and $\tilde{A}^{ij}$, whilst it is $w = 1$ for χ. Therefore, the final expressions for the BSSN evolution equations are

$$\boxed{\begin{aligned}\partial_t\chi =& \frac{2}{3}\chi(\alpha K - \partial_k\beta^k) + \beta^k\partial_k\chi\,, && (2.74)\\ \partial_t\bar{\gamma}_{ij} =& -2\alpha\tilde{A}_{ij} + \beta^k\partial_k\bar{\gamma}_{ij} + \bar{\gamma}_{ik}\partial_j\beta^k + \bar{\gamma}_{jk}\partial_i\beta^k - \frac{2}{3}\bar{\gamma}_{ij}\partial_k\beta^k\,, && (2.75)\\ \partial_t\tilde{A}_{ij} =& \chi\left\{-D_iD_j\alpha + \alpha\left({}^{(3)}R_{ij} - 8\pi\alpha S_{ij}\right)\right\}^{TF} + \alpha\left(\tilde{A}_{ij}K - 2\tilde{A}_{ik}\tilde{A}^k_j\right) && \\ &+ \beta^k\partial_k\tilde{A}_{ij} + \tilde{A}_{ik}\partial_j\beta^k + \tilde{A}_{jk}\partial_i\beta^k - \frac{2}{3}\tilde{A}_{ij}\partial_k\beta^k\,, && (2.76)\\ \partial_t K =& -D_iD^i\alpha + \alpha\left(\tilde{A}_{ij}\tilde{A}^{ij} + \frac{1}{3}K^2\right) + 4\pi\alpha(\rho + S) + \beta^k\partial_k K\,, && (2.77)\\ \partial_t\bar{\Gamma}^i =& \bar{\gamma}^{jk} + \frac{1}{3}\bar{\gamma}^{ij}\partial_j\partial_k\beta^k + \beta^j\partial_j\bar{\Gamma}^i - \bar{\Gamma}^j\partial_j\beta^i + \frac{2}{3}\bar{\Gamma}^i\partial_j\beta^j - 2\tilde{A}^{ij}\partial_j\alpha && \\ &+ 2\alpha\left(\bar{\Gamma}^i_{jk}\tilde{A}^{jk} + \frac{3}{2}\tilde{A}^{ij}\partial_j\chi - \frac{2}{3}\bar{\gamma}^{ij}\partial_j K - 8\pi\chi S^i\right)\,. && (2.78)\end{aligned}}$$

2.3.2 Gauge conditions

As the constraints do not depend on the gauge variables, these are independent of the data specified on the initial slice. However, their choice plays a crucial role in obtaining robust and long-term stable numerical solutions.

Choice of the lapse

Defining the proper acceleration of an observer as

$$a^\mu \equiv n^\nu \nabla_\nu n^\mu \,, \tag{2.79}$$

and using the definition of the unit normal vector (2.6),

$$\begin{aligned} a_\mu \equiv n^\nu \nabla_\nu n_\mu &= -n^\nu \nabla_\nu (\alpha \nabla_\mu t) = -n^\nu \nabla_\nu \alpha \nabla_\mu t - n^\nu \alpha \nabla_\nu \nabla_\mu t \,, \\ &= \frac{1}{\alpha} n_\mu n^\nu \nabla_\nu \alpha + \alpha n^\nu \nabla_\mu \left(\frac{-1}{\alpha} n_\nu \right) = \frac{1}{\alpha} \left(n_\mu n^\nu \nabla_\nu \alpha + \nabla_\mu \alpha \right) \,, \\ &= \left(\delta_\mu^\nu + n_\mu n^\nu \right) \frac{1}{\alpha} \nabla_\nu \alpha = P_\mu^\nu \nabla_\nu \ln \alpha = D_\mu \ln \alpha \,, \end{aligned} \tag{2.80}$$

where $n^\mu n_\mu = -1$ and $n^\nu \nabla_\mu n_\nu = 0$ has been used. Therefore, a spatially varying lapse results in an acceleration of the observers.

Geodesic slicing is the simplest (but not the best) choice, taking $\alpha = 1$ and $\beta^i = 0$, so that observers stay at fixed location in space with zero proper acceleration. However, as geodesics tend to focus on regions of high density, the observers will end up collapsing, making all the coordinate points to converge on the same physical point. This is a consequence of the evolution equation (2.77) if $\partial_t K > 0$, meaning that K is always growing and therefore collapsing.

Maximal slicing condition partially solves the problem setting $K = \partial_t K = 0$ on all slices, so that (2.77) gives an elliptic differential equation for the lapse

$$D^2 \alpha = \alpha \left[A_{ij} A^{ij} + \frac{1}{3} K^2 + 4\pi (\rho + S) \right] \,, \tag{2.81}$$

which needs to be solved at every timestep. Unfortunately, solving a three-dimensional elliptic equation is very time-consuming.

Hyperbolic formulations are an example of dynamical gauges that have been proven to be very successful with spacetimes containing black holes. One of the most popular choice is

$$\partial_t \alpha = -\mu_{\alpha_1} \alpha^{\mu_{\alpha_2}} K + \mu_{\alpha_3} \beta^i \partial_i \alpha \,. \tag{2.82}$$

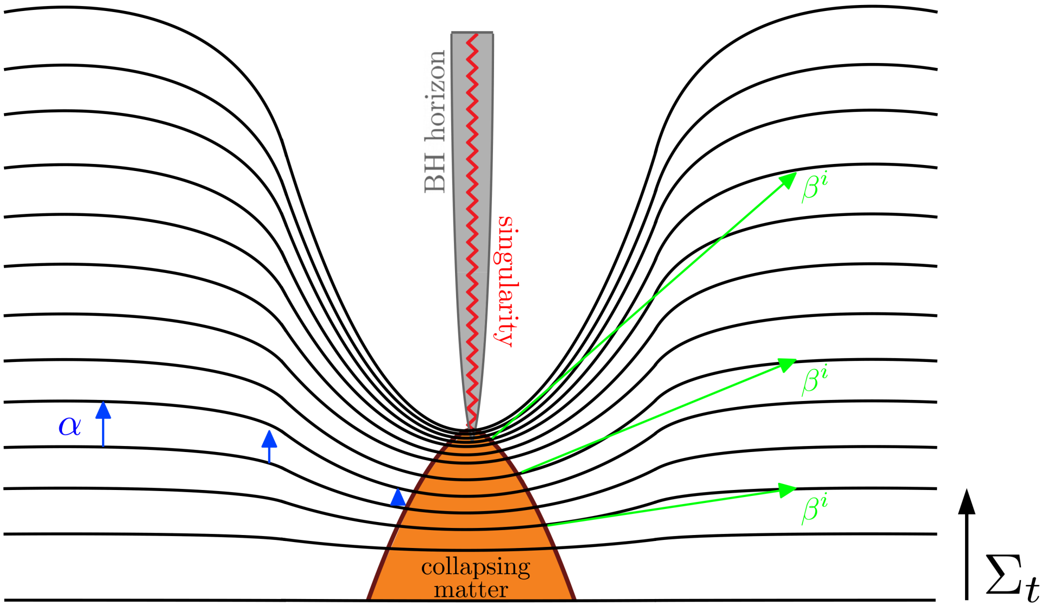

Fig. 2.3 “Trumpet”-like solution for the lapse function illustrating the slice stretching. The blue arrows measure the proper time elapsed αdt between neighbouring 3-surfaces. The green arrows illustrate the effect of the shift function using the gamma-driver condition, which reduces the stretching developed by the evolution of the lapse.

The basic idea is to avoid the singularity by reducing the lapse and therefore slowing down the evolution close to it. The values of the coefficients μ_{α_i} are physics dependent, but one of the most successful choices is setting $\mu_{\alpha_1} = 2$, $\mu_{\alpha_2} = \mu_{\alpha_3} = 1$, known as $1+\log$ slicing [102]. An intuitive way of understanding this is by setting $\beta^i = 0$, so that the condition becomes $\partial_t \alpha = -2\alpha K$, which can be integrated to get $\alpha \propto \exp(-2Kt)$. Then, collapsing regions of spacetime where $K > 0$ will drive the lapse to zero $\alpha \to 0$. Noting that the proper time is defined as $d\tau^2 = \alpha^2 dt^2$, this gauge condition will “freeze” the evolution near regions that are collapsing. Together with excision techniques where the region close to the singularity is ignored and “removed” from the simulation grid [432, 417, 161, 42, 44, 396], this is one of the most successful methods to avoid black hole singularities in numerical relativity simulations.

Unfortunately, this trumpet-shaped lapse function leads to the stretching of slices as shown in Fig. (2.3). Whilst time freezes inside the black hole, it keeps advancing outside and the spatial slices become distorted. This stretching often leads to the development of large gradients near the throat of the black hole, causing the failure of the simulation. One of the ways that this problem can be resolved is by choosing a clever shift vector condition for β^i.

Choice of the shift

As we have already discussed in Fig. 2.1, the shift functions β^i measure the amount by which spatial coordinates are shifted within a slice with respect to the normal vector. Therefore, cleverly choosing the evolution equations for β^i allows us to pull the positions away from the throat of the black hole, thus reducing the slice stretching developed by the evolution of the lapse. A very successful choice is the so-called gamma-driver condition [43]

$$\begin{aligned} \partial_t \beta^i &= \eta_{\beta_1} B^i \,, \\ \partial_t B^i &= \mu_{\beta_1} \alpha^{\mu_{\beta_2}} \partial_t \bar{\Gamma}^i - \eta_{\beta_2} B^i \,, \end{aligned} \tag{2.83}$$

with $\eta_{\beta_1} = 3/4$, $\eta_{\beta_2} = \mu_{\beta_1} = 1$ and $\mu_{\beta_2} = 0$ the common choices. The combination of the $1 + \log$ slicing for the lapse and the gamma-driver condition for the shift is called the moving-puncture method [67, 124, 445], that has been proven to be very robust in dealing with singularities.

Part II

Research work

Chapter 3

The effects of potential shape on inhomogeneous inflation

This chapter contains the article "The effects of potential shape on inhomogeneous inflation" [61], published in the *Journal of Cosmology and Astroparticle Physics (JCAP)*.

We study the robustness of single-field inflation against inhomogeneities. We derive a simple analytic criterion on the shape of the potential for successful inflation in the presence of inhomogeneities, and demonstrate its validity using full 3+1 dimensional numerical relativity simulations on several classes of popular models of single-field inflation. We find that models with convex potentials are more robust to inhomogeneities than those with concave potentials, and that concave potentials that vary on super-Planckian scales are significantly more robust than those that vary on sub-Planckian scales.

3.1 Introduction

Cosmic inflation [244, 333, 36, 429] is the leading paradigm for the early universe. It posits an early period of accelerated expansion in order to dynamically explain the current homogeneous and spatially flat state of the universe. One of the most remarkable successes of the paradigm is the observational confirmation of some of its key predictions, a nearly scale-invariant and Gaussian spectrum of primordial perturbations [31].

Inflation was introduced as a solution to several problems of standard big-bang cosmology [244]. One of these problems is the horizon problem. However, inflation can only constitute a solution to the horizon problem, if it does not have a horizon problem of its own. So it is natural to ask what came before inflation and how it began. There is certainly no guarantee that the universe was semi-classical at the time inflation began, and it is difficult to talk about the beginning of inflation in complete generality. To make progress, we make the simplifying assumption that at the time inflation began the universe was already described by general relativity minimally coupled to a scalar field, the inflaton.

In this case, the space of initial conditions for inflation is parameterized by the degrees of freedom of the spatial metric and its conjugate momentum, and the corresponding degrees of freedom of the inflaton. For each degree of freedom, we are free to specify its configuration on the initial Cauchy hypersurface. It is then natural to ask for which initial data inflation will be successful. By “successful” we mean that some region of the initial hypersurface undergoes accelerated expansion for 60 e-foldings or more. Whether inflation is successful depends both on the dynamics of the inflaton model and the initial conditions, as well as the interplay between them.

In this work, we will explore one particular aspect of this interplay, the effect of the initial amplitude of the inhomogeneities in the inflaton field (and their associated metric perturbations) on different models of inflation.

Inflationary models are broadly classified as “concave” and “convex” models, depending on the shape of their potentials. We propose an analytic criterion as a diagnostic for whether inflation will be successful for a given potential. We test this criterion using full 3+1 numerical general relativity solutions and show that convex models are more robust to inhomogeneities than concave models. Furthermore, we show that for concave potentials the scale in field space over which the potential varies appreciably plays an important role. Finally, we will argue that for some potentials there exists a bound on the initial mean value of the inflaton field, beyond which inflation will be successful regardless of the amplitude of the inhomogeneities.

3.2 Initial conditions and models

The problem of initial conditions for inflation has been studied extensively using analytic and semi-analytic methods [224, 257, 459, 430, 73, 33, 74, 225, 291, 260, 386, 359, 313, 314, 117, 341, 226, 103, 118, 358, 72, 86, 125, 441, 71, 70, 395, 342, 436, 113, 223, 343, 116, 142, 164, 415, 402, 165, 357, 403, 82, 316, 344, 205, 98], as well as numerically [34, 35, 326, 199, 115, 228, 227, 114, 327, 229, 325, 193, 190, 107, 46, 47] (see [110] for a short review).

Recently it has become possible to use numerical relativity codes to evolve different initial configurations in the time domain even in the regime in which black holes form [190, 157], allowing for a fully non-perturbative investigation of the field dynamics in response to the initial conditions. This work was limited to a small number of "typical" models, and quantified their success for different choices of parameterized initial inhomogeneities.

One natural way to extend these investigations is to expand the classes of inhomogeneities, which was initiated in [155]. Another interesting direction is to expand the classes of inflationary models under investigation, which we will do in the present work.

In this section we summarize the key features of the space of initial conditions on which we focus, as well as the larger class of inflationary models.

3.2.1 The space of initial conditions

We decompose the spacetime metric using the standard ADM decomposition [57],

$$ds^2 = -\alpha^2\, dt^2 + \gamma_{ij}(dx^i + \beta^i\, dt)(dx^j + \beta^j\, dt)\,. \tag{3.1}$$

Here γ_{ij} is the 3-metric on the spatial hypersurface, while α and β^i are the lapse and shift. We are free to choose the initial Cauchy hypersurface. The metric initial conditions are then fully specified by a choice of γ_{ij} and the extrinsic curvature K_{ij} at each point in the spatial domain. The extrinsic curvature can further be decomposed into the expansion $K = \gamma^{ij}K_{ij}$ and trace-free tensor components A_{ij},

$$K_{ij} = \frac{1}{3}K\gamma_{ij} + A_{ij}\ . \tag{3.2}$$

In the perturbative limit, the transverse part of A_{ij} represents "gravitational wave" modes, though we emphasize that in the non-perturbative limit they are not solutions to a linear wave equation. In our sign convention, $K < 0$ denotes a locally expanding spacetime.

Meanwhile, the space of initial conditions for the inflaton ϕ is given by the value of the field and its canonical momentum

$$\Pi \equiv \alpha^{-1}(\dot{\phi} - \beta^i\partial_i\phi)\,, \tag{3.3}$$

at each point.

A more subtle aspect of the initial conditions is the choice of spatial boundary conditions. In what follows we will assume periodic boundary conditions for the spatial domain, which imposes a T^3 topology on the space. Alternatively, this can be thought of as imposing a scale of homogeneity on the initial conditions with the Universe made up of many (inhomogeneous) boxes of size L. One can always make L larger, thus increasing the scale of homogeneity relative to our patch of the Universe, and it is usually considered that taking L to be greater than the initial Hubble scale of inflation is a sufficiently conservative approach. Other topologies, in particular those that can support a positive-definite ${}^{(3)}R$ can lead to different conclusions [74, 316], so that this is a choice that should be made explicit.

In summary, the space of initial conditions for single-field inflation consists of the values of the variables $(\gamma_{ij}, K_{ij}, \phi, \Pi)$ on the initial hypersurface. Their values are not completely independent because they are subject to the Hamiltonian and momentum constraints.

The constraints are a set of four non-linear coupled partial differential equations, which are non-trivial to solve for a general matter distribution (see e.g. [41, 79]). To simplify this task, some variables are often set to zero, severely restricting the available space of initial conditions. In Refs. [190, 157, 155], γ_{ij} is, for example, assumed to be conformally flat $\gamma_{ij} \equiv \chi^{-1}\delta_{ij}$ where χ is a conformal factor. In addition, Refs. [190, 157] set the trace-free part of the extrinsic curvature to zero $A_{ij} = 0$. Combined with the additional simplifying conditions that $\Pi = 0$ and the expansion rate is spatially constant $K = \text{const} < 0$ (i.e. uniformly expanding), the momentum constraint is then trivially satisfied. The parameter space in this case is then just the scalar configuration $\phi(\mathbf{x})$, with the value of K imposed by an integrability condition in the case of periodic boundary conditions (see [81]). The Hamiltonian constraint then determines the conformal factor, χ.

Two more general classes of deviations from homogeneity have been explored. First, in [157], a special case where $K(\mathbf{x}) = -C\phi(\mathbf{x}) + K_0$ where $C > 0$ is a free parameter, and the value of K_0 is set by integrability on the periodic domain. This *Ansatz* keeps the momentum constraint trivial but allows us to explore initial conditions which mix regions of local expansion $(K < 0)$ and contraction $(K > 0)$. It was found that, as long as the initial hypersurface is expanding on average, $\langle K \rangle < 0$, inflation will occur in some patch, even if part of the spacetime collapses. Second, in [155], non-zero transverse modes $A_{ij}^{TT} \neq 0$ were studied. It was found that the amplitude of the scalar perturbations remained the main driver of inflationary success, with the tensor modes generally reducing the number of e-folds, but not causing failure in isolation even at high relative energy densities.

It is clear from this discussion that a large space of initial conditions remains to be explored. As we mentioned before, we will not pursue this direction here and reserve it for future work. We instead consider initial conditions such that $\tilde{\gamma}_{ij} = \delta_{ij}$, $\Pi = 0$, $A_{ij} = 0$ and $K = \text{const} < 0$, and we expand the classes of inflationary models.

3.2.2 The space of models

Inflation a priori only predicts that the observed primordial spectrum of density perturbations should be nearly scale-invariant but does not predict the sign of the departure from scale invariance. The space of inflationary models is vast, encompassing a diverse variety of single field and multi-field models with many mechanisms (see e.g. [346]). Without the guidance of some fundamental theory of inflation, models which are not already ruled out by observations are in principle all valid. Nevertheless, useful classifications of models can be made, such as categorizing the models in terms of their energy scale, or the field range. As one might expect, it was shown in [157] that small field inflation is generally less robust than large field inflation.

In this work, we will rely on a slightly more refined classification to guide our choice of inflationary models. In the slow-roll approximation, we know that the slow-roll parameter $\epsilon = -\dot{H}/H^2$ obeys the differential equation

$$\frac{d \ln \epsilon}{d\mathcal{N}} = (n_{\rm s}(\mathcal{N}) - 1) + 2\epsilon \,. \tag{3.4}$$

Suppose the observed sign and magnitude of the departure from scale-invariance are not mere accidents but arise because the scalar spectral index has the functional form [356, 408][1]

$$n_{\rm s}(\mathcal{N}) - 1 = -\frac{p+1}{\mathcal{N}}\,, \tag{3.5}$$

where $\mathcal{N}$ is the number of e-folds (counted from the end of inflation), and p is number of order unity. The most general solution to the differential equation (3.4) is then given by

$$\epsilon(\mathcal{N}) = \frac{p}{2\mathcal{N}} \frac{1}{1 \pm (\mathcal{N}/\mathcal{N}_{\rm eq})^p}\,, \tag{3.6}$$

where $\mathcal{N}_{\rm eq}$ is an integration constant. Unless there are additional hierarchies, we expect it to be of order unity.

If we further assume that we observe modes at a typical moment so that either the first or the second term in the denominator dominate, we are left with two solutions

---

[1] There is no guarantee that this is the case, but models that deviate from this will require additional small parameters to account for the near scale-invariance.

that are compatible with current data

$$\epsilon(\mathcal{N}) = \frac{p}{2\mathcal{N}} \qquad \text{and} \qquad \epsilon(\mathcal{N}) = \frac{p}{2\mathcal{N}} \left(\frac{\mathcal{N}_{\text{eq}}}{\mathcal{N}} \right)^p . \tag{3.7}$$

Because $p < 0$ is disfavored by data, we will restrict our attention to $p > 0$.

So far this is general and makes no mention of a potential. If we assume that the dynamics is governed by a single scalar field with canonical kinetic term

$$L_\phi = -\frac{1}{2} g^{\mu\nu} \partial_\mu \phi \partial_\nu \phi - V(\phi) \,, \tag{3.8}$$

we can reconstruct the potential from the equations[2]

$$\frac{d\phi}{d\mathcal{N}} = \frac{M_{\text{Pl}}^2}{8\pi} \frac{V'}{V} \qquad \text{and} \qquad \left(\frac{d\phi}{d\mathcal{N}} \right)^2 = \frac{\epsilon M_{\text{Pl}}^2}{4\pi} . \tag{3.9}$$

One finds that the first class corresponds to monomial (or power law) potentials

$$V(\phi) = \lambda M_{\text{Pl}}^{4-2p} \phi^{2p} . \tag{3.10}$$

For the second class of models the potential during inflation is well approximated by

$$V(\phi) \simeq \Lambda^4 \left[1 - \left(\frac{\phi}{\mu_n} \right)^n \right] , \tag{3.11}$$

where $n = 2p/(p-1)$ provided $p > 1$, and by

$$V(\phi) \simeq \Lambda^4 \left[1 - \left(\frac{\mu_n}{\phi} \right)^n \right] , \tag{3.12}$$

with $n = 2p/(1-p)$ provided $0 < p < 1$. For potentials of the form (3.11) inflation occurs as the inflaton rolls off a hilltop, and we will sometimes refer to them as hilltop models. Similarly, for the form (3.12) inflation occurs as the inflaton rolls off a plateau, and we will sometimes refer to them as plateau models. For $p \neq 1$ the departure from the plateau is described by a power law. The case $p = 1$ is special and the departure becomes exponential

$$V(\phi) \simeq \Lambda^4 \left[1 - e^{-\phi/\mu} \right] . \tag{3.13}$$

We see that the hilltop and plateau models involve an additional scale, denoted μ in the exponential models and μ_n in the power law models, which describes the distance

---

[2] We will use the Planck mass $M_{\text{Pl}}^2 = \hbar c/G$ throughout the chapter.

in field space over which the plateau is approached. As we will see, this scale plays an important role for the robustness against inhomogeneities. Roughly, we will see that models are robust if this scale is Planckian or super-Planckian, and are susceptible to inhomogeneities if this scale is sub-Planckian. Incidentally, this is closely tied to the question whether gravitational waves from these models are detectable with upcoming CMB experiments, which will be capable of detecting gravitational wave signals from models with a super-Planckian characteristic scale [3].

3.3 An analytic criterion for robustness

In this section, we will derive a simple analytic criterion that allows us to infer the robustness of a given single-field model against inhomogeneities. From [190, 157, 155] we know that the amplitude of the inhomogeneity plays an important role. At fixed energy density in the gradients, the amplitude is generically larger if only one or a few modes are excited than if the energy density is distributed over a large number of modes. So in what follows we will assume that the inhomogeneous initial conditions for the inflaton field are given by a superposition of modes in the 3 spatial directions [190, 157, 155]

$$\phi(t=0,\mathbf{x}) = \phi_0 + \frac{\Delta\phi}{3}\left(\cos kx + \cos ky + \cos kz\right) , \tag{3.14}$$

with vanishing canonical momentum

$$\Pi(t=0,\mathbf{x}) = 0 , \tag{3.15}$$

where $k = 2\pi N/L$ is the wavenumber associated with the inhomogeneity, $N = 1, 2, \dots$ is an integer, and we set L to be the Hubble length H_i^{-1} in the absence of inhomogeneities

$$L = \frac{3M_{\rm Pl}}{\sqrt{24\pi V(\phi_0)}} . \tag{3.16}$$

If we assume that the spatial metric is initially conformally flat, $\gamma_{ij} = \chi^{-1}\delta_{ij}$, and $K = \text{const} < 0$ as discussed in Sec. 3.2, then the scalar field dynamics *near the initial hyperslice* is approximately described by the Klein-Gordon equation

$$\ddot{\phi} \approx \nabla^2\phi - \frac{dV(\phi)}{d\phi} , \tag{3.17}$$

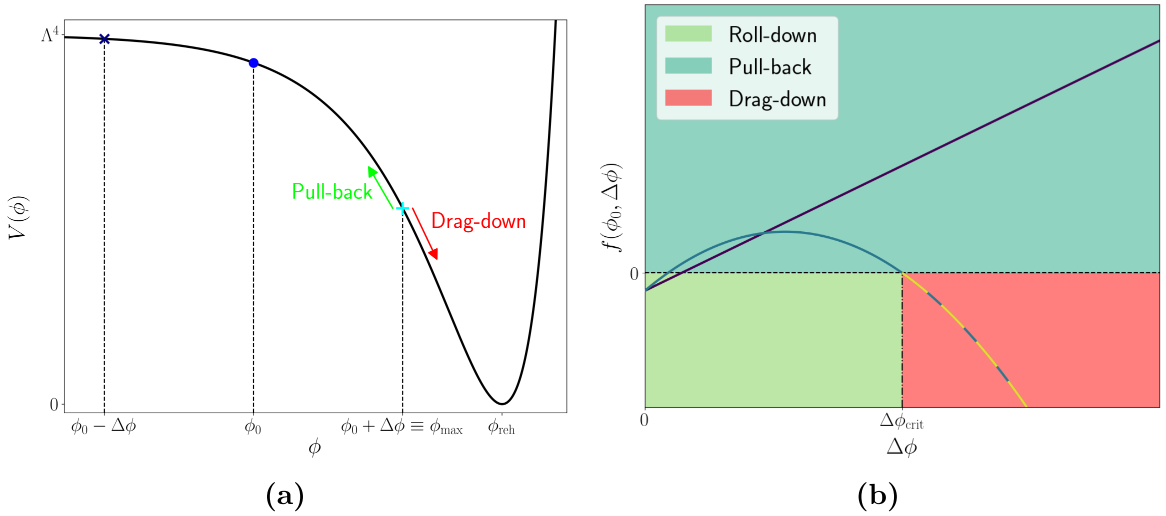

(a) (b)

Fig. 3.1 (a): Example of inflationary potential with inhomogeneous initial conditions reaching $\phi_{\rm max} \equiv \phi_0 + \Delta\phi$ and $\phi_0 - \Delta\phi$. The inflaton rolls down the potential to the reheating minimum $\phi_{\rm reh}$ in the positive ϕ direction **(b): Sketch of** $f(\phi_0, \Delta\phi)$ **for a concave and convex model:** The main difference between models (different solid lines) is whether f has a maximum and there exists a "drag-down" region where $f < 0$. Away from the trivial $\Delta\phi = 0$ homogenous point, convex models do not have such maximum and always stay within the $f > 0$ region where the field is pulled back. Concave models however, can have a turning point followed by a zero crossing and values of $\Delta\phi$ for which $f < 0$ (dashed line) and hence the field is dragged towards the minimum, ending inflation. The shaded colours illustrate different outcomes of the maximum of the field $\phi_{\rm max} \equiv \phi_0 + \Delta\phi$.

where the subdominant friction term has been ignored since initially $\dot{\phi} \sim 0$. Without loss of generality, we assume that the inflaton rolls down the potential to the reheating minimum $\phi_{\rm reh}$ in the positive ϕ direction – see Fig. 3.1a. Consider the dynamics of the inflaton at the point of maximum amplitude $\phi_{\rm max}$ – this is the field value closest to the reheating minimum and thus the point at which the inflaton is most at risk of falling into the reheating minimum and ending inflation. Our question is then whether the inflaton field at this point will initially be "pulled back" towards ϕ_0 to safety, or whether the gradient of the potential $dV/d\phi < 0$ will drag the inflaton into the minimum, ending inflation early or preventing it from taking place altogether. For compactness, we will sometimes refer to the former as "pull-back" and the latter as "drag-down".

Initially, $\phi_{\rm max} = \phi_0 + \Delta\phi$. Using Eqn. (3.17) and Eqn. (3.14), its initial evolution is given by

$$\ddot{\phi}_{\rm max} = -k^2\Delta\phi - \frac{dV(\phi_{\rm max})}{d\phi} = -f(\phi_0, \Delta\phi), \tag{3.18}$$

where

$$f(\phi_0, \Delta\phi) = k^2\Delta\phi + \frac{dV(\phi_0 + \Delta\phi)}{d\phi} \; . \tag{3.19}$$

In Fig. 3.1b we sketch the shape of the function $f(\phi_0, \Delta\phi)$ at fixed ϕ_0 for different inflationary models. In the absence of inhomogeneities, $\Delta\phi = 0$, $f(\phi_0, \Delta\phi) < 0$ which means that $\ddot{\phi}_{\rm max} > 0$, i.e. the field rolls towards the reheating minimum as expected. As we increase the amplitude of the inhomogeneities the gradients contribute as $-\nabla^2\phi = k^2\Delta\phi > 0$ which is positive definite.[3] For small $\Delta\phi$, we can approximate the potential contributions

$$\begin{aligned} \frac{dV(\phi_0 + \Delta\phi)}{d\phi} &\approx \frac{dV(\phi_0)}{d\phi} + \frac{d^2V(\phi_0)}{d\phi^2}\Delta\phi \\ &= -3\sqrt{\frac{\epsilon_V}{4\pi}}H_i^2 M_{\rm Pl} + 3\eta_V H_i^2 \Delta\phi \, , \end{aligned} \tag{3.20}$$

where ϵ_V and η_V are the usual potential slow-roll parameters evaluated at ϕ_0. In the region of the potential that supports inflation these are small so that the contribution from gradients eventually overcomes the potential contribution. This implies that $\phi_{\rm max}$ is pulled back into the inflationary region as described in [157].

However, as $\Delta\phi$ increases further, expanding $dV/d\phi$ is no longer a good approximation, and the potential contribution may overcome the gradient contribution, $k^2\Delta\phi$, so that $f(\phi_0, \Delta\phi)$ may take on negative values. Suppose this occurs at an inhomogeneous amplitude of $\Delta\phi_{\rm crit}$ and correspondingly $\phi_{\rm crit} = \phi_0 + \Delta\phi_{\rm crit}$, such that a zero exists at

$$f(\phi_0, \Delta\phi_{\rm crit}) = k^2\Delta\phi_{\rm crit} + \frac{dV}{d\phi}(\phi_0 + \Delta\phi_{\rm crit}) = 0 \; . \tag{3.21}$$

Then as $\Delta\phi > \Delta\phi_{\rm crit}$, the inflaton will tend to roll towards the reheating minimum at least initially, and has a greater chance of failure[4]

---

[3] Note that while it is assumed that ϕ has a periodic profile with wavelength k, this positive definiteness is general even if ϕ takes on a more complicated profile as $\phi_{\rm max}$ is a maximum of the profile by definition.

[4] In [190], a criterion based on the *spatially average* (i.e. global) force $\langle V'(\phi)\rangle > V'(\langle\phi\rangle)$ was introduced, which led to the simple condition that inflation is likely to fail when $\Delta\phi$ reaches the end of the inflationary plateau. This is consistent with our findings. Our condition, on the other hand, relies on the balancing of the local force at the point of maximal fluctuation, and as we will

Ignoring the trivial case of $f(\phi_0, \Delta\phi) < 0$, $\Delta\phi \approx 0$, where inflation is well-known to succeed, we begin with $f(\phi_0, \Delta\phi) > 0$ – we assume there exists some region where inflation will succeed as long as $\Delta\phi$ is small enough. As we increase $\Delta\phi$, the slope of $f(\phi_0, \Delta\phi)$ is initially positive because $\eta_V \ll 1$ and $k \gtrsim H_i$. We can further relate this to the overall shape of the potential as follows.

If the potential is convex, $d^2V/d\phi^2 > 0$, then $f(\phi_0, \Delta\phi)$ must increase as $\Delta\phi$ is increased and remains positive. This means that convex models are automatically robust to inhomogeneities in the inflaton sector. The inhomogeneous field is initially always pulled back, away from the reheating minimum. The time scale is roughly given by the inverse of its wavenumber, $t_{\rm pb} \sim k^{-1}$. For $N = 1$ (i.e. near horizon size mode), this is then $t_{\rm pb} \sim H^{-1}$, which means that the field is pulled back within a Hubble time. We will confirm this intuition numerically in Sec. 3.4.

On other hand, if the potential is concave, $d^2V/d\phi^2 < 0$, then $f(\phi_0, \Delta\phi)$ may turn over as $\Delta\phi$ increases. If the potential is sufficiently concave before the reheating minimum (which is convex by construction), then a zero crossing at $\phi_{\rm crit}$ can exists such that $f(\phi_0, \Delta\phi_{\rm crit}) = 0$. In this case $f(\phi_0, \Delta\phi) < 0$ at $\phi_{\rm max} > \phi_{\rm crit}$, and the inflaton will fall into the reheating minimum and end inflation. Once a sufficiently large spatial region falls into the reheating minimum, the remaining space will be dragged down by the pressure difference between the inflating plateau and the minimum, resulting in the end of inflation within a few e-folds.

This discussion implies that convex potentials are generically more robust to inhomogeneities than concave potentials. We also see that decreasing the wavelength of the inhomogeneities (and hence increasing k^2) makes models more robust – the most dangerous modes are the long wavelength near horizon modes, consistent with the numerical results of [157].

As we will discuss now, robustness for *concave* potentials is closely related to the characteristic scale of the potential. To see this, note that in order for f to vanish at $\Delta\phi_{\rm crit}$, and to turn negative for $\Delta\phi > \Delta\phi_{\rm crit}$, it must possess a maximum, i.e.

$$\frac{\partial f}{\partial \Delta\phi} = k^2 + V''(\phi_0 + \Delta\phi)\,, \tag{3.22}$$

must have a zero for some value of $\Delta\phi$. We now consider this requirement for different models, beginning with the monomial potentials defined in Eqn. (3.10). In this case

---

see, can accurately predict the point of failure (or not) even when $\Delta\phi$ reaches beyond the end of the inflationary plateau.

we write

$$\begin{aligned}\frac{\partial f}{\partial \Delta\phi} &= k^2 + 2p(2p-1)\frac{V(\phi_0+\Delta\phi)}{M_{\rm Pl}^2}\frac{M_{\rm Pl}^2}{(\phi_0+\Delta\phi)^2} \\ &= k^2\left[1+\frac{6p(2p-1)}{(kL)^2}\left(\frac{\phi_{\rm max}}{\phi_0}\right)^{2p}\frac{M_{\rm Pl}^2}{8\pi\phi_{\rm max}^2}\right],\end{aligned} \tag{3.23}$$

where we have used Eqn. (3.16) in going from the first to the second line. The first term proportional to k^2 is the gradient term, while the second is the potential term. From the denominator of the second term we again see that increasing the wavenumber suppresses the importance of the potential term relative to the gradient term, and that inflation is more robust to inhomogeneities with higher wavenumbers. If the potential is concave, $p < 1/2$, the second term in the parentheses is negative as expected. However, since $|\phi_{\rm max}| < |\phi_0|$ and $p > 0$, it is negligible until $\phi_{\rm max}$ drops well below the reduced Planck mass. If the potential is still well approximated by a power law at this point, an instability may develop (see $\phi^{2/3}$ case in Sec. 3.4). However, the functional form assumed here only describes the potential during the inflationary period, and as the magnitude of ϕ decreases the potential in a single-field model must eventually turn over and develop a minimum. This implies that for sufficiently small $|\phi|$ the potential again becomes convex. If this transition occurs before the second term becomes large, we expect the model to be robust irrespective of whether the inflationary part of the potential is convex or concave.

We can readily extend this discussion to the other classes of models introduced in 3.2.2. For the hilltop models (3.11), we can write (again using Eqn. (3.16))

$$\begin{aligned}\frac{\partial f}{\partial \Delta\phi} &= k^2 - n(n-1)\frac{\Lambda^4}{M_{\rm Pl}^2}\frac{M_{\rm Pl}^2}{\mu_n^2}\left(\frac{\phi_{\rm max}}{\mu_n}\right)^{n-2} \\ &= k^2\left[1-\frac{3n(n-1)}{(kL)^2}\frac{M_{\rm Pl}^2}{8\pi\mu_n^2}\left(\frac{\phi_{\rm max}}{\mu_n}\right)^{n-2}\right].\end{aligned} \tag{3.24}$$

Again the potential is only well approximated by equation (3.11) provided $\phi_{\rm max} < \mu_n$. So a maximum can only occur if μ_n is well below the reduced Planck mass, implying that models in which the characteristic scale over which the potential departs from Λ^4 is Planckian are robust even against large field excursions.

For the plateau models (3.12), defining the potential so the field rolls towards larger values of ϕ, we can similarly write

$$\frac{\partial f}{\partial \Delta\phi} = k^2 \left[1 - \frac{3n(n+1)}{(kL)^2} \frac{M_{\rm Pl}^2}{8\pi\mu_n^2} \left(\frac{\mu_n}{|\phi_{\rm max}|} \right)^{n+2} \right] . \tag{3.25}$$

In this case the potential is only well approximated by (3.12) if $|\phi_{\rm max}| > \mu_n$, and as for the hilltop models, plateau models with a Planckian characteristic scale are robust against large field excursions, and the function f can only change sign for models with sub-Planckian μ_n.

For models in which the potential approaches the plateau exponentially as in (3.13), but defined so that the field rolls towards the minimum in the positive ϕ direction

$$\begin{aligned} \frac{\partial f}{\partial \Delta\phi} &= k^2 - \frac{\Lambda^4}{\mu^2} e^{\phi_{\rm max}/\mu} \\ &= k^2 \left[1 - \frac{3}{(kL)^2} \frac{M_{\rm Pl}^2}{8\pi\mu^2} e^{\phi_{\rm max}/\mu} \right] , \end{aligned} \tag{3.26}$$

we see that for μ of order the reduced Planck mass, $\partial f/\partial \Delta\phi > 0$ in the regime in which the potential is well approximated by (3.13), so that there is no maximum in f and no zero crossing can exist for any value of $\Delta\phi$ and ϕ_0. Starobinsky inflation is an example of this case and will be studied in the following section.

The condition defined by (3.19) is valid for the initial hyperslice. We will now show that it still broadly remains valid at a later time of the evolution. At later times the gradients dilute due to the expansion as $\nabla^2\phi \sim k^2\Delta\phi^2/a(t)^2$, where $a(t) \sim e^{Ht}$ is the scale factor, such that (3.21) becomes

$$f(\phi_{\rm crit}, t) \approx k^2 \Delta\phi_{\rm crit}\, e^{-2Ht} + \frac{dV(\phi_{\rm crit})}{d\phi}, \tag{3.27}$$

and $\Delta\phi_{\rm crit}$ will take different values over time.

Hence, the robustness of a model is not only determined by the existence of a critical value $\phi_{\rm crit}(t=0) = \phi_0 + \Delta\phi_{\rm crit}(t=0)$ for which the field will initially roll towards the minimum, but the field should also restore as close as possible to ϕ_0 before crossing $\phi_{\rm crit}$ at later times to inflate by enough e-folds. If the rate of change of $\phi_{\rm crit}(t)$ is small, the pull-back will have time to homogenize the field before crossing $\phi_{\rm crit}$, and the spacetime will inflate as in the homogeneous case (see D-brane inflation in Fig. 3.4b and an α-attractor model in Fig. 3.5b). However, if $\Delta\phi_{\rm crit}(t)$ decreases with $\mathcal{N}$ faster than the pull-back reduces the amplitude, the field will fall to the minimum, ending inflation (see Fig. 3.3b).

3.4 Numerical validation

In this section we demonstrate the validity of our criterion by solving the equations of general relativity numerically using the numerical relativity package GRCHOMBO [55, 154]. The metric initial conditions for the simulations are described in Sec. 3.2, with near-horizon scale inhomogeneity as defined in Eqn. (3.14) and Eqn. (3.15). The evolution equations and a summary of the parameters used for the simulations (Tab. B.1) are shown in the Appendix. A summary video of the field evolution for different models can be found in this link.

3.4.1 Convex potentials

As discussed above, for convex potentials $\partial f/\partial\Delta\phi > 0$, so that the gradients will always pull the field back. As a concrete representative of this class, we consider

$$V(\phi) = \lambda M_{\rm Pl}^{8/3}(-\phi)^{4/3}. \tag{3.28}$$

A homogeneous initial value of the field of $\phi_0 = -3.26M_{\rm Pl}$ with $\lambda = 2.57\times10^{-14}$ would result in 100 e-folds. Note that the potential as written in Eqn. (3.28) is only a good approximation during inflation, and the full potential is expected to be analytic at the origin. However, the details of the transition do not affect the conclusions.

Fig. 3.2a shows that even for field excursions that reach the reheating minimum, with $\Delta\phi = 3.26M_{\rm Pl}$ (corresponding to $\Omega \equiv \rho_{\rm grad}/\rho_V \approx 50$), the maximum of the field $\phi_{\rm max}$ is pulled back into the inflating region, as predicted by our criterion. In the latter case, the scalar field has support well in the regime where a homogeneous field would have failed. Similar results were found for the quadratic model $V = (1/2)m^2\phi^2$ in [157], which is also robust.

Perhaps the most interesting point here is that convex models are robust even if the inflaton explores regions of the potential that do not support inflation. This was first observed in [157] for $m^2\phi^2$ potentials, and here we see that this remains true more generally.

It is also worth noting that different regions begin inflation for rather different values of the scalar field, so that the resulting spacetime will be highly inhomogeneous

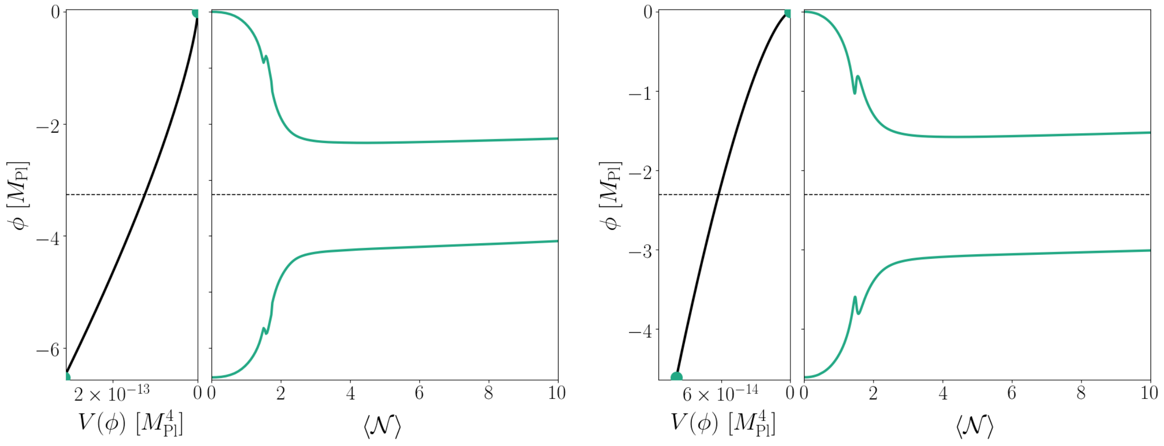

(a) **(b)**

Fig. 3.2 (a): Convex monomial: The left panel shows the convex model potential $\phi^{4/3}$ (3.28) rotated by 90°. The right panel shows the evolution of the maximum $\phi_{\rm max} = \phi_0 + \Delta\phi$ and minimum $\phi_{\rm min} = \phi_0 - \Delta\phi$ field points as a function of e-folds $\mathcal{N}$ (time runs from left to right). If these extremal points restabilize to values closer to ϕ_0, inflation can proceed. Failure occurs when one of the points diverges to the reheating minimum, but this model shows robustness to this failure mode, as expected from our analytic prescription. **(b): Concave monomial:** As Fig. 3.2a but for the concave monomial model $\phi^{2/3}$ (3.29). The dashed black line corresponds to the mean value ϕ_0, which is set to be the value that would result in 100 e-folds for the homogeneous case. See Tab. B.1 for more details about the parameters used. The field at the reheating minimum is pulled back and enters slow-roll inflation from the restored field value. The features at $\mathcal{N} \approx 2$ correspond to black holes that form and inflate out of the simulation grid after the pull-back – with the time scale roughly given by the inverse of its wavenumber.

on very large scales and inflation only leads to homogeneity and isotropy within the different regions.

3.4.2 Concave potentials

As we saw in our analytic treatment, a more careful discussion is required for concave potentials because the robustness depends on the characteristic scale of the potential μ. We will now test our analytic predictions for different concave models.

Monomial potentials

An example of a concave monomial potential which is compatible with the observed value of the spectral index n_s is the so-called $\phi^{2/3}$ model which arises in the context of string theory [424]. During inflation, the potential is well approximated by

$$V(\phi) = \lambda M_{\rm Pl}^{10/3}(-\phi)^{2/3} \, . \tag{3.29}$$

This is a large field model in which $\phi_0 = -2.31 M_{\rm Pl}$ and $\lambda = 3.58 \times 10^{-14}$ lead to 100 e-folds of inflation in the absence of inhomogeneities. As mentioned previously, for typical values of the parameters, these models develop a maximum of f very close to the bottom of the potential. In fact, the critical point where $f = 0$ is at $\Delta\phi_{\rm crit} \approx -1.25 \times 10^{-10} M_{\rm Pl}$ for $N = 1$ and thus it is challenging to simulate a region where $f < 0$.

We show the results for this model in Fig. 3.2b. As expected, for concave monomial models the results are similar to those with convex potentials.

Hilltop models

For concave models, like hilltop models (3.11), f may develop a zero at $\Delta\phi_{\rm crit}$. Our condition implies that there is a maximum in f if and only if $n > 2$ since for $n = 2$ f is linear in $\Delta\phi$ and a second zero crossing cannot exist. In this section we will focus in the cubic hilltop model $n = 3$,

$$V(\phi) = \begin{cases} \Lambda^4 \, , & \phi < 0 \\ \Lambda^4 \left[1 - \left(\frac{\phi}{\mu_3}\right)^3\right] \, , & 0 < \phi < \phi_{\rm cc} \\ \frac{1}{2} m^2 (\phi - \phi_{\rm reh})^2 \, , & \phi \geq \phi_{\rm cc} \end{cases} \tag{3.30}$$

To simulate these models, we extend the inflationary potential with a quadratic minimum beyond some value $\phi_{\rm cc}$, and a flat plateau $V(\phi) = \Lambda^4$ for $\phi < 0$. The potential we use for reheating is $V_{\rm reh}(\phi) = (1/2)m^2(\phi - \phi_{\rm reh})^2$, where m and $\phi_{\rm reh}$ are chosen such that $V_{\rm inf}(\phi_{\rm cc}) = V_{\rm reh}(\phi_{\rm cc})$ and $dV_{\rm inf}(\phi_{\rm cc})/d\phi = dV_{\rm reh}(\phi_{\rm cc})/d\phi$. The reheating potential is clearly convex, but we choose $\phi_{\rm cc}$ sufficiently deep into the non-inflating regime (i.e. the slow-roll parameter $\epsilon \geq 1$). This is conservative in the sense that the model would be more robust if the transition occurred earlier[5]. This model of reheating is chosen for simplicity – one could also imagine other examples like

---

[5] Note that such extensions may change their observational constraints, see e.g. [298].

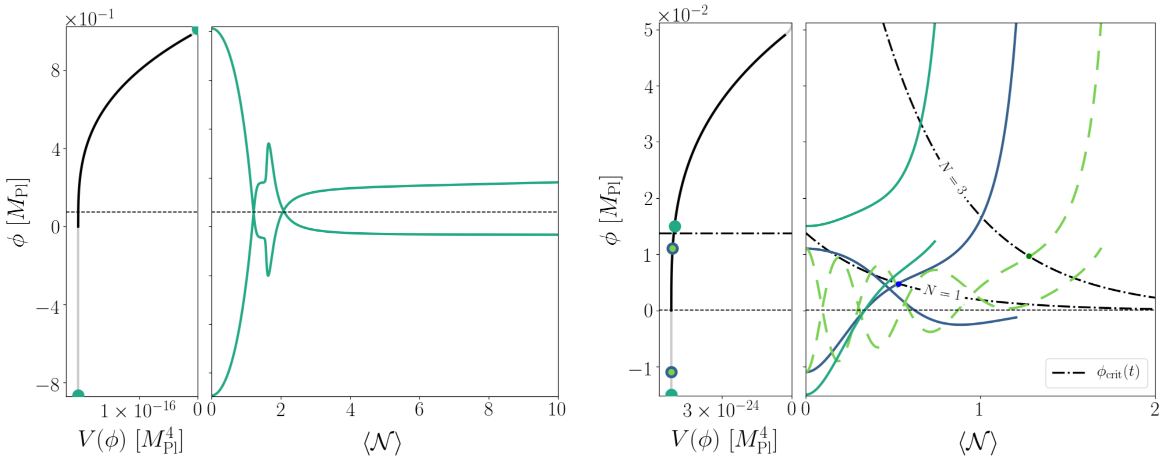

(a) **(b)**

Fig. 3.3 (a): Cubic hilltop with $\mu_3 = M_{\rm Pl}$. The left panel shows the potential (3.30) rotated 90^o where the solid black part of the curve is the inflationary potential we want to test and the grey parts correspond to extensions of the model as described in the text. The dashed black line corresponds to the mean value of the field ϕ_0 that would result in 100 e-folds in the absence of inhomogeneities. The right panel shows the evolution of the maximum and minimum of the field $\phi_{\rm max}$ and $\phi_{\rm min}$ where we have chosen $\Delta\phi$ such that the field configuration reaches the minimum of the potential. As there exists no $\Delta\phi_{\rm crit}$, the extrema of the field pull back towards ϕ_0 during the evolution (blue solid line). At $\mathcal{N} \approx 2$ black holes form and shortly afterwards inflate out of the simulation when they fall below the numerical resolution of the grid. **(b): Cubic hilltop** with $\mu_3 = 5 \times 10^{-2} M_{\rm Pl}$. The dash-dotted black lines correspond to the critical values of the field $\phi_{\rm crit}(t)$ by solving (3.27) for different wavelengths: $k = 2\pi H$ ($N = 1$) and $k = 6\pi H$ ($N = 3$). If some value crosses to $> \phi_{\rm crit}(t)$, the field will fall from the inflationary plateau to the reheating minimum, dragging the rest down. For example, for $N = 1$ the minimum of the field $\phi_{\rm min}$ (blue solid line) crosses the dash-dotted line $\phi_{\rm crit}$ and hence rolls down. For fixed $\Delta\phi$, the $N = 3$ case (dashed green line) falls to the minimum when $\phi_{\rm max}$ crosses the $\phi_{\rm crit}$ that corresponds to $N = 3$, but stays longer in the inflationary plateau than the $N = 1$ case. As expected, this shows that inflation is more robust to inhomogeneities with shorter wavelengths. The parameters used in this plot are shown in Tab. B.1.

hybrid inflation where the reheating field is not the inflaton, but this would require working with an additional scalar field.

As discussed above, the robustness of this model depends on the characteristic scale of the potential μ_3. For $\mu_3 = M_{\rm Pl}$ we find that $\phi_0 = 7.43 \times 10^{-2} M_{\rm Pl}$ and $\Lambda^4 = 2.05 \times 10^{-16} M_{\rm Pl}^4$ would result in 100 e-folds for the homogeneous case. As argued in the previous section, f does not have a maximum, so that the field is pulled back even when it explores the minimum of the potential. This is shown in Fig. 3.3a.

On the other hand, for $\mu_3 = 5 \times 10^{-2} M_{\rm Pl}$ together with $\phi_0 = 1.05 \times 10^{-5} M_{\rm Pl}$ and $\Lambda^4 = 5.15 \times 10^{-24} M_{\rm Pl}^4$, f develops a maximum at $\Delta\phi_* = 6.87 \times 10^{-3} M_{\rm Pl}$ and a zero crossing at $\Delta\phi_{\rm crit} = 1.38 \times 10^{-2} M_{\rm Pl}$. So for an initial amplitude of $\Delta\phi = 1.10 \times 10^{-2} M_{\rm Pl} \ < \Delta\phi_{\rm crit}$ the field will initially be pulled back, whereas for $\Delta\phi = 1.50 \times 10^{-2} M_{\rm Pl} \ > \Delta\phi_{\rm crit}$, the the inflaton will fall from the inflating plateau into the reheating region, Fig. 3.3b.

However, even if the field is initially pulled back, inflation may fail at later times because $\phi_{\rm max} > \phi_{\rm crit}(t)$ (see dash-dotted black line). For these two cases in which $\Omega \approx 10^{-3}$, inflation fails to provide more than 1.5 e-folds. In addition, we show that inflation is more robust to inhomogeneities with higher wavenumbers. Starting with the same amplitude, we see that $N = 3$ leads to more e-folds of inflation than the $N = 1$ case, although this is not sufficient to save inflation in this case. Similar results were found for the hilltop quartic model ($n = 4$) in [157], in agreement with the theoretical prediction. We conclude that small field hilltop models with $n > 2$ are sensitive to initial inhomogeneities in the scalar field.

Plateau models

We also consider the third class of concave potentials (3.12), which arises in string theory as D-brane inflation [296, 211, 189]. In the best-studied case the inflaton describes the position of a $D3$ brane, which corresponds to $n = 4$. As in the hilltop model, we smoothly extend the potential with a convex model at $\phi_{\rm cc} = -1.05\mu_4$ (such that $\epsilon(\phi_{\rm cc}) \gg 1$), giving us the following approximation to the potential

$$V = \begin{cases} \Lambda^4 \left[1 - \left(\frac{\mu_4}{\phi}\right)^4\right] \ , & \phi < \phi_{\rm cc} \\ \frac{1}{2} m^2 (\phi - \phi_{\rm min})^2 \ , & \phi \geq \phi_{\rm cc} \end{cases} \tag{3.31}$$

As before, we first consider $\mu_4 = M_{\rm Pl}$, $\phi_0 = -2.18 M_{\rm Pl}$ and $\Lambda^4 = 5.58 \times 10^{-15} M_{\rm Pl}^4$ so that observational constraints on the scalar power index are satisfied. We choose $\Delta\phi = 1.25 M_{\rm Pl}$ for which $\phi_{\rm max} = \phi_{\rm reh}$ and observe that the field is pulled back to safety concluding that the model is robust. This is shown in Fig. 3.4a.

On the other hand, for $\mu_4 = 10^{-2} M_{\rm Pl}$ with $\phi_0 = -9.92 \times 10^{-2} M_{\rm Pl}$ and $\Lambda^4 = 1.29 \times 10^{-24} M_{\rm Pl}^4$, we predict a value of $\Delta\phi_{\rm crit} = 8.21 \times 10^{-2} M_{\rm Pl}$ for which the field falls from the inflationary plateau. We test this numerically in Fig. 3.4b by exploring the evolution of field configurations with $\Delta\phi = 8.40 \times 10^{-2} M_{\rm Pl}$ and $\Delta\phi = 8.10 \times 10^{-2} M_{\rm Pl}$. As shown in the figure the former is immediately dragged down ending inflation while

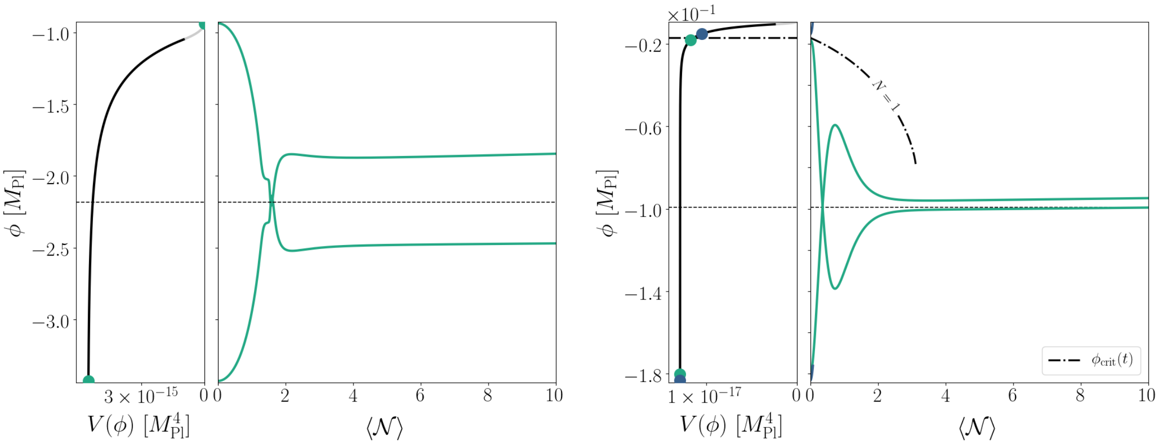

(a) **(b)**

Fig. 3.4 (a): Large field *D*-brane model with $\mu_4 = M_{\rm Pl}$. The black curve is the inflationary model and the grey parts of the curve show the reheating extension which is attached. No $\phi_{\rm crit}$ exists so even field configurations that reach the minimum are pulled back to the inflationary plateau. As for other large field models, the gradient energy density collapses and forms black holes at $\mathcal{N} \approx 2$. The dashed black line is the value of ϕ_0 that would inflate for 100 e-folds in the absence of inhomogeneities, see Tab. B.1 for more details. **(b): Small field *D*-brane:** As Fig. 3.4a but with $\mu_4 = 10^{-2}M_{\rm Pl}$. For the wavenumber $N = 1$, (3.27) predicts the field critical values $\phi_{\rm crit}(t)$ (dash-dotted black line). If we choose $\Delta\phi$ such that $\phi_{\rm max} > \phi_{\rm crit}$ the field will immediately fall down to the reheating minimum (blue line). The value of $\phi_{\rm crit}$ decrease more slowly than in the cubic hilltop case (see Fig. 3.3b), so the field has time to pull back to values close to ϕ_0 and slow-roll down from the plateau (green line).

the latter is pulled back from the brink and inflates, as our criteria predicted. We conclude that small field *D*-brane inflation is not generically robust because there exist values of $\Delta\phi$ that can rapidly end it.

The *D*-brane model is discussed further in Sec. (3.5), in the context of constraints on the initial value of ϕ_0.

Exponential plateau models

For completeness, we also consider models in which the potential approaches the plateau exponentially rather than like a power law. The best-known model in this class is the Starobinsky model [428]

$$V(\phi) = \Lambda^4 \left(1 - e^{\phi/\mu}\right)^2 \,, \tag{3.32}$$

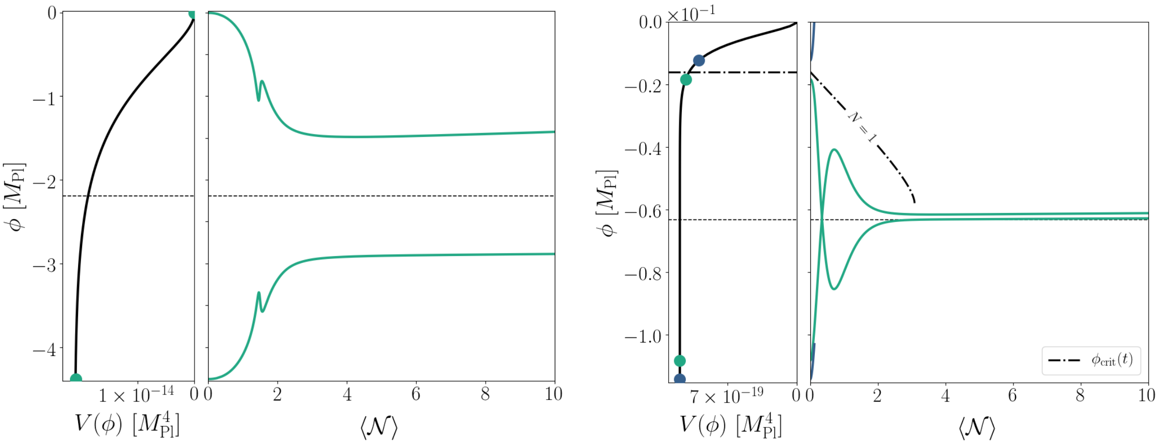

(a) **(b)**

Fig. 3.5 (a): The **Starobinsky model** is an example of an exponential plateau model with $\mu = \sqrt{3/16\pi} M_{\rm Pl}$ and hence with large field excursions. As f does not have a maximum, it will remain positive for any $\Delta\phi$, so that the model will support inflation even if the field configuration starts in non-inflationary regions of the potential (blue solid line). Similar to other large field cases (Fig. 3.2b, 3.2a, 3.3a and 3.4a) in which there are large gradient energy densities, black holes form at $\mathcal{N} \approx 2$. See Tab. B.1 for details of the parameters used. **(b):** Example of an α-**attractor model** with $\mu = 5 \times 10^{-3} M_{\rm Pl}$. In this case there exists a $\Delta\phi_{\rm crit}$ such that the field will initially roll towards the non-inflationary regime and reach the minimum (blue line). As for the small field D-brane model (Fig. 3.4b), the values taken by $\phi_{\rm crit}(t)$ over time change more slowly than the pull back. So as long as initially $\Delta\phi < \phi_{\rm crit}(t = 0)$ (green line), the field will restabilise to values close to ϕ_0 before any region crosses $\phi_{\rm crit}(t)$ and therefore the spacetime approaches inflation during the 10 e-folds for which we follow the evolution, unlike the small field cubic hilltop model (see Fig. 3.3b).

where $\mu \equiv \sqrt{3/16\pi} M_{\rm Pl}$ [429]. The transition from the concave to the convex domain of the potential occurs at $d^2V/d\phi^2(\phi_{\rm cc}) = 0$, or $\phi_{\rm cc} = -\mu \ln 2$ so there is no need to extend it. In this model f does not possess a maximum, and the field is pulled back into the inflationary plateau even if it initially explores the minimum.

We show this in Fig. 3.5a for the parameters shown in Tab. B.1 in the appendix. As expected, even field configurations that reach the bottom of the potential are restabilised to values closer to ϕ_0, and we follow their evolution numerically for $\mathcal{N} > 10$ e-folds, at which point the inhomogeneities have redshifted away and the local regions undergo slow-roll inflation.

In the Starobinsky model the scale μ and the Planck scale share a common origin, but this is not the case for all exponential plateau models. The so-called α-attractors

[297, 299] are a class of models in which μ can vary over a wide range of scales. For sufficiently small values f will cross zero for a large enough value of $\Delta\phi$ as we will show below.

Using (3.19) we see that for $\mu < 2.7 \times 10^{-2} M_{\rm Pl}$, f will gain a maximum, and crosses zero before $\phi_{\rm cc}$ if $\mu < 10^{-2} M_{\rm Pl}$. We show this for $\mu = 5 \times 10^{-3} M_{\rm Pl}$ in Fig. 3.5b. As before, we set ϕ_0 to the value of the field that would result in 100 e-folds in the absence of inhomogeneities. For this value f crosses zero at $\Delta\phi_{\rm crit} = 4.74 \times 10^{-2} M_{\rm Pl}$. We confirm that for $\Delta\phi = 5.1 \times 10^{-2} M_{\rm Pl} > \Delta\phi_{\rm crit}$ the field is dragged down, and that it is pulled back for $\Delta\phi = 4.5 \times 10^{-2} M_{\rm Pl} < \Delta\phi_{\rm crit}$. Similar to the small-field D-brane inflation model, the rate of change of $\phi_{\rm crit}(t)$ over time is smaller than the pull-back, so that there is no crossing at later times and the field can restore to values close to ϕ_0. We again follow the evolution for $\mathcal{N} > 10$ e-folds.

3.5 Constraints on the initial value of the scalar field

So far we have focused the discussion on models of inflation with ϕ_0 chosen to yield 100 e-folds in the absence of inhomogeneities. We will now consider both ϕ_0 and the amplitude $\Delta\phi$ as free parameters and study the behavior of f when varying them. Models that are always robust to inhomogeneities do not offer further insight into the initial value of the inflaton field ϕ_0 required for successful inflation. However, for models that suffer the weakness of having $f < 0$ for some range of $\Delta\phi$, we can obtain a constraint on ϕ_0.

To see this, let us denote the value of ϕ for which $dV(\hat{\phi})/d\phi$ is the most negative by $\hat{\phi}$. This is the value of the field for which the model is most likely to fail for any value of $\Delta\phi$ as we can see from Eqn. (3.21). If $f(\phi_0, \hat{\phi} - \phi_0) > 0$, the model will be robust to inhomogeneities. This condition leads to a bound

$$\hat{\phi} - \phi_0 > -\frac{1}{k^2}\frac{dV(\hat{\phi})}{d\phi}\,, \tag{3.33}$$

that guarantees robustness for any value of $\Delta\phi$.

Of course, not all values of $\Delta\phi$ are allowed because we must ensure that the energy density in gradients remains sub-Planckian, which imposes a bound of the form

$$\hat{\phi} - \phi_0 \ll \frac{M_{\rm Pl}^2}{k}\,. \tag{3.34}$$

So one may ask whether one can find values of ϕ_0 such that $f(\phi_0, \Delta\phi) > 0$ for all energetically allowed values of $\Delta\phi$, and by combining the bounds, we see that this will be the case provided

$$-\frac{1}{k}\frac{dV(\hat{\phi})}{d\phi} \ll M_{\rm Pl}^2 \,. \tag{3.35}$$

This bound is fairly weak for any model in which the inflationary Hubble scale is well below the Planck scale, and often there will be stronger constraints on $\Delta\phi$, for example, because the potential is only of the assumed form over a much smaller field range than $M_{\rm Pl}^2/k$. These constraints should then be taken into account.

Let us, for example consider D-brane inflation. In this case, inflation must certainly end before $V(\hat{\phi}) = 0$, and we will take $\hat{\phi} = -\mu$ to approximate the point when $dV(\hat{\phi})/d\phi = -4\Lambda^4/\mu$ is most negative. Hence (3.33) leads to

$$\phi_0 < -\mu - \frac{1}{k^2}\frac{4\Lambda^4}{\mu} \,. \tag{3.36}$$

This constraint on the initial mean value of the field is shown in Fig. 3.6 for different wavenumbers of the inhomogeneities $k = 2\pi N/L$ with $L = H_i^{-1}$ and $N = 1$, $N = 10$, and $N = 100$. The green shaded regions indicate the initial conditions for which the model is not robust, in the sense that the existence of sufficiently large pertubations will cause it to fail.

In addition, we approximately sketch the constraints imposed by the *Planck* data, which roughly exclude values of $\mu < 2 \times 10^{-7} M_{\rm Pl}$ and $\mu > 2 \times 10^{-1} M_{\rm Pl}$ [31], together with the requirement that inflation lasts for at least $\mathcal{N} = 100$.

As we discussed, the energy density stored in gradients must be sub-Planckian, which imposes the additional constraint

$$|\phi_0| - \mu \ll \frac{M_{\rm Pl}^2}{k} \,. \tag{3.37}$$

Since this bound is rather weak for typical parameters, it is not shown in Fig. 3.6.

From the perspective of low energy effective field theory, the plateau may extend over large or possibly even infinite distances in field space. However, in the context of string theory there is another constraint we should impose on $\Delta\phi$ to ensure our discussion remains valid. The inflaton parameterizes the position of a brane along a warped throat in the internal space whose size is limited. As a consequence, the plateau only extends over a finite range, and we only expect the potential to be well-approximated by our model for sub-Planckian $\Delta\phi$ [76]. So in string theory, only

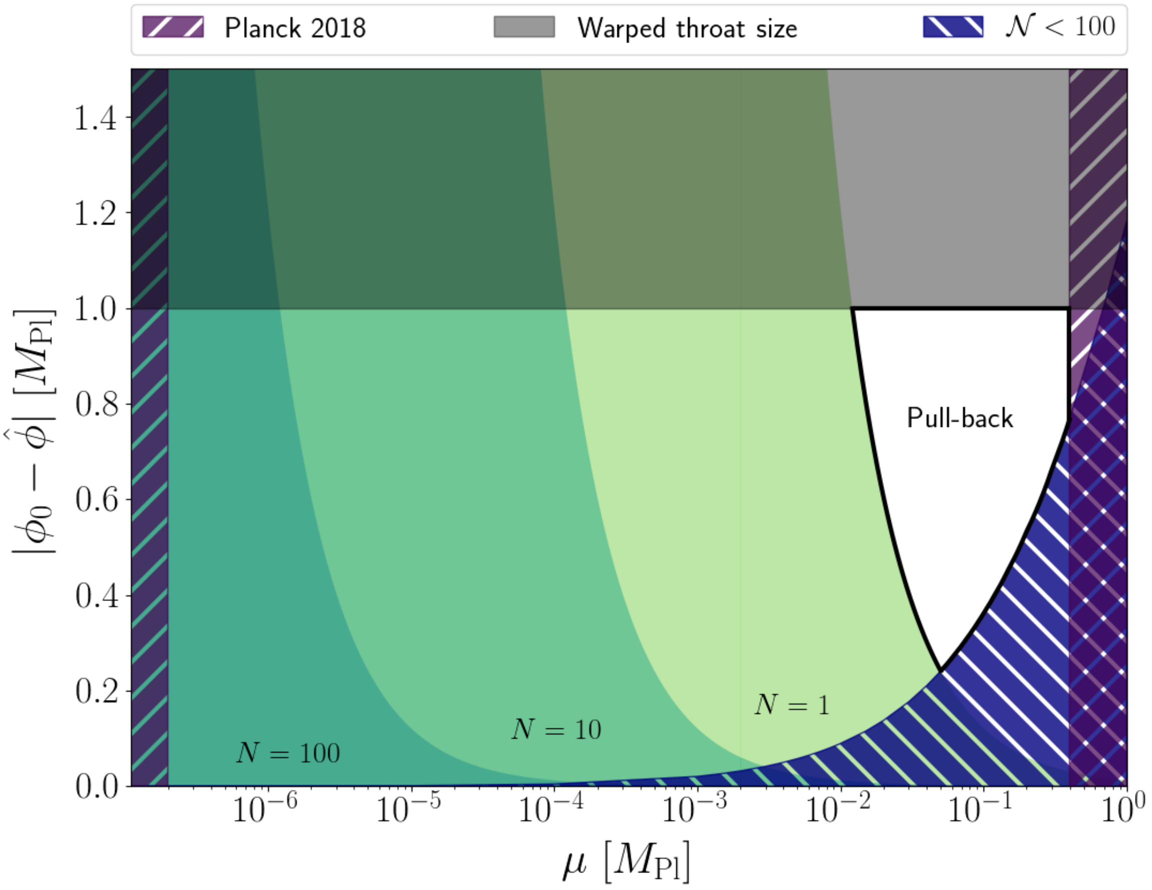

Fig. 3.6 Constraints on ϕ_0 and μ for successful inflation in D-brane model, given by (3.31). We define successful inflation if a model with a mean value of ϕ_0 has $f > 0$ for all choices of $\Delta\phi$ so that only pull-back effects can be observed. Small field models are more sensitive to inhomogeneities since smaller values of μ make the model more concave and hence less robust, requiring stronger constraints for the initial mean field value ϕ_0. Higher modes (greater N) are more robust, and therefore relax the constraints on ϕ_0.

the area below the grey region is available, and we see that the sweet-spot for which the model is robust to inhomogeneities lies at around $\mu \sim 10^{-1} M_{\rm Pl}$.

These constraints should not be taken as definitive, but rather illustrative, because other factors may influence the dynamics. For example, the presence of a sharp rise in the potential was seen to make the model less robust in [157], and we are only studying a subset of possible inhomogeneous initial conditions. Overall, however, such differences are likely to make the constraints on the model more restrictive, rather than less.

3.6 Summary and discussion

We studied the robustness of different single-field models of inflation to inhomogeneities in the scalar field. We found a simple analytic criterion that successfully predicts whether a given model for a given set of initial data will successfully inflate in our $3 + 1$ dimensional numerical relativity simulations. For convex potentials, we showed that inflaton eventually begins even if the inhomogeneities in initial configuration are large enough to explore the minimum of the potential. For concave models, we see that effects of inhomogeneities strongly depend on the characteristic scale of the potential. For potentials with super-Planckian characteristic scale the inflaton is pulled back towards field values for which the model supports inflation, even if the field initially explores the minimum. For potentials with sub-Planckian characteristic scales the potential gradients win over gradients in the scalar field, and inflation rapidly ends. As a consequence, concave potentials with sub-Planckian characteristic scale will require additional physical mechanisms (or tuning) to set up initial conditions suitable for inflation.

For example, from Fig. 3.6, we see that D-brane inflation with $\mu < 10^{-2} M_{\rm Pl}$ will only be robust to inhomogeneities in the field if the mean initial value is super-Planckian. This is in tension with the bound on the field range derived in [76] and implies that inflation will not succeed if the brane is initially highly perturbed.[6]

While we have assumed that the metric sector is initially conformally flat in our analysis, since $f(\phi) \subset -dV/d\phi$, we expect the result that concave potentials with sub-Planckian characteristic scales are less robust to hold more generally. The condition Eqn. (3.19) will in general contain additional curvature terms of order $\lesssim K\partial_\mu\phi$ which may change the position of the zero of f, but these will not dominate the $k^2\Delta\phi$ term. We leave a more detailed study of the larger space of initial conditions for future work.

---

[6] The brane is usually assumed to be homogeneous in most constructions of such models. See for example [111, 207] for studies that deviate from this assumption.

Chapter 4

Abelian Higgs cosmic strings with full numerical relativity

This chapter contains the articles "Cosmic string loop collapse in full general relativity" [264], published in *Physical Review D (PRD)*, and "Coherent gravitational waveforms and memory from cosmic string loops" [64], published in *Classical and Quantum Gravity (CQG)*.

We present the first fully general relativistic dynamical simulations of Abelian Higgs cosmic strings using 3+1D numerical relativity. Focusing on cosmic string loops, we show that they collapse due to their tension and can either (i) unwind and disperse or (ii) form a black hole, depending on their tension $G\mu$ and initial radius. We show that these results can be predicted using an approximate formula derived using the hoop conjecture, and argue that it is independent of field interactions. We extract the gravitational waveform produced in the black hole formation case and show that it is dominated by the $l = 2$ and $m = 0$ mode. In addition, we also construct its first-time-ever time-domain gravitational-wave strain waveform, which exhibits a large memory effect during merger, ending with a burst and the characteristic ringdown as a black hole is formed. Furthermore, we investigate the waveform and energy emitted as a function of string width, loop radius and string tension $G\mu$. We find that the mass normalized gravitational-wave energy displays a strong dependence on the inverse of the string tension $E_{\mathrm{GW}}/M_0 \propto 1/G\mu$, with $E_{\mathrm{GW}}/M_0 \sim \mathcal{O}(1)\%$ at the percent level, for the regime where $G\mu \gtrsim 10^{-3}$. Conversely, we show that the efficiency is only weakly dependent on the initial string width and initial loop radii. Using these results, we argue that gravitational wave production is dominated by kinematical instead of geometrical considerations. Lastly, we use our results to put a bound on the production rate of planar cosmic strings loops as $N \lesssim 10^{-2}$ Gpc^{-3} yr^{-1}.

4.1 Introduction

The detection of Gravitational Waves (GW) from black hole (BH) binaries [8] by the LIGO/Virgo collaboration marked the start of a new era of observations. Beyond astrophysical objects such as BH and neutron stars, this paved the way for the use of GW to search directly for signatures of new physics. One of the key targets of this search is the existence of a network of cosmic strings [6, 1, 4, 15].

Cosmologically, cosmic string networks naturally arise after a phase transition in the early universe, possibly during GUT symmetry breaking[1] [308, 448, 271, 454, 287, 163]. These networks may manifest themselves through several channels, such as imprints via lensing on the Cosmic Microwave Background [23] and emitting gravitational waves. There is a large literature concentrating on the *stochastic* background of weak field emission of GW through cusps, travelling kinks and kink-kink interactions of the strings [451, 443, 274, 440, 217, 218, 398, 413, 269, 121, 53, 50, 143, 122, 51, 172–174, 88, 406, 93, 289, 186, 60], which is recently searched for by the LIGO/Virgo collaboration [6, 1, 4, 15, 13, 18]. This signal is the total integrated power of *incoherent* GW from all such individual emissions, i.e. the sum of all individual emissions which themselves are too weak to be directly detected. Furthermore, these networks may manifest themselves through other channels, such as their imprints via lensing on the Cosmic Microwave Background [452, 23].

Complementarily, one can also search for localized *coherent* events of these strings. Coherent events are those that are individually energetic enough to be detected directly. Such events can occur, for example, when the strings self-interact through the formation of sharp cusps, through the collisions of travelling kinks that are formed during the intercommutation (i.e. collisions) of cosmic strings, or when cosmic string loops collapse. Such a search requires the construction of GW waveform templates – parameterized coherent time/frequency domain signals which can then be searched via match-filtering in the detector signal stream or identified within a burst search. We emphasise that searches for stochastic and coherent signals are complementary – the non-detection/detection of one does not imply the non-detection/detection of the other.

---

[1] More speculatively, string theory also suggests the presence of cosmological fundamental superstrings, especially through the mechanism of brane inflation [388, 295].

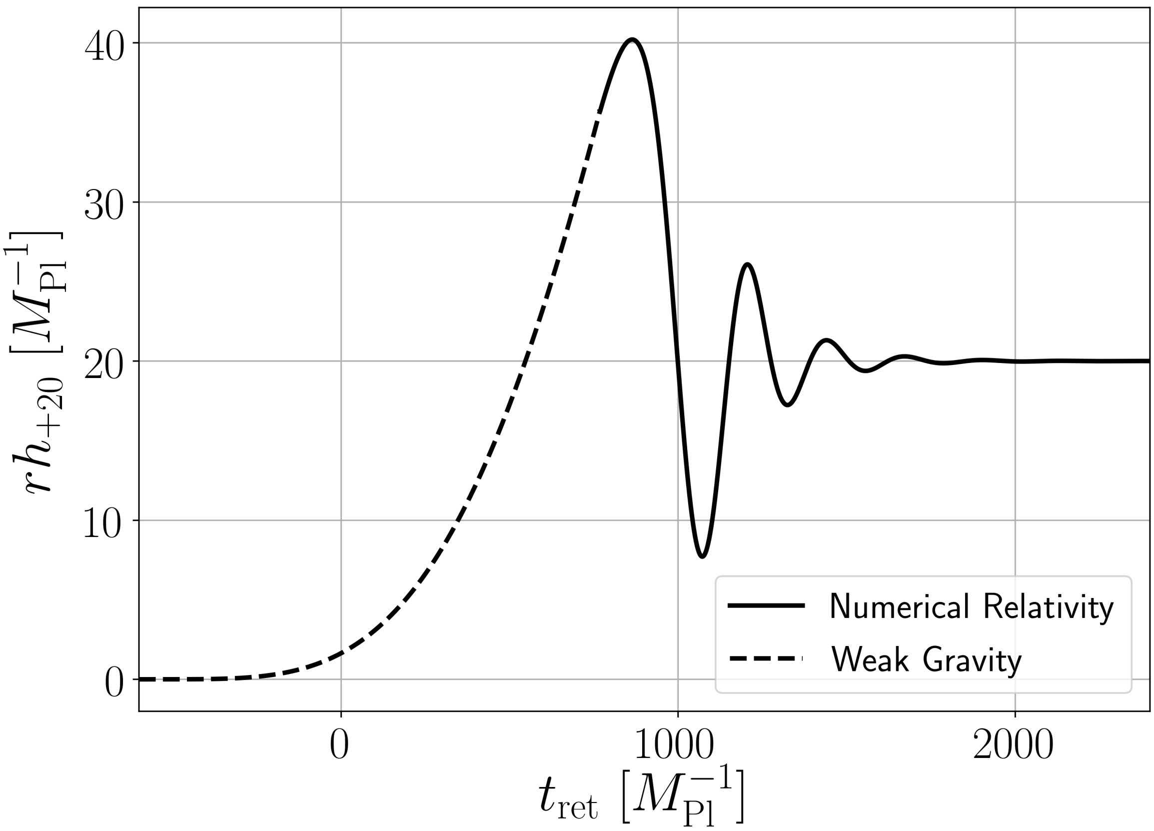

Fig. 4.1 Strain waveform: The $l = 2$, $m = 0$ strain mode for a cosmic string loop collapse into a black hole with $G\mu = 4 \times 10^{-3}$ and $R_0 = 600\ M_{\rm Pl}^{-1}$. The dotted signal was calculated using the semi-analytical approach while the solid line is from the integration of the NR signal (see Appendix (C.6)). The strain exhibits a large memory due to the aspherical loss of matter ejecta during merger, ending with a characteristic ringdown after the black hole is formed. A summary movie of the simulation can be found here [233]. A set of strain waveforms for different $G\mu$ are plotted in C.9.

Before this work, the two primary methods of modeling cosmic strings have been through solving the field theory equations in flat or expanding spacetime, or through an effective Nambu-Goto prescription with weak coupling to gravity (see e.g. [454]). In either case, by considering the stress-energy of a network of strings, one can then compute in the weak gravity limit a stochastic GW background [451, 174]. Local events such as the collisions of traveling kinks and cusps along the strings are expected to produce bursts of GW – these bursts events have been computed using the Nambu-Goto approximation, again in the weak field limit [174]. These two methods do not coincide in general, mainly due to their disagreement on the primary energy loss mechanism of the cosmic strings (see [270, 455, 352, 378, 353, 91]).

Going beyond the weak field limit requires the finding of the solutions to the full field theory coupled to general relativity – and in this work we present the *first numerical relativity simulation of Abelian Higgs cosmic strings in full general relativity*[2]. In this chapter, we numerically explore the collapse of a circular cosmic string loop in extreme regimes ($4 \times 10^{-3} < G\mu < 4 \times 10^{-2}$). In the literature, collapsing cosmic string loops have been considered as seeds in the formation of primordial black holes [273, 253, 393, 220, 120, 99, 338, 462, 245, 366, 137, 109, 84, 286]. We show that whether the loop collapses into a BH or unwinds itself depends on a simple analytic relation derived using the hoop conjecture.

In this chapter, we compute the corresponding coherent GW *strain* in the time-domain – see Fig. 4.1. In other words, we compute the GW strain waveform from individual GW events from the collapse to black holes of cosmic string loops, which is manifestly a strong gravity event. We show that the coherent GW strain signals from the collapse of cosmic string loops are dominated by two major components. The first component is that of a large gravitational wave memory [434, 147] effect during the merger, generated by a large aspherical "jet-like" ejection of matter radiation. The second component is that of the final ringdown phase post-BH formation, with the initial collapse stage being a subdominant contribution to the total signal. We also find that the efficiency of GW production is around $\mathcal{O}(1)\%$ of the total cosmic string mass, which is in agreement with the bound of $< 29\%$ [254]. This efficiency is dependent on the cosmic string tension $G\mu$, with *lower* tension producing *more* GW – up to 2.2% for $G\mu = 2 \times 10^{-3}$, which is the lower bound of the parameter space studied in this work. In comparison, the efficiency for head-on BH mergers and inspiral merger is 0.06% and $\sim 5\%$ respectively [426, 397]. We will comment on this somewhat counter-intuitive result in section 4.6.

Coherent GW events are categorized by its energy ("loudness") and its characteristic frequency. The distance d from which one of these events could be observed by current and future GW detectors is given by

$$\left(\frac{d}{10\text{ Mpc}}\right) \sim \sqrt{\frac{E_{\text{GW}}}{M_\odot}}\left(\frac{10^{-19}}{h}\right) \tag{4.1}$$

---

[2] Work had been done in the past for infinite straight strings and traveling waves in the context of full general relativity [213, 242, 334, 330, 209, 214, 219].

where E_{GW} is the energy emitted in GWs and h is the strain sensitivity of the detector. Roughly speaking, interferometers are optimized to detect GW induced strain of $h \sim 10^{-21}$ around a finite frequency domain – for the LIGO/Virgo interferometers this is $f \sim 10 - 1000$ Hz. In the case of GW events when a black hole is formed, the quasinormal mode (QNM) frequency of the characteristic ringdown phase is determined by its mass. Combined, this means that LIGO/Virgo is sensitive to $E_{\mathrm{GW}} \sim M_\odot$ events at around 100 Gpc. Thus to produce coherent GW observable by LIGO/Virgo one must produce sufficiently energetic ("loud") events at its detector frequency[3]. This means that LIGO/Virgo will be sensitive to cosmic string loop events[4] of around $100M_\odot$ at a distance of about 1 Gpc [264].

To check the dependency of the waveforms and energy as a function of the initial conditions and parameter of the cosmic string loops, we compute the waveforms for the three main parameters of the system. The first parameter is the string tension $G\mu$ which specifies the underlying theory. The next two parameters, the initial radius R_0 and the width of the string δ, define the initial string geometry. We find evidence that the *the mass normalized waveforms depend strongly on the string tension $G\mu$, and weakly on the string width δ and initial string radii R_0*, for the regime $G\mu > 10^{-3}$. Hence, it follows that the GW production efficiency of collapsing cosmic string loops is only weakly dependent on initial string loop radii R and the width of the string δ – at least for the parameter space studied in this work. Combined with the fact that the power is dependent on string tension $G\mu$ – and this sets the loop velocity at BH formation – we argue that the generation of GW is driven by collapse kinematics instead of the geometry of the system.

The chapter is organized as follows. In section 4.2, we describe the abelian Higgs cosmic string model and recap some previous results. In section 4.3, we discuss the possible outcomes of a collapsing circular cosmic string loop and introduce a formula to predict such a result. In section 4.4, we describe the parametric dependences of GW power from both string geometry and string model for cosmic string collapse events. In section 4.5, we show how the waveform is not degenerate to other known BH merger processes, and we derive the full coherent time-domain GW strain waveform from a combination of semi-analytic and numerical results. We discuss the prospects and strategies for a direct detection search and conclude in section 4.6.

---

[3] The signal is redshifted as it travels from the progenitor to the detectors, but this effect is small.

[4] For binary black hole mergers, the efficiency is about 5%, i.e. 5% of the merger mass is converted to E_{GW}, putting them into the peak sensitivity window of LIGO/Virgo ($\mathcal{O}(1 \sim 100)M_\odot$ black holes) as designed.

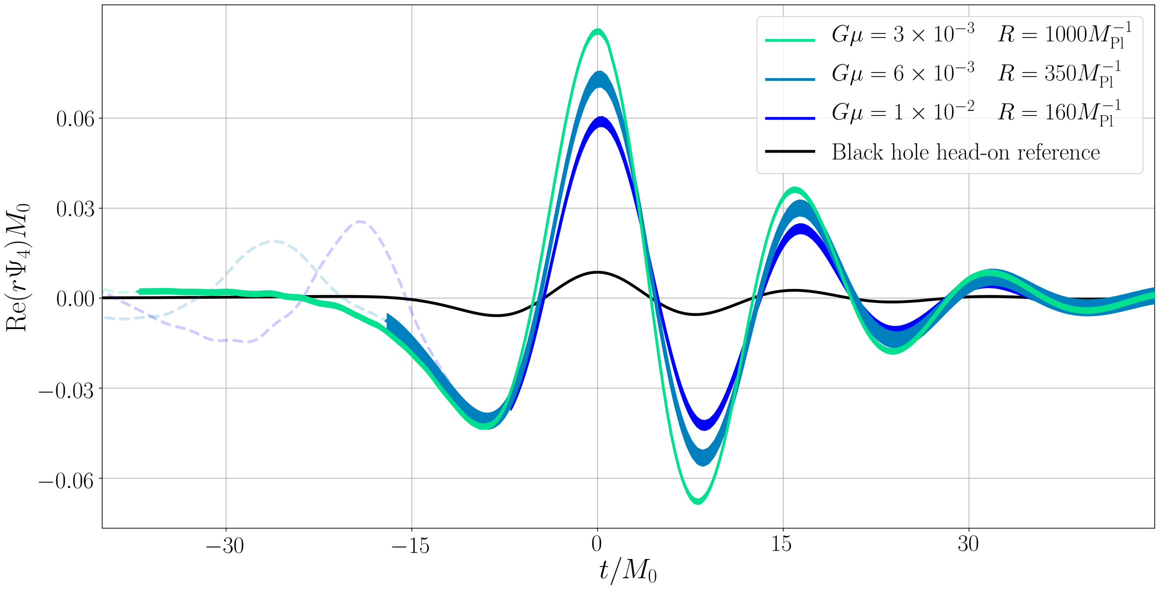

Fig. 4.2 Gravitational wave signals as a function of string tension $G\mu$ and black hole head-on reference [154]: The signal is normalised with the initial mass of the system and shifted such that the maximum of $r\Psi_4$ coincides at time $t = 0$, for three cases from table (C.1) for $G\mu = \{3\times10^{-3},\ 6\times10^{-3},\ 1\times10^{-2}\}$ and corresponding mass $M_0 = \{18.85M_{\rm Pl},\ 13.19M_{\rm Pl},\ 10.05M_{\rm Pl}\}$. The relationship between Ψ_4 and detector strain h is given in (4.21). The thickness of the line is an estimate of the numerical error. Unphysical parts of the signal are de-emphasised using ticked lines with different transparencies. We find that smaller $G\mu$ have larger amplitudes and hence produce more gravitational wave radiation (with 2.2% for $G\mu = 2\times10^{-3}$ with $R = 1600M_{\rm Pl}^{-1}$). The rest of the initial mass goes into the black hole and matter radiation. A table summary of all the runs is shown in (C.1).

4.2 Abelian Higgs with gravity

The action of the Abelian Higgs model minimally coupled to gravity[5] is

$$S = S_{EH} - \int d^4x\sqrt{-g}\left[(D_\mu\phi)^*(D^\mu\phi) + \frac{1}{4}F_{\mu\nu}F^{\mu\nu} + V(\phi)\right], \tag{4.2}$$

where $S_{EH} = \int dx^4\sqrt{-g}(R/16\pi G)$, $D_\mu = (\partial_\mu - ieA_\mu)$ is the covariant derivative with its $U(1)$ gauge field A^μ with field strength tensor

$$F_{\mu\nu} = \partial_\mu A_\nu - \partial_\nu A_\mu\,, \tag{4.3}$$

---

[5] We use the $-+++$ convention for the metric, and set $\hbar = c = 1$ and $M_{\rm Pl} = 1/\sqrt{G}$.

and $V(\phi)$ is the sombrero potential of the complex scalar field ϕ

$$V(\phi) = \frac{1}{4}\lambda\left(|\phi|^2 - \eta^2\right)^2 , \tag{4.4}$$

where η is the symmetry breaking scale.

For simplicity, we set the charge e and the dimensionless coupling constant λ to obey the critical coupling limit

$$\beta = \frac{\lambda}{2e^2} = 1 , \tag{4.5}$$

in which the Higgs and vector masses are identical and the string tension μ is related to the symmetry breaking scale as

$$\mu = 2\pi\eta^2 . \tag{4.6}$$

The coupling constant λ and the string tension $G\mu$ set the width of string as

$$\delta = \sqrt{\frac{2\pi}{\lambda\mu}} . \tag{4.7}$$

As a check of our code, we numerically construct a fully relativistic infinite static string coupled to gravity and demonstrate that its evolution is indeed static and stable. The details of this construction can be found in Appendix C.3.

In this work, we consider circular string loops of radius R_0, with mass given by

$$M_0 = 2\pi\mu R_0 \tag{4.8}$$

which is independent of the coupling constant λ. To construct the initial conditions, we define toroidal coordinates

$$\begin{aligned} x &= \cos\varphi(R + r\cos\theta) , \\ y &= \sin\varphi(R + r\cos\theta) , \\ z &= r\sin\theta , \end{aligned} \tag{4.9}$$

and choose the following ansatz for the field variables

$$\phi = f(r)e^{in\theta} , \qquad A_\theta = \frac{n\alpha(r)}{e} , \tag{4.10}$$

where n is the winding number of the string which is set to one throughout this work. To construct the loop we use the profile $f(r)$ from the static string[6]. After making the conformal metric ansatz

$$\gamma_{ij}dx^i dx^j = \chi(dx^2 + dy^2 + dz^2)\,, \tag{4.11}$$

we solve the Hamiltonian constraint to obtain the conformal factor χ.

4.3 Dispersion vs BH formation

We simulate the collapse of circular loops, scanning through the initial condition parameter radius R_0 and the model symmetry-breaking scale η (and hence string tension via Eqn. (4.6)), in the critical coupling limit with $e = 1$ and $\lambda = 2$. The loop begins at rest but quickly accelerates to close to the speed of light due mainly to the string tension. We find this motion to be consistent with the Nambu-Goto action dynamics (see Appendix C.4)

$$r = R_0 \cos\frac{\tau}{R_0}\,, \tag{4.12}$$

up to $r \sim \delta$ which is the thickness of the string given by Eqn. (4.7) and τ is the time coordinate at spatial infinity. Depending on the choice of μ and R_0, there are two possible outcomes: (i) the string unwinds itself and the resulting radiation disperses or (ii) a BH forms.

This result can be predicted using the hoop conjecture as follows. A BH forms if the loop mass $M_0 = 2\pi\mu R_0$ is enclosed within a radius smaller than its Schwarzschild radius $2GM_0$. In addition, the smallest volume in which a loop can be contained before the string unwinds has radius δ, which sets the Schwarzschild radius the lower bound for BH formation to be $2GM_0 > \delta$, or

$$R_0 > \sqrt{\frac{1}{8\pi\lambda}}(G\mu)^{-3/2}M_{\rm Pl}^{-1}\,. \tag{4.13}$$

Moreover, as the minimum radius of a loop is $R_0 = \delta$, we don't expect dispersion cases for $G\mu > (4\pi)^{-1}$ and all loops will form BHs. We find this estimate to be a good predictor (see Fig. 4.3), which suggests that black hole formation is broadly independent of field interactions.

---

[6] See Appendix C.3 for details.

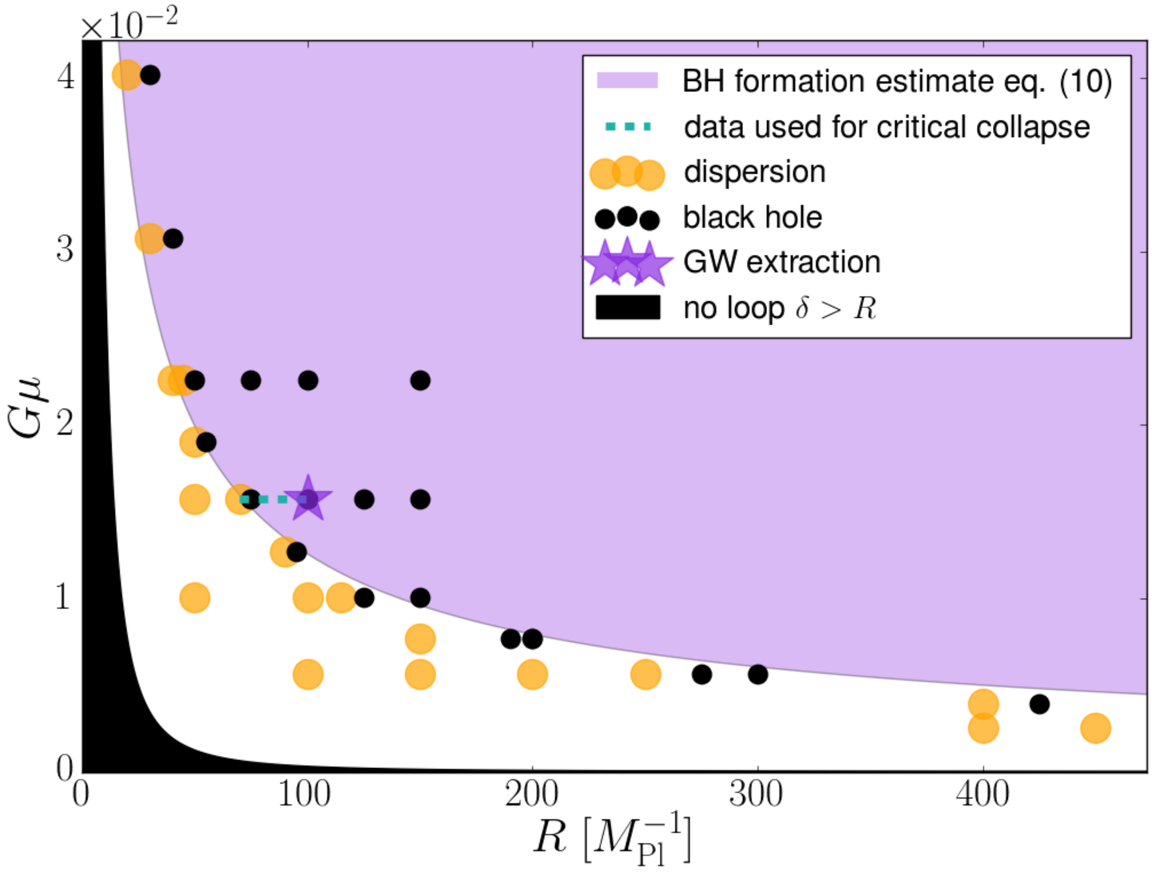

Fig. 4.3 Overview of simulations : The loop can either form a BH or unwind and radiate all its mass. The analytical expression derived from the hoop conjecture accurately predicts the outcome. Movie links for the evolution over time of the collapse are available for the dispersion [232] and black hole [231] cases.

If a black hole forms, the amount of initial mass that falls into the black hole depends on the initial radius R_0 for fixed $G\mu$, with the rest being radiated in either gravitational waves or matter.

We investigate whether this collapse is a Type I or Type II transition[7] [243] by studying the mass of the black hole close to the critical radius. Supposing it is a Type II collapse and let R_* be the critical point such that $M_{\rm BH}(R_*) = 0$, one can compute the critical index γ defined by

$$M_{\rm BH} \propto (R_0 - R_*)^\gamma \ . \tag{4.14}$$

---

[7] Whether the mass is always finite (Type I) or it is continuously turned on as $R_0 \to R_*$ (Type II).

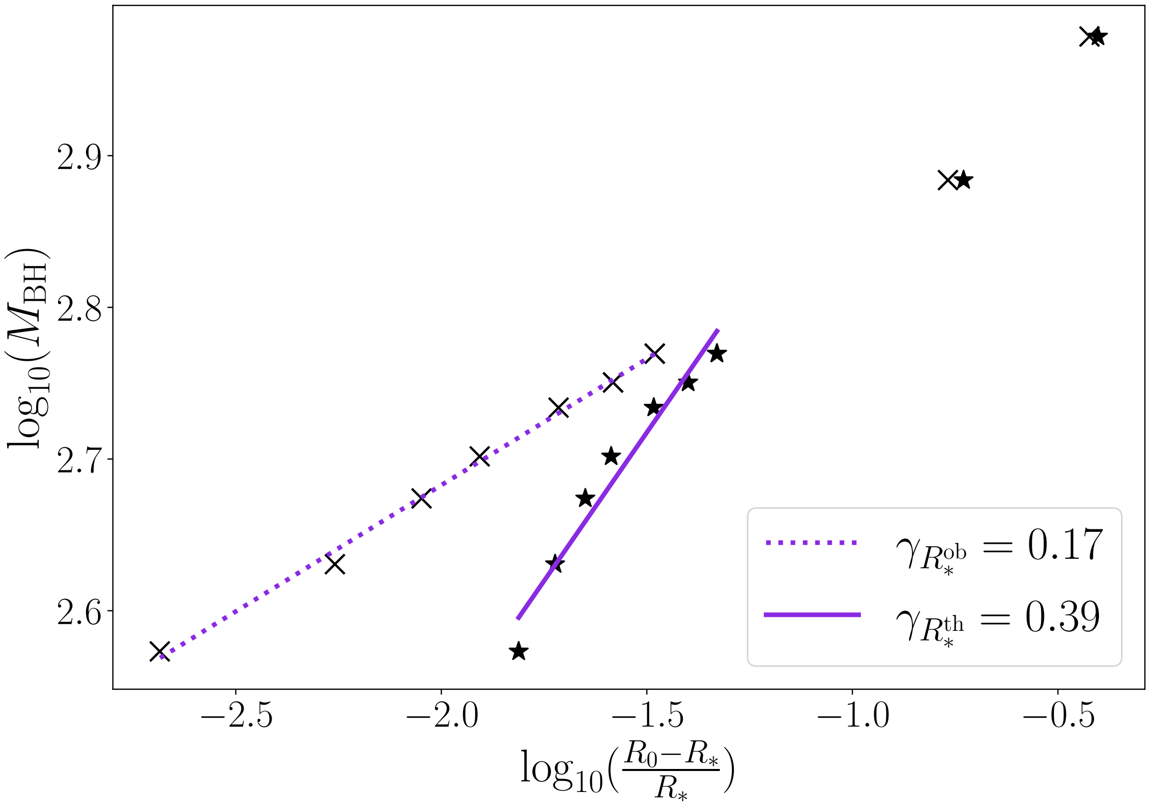

Fig. 4.4 Critical collapse: We plot the logarithm of the mass of the black hole vs the logarithm of the difference between the initial and the theoretical(star)/observed(cross) critical radius for $G\mu = 1.6 \times 10^{-2}$. As we argued in the text, our simulation showed that the actual $R_*^{\rm ob} > R_*^{\rm th}$, resulting in a critical index within $0.17 < \gamma < 0.39$, where the error is due to the uncertainty in determining numerically $R_*^{\rm th} < R_* < R_*^{\rm ob}$. Note that we only use the first 7 points to compute the critical index for $R_0 \leq 0.05R_*$ as the critical relation is only expected to hold perturbatively.

The value asumming the theoretical prediction of Eqn. (4.13), $R_*^{\rm th} = \sqrt{1/8\pi\lambda}(G\mu)^{-3/2}M_{\rm Pl}^{-1}$, is $\gamma = 0.39$, see Fig. 4.4. However, in our simulations we have observed $R_*^{\rm ob} > R_*^{\rm th}$, giving $\gamma = 0.17$, showing that γ is highly dependent on the choice of the actual value of R_* – of which we are unable to identify with confidence due to the lack of computational resources. Therefore, we conclude that $\gamma = 0.28 \pm 0.11$.

In the subcritical limit where $2GM_0 < \delta$, the loop unwinds as it collapses, transferring all the mass into matter and gravitational radiation. If $R_0 \gg \delta$ the velocity at unwinding is much larger than the escape velocity and all the energy is radiated away. However, if $R_0 \sim \delta$, the velocity can be small enough so that instead of full dispersal the mass slowly decays at the center and a soliton might form.

4.4 Parametric dependence of GW signals

In this section we study how the gravitational wave signal changes when we vary the parameters of the model: the string tension $G\mu$, the initial loop radius R_0 and the string width δ.

We first focus on the string tension $G\mu$. We performed a series of simulations with the string parameters shown in table (C.1) with fixed $\lambda = 2$. Since varying $G\mu$ substantially changes the mass of the string (see (4.8)), for each choice, we choose its initial R_0 to ensure that a black hole can be formed (i.e. obey the condition (4.13)).

In Fig. 4.2, we show the time domain gravitational waveforms in terms of the (mass normalized) $r\Psi_4$ Weyl scalar for the cases[8] of $G\mu = \{3 \times 10^{-3},\ 6 \times 10^{-3},\ 1 \times 10^{-2}\}$ with corresponding mass $M_0 = \{18.85,\ 13.19,\ 10.05\}M_{\mathrm{Pl}}$. For the cases investigated, we find the maximum efficiency is 2.2% for the case of $G\mu = 2 \times 10^{-3}$.

The energy radiated in GWs can be estimated from the $r\Psi_4$ Weyl scalar by (C.42). The efficiency of GW production normalized over total string mass, E_{GW}/M_0 is shown in Fig. 4.5. Interestingly, we find that this scales as

$$\frac{E_{\mathrm{GW}}}{M_0} = \frac{\mathcal{A}}{16\pi^2}\frac{1}{G\mu} \tag{4.15}$$

where $\mathcal{A}$ is a numerical factor found to be approximately $\mathcal{A} \approx 10^{-2}$. Intriguingly, this means that *smaller tension leads to greater efficiency*, with the caveat that we have only explored a small regime of the total possible parameter space. This scaling clearly cannot be unbounded as $G\mu \to 0$, and must turnover at some point. We will discuss this further in section 4.6. Even though the velocity of the loop at collision is ultra-relativistic, $\sim 0.99\ c$, the GW production is strongly suppressed when compared to other ultra-relativistic events. For comparison, a boosted head-on black hole merger ($14 \pm 3\%$) and relativistic fluid particle collapse ($16 \pm 2\%$) radiates a much larger fraction of its total mass in gravitational waves [427, 191]. This suggests that the initial apparent horizon is very spherical – possibly due to the thickness of our strings when compared to the Schwarzschild radius, i.e. $2GM_{\mathrm{loop}} \sim \mathcal{O}(1) \times \delta$. In the limit of infinitisimally thin strings, the maximum GW production was calculated by Hawking to be 29% [254]. Hence, we believe that one can boost the efficiency by colliding thinner strings (i.e. $2GM_{\mathrm{loop}} \gg \delta$) – in this limit the hoop conjecture argument above suggests that a black hole will form before the loop has a chance to interact and unwind, thus

---

[8] We show the results of the other simulations in the appendix, Fig. C.10.

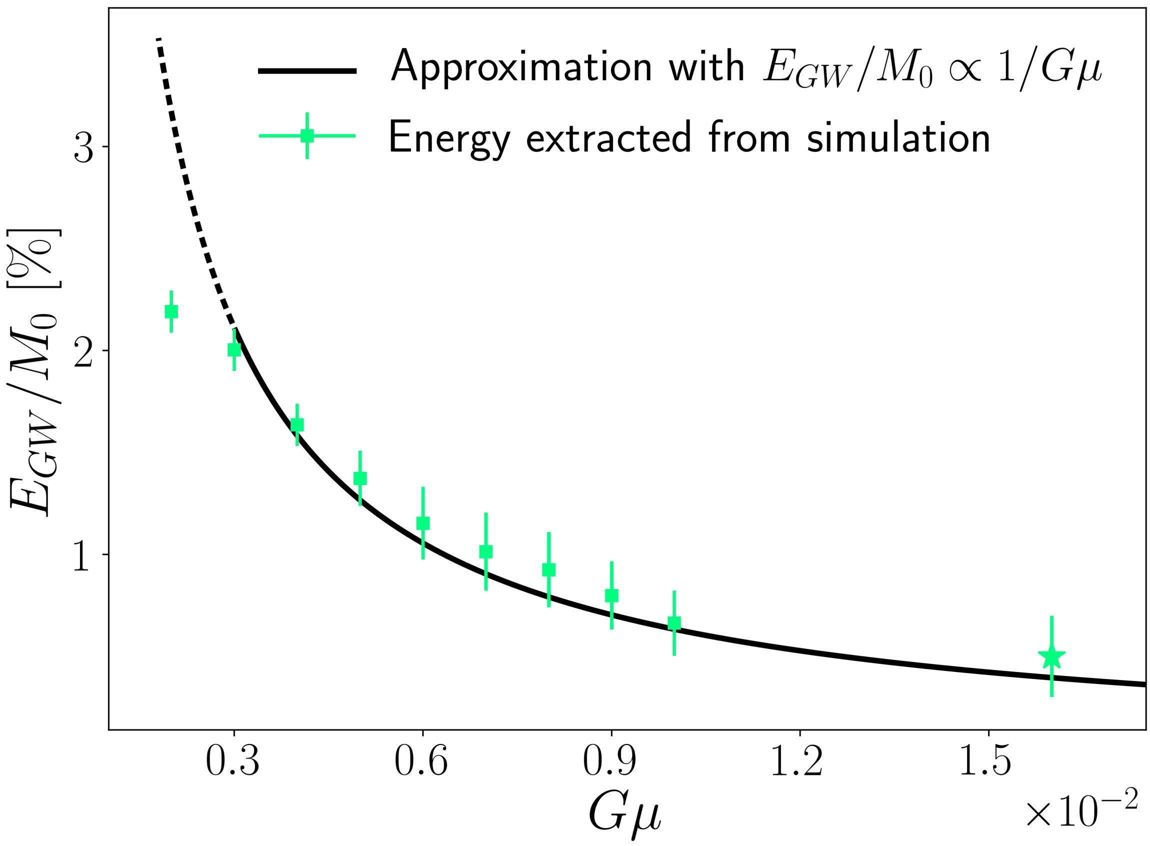

Fig. 4.5 Efficiency in GW production vs string tension: We find that the efficiency $E_{\mathrm{GW}}/M_0 \propto \mathcal{A}\,(16\pi^2 G\mu)^{-1}$ obey a simple power law with $\mathcal{A} = 10^{-2}$ (solid line). The simulation parameters and results are tabulated in Tab. (C.1) while the star-dotted point on the right is the result from the paper [264]. Note that the last data point to the left may signal the turnover of the inverse power law $1/G\mu$.

it is possible that the GW emission will be larger via Hawking's argument, though this has not been demonstrated numerically.

We can also explore the dependence of GW emissions as a function of string width δ and initial radius R_0. In [254], using purely geometrical arguments, Hawking computed the efficiency of GW emitted from an infinitesimally thin cosmic string loop, and showed that it has an upper bound of 29%. This is obtained by assuming that the initial horizon of the black hole is a thin disk, and then computing the difference of the disk's total area with the area of the final Schwarzschild black hole. Hence, it is plausible that if the initial horizon of the black hole is less disk-like and more spheroidal, the efficiency will become smaller since the initial horizon area will then be greater (and the difference with the area of the Schwarzschild black hole is smaller). To test

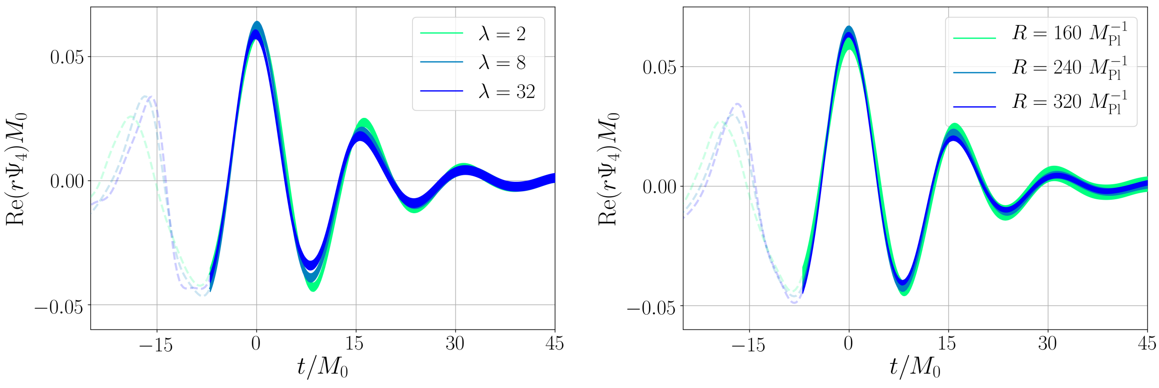

(a) **(b)**

Fig. 4.6 (a): Gravitational wave signals for different width δ: The plot shows the mass normalized Weyl scalar $r\Psi_4$ for $G\mu = 1 \times 10^{-2}$, $R_0 = 160 M_{\rm Pl}^{-1}$ but with different configurations obtained by varying the string width δ using expression (4.7) by half ($\lambda = 8$) and quarter ($\lambda = 32$). The thickness of the lines indicates the numerical error. This illustrates that the GW signal does not strongly depend on string width δ. **(b): Gravitational wave signals for different radii** R: The plot shows the mass normalized Weyl scalar $r\Psi_4$ for the radii R_0 $\{160,\ 240,\ 320\} M_{\rm Pl}^{-1}$, with fixed width $\delta = 17.72 M_{\rm Pl}^{-1}$ and constant tension $G\mu = 1 \times 10^{-2}$. The thickness of the lines indicates the numerical error. This illustrates that the GW signal does not strongly depend on the string radii.

for this idea, we can define a dimensionless "thickness" parameter,

$$\frac{\delta}{R_0} = \sqrt{\frac{2\pi}{\lambda\mu}} \frac{1}{R_0} \,, \tag{4.16}$$

such that a cosmic string is "thin" if δ/R_0 is small and "thick" if δ/R_0 is close to unity. In the infinitesimally thin limit, $\delta/R_0 \to 0$. Our argument above suggests that the GW efficiency should increase as δ/R_0 decrease, with the Hawking limit being $\delta/R_0 = 0$. However, as we will show in below, this is not borne out by our numerical simulations, at least in the limited range of parameters we are able to explore. We test this argument by performing simulations with varying string width δ and radius R_0, while keeping other parameters fixed as follows.

String width δ dependence: We performed three simulations with varying $\lambda = \{2,\ 8,\ 32\}$ which corresponds to string widths $\delta = \{\delta_2,\ \delta_2/2,\ \delta_2/4\})$ with $\delta_2 = 17.72 M_{\rm Pl}^{-1}$, while fixing $G\mu = 1 \times 10^{-2}$ and initial radius $R_0 = 160 M_{\rm Pl}^{-1}$. From the results shown in Fig. 4.6a, we see that the signals only depend weakly on string width.

Initial radius R_0 dependence : We performed three simulations with varying $R_0 = \{160,\ 240,\ 320\}M_{\rm Pl}^{-1}$ at fixed $G\mu = 1\times10^{-2}$ and $\lambda = 2$. Since the mass scales with R_0 and the ringdown frequency of a black hole is inversely proportional to its mass, we normalise the signal with their initial mass. From the results shown in Fig. 4.6b, we find that the normalised signal at most scales weakly with R_0.

The above results suggest that the GW emission efficiency is only weakly dependent on initial string dimensionless thickness δ/R_0.

On the other hand, the numerically obtained scaling (4.15) can be suggestively rewritten as

$$\frac{E_{\rm GW}}{M_0} = \mathcal{A}\frac{\gamma(t_{\rm BH})}{4\pi}\ , \tag{4.17}$$

where γ is the Lorentz factor of the string infall velocity and $t_{\rm BH}$ is black hole formation time, i.e.

$$\gamma(t_{\rm BH}) = \frac{1}{4\pi G\mu}\ . \tag{4.18}$$

We can derive (4.18) as follows. In [264], we have shown that the dynamics of a radius R_0 cosmic string loop during the infall is well described by the Nambu-Goto approximation [367], for which the position and velocity at some given time are given by

$$R(t) = R_0\cos\left(\frac{t}{R_0}\right) \qquad\qquad v_R(t) = \sin\left(\frac{t}{R_0}\right)\ . \tag{4.19}$$

The black hole forms approximately when $r_{\rm BH} = 2GM_0 = 4\pi R_0 G\mu$, which using (4.19) happens at time $t_{\rm BH} = R_0\cos^{-1}(4\pi G\mu)$, so that the velocity at black hole formation is

$$v_R(t_{\rm BH}) = \sqrt{1 - 16\pi^2\,(G\mu)^2}\ , \tag{4.20}$$

which using $\gamma = (1-v^2)^{-1/2}$ leads to (4.18). For $G\mu = 1\times10^{-2} - 2\times10^{-3}$, this corresponds to $v(t_{\rm BH}) \approx 0.9920 - 0.9997$, so it is an ultra-relativistic event. Note that the velocity equation (4.20) does not depend on λ and R_0. Physically, the smaller the string tension, for a fixed loop mass M_0 the larger the radius of the loop has to be, the longer it takes for the loop to reach the Schwarzschild radius and hence the faster the loop will be moving when the black hole is formed.

Hence we conjecture that the GW emission process is dominated by the kinetic energy of the system, with the string geometry playing only a minor role. Finally, loops in general are generated non-circularly with many different oscillating stable configurations. Nevertheless, in the presence of gravity, we expect gravity to eventually win out, with roughly the timescale of their gravitational collapse to be the free-fall time-scale. In the final stages of collapse, we expect the tension to circularize the loops and thus our results should hold in general.

4.5 Gravitational strain waveforms

Our goal in this section is to construct the strain waveform. The gravitational wave strain h as seen by a detector is related to the Weyl scalar Ψ_4 by the following equation of motion

$$\ddot{h} = \ddot{h}_+ + i\ddot{h}_\times = \Psi_4 \; . \tag{4.21}$$

Thus we would need to integrate (4.21) to obtain h. The details of this integration are described in Appendix (C.6).

Furthermore, as we have already described, numerically the early time infall signal is contaminated by the presence of unphysical artefacts from the numerical construction of its initial conditions[9]. To circumvent this, we note that during this early time period, the infall tracks the trajectory of a Nambu-Goto string until a distance of $\mathcal{O}(\delta)$ [264]. We use this fact to construct a semi-analytic model of the GW emission during infall as follows. The modified trajectory is given by

$$R(t) = R_0 \left[\Theta(t_0 - t) + \cos\left(\frac{t}{R_0}\right) \Theta(t - t_0) \right] \; , \tag{4.22}$$

where the Heaviside functions ensure consistency with the initial data of our numerical simulations where the loop is static for $t < t_0$ (see Fig. C.6 and Fig. C.5b). In Cartesian coordinates (x, y, z) such that $r = \sqrt{x^2 + y^2 + z^2}$, the stress tensor in the corresponding basis is

$$T^{\alpha\beta}(t, \mathbf{x}) = \mu v^\alpha v^\beta \gamma \; \delta(r - R(t))\delta(z) \; , \tag{4.23}$$

where the velocity is $v^\alpha = (1, \; v_R \sin(\phi), \; v_R \cos(\phi), \; 0)$ with

$$v_R(t) = \frac{dR}{dt} = \sin\left(\frac{t}{R_0}\right) \Theta(t - t_0) \; . \tag{4.24}$$

The gravitational wave signal of such system is then given in the weak field limit by the standard formula [340]

$$r h^{TT}_{ij}(t) = 4G\Lambda_{ij,kl}(\mathbf{n}) \int_{-\infty}^{\infty} \frac{d\omega}{2\pi} \tilde{T}_{kl}(\omega, \omega\mathbf{n}/c) e^{-i\omega t_{\rm ret}} \tag{4.25}$$

---

[9] These artefacts are generically present for most numerical relativity initial conditions.

where $t_{\rm ret} = t - r/c$ is the retarded time and is valid for arbitrary velocities, and $\Lambda_{ij,kl}$ is the projector to the traceless-transverse gauge. The result and details of this calculation for various methods as well as a convergence test can be found in Appendix (C.6.2) and Fig. C.5a. We plot the resulting gravitational wave strain for $G\mu = 4 \times 10^{-3}$ with $R_0 = 600 M_{\rm Pl}^{-1}$ in Fig. 4.1.

As one can see, $r\Delta h_+ = rh_+(\infty) - rh_+(-\infty) > 0$. This is known as the *gravitational wave memory effect* [475, 108, 147, 89, 434], which is a large permanent shift in the strain waveform. The nature of this memory arises from the fact that post-merger, there is a loss of matter emitted axially in an ultra-relativistic jet (Fig. C.11) – and hence is highly aspherical – while its "incoming" velocity is zero (i.e. the loop is initially static). This generates a large linear memory shift [198] akin to that of a core-collapse supernova [381].

We can estimate the magnitude of this memory using the linear memory formula [108, 147]

$$r\Delta h_{ij}^{\rm TT}(\theta_A) = \Delta \sum_A \left[\frac{4GM_A}{\sqrt{1 - v_A^2}} \left(\frac{v_A^j v_A^k}{1 - v_A \cos\theta_A} \right)^{\rm TT} \right] , \tag{4.26}$$

where M_A an v_A are the rest mass and asymptotic velocity respectively of ejecta particle A and θ_A is the angle between v_A^i and the direction to the detector. The Δ expresses the difference between the initial "incoming" and "outgoing" values. The initial velocity of the loop is $v_A^i = 0$. From numerical simulations, it can be seen that the outgoing ejecta is highly beamed like jets in the direction axial to the loop (see Fig. C.11). In general, to use this formula, one must calculate the flux of ejecta as a function of angle. Since our goal is not to make a precise prediction of its value (we directly obtain this from numerical simulations), but to simply demonstrate that our numerical result is indeed gravitational wave memory, we approximate its magnitude as follows. We assume that all the ejecta is travelling at a constant velocity axially (i.e. perpendicular to the plane of the loop) at $v_A^i = (0, 0, \pm v_z)$ where $v_z \sim 1$ (the exact value does not affect the final answer significantly).

We express the right hand side of Eqn. (4.26) onto a spherical basis at radius r by first rotating each instance of the metric $r\Delta h_{ij} \to r\Delta h_{i'j'}(\theta, \phi)$ where (θ, ϕ) are the coordinates on the sphere. We then project the metric onto their traceless and transverse components to obtain

$$\Delta h_{i'j'}^{TT}(\theta, \phi) = \begin{pmatrix} \Delta h^+ & \Delta h^\times & 0 \\ \Delta h^\times & -\Delta h^+ & 0 \\ 0 & 0 & 0 \end{pmatrix} , \tag{4.27}$$

where it can be shown that

$$r\Delta h^{+} = 2GE_{\mathrm{total}}\frac{v_z^2\sin^2\theta}{v_z^2\cos^2\theta - 1} \ , \qquad r\Delta h^{\times} = 0 \ . \tag{4.28}$$

and $E_{\mathrm{total}} \approx M_0 - M_{\mathrm{BH}} = 1.32 M_{\mathrm{Pl}}$ (see Tab. (C.1)) is the total integrated relativistic flux energy for both matter and GW we directly measured from our simulations. To compare this to our numerical result in Fig. 4.1, we project (4.28) onto the $l = 2$, $m = 0$ mode as

$$r\Delta h^{+}_{2,0} = \int d\Omega \ r\Delta h^{+}({}_{-2}Y^{2}_{0})^{*} \approx \ 8 \ M_{\mathrm{Pl}}^{-1} \ , \tag{4.29}$$

which about a factor of 2 smaller when compared to the numerical value we obtained, but at the right order of magnitude. We emphasise that (4.29) is just an estimate of the memory assuming the interactions stay within the linear regime, and hence it is not surprising that the true memory is larger.

4.6 Summary and discussion

In this work, we showed that GW production of cosmic string loops that collapse and form black holes scales as

$$\frac{E_{\mathrm{GW}}}{M_0} = \frac{\mathcal{A}}{16\pi^2}\frac{1}{G\mu} \ , \qquad \mathcal{A} \approx 10^{-2} \ , \tag{4.30}$$

but depends weakly on its initial string width and loop radius. We argue that this strongly suggests that the GW production in such a collapse is dominated by kinematic processes, and not geometric ones.

Clearly, since $G\mu$ is theoretically not bounded from below, (4.30) cannot scale without bound to smaller values as it violates the Hawking bound $E_{\mathrm{GW}}/M_0 \to 0.29$ at $G\mu \approx 2\times 10^{-5}$. This suggests that there must exist some new scale where this turnover from the inverse power law to some other relationship. This turnover may already be hinted in Fig. 4.5, where the $G\mu = 2 \times 10^{-3}$ point is diverging from expression (4.30), and will be a focus of our future investigations.

Observations of the CMB [23] and the LIGO/Virgo search for stochastic GW [6, 1, 4, 15, 13, 18] constraints the current cosmic string tension to $G\mu \lesssim 10^{-14} - 10^{-7}$ – this value is dependent on the details of the cosmic strings network evolution which is uncertain (and model dependent) [405, 423, 337, 91, 92, 96, 336]. This regime is obviously beyond the validity of our scaling argument. While we have only explored a small regime of the possible parameter space and the amplitude of the GW signal may differ for other parameters, we do not expect the *form* of the GW strain signal shown in Fig. 4.1 to differ substantially at lower $G\mu$. We also emphasise that strongly gravitating strings such as fundamental strings with $G\mu \sim 10^{-2}$ can also be produced in many popular brane inflation models [466, 294, 295, 392]. Modulo such theoretical concerns about the probability distribution of such events which can only be estimated from large network simulations, we take the agnostic view that their existence can be put into observational test.

On the other hand, we believe that the large gravitational wave memory of these events is a robust result regardless of the string parameters[10], since it is sourced by the large aspherical emission of post-collapse debris which we expect to occur regardless. While GW memory is historically removed from both the detector data streams and theoretical predictions, there is now increasing interest in their search [180, 100] and is currently a goal of the LIGO/Virgo collaboration [277].

Both such short signals with little GW production during the infall phase suggests that this it is best looked for in the transient short-during burst channel [2, 10, 9, 12, 14]. This channel makes only minimal assumptions on the expected signal waveform, at the cost of reduced sensitivity to weaker signals. One may wonder whether the string loop burst waveform is degenerate with other processes such as a black hole inspiral or head-on mergers – and hence can be picked up by already existing match-filtered searches. The former case might be trivial since the lack of an oscillatory pre-merger signal and the fact that the black hole formed from the collapse has no spin could be sufficient features to distinguish from a binary black hole inspiral system. On the other hand, if the orbiting binary consisted of very massive components such as GW190521 [16], we would only have access to the late stages of the event and could look very similar to the waveforms computed in this work. The analysis done in [17] excluded the cosmic string origin of GW190521, but used weak-gravity cusp signal templates [172], which inherently do not incorporate a ringdown phase. Thus, the fitting would very likely be improved when cosmic string loop templates are used instead.

For a more symmetric scenario such as a head-on BH-BH merger, in Fig. (4.7) we show that it is not degenerate. While the ringdown signal from the black hole formed from a loop is degenerate with a black hole with the same mass formed from a head-on merger 16× closer, the pre-merger and the merger itself differ considerably. Therefore, it should be distinguishable as long as one has access to the full waveform.

To detect such weaker signals, one would need to make use of the full match-filtering search, which requires the construction of a parameterised GW waveform template. In

---

[10] See [290] for a recent calculation from cosmic string cusps and kinks.

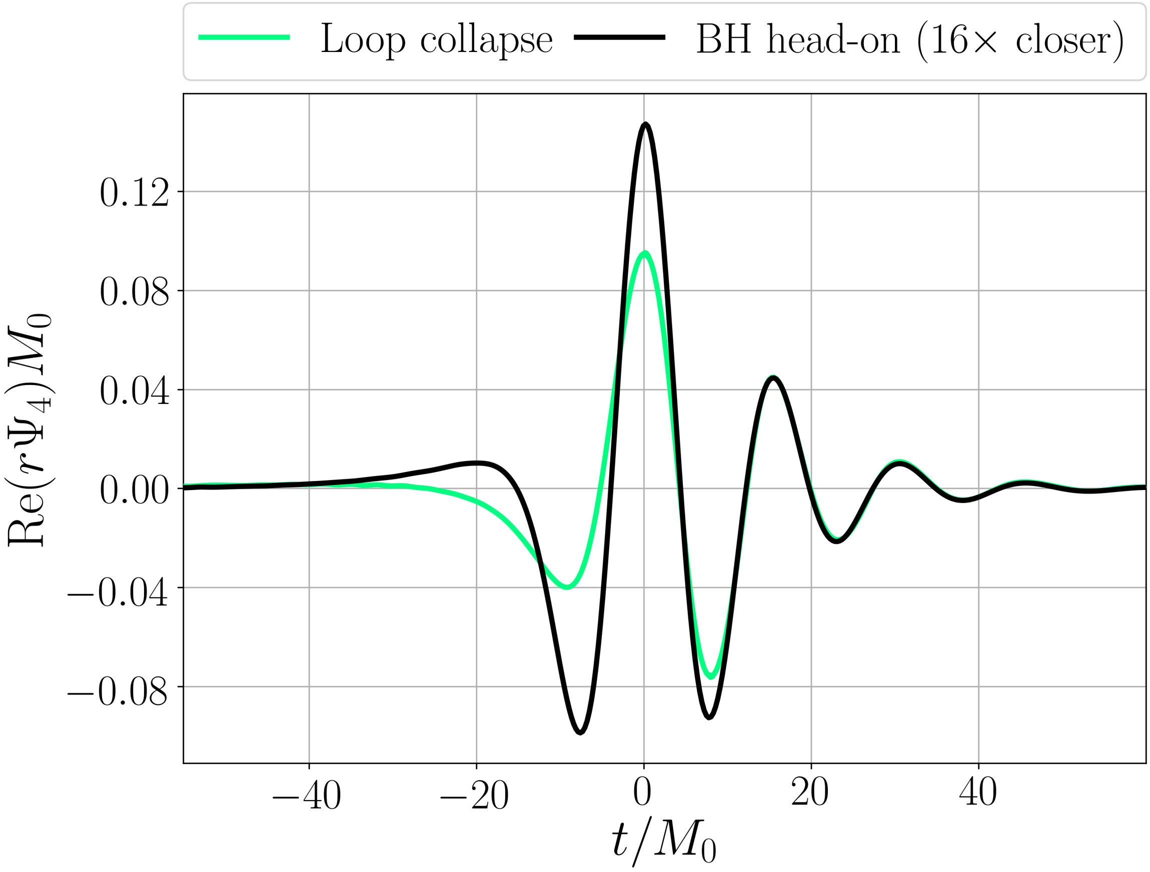

Fig. 4.7 String loop and black hole head-on merger comparison: The $l = 2$ $m = 0$ strain mode for $G\mu = 2\times10^{-3}$ with $R_0 = 1600M_{\rm Pl}^{-1}$. Both signals are normalized to mass, but the black hole formed from the head-on collision is 16× closer to the detector. This shows that the signal of the collapse of a cosmic string loop is not degenerate with distance to spin-free BH merger.

this work, we argue that the primary parameter for the construction of such waveform templates is the string tension $G\mu$, with secondary parameters being the initial string width and radii. We undertook the first steps in the construction of the GW strain waveform template (Fig. 4.1). we can ask whether we can detect suitably massive cosmic strings loops with current or future detectors. The two key parameters are (i) the frequency and (ii) the luminosity of the event, both which depend on the masses. The former constraints our loop parameter space to $2\pi\mu R_0 \approx M_{\rm detector}$. We choose $M_{\rm detector}$ such that its frequency lies at peak sensitivity of LIGO/Virgo ($f\sim$ 100Hz).

For the latter, the strain h observed at a distance d from a source of GWs is

$$\left(\frac{h}{10^{-21}}\right) \sim \sqrt{\frac{E_{\rm GW}}{3\times 10^{-3}M_{\odot}}}\left(\frac{10~\text{Mpc}}{d}\right) . \tag{4.31}$$

Cosmic string loops are generated during the evolution of the string network when strings intercommute, although there is presently no consensus on the probability distribution of loops and their classification (see e.g. [90, 406]). Furthermore, it is not clear that all loops will collapse due to the presence of non-intersecting loop configurations and the uncertainty in their angular momentum loss mechanisms. Hence, we will take the agnostic view that only planar loops will collapse – assuming that planar loops will circularize as argued by [256]. Suppose then $N(R_0, z)$ is the co-moving production density rate of planar loops of radius R_0 at redshift z (i.e. it has dimensions $[N(R_0, z)] = L^{-3}T^{-1}$), then the detection rate is given by

$$\Gamma = \int_0^{z_d} 4\pi\left[\int_0^z \frac{dz'}{H(z')}\right]^2 \frac{N(r,z)dz}{H(z)} , \qquad d = \int_0^{z_d} \frac{dz}{(1+z)H} , \tag{4.32}$$

such that z_d is the maximum range in redshift of the detector, which itself depends on the energy of the GW $E_{\rm GW}$ emitted. Our numerical results suggest that $\mathcal{O}(1)\%$ of the total string loop mass is emitted, which is an order of magnitude smaller than that of the typical BH-BH mergers, translating to about a factor of 3 shorter in detectable distance d. For LIGO/Virgo and the Einstein Telescope (ET), the maximum redshift range is then $z_d \sim 0.005$ and $z_d \sim 0.05$ respectively. In this limit, Γ can be approximated as

$$\Gamma \approx \epsilon^{3/2}\left(\frac{R_0}{GM_{\odot}}\right)^{3/2}(G\mu)^{3/2}\left(\frac{10^{-19}}{h}\right)^3\left(\frac{N(R_0,z)}{\text{Mpc}^{-3}}\right) . \tag{4.33}$$

Clearly, Γ depends linearly on $N(R_0, z)$, which itself depends on the cosmic string model and its network evolution, which at present is still being debated vigorously as mentioned above. For example, in [256], it was estimated that $N(R_0, z) \propto (G\mu)^{2R_0/s-4}$ where s is the correlation length of the loop. Other estimates are given in [393, 123]. On the other hand, we can use the non-detection of such collapse events in the present LIGO/Virgo to put a constraint on $N(R_0, z)$. For $G\mu \sim 10^{-10}$ which leads to solar system sized loops of $R_0 \sim \mathcal{O}(100)$ a.u., this is $N(R_0, z) < 10^{-2}$ Gpc^{-3} yr^{-1} [11], which

---

[11] If we assume that these GW are *incoherent*, this leads to a stochastic background energy of $\Omega_{\rm GW}h^2 \sim 10^{-10}$.

is a lower detection rate than what is expected from BH mergers of $\mathcal{O}(10)$ Gpc^{-3} yr^{-1} [11].

Finally, we note that this is a conservative estimate since these solar system sized loops satisfy $R_{\rm BH} \sim \mathcal{O}(10^{40}) \times \delta$ and hence are thin loops. In this limit, ϵ might be closer to 29 %, with a corresponding increase in d. In an upcoming publication, we will complete the construction of these templates, and use them to search for cosmic string loop collapse signatures in the LIGO/Virgo data stream.

Chapter 5

Primordial black hole formation with full numerical relativity

This chapter contains the article "Primordial black hole formation with full numerical relativity" [176], published in the *Journal of Cosmology and Astroparticle Physics (JCAP)*.

We study the formation of black holes from subhorizon and superhorizon perturbations in a matter dominated universe with 3+1D numerical relativity simulations. We find that there are two primary mechanisms of formation depending on the initial perturbation's mass and geometry – via *direct collapse* of the initial overdensity and via *post-collapse accretion* of the ambient dark matter. In particular, for the latter case, the initial perturbation does not have to satisfy the hoop conjecture for a black hole to form. In both cases, the duration of the formation the process is around a Hubble time, and the initial mass of the black hole is $M_{\mathrm{BH}} \sim 10^{-2} H^{-1} M_{\mathrm{Pl}}^2$. Post formation, we find that the PBH undergoes rapid mass growth beyond the self-similar limit $M_{BH} \propto H^{-1}$, at least initially. We argue that this implies that most of the final mass of the PBH is accreted from its ambient surroundings post formation.

5.1 Introduction

Primordial black holes (PBHs) form in the early stages of the universe, and their idea was first conceived in the late sixties and early seventies [136, 252, 474]. It is notable that it was the potential existence of small black holes from primordial origin that led Hawking to theorize black hole evaporation [255]. It was realised shortly after that PBHs could constitute a significant part of cold dark matter [144], and interest in PBHs has spiked in the recent past as a result. Evaporating PBHs have been suggested as explanations for galactic and extra-galactic γ-ray backgrounds, short γ-ray bursts and anti-matter in cosmic rays [382, 133, 467, 332, 312, 339, 149] and PBHs could provide seeds for the formation of supermassive black holes and large-scale structure [140, 80]. Moreover, PBHs could be responsible for certain lensing events [261, 262], with recent analysis suggesting that the population of BHs detected by the LIGO/Virgo/KAGRA (LVK) observatories [19] may be primordial [17, 208]. Additionally, work is underway to use next generation gravitational wave experiments to detect PBH formation and mergers [323, 373]. Results obtained by the NANOGrav Collaboration [59] have been associated to PBHs, as well [177, 447, 318, 185].

Various formation mechanisms could be relevant for PBHs [127, 239]. These mechanisms include the formation of PBHs during inflation [148, 282, 212, 197], the collision of bubbles that result from first order phase transitions [170, 258, 317, 331, 354, 315, 301, 322, 302, 303], the collapse of cosmic strings [308, 273, 253, 393, 220, 120, 338, 462, 245, 366, 137, 109, 264, 84, 286, 64, 288, 94], the collapse of domain walls produced during a second order phase transition [181, 409, 410, 221, 178, 335], the collapse of a scalar condensate in the early universe [167, 166, 169, 168] and specific baryogenesis scenarios [184, 183, 238, 182, 300]. However, the mechanism that is most relevant for this work is the collapse of overdense regions that are present in the early universe [132, 365, 87, 146, 196, 375, 376, 240, 363, 471], which may originate from e.g. pre-inflation quantum fluctuations [138, 135, 272, 284, 210, 401, 431, 75].

In the standard picture, these fluctuations collapse post inflation, while the universe is dominated by radiation energy. The nonzero radiation pressure resists collapse, meaning that the inhomogeneities must be fairly large for PBHs to form. It was suggested early on that an overdensity δ must be larger than a critical value δ_c equal to 1/3 if PBHs are to form [132]. This statement was checked analytically and numerically soon after [365, 87, 377] and more recently [374, 422, 251, 364, 248, 361, 362], supporting the need for a perturbation larger than some threshold with values that broadly agree.

PBH formation in matter dominated epochs has also been extensively studied analytically and semi-analytically. In various non-standard universe histories, inflation is followed by a period of matter domination [305, 126, 345, 49]. PBH formation in such an early epoch of matter domination was considered early on [304]. More recently, a threshold amplitude for the collapse of a scalar field overdensity was found [267], the effects of non-sphericity [250] and inhomogeneity [320] on the collapse were investigated, the resulting spin of the PBHs was studied [249], the duration of an early epoch of matter domination was constrained by considering the PBH abundance [141]

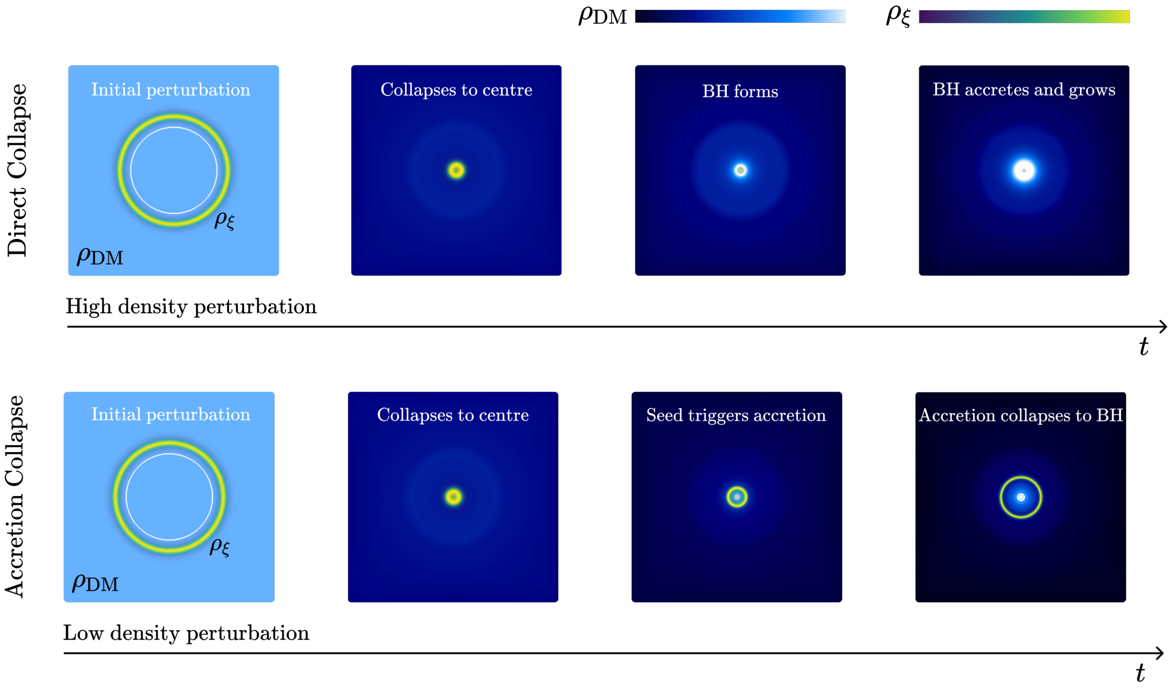

Fig. 5.1 Direct collapse and accretion driven mechanisms: The figure summarizes the two distinct processes of PBH formation studied in this work. Top panel shows the *direct collapse* mechanism where the initial superhorizon perturbation is dense enough to directly form a black hole when the perturbation reaches the centre. Bottom panel depicts the *accretion driven collapse* mechanism, where the initial perturbation is insufficiently dense but acts as a seed to trigger the accretion of the background dark matter, which subsequently collapses to form a black hole. Both start from the same initial radius R_0, but with different initial amplitudes $\Delta\xi$. In the leftmost figures, we show the initial size of the Hubble horizon (white solid line) which will grow as time evolves. In the other figures, the Hubble horizon has grown larger than the box size. Colourbars are shown in the top right, with lighter (darker) colours signifying higher (lower) energy densities, and scales fixed per mechanism. Colourbars are shown in the top right, with lighter (darker) colours signifying fixed higher (lower) energy densities per mechanism. Video comparisons of these mechanisms can be found here [235] and here [236].

and constraints on the amplitude and spectral index of the collapsing scalar field were obtained [130].

In this work, we use full 3+1D numerical relativity simulations to investigate the collapse of subhorizon and superhorizon non-linear perturbations in an expanding universe that is dominated by matter. We model the expanding background and the collapsing perturbation using an oscillating massive scalar field and massless scalar field respectively. The massless scalar field's initial energy is thusly contained purely in its gradients. We will show that there are two broad mechanisms of black hole formation – via *direct collapse* for the case where the overdensity is sufficiently large that it will form a black hole, and via *post-collapse accretion* for the case where the overdensity is smaller. In both cases, the process is rapid and its duration is around a single Hubble time, forming PBHs with initial masses of $M_{\rm BH}H \sim 10^{-2}M_{\rm Pl}^2$. We illustrate these mechanisms in Fig. 5.1.

Our choice of fundamental scalar fields as dark matter, instead of a pressureless cold fluid (as suggested by [192]), is prompted by our focus on an early time (i.e. pre-BBN) matter dominated phase instead of the present late time matter dominated phase. Such early era matter domination is often driven by a non-thermal fundamental scalar or moduli dynamics [21] instead of the more familiar cold pressureless fluid such as thermal WIMP dark matter. Furthermore, early matter phases will eventually transition into a radiation domination epoch, such that the standard Hot Big Bang cosmological evolution can proceed. Such a phase transition from matter domination into radiation domination can then be achieved through the decay of the scalar field into either standard model particles or intermediaries.

This chapter is organised as follows. In section 5.2 we explain the numerical setup we use for evolving a scalar perturbation in a dark matter dominated background. In section 5.3 we introduce the two aforementioned formation mechanisms and their characteristics, and we study the properties of the black holes that are formed post collapse. In section 5.4 we comment on the post formation growth of the black holes (BHs), and we conclude in section 5.5.

5.2 Early matter domination epoch with scalar fields

We will use a metric with $-+++$ signature, in Planck units $\hbar = c = 1$ such that $G = M_{\rm Pl}^{-2}$. The action we will consider is

$$S = \int d^4x\sqrt{-g}\left[\frac{M_{\rm Pl}^2}{16\pi}R - \mathcal{L}_\phi - \mathcal{L}_\xi\right] , \tag{5.1}$$

involving a massive scalar field ϕ with mass m that models the ambient dark matter, and a massless scalar field ξ that sources the initial perturbation. They are both minimally coupled to gravity but not otherwise coupled to one another, i.e.

$$\mathcal{L}_\phi = \frac{1}{2}\nabla_\mu\phi\nabla^\mu\phi + \frac{m^2\phi^2}{2}\ ,\ \text{and} \tag{5.2}$$

$$\mathcal{L}_\xi = \frac{1}{2}\nabla_\mu\xi\nabla^\mu\xi\ . \tag{5.3}$$

Since the field ξ has no potential, it will only influence dynamics via its gradients. Furthermore, it will dilute much more rapidly than dark matter, and hence not affecting the long term dynamics of the system once its initial job of sourcing a perturbation is done[1].

When the gradients in ξ are negligible, the spacetime dynamics are dominated by the behaviour of the background scalar field ϕ. When ϕ is additionally homogeneous on a given spatial hyperslice, the metric of the spacetime is well described by the Friedman-Lemaître-Robertson-Walker (FLRW) line element

$$ds^2 = -dt^2 + a(t)^2(dr^2 + r^2 d\Omega_2^2)\ , \tag{5.4}$$

where $d\Omega_2^2 = d\theta^2 + \sin^2\theta d\phi^2$. The scale factor $a(t)$ evolves according to the Friedmann equation $H^2 = 8\pi\rho/3M_{\rm Pl}^2$, where $H(t) \equiv \dot{a}/a$ is the Hubble parameter[2]. The equation of motion for ϕ reduces to the Klein-Gordon equation

$$\ddot{\phi} + 3H\dot{\phi} + \frac{dV}{d\phi} = 0\ , \tag{5.5}$$

where the Hubble parameter is

$$H^2 \equiv \frac{8\pi}{3M_{\rm Pl}^2}\left(\frac{1}{2}\dot{\phi}^2 + V(\phi)\right)\ , \tag{5.6}$$

and the corresponding pressure is given by

$$p_{\rm DM} = \frac{1}{2}\dot{\phi}^2 - V(\phi)\,. \tag{5.7}$$

If the oscillation of ϕ is sufficiently undamped, which is the case if $2m \gg 3H$, the friction term in Eqn. (5.5) can be neglected. The dynamics of ϕ are then approximately given by a simple harmonic oscillator $\phi(t) = \phi_0 \cos\Big(mt\Big)$, whose pressure is

---

[1] In principle, we could use a single massive scalar ϕ. However, in practice, we find that large perturbations of the massive scalar would introduce a large infusion of potential energy into the dynamics of the background resulting in non-matter dominated evolution, at least initially.

[2] Dotted variables are derivatives with respect to cosmic time t.

$$p_{\mathrm{DM}} = \frac{\phi_0^2 m^2}{2}\Big(\sin^2\big(mt\big) - \cos^2\big(mt\big)\Big)\,. \tag{5.8}$$

As long as the oscillation period T is sufficiently smaller than one Hubble time, this averages to zero over one Hubble time, i.e. $\langle p_{\mathrm{DM}}\rangle = 0$, resulting in a dark matter dominated expansion, which can be interpreted as a model for pressureless dust [54] at large scales.

Meanwhile, the massless scalar field ξ provides the energy density perturbation that will trigger BH formation. In this work, we exclusively consider initially static spherically symmetric perturbations and we leave the generalisation to fewer degrees of symmetry for future work. We choose the initial configuration of ξ to be space dependent as

$$\xi(t=0,r) = \Delta\xi\ \tanh\left[\frac{r-R_0}{\sigma}\right], \tag{5.9}$$

where $\Delta\xi$, σ and R_0 are the amplitude, width and the initial size of the perturbation respectively. The mass of the initial perturbation scales roughly as R_0^2. We emphasise that this perturbation is non-linear, despite its moniker. Nevertheless, its massless nature means that it will propagate very close to the speed of light. Given the initial static configuration, we expect to see the perturbation split into an infalling mode, which drives the PBH formation, and an outgoing mode, which rapidly disperses.

The background scalar field ϕ starts from rest, so that $\dot{\phi} = 0$ and the initial Hubble parameter in the absence of inhomogeneities is $H_0^2 = 8\pi M_{\mathrm{Pl}}^{-2} V(\phi_0)/3$ via Eqn. (5.6).

Since the configuration of ξ breaks the homogeneity of the initial spatial hyperslice, to set up the correct initial conditions for the metric, we will solve the Hamiltonian constraint. We choose a conformally flat ansatz for the 3-metric γ_{ij},

$$dl^2 = \psi^4(dx^2 + dy^2 + dz^2)\,. \tag{5.10}$$

Then, the Hamiltonian constraint reduces to an equation for the conformal factor ψ

$$\mathcal{H} = \partial^i\partial_i\psi - \frac{\psi^5}{12}K^2 + 2\pi M_{\mathrm{Pl}}^{-2}\psi^5\rho = 0\,, \tag{5.11}$$

where

$$\rho = \rho_\xi + \rho_{\mathrm{DM}} = \frac{\psi^{-4}}{2}\left(\partial_i\xi\right)^2 + V(\phi_0)\ . \tag{5.12}$$

Here the local expansion K is the trace of the extrinsic curvature, $K = \mathrm{Tr}K_{ij}$. Eqn. (5.11) then becomes

$$\partial^i \partial_i \psi - \frac{\psi^5}{12}\left(K^2 - 9H_0^2\right) + \pi M_{\mathrm{Pl}}^{-2}\psi \left(\partial_i \xi\right)^2 = 0\,. \tag{5.13}$$

We choose an initially expanding spacetime with $K = -3H_0$, so that the periodic integrability condition is satisfied[3] [81, 472, 157]. The eventual Hamiltonian constraint only depends on the radial coordinate r due to the spherical symmetry of the setup, and we solve for the conformal factor ψ numerically

$$\frac{\partial^2 \psi}{\partial r^2} + \frac{2}{r}\frac{\partial \psi}{\partial r} + \frac{\pi\psi}{M_{\mathrm{Pl}}^2}\left(\frac{\partial \xi}{\partial r}\right)^2 = 0\,. \tag{5.14}$$

5.3 Primordial black hole formation

Our main scale of reference will be the initial size of the unperturbed Hubble horizon H_0, which is fixed for all simulations by choosing the initial value of the scalar field ϕ to be $\phi_0 = 7.8 \times 10^{-3} M_{\mathrm{Pl}}$, with $m \approx 10^2 H_0$. In the following, we will vary the initial size of the perturbation from subhorizon to superhorizon, $R_0 H_0 \in [0.575,\ 1.6]$. We will also vary the perturbation amplitude within the range $\Delta\xi M_{\mathrm{Pl}}^{-1} \in [0.075,\ 0.12]$, whilst keeping the initial width fixed to $\sigma_0 = 0.15 H_0^{-1}$, such that the ratio between the maximum gradient energy density to dark matter energy density is $\rho_\xi/\rho_{\mathrm{DM}} \sim 1$.

We find that, for both subhorizon and superhorizon perturbations, PBH formation occurs via two possible mechanisms – a *direct collapse* mechanism whereby the PBH is formed by the initial perturbation of ξ itself, and a *post-collapse accretion* mechanism whereby the initial perturbation of ξ sources a gravitational potential that then accretes the background dark matter ϕ until a PBH forms. What determines the type of PBH formation process depends (unsurprisingly) on both the geometry and mass of the initial perturbation shell, as well as the expansion rate of the background cosmology. We will discuss these two mechanisms below[4].

---

[3] The initial energy density of the system is completely dominated by the scalar potential of the homogeneous dark matter field ϕ, which allows us to neglect the perturbation field ξ. Then, the main contribution to the initial energy density is given by the (homogeneous) value of the potential and thus $K^2 = 24\pi V(\phi_0)$.

[4] In this work, we have used the background energy density, or equivalently the background scale factor, as time. This corresponds to the cosmic time infinitely far away from the centre of the PBH. However, in numerical relativity simulations, the foliation of spatial hyperslices is dynamically driven by the so-called puncture gauge, which is required to enforce numerical stability in the presence of future singularities. In this work, we have assumed that masses of PBHs are identified with its

5.3.1 Direct collapse

In the direct collapse scenario, the perturbation collapses towards its geometric centre (to which we will henceforth simply refer as the centre) and forms a black hole directly on its own, without significant accretion of the background DM density. We will now estimate the time a shell takes to undergo direct collapse. The perturbation field ξ is massless, and hence if we ignore the backreaction of the shell on the background geometry, it propagates along null-like geodesics [5]. In an FLRW background, the scale factor a is given by the null element $dt^2 = a^2(t)dr^2$. Solving this kinematic equation, the co-moving radius of the shell is then

$$r_{\text{shell}} = R_0 a_0^{-1} - 2H_0^{-1} a_0^{-1} \left[\left(\frac{a}{a_0} \right)^{1/2} - 1 \right] , \tag{5.15}$$

where we set $a_0 \equiv 1$ to be the initial scale factor at the initial time. The value of the scale factor at the moment the shell collapses to the centre a_* is then the solution to the equation $r_{\text{shell}}(a_*) = 0$, namely

$$a_* = a_0 \left[1 + \frac{R_0 H_0}{2} \right]^2 , \tag{5.16}$$

which is roughly a Hubble time. Notice that a_* is independent of the initial mass and depends only on R_0. We show in Fig. 5.2 that this analytic estimate is in good agreement with our numerical results.

To determine whether or not a given initial perturbation shell will undergo direct collapse into a black hole, we consider the *width* of the shell at the time when the shell reaches the centre $\sigma_* = \sigma(a_*)$. Ignoring backreaction again, since the field ξ is massless, the width of the shell as it collapses towards the centre scales as the expansion rate, i.e.

$$\sigma(a) = \sigma_0 a \ . \tag{5.17}$$

Thus the width of the shell when it reaches the centre is simply $\sigma(a_*) = \sigma_0 a_*$. At this moment, applying the hoop conjecture[6] suggests that if the condition

$$\sigma(a_*) < 2GM_{\text{infall}} \ , \tag{5.18}$$

---

foliation, when in principle one should identify it via null geodesics from the black hole horizon to infinity. This inaccuracy should be minor and would not affect the main conclusions of the chapter.

[5] If the perturbation field ξ instead has mass $m_\xi \sim m_\phi$, then the collapse time is roughly the free fall time $\tau_{\text{ff}} \sim \sqrt{M_{\text{Pl}}/m_\xi \xi}$ which is also roughly one Hubble time.

[6] The presence of an expanding background modifies the hoop conjecture somewhat in general [411], but we checked that the effects are negligible in our analytic estimates.

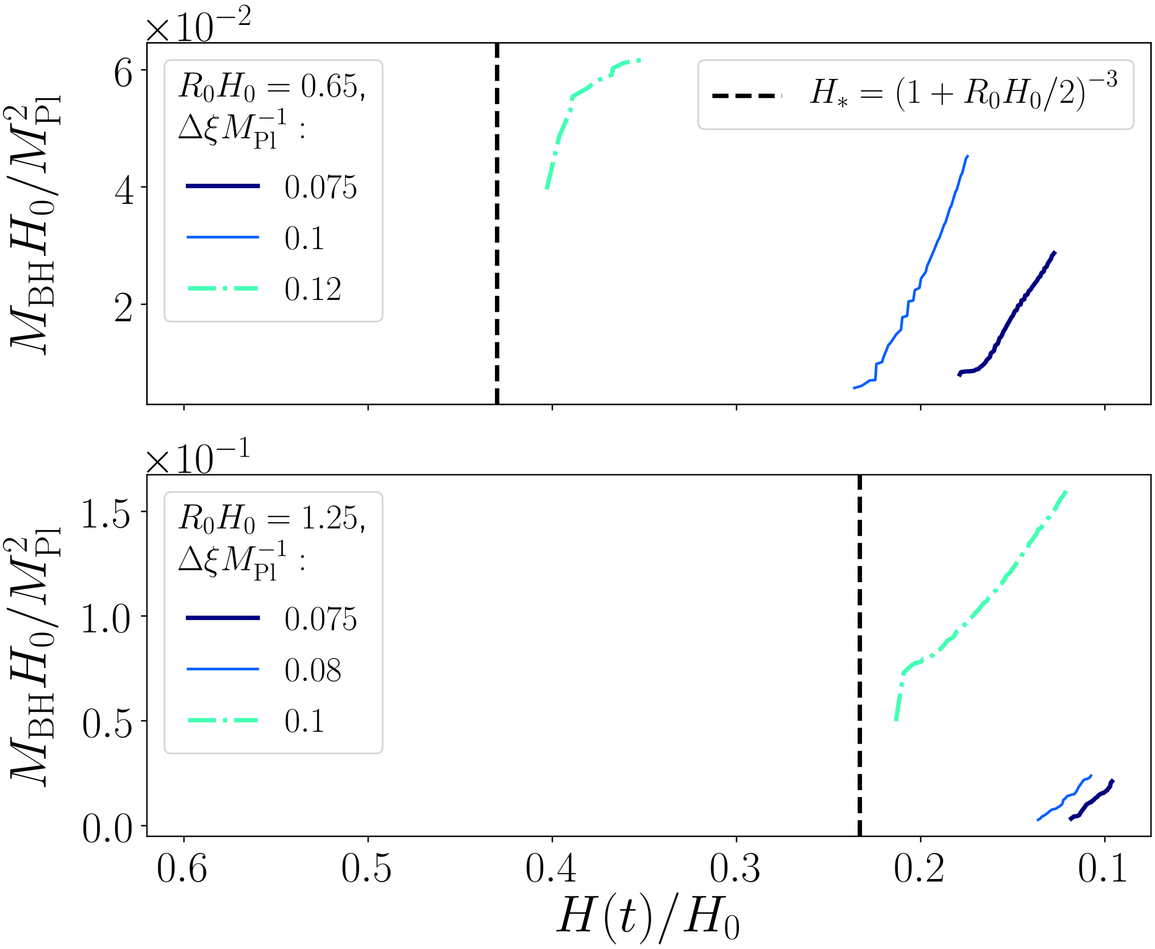

Fig. 5.2 Black hole formation for different perturbation amplitudes. The top (bottom) panel shows mass of the formed BHs as a function of the Hubble parameter $H(t)$ at infinity, for subhorizon (superhorizon) collapse respectively. Vertical dashed black lines correspond to the time at which the perturbation reaches the centre according to Eqn. (5.16). BHs formed through direct (accretion) collapse are shown in dash-dotted (solid) lines. For accretion collapse BHs, increasing the amplitude $\Delta\xi$ makes that the BH forms earlier with a smaller initial mass. Our simulations are in good agreement with the hoop conjecture prediction that the threshold is $\Delta\xi M_{\rm Pl}^{-1} \approx 0.1$ for $R_0H_0 = 0.65$ and $\Delta\xi M_{\rm Pl}^{-1} \approx 0.07$ for $R_0H_0 = 1.25$. In direct collapse, part of the collapsing perturbation ends up within the black hole, corresponding to a larger initial mass.

is satisfied, where $M_{\rm infall}$ is half[7] the initial mass of the shell obtained by integrating the gradient energy of the profile $\xi(r)$ roughly given by Eqn. (5.9) in flat space

$$M_{\rm infall} \approx \frac{1}{2}\int dr\ 4\pi r^2 \frac{1}{2}\left(\frac{\partial\xi}{\partial r}\right)^2 , \tag{5.19}$$

---

[7] The infalling mass is half the initial mass, since the other half will radiate outwards to infinity, so the shell's initial (vanishing) momentum is conserved.

then a black hole will form. This result is again in good agreement with our numerical results, as shown in Fig. 5.2.

The fact that such simple estimates agree with our numerical results suggests that the backreaction of the perturbation on the background dynamics is not very important, at least at the level of determining when and how a black hole will form, even if the shell density is large and locally $\rho_\xi > \rho_{\rm DM}$. This is backed up by our numerical simulations, where we see that the $\rho_{\rm DM}$ profile is not strongly affected by the presence of ρ_ξ, at least initially, as can be seen in a video of the numerical evolution of the energy densities here [236].

5.3.2 Accretion collapse

On the other hand, if $\sigma(a_*) > 2GM_{\rm infall}$, a black hole does not form directly. In this case, the energy density of the perturbation ρ_ξ disperses after reaching the centre and becomes locally sub-dominant to the background energy density $\rho_{\rm DM}$. Nevertheless, the presence of ξ generates a gravitational potential well in the centre, which seeds accretion of the background DM and eventually causes a collapse into a black hole. We illustrate this process in Fig. 5.3.

In this phase, the initially homogeneous and expanding background spacetime is made to locally collapse by the perturbation, with the expansion K locally changing sign from negative (expanding) to positive (contracting), decoupling the region near the centre from the rest of the expanding background. The local dark matter begins to accrete at an extremely high rate $\delta\rho_{\rm DM}/\rho_{\rm DM} \propto a^{34}$, as shown in Fig. 5.4a. Once sufficient DM mass has accumulated, a PBH forms. This process takes around an e-fold to complete. This rapid accretion rate is much higher than that predicted from linear theory, which is $\delta\rho_{\rm DM}/\rho_{\rm DM} \propto a$, indicating that the process is highly non-linear.

From our simulations, we note two salient points. Firstly, if we consider shells that undergo accretion collapse, for fixed initial amplitude $\Delta\xi$, the smaller the initial R_0 (and therefore the smaller the mass) of the initial perturbation, the more massive the initial mass of the PBH. This somewhat counter-intuitive result is due to the fact that the PBH forms via accreting DM, thus a more massive seed will generate a *steeper* potential well, and hence the Schwarzschild radius is reached earlier and at a smaller value for the BH mass. To confirm this, we checked that keeping R_0 fixed but increasing $\Delta\xi$ also yields a less massive initial PBH – this is true for both subhorizon and superhorizon cases, as can be seen in Fig. 5.2. In Fig. 5.4b we plot the dark matter energy density for two different values for R_0 and $\Delta\xi$. We confirm that larger amplitudes (and thus more massive seeds) result in a faster accretion rate.

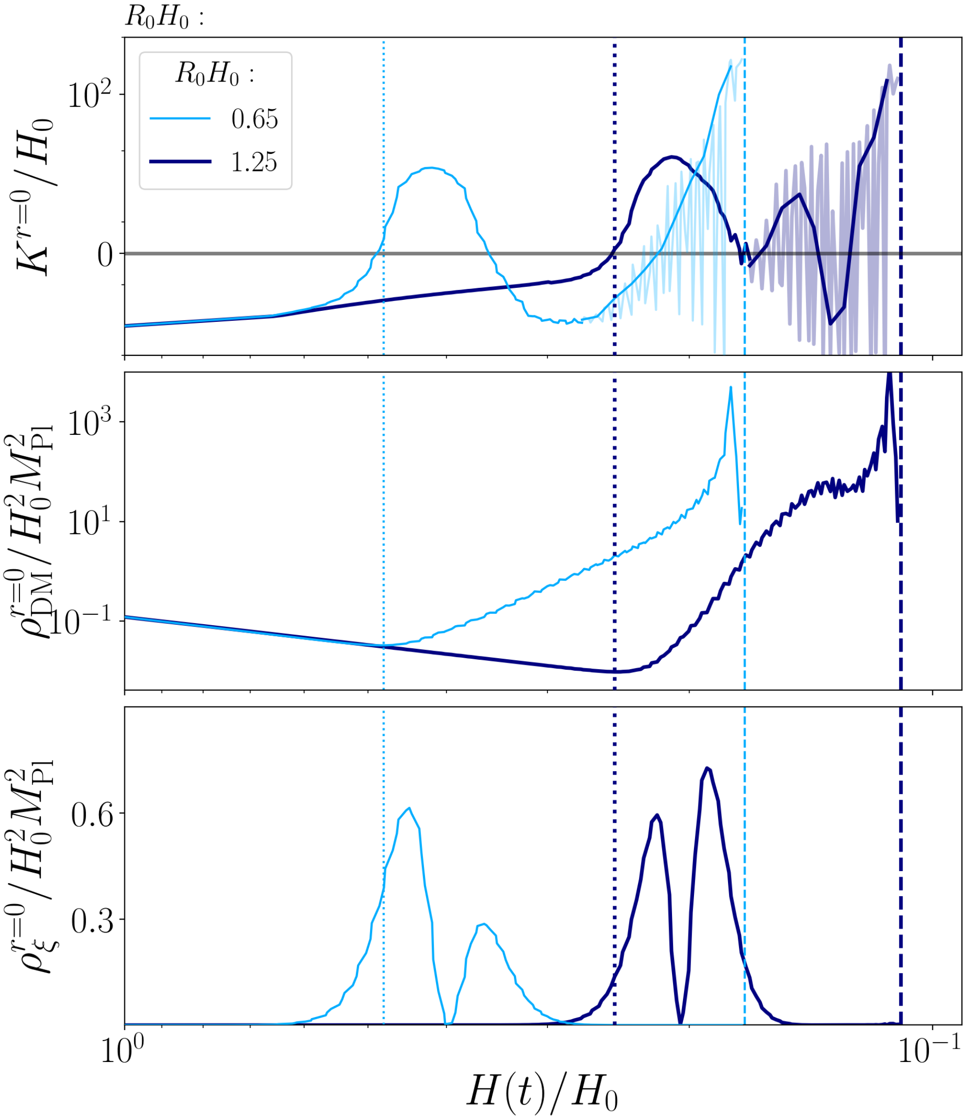

Fig. 5.3 Evolution of the local expansion K and energy densities ρ_{DM} and ρ_ξ at the centre of the collapse $r = 0$, as a function of the Hubble parameter $H(t)$ at infinity – recall that $K > 0$ corresponds to locally collapsing spacetime. A representative subhorizon (superhorizon) is shown in thin light blue (thick dark blue) in the **accretion collapse case**. The top, middle and bottom panels show the evolution of the expansion, the background energy density and gradient energy density respectively. Initially, the background energy density decays as $\rho_{\rm DM} \sim a(t)^{-3}$. When the perturbation reaches the centre (dotted vertical lines) and disperses, gravitational effects decouple the system and stop the local expansion, acting as a seed for the accretion of the background matter $\rho_{\rm DM}$. The accretion of the background matter continues until and after a black hole forms (dashed vertical lines).

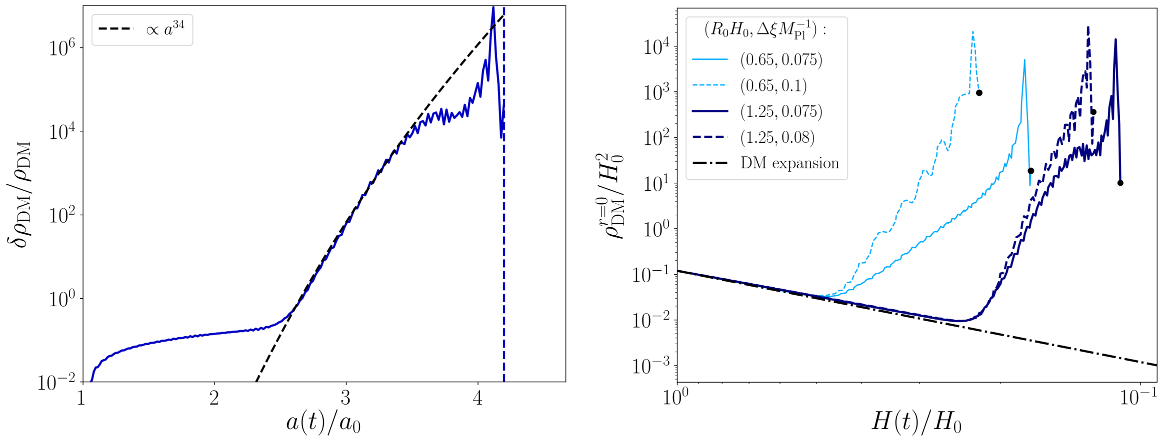

(a) **(b)**

Fig. 5.4 (a): Rate of growth for the local dark matter overdensity $\delta\rho_{\rm DM}/\rho_{\rm DM}$ at the centre of the collapse is well beyond the linear approximation as $\delta\rho_{\rm DM}/\rho_{\rm DM} \propto a^{34}$. Near black hole formation (vertical dashed blue line), the accretion rate tapers off, although some of this tapering effect is due to our gauge condition. **(b): Evolution of the dark matter energy density** at the centre of the collapse for a set of initial radii R_0 and amplitudes $\Delta\xi$. For same radii perturbations, accretion begins at the same time. However, the accretion rate is larger for larger amplitudes, which results in the formation of a black hole at an earlier time.

Secondly, as R_0 approaches H_0^{-1}, the expansion rate of the universe begin to exert a competing effect. For shells with larger R_0, it takes *longer* for the shell to reach the centre, and thus a smaller ρ_ξ and less steep potential when accretion begins. This leads to an increase in the initial mass of the PBH following our argument above – resulting in the "bump" in the initial mass of the black holes (e.g. the black dots in Fig. 5.5).

5.4 PBH growth and final mass

In the cases of both direct and accretion collapse, the initial mass of the PBH formed is small compared to the Hubble horizon, $M_{\rm BH}H_0 \sim 10^{-2}M_{\rm Pl}^2$ – see Fig. 5.5. Once the initial PBH has formed, the PBH accretes DM from its surroundings in the growth phase at a rate that depends on the steepness of the potential and the density of the surrounding DM "scalar cloud" [276, 153, 68, 275]. In general and regardless of the details of the parameters, we find that the initial accretion rate is much higher than the linear theory prediction of $\delta\rho_{\rm DM}/\rho_{\rm DM} \propto a$, as mentioned above. This growth rate is roughly constant, at least initially, and its contribution to the mass of the PBH will rapidly dwarf that of its initial mass.

In a matter dominated universe, naive Newtonian collapse suggests that the maximum mass of the black hole is bounded by $M_{\rm BH}H \sim \alpha M_{\rm Pl}^2$ [136], where $\alpha \lesssim 1$ is some constant which depends on the exact details of the accretion. This suggests a self-similar growth at some equilibrium point. In references [246, 247], it was demonstrated numerically that while the initial growth can be rapid, it will not achieve self-similar growth as accretion is not efficient once the black hole decouples from the background spacetime. However, these works used a stiff massless scalar field as ambient matter instead of a massive scalar field, which more accurately models the ambient DM. From Fig. 5.5, we find that $M \sim H^{-\beta}$ where $\beta \gg 1$. As M approaches the Hubble horizon, we expect $\beta \leq 1$ although unfortunately, we were unable to track the growth of PBH beyond a few factors of their initial mass, as the numerical cost becomes prohibitive.

As long as the universe is dominated by DM, the black hole will continually accrete and grow without end. This would be the case if the PBH is formed in the present late time DM dominated epoch – however such late time PBH has already been ruled out [127, 239]. As we mentioned in the introduction, we consider instead an early phase of DM domination before transitioning into the era of radiation domination prior to the onset of Big Bang Nucleosynthesis (BBN), i.e. before the temperature of the universe is around 1 MeV. This provides a natural cut-off for the growth of the PBH.

Nevertheless, if we assume that the rapid growth we observe continues until $M_{\rm BH}H \sim M_{\rm Pl}^2$, and that the BH grows self-similarly after, it is implied that the final mass of the PBH is independent of when it forms. This means the final mass of the PBH is given by

$$M_{\rm BH} \approx 10^{38}\left(\frac{1\ \rm MeV}{T}\right)^2 g \approx 10^5\left(\frac{1\ \rm MeV}{T}\right)^2 M_\odot\ , \tag{5.20}$$

where T is the temperature of the universe at the onset of radiation domination. Taking $T_{\rm BBN} = 1$ MeV as the natural cut-off for the growth of the PBH, the most massive black holes that can be formed via this accretion mechanism are $M_{\rm BH} \approx 10^{38} g \approx 10^5 M_\odot$ [134, 237].

On the other hand, if the PBH growth asymptotes to a slower rate than the self-similar rate, or achieve self-similarity before $M_{\rm BH} \sim H^{-1}M_{\rm Pl}^2$, then our simulations suggests that $M_{\rm BH} \gtrsim 10^{-2}H^{-1}M_{\rm Pl}^2$, where H is the Hubble parameter when the PBH forms. This means that PBH formed around $T \sim 5$ MeV, $M_{\rm BH} \gtrsim 40 M_\odot$ could form the basis of the population of massive BH that are being detected today by the LVK observatories.

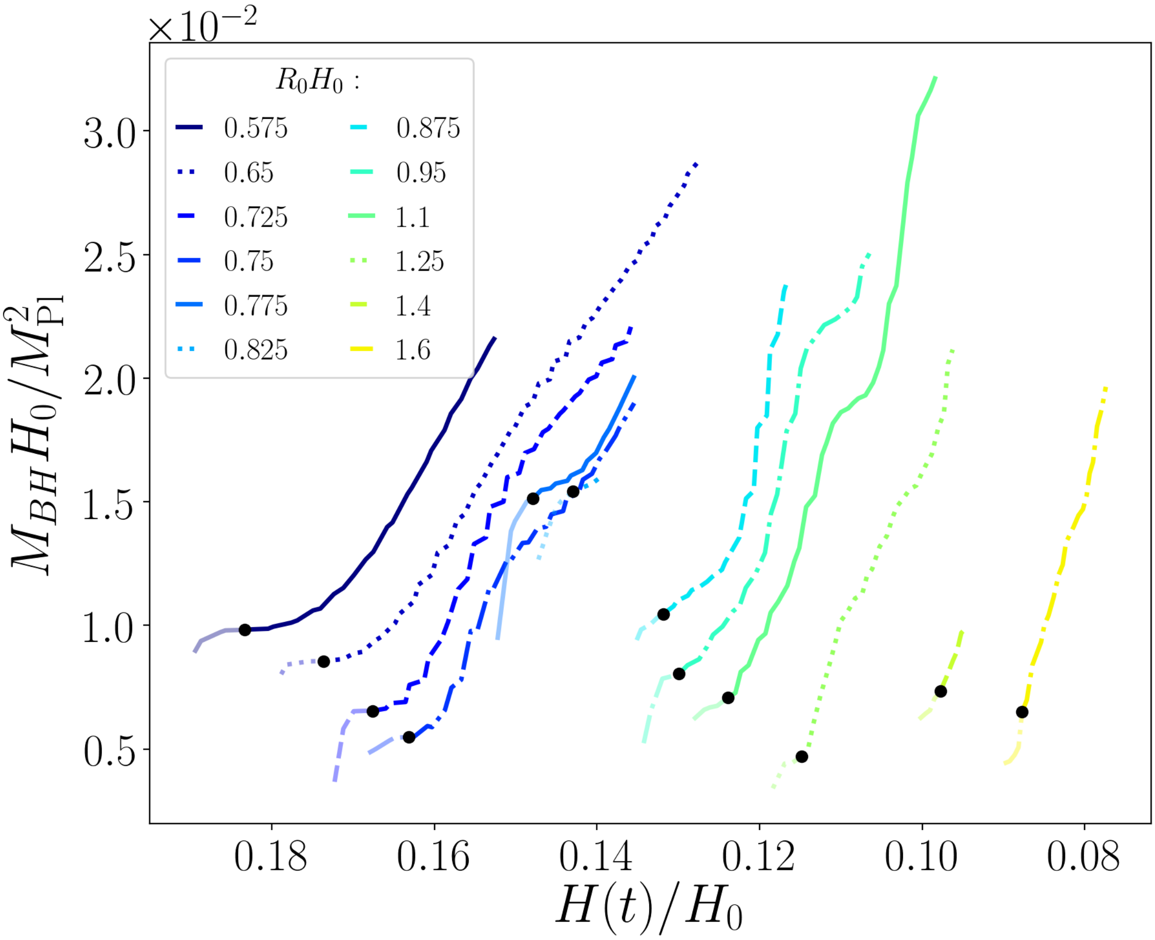

Fig. 5.5 Summary of simulations showing the black hole $M_{\rm BH}$ as a function of the Hubble parameter $H(t)$ at infinity, for various initial radii R_0, for $\Delta\xi M_{\rm Pl}^{-1} = 0.075$. The growth rate of the black hole mass is larger for larger shells, because they source a larger gravitational potential. Black dots correspond to the initial black hole masses at formation, identified using an apparent horizon finder.

5.5 Summary and discussion

In this chapter, we demonstrated that superhorizon non-linear perturbations can collapse and form PBHs in a matter dominated universe, using full numerical relativity. We show that, depending on the mass of the initial perturbation shell, this happens via either the direct collapse or the accretion collapse mechanisms. We provide an analytic criterion Eqn. (5.18) using the hoop conjecture to determine which mechanism is relevant for a given setting, and compute the timescale of collapse using the same prescription. Despite the $\mathcal{O}(1)$ non-linearity, we find that the dynamics of collapse can be modeled as a simple superhorizon mass shell collapsing in an expanding background.

This suggests that semi-analytic estimates of PBH formation in a matter dominated era are broadly accurate.

On the other hand, details matter. We showed that even in the cases where the perturbation is insufficient on its own to form a PBH in a direct collapse, non-linear accretion rates are far higher than what standard linear theory predicts, causing a rapid collapse into a PBH via accretion of ambient DM. In both the direct collapse and accretion collapse formation cases, the initial mass of the PBH is roughly $M_{\rm BH} \sim 10^{-2}H^{-1}M_{\rm Pl}^2$, but formation is followed by an extremely rapid growth $M \propto H^{-\beta}$ where $\beta \gg 1$. Presumably, this growth will asymptote to either the self-similar rate $\beta = 1$ or the decoupled rate $\beta < 1$ [246, 247].

Interestingly, even if the self-similar rate is not achieved, the fact that most of the mass of the PBH is gained through post-formation accretion suggests that there might be a mechanism to generate PBHs with non-trivial spin. Such non-trivial spin might for example be generated by the collapse of a non-spherically symmetric shell, even if the shell is initially spinless. In that case, the PBH might not form in the centre of the initial mass distribution and thus form with spin, whilst outgoing radiation carries away angular momentum of opposite sign, such that angular momentum is still globally conserved, as suggested by [250, 249]. We will explore this possibilty in a future publication.

Chapter 6

Conclusions

6.1 Summary

In this thesis we have applied modern numerical relativity techniques to study the role of strong gravity in three open problems in the early universe: inhomogeneous inflation, cosmic strings and primordial black holes. The thesis has been structured in three parts: background, research and extra material.

We started Chapter 1 reviewing general relativity and introduced the basics of the inflationary universe, cosmic strings and primordial black holes as extensions of the current standard cosmological model. In Chapter 2 we concluded the background material by introducing the methods of numerical relativity to cast Einstein's equations in a 3+1 form, ready to be solved as an initial value problem. We also discussed novel approaches to solve the initial data constraints for spacetimes that contain both black holes and fundamental fields.

The core research material consists of Chapters 3, 4, and 5, where we have presented the main original results of this thesis.

6.1.1 Inhomogeneous inflation

In Chapter 3, we explored whether inflation can begin from inhomogeneous initial conditions. In particular, we derived and tested the high accuracy of an analytical criterion to predict when a given inflationary model will succeed regardless of its initial conditions in the scalar field ϕ. We argued that for a perturbation with wavenumber k, inflation fails if there exists a $\Delta\phi$ such that

$$k^2\Delta\phi + \frac{dV}{d\phi}(\phi_0 + \Delta\phi) = 0\ . \tag{6.1}$$

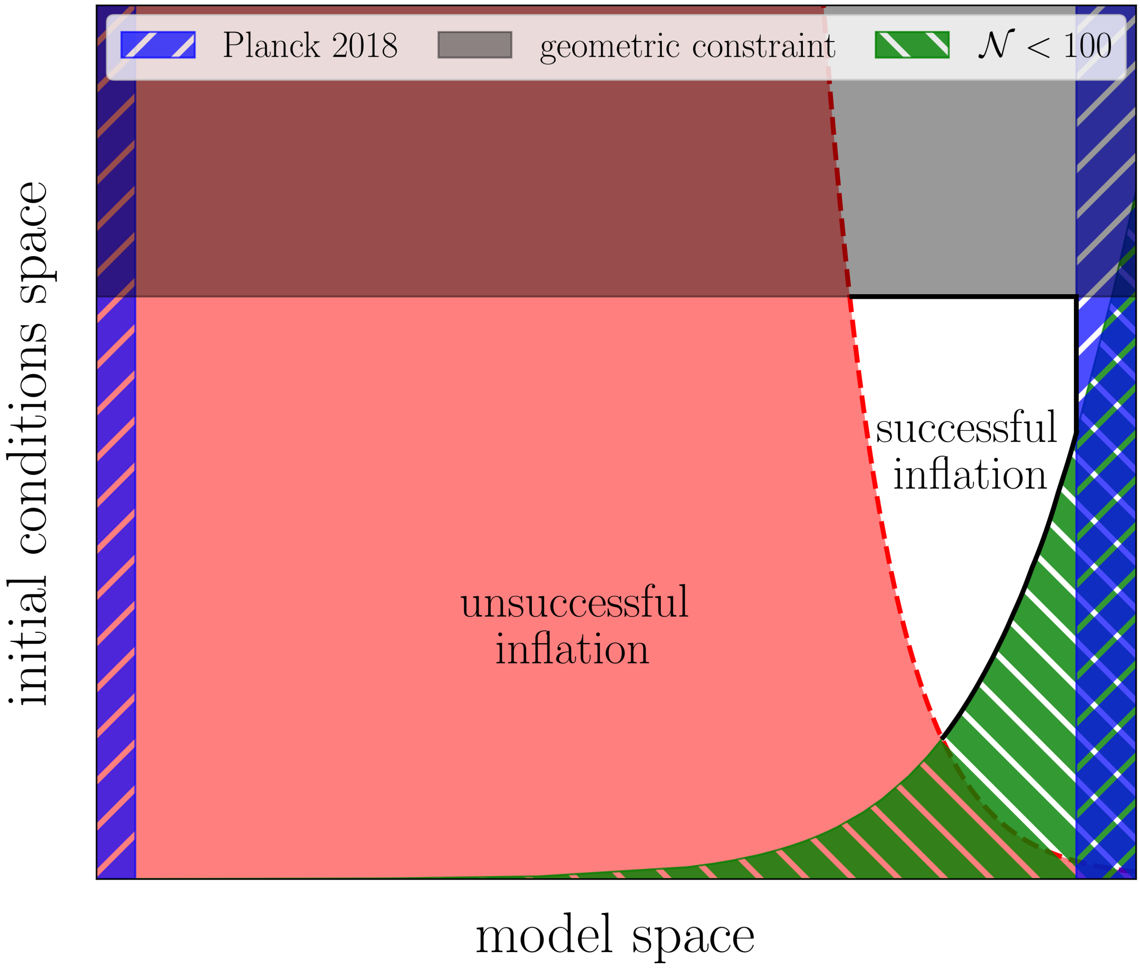

Fig. 6.1 Additional constraints on the joint parameter space for brane inflation in both its initial conditions space (y-axis) and its model space (x-axis) by combining numerical simulations (red vs white regions), observational data [31] (blue shading), the requirement for a minimum of $\mathcal{N} = 100$ efolds of inflation (green shading) and a geometric constraint (grey shading).

We related this to a condition in the shape of the potential by taking the derivative

$$k^2 + V''(\phi_0 + \Delta\phi) = 0\,. \tag{6.2}$$

The first term is always positive, whilst the second one depends upon the shape of the potential. For convex potentials $V'' > 0$, and thus inflation can never fail. For concave potentials, on the other hand, $V'' < 0$ allows the zero crossing to exist depending on the value of k^2 and the scale of the potential. We confirmed that decreasing the wavelength of the inhomogeneities (and thus increasing k^2) makes models more robust, so the most dangerous modes are the long wavelength near horizon modes. However, $V''(\phi)$ is larger for small-field potentials – those in which the field ϕ transverses a small region – and we showed that their robustness is closely related to the characteristic scale of the potential. We demonstrated that convex models are generically more robust than small field concave ones, as opposed favoured observations by the Planck Collaboration, see Fig. 1.1. In addition, we argued that for some potentials there exists a bound on the initial mean value of the inflaton field, beyond which inflation will be successful regardless of the amplitude of the inhomogeneities.

Our work emphasises that whether inflation is successful depends jointly on both the inflationary model and the initial conditions. In particular, Fig. 6.1 clearly demonstrates a way forward in placing more stringent constraints by combining observational data, theoretical models and initial condition space together.

6.1.2 Cosmic strings with NR

In Chapter 4, we performed the first-ever fully general relativistic simulations of abelian Higgs cosmic strings. Focusing on circular loops of radius R_0 whose mass is given in terms of the string tension $G\mu$ as $GM_0 = 2\pi R_0 G\mu$, our numerical results showed that the loop can either (i) unwind and release its energy in a mixture of gravitational waves, scalar and vector fields, or (ii) form a black hole radiating $\mathcal{O}(1)\%$ of the initial total mass of the system in gravitational waves. Using the hoop conjecture we derived a formula for R_0 to predict such an outcome

$$R_0 > \sqrt{\frac{1}{8\pi\lambda}}\,(G\mu)^{-3/2}\,M_{\rm Pl}^{-1}, \tag{6.3}$$

and confirmed its accuracy in Fig. 4.3.

We also performed a parameter space study by simulating lower string tension loops $G\mu \approx 10^{-3} - 10^{-2}$, and varying both the radius R_0 and the string width $\delta = (\sqrt{\lambda}\eta)^{-1}$. Surprisingly, we found that the gravitational waves of the collapse only weakly depend on the latter two whilst lighter strings – smaller $G\mu$ and thus weaker coupling to gravity – lead to greater eficciency, radiating up to $\sim 2\%$ of the initial mass in gravitational waves, see Fig. 4.5. We explained this counter-intuitive result by looking at the Lorentz factor of the string right before the black hole forms, which increases for smaller string tensions as $\gamma(t_{\rm BH}) = (4\pi G\mu)^{-1}$, with the efficiency scaling with the Lorentz factor of the string approximately as $E_{\rm GW}/M_0 \propto (G\mu)^{-1}$, for the parameter space studied in this work. We argued that this strongly suggests that the GW production in such a

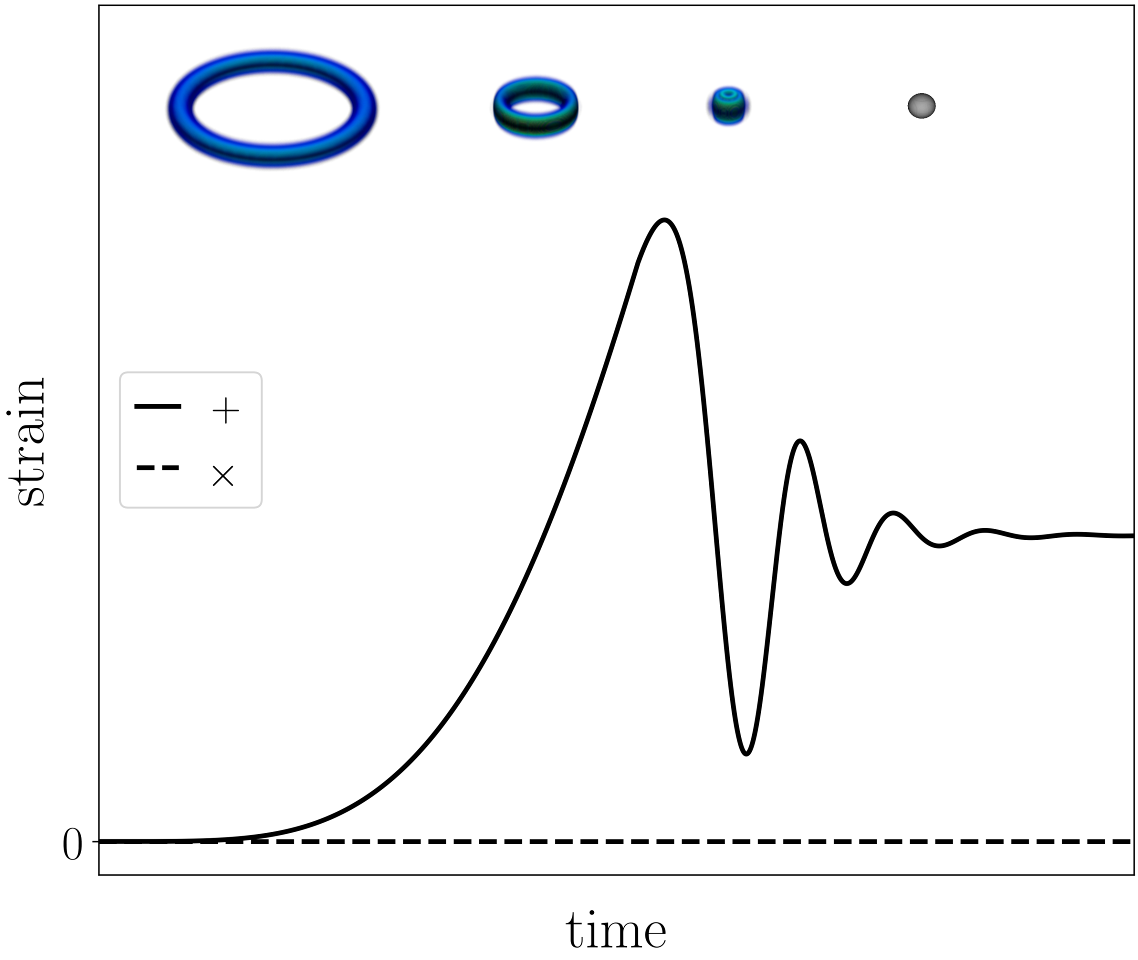

Fig. 6.2 “Plus” and “cross” polarisations of the strain waveform of a collapsing circular cosmic string loop. The top of the figure displays snapshots of the process: loop infall, merger and ringdown of the black hole. The contribution to the cross polarisation vanishes due to the S_1 symmetry of the collapse.

collapse is dominated by kinematic proceesses, and not geometric ones, such as the thickness of the loop.

The ultimate goal of this research line is illustrated in Fig. 6.2, where motivated by current gravitational-wave searches by the LVK observatories we constructed the first-ever time-domain gravitational strain waveform of such an event. The signal features a low frequency infall followed by a characteristic merger and standard ringdown of a Schwarzschild black hole. In addition, it shows very interesting phenomenology such as the large permanent shift in the “plus” polarisation of the strain, called gravitational-wave memory. Its origin resides in the large aspherical emission of energy that is sourced post-collapse, so we believe this is a robust result regardless of the string parameters.

6.1.3 PBH formation with NR

We have demonstrated that in a matter dominated universe, superhorizon non-linear perturbations can collapse and form PBHs via the direct collapse or the accretion collapse mechanisms, when the perturbation is insufficient on its own to form a PBH but it triggers an accretion process that causes a rapid collapse of the ambient DM. We have tested an analytic criterion (Eqn. (5.18)) using the hoop conjecture to determine which mechanism is relevant for a given setting, and compute the timescale of collapse using the same prescription. In both processes the PBH forms within an efold and with a small initial mass compared to the Hubble horizon, $M_{\mathrm{BH}}H_0 \sim 10^{-2}M_{\mathrm{Pl}}^2$. However, we found that the formation is followed by an extremely rapid growth $M \propto H^{-\beta}$ with $\beta \gg 1$, where the PBH acquires most of its mass.

Last but not least, Appendix A, B, C and D comprise the extra material of this thesis. They include detailed calculations that have been omitted throughout the text, such as the projections of the 3+1 Einstein's equation or the construction and fitting of the gravitational-wave signal corresponding to the infall of the cosmic string loop. In these sections we also prove the robustness of our work by presenting details about the implemented evolution equations as well as numerical checks and convergence tests.

6.2 Future work

In Chapter 3 we focused on popular inflationary models and restricted the study of the robustness of inflation to inhomogeneities in the initial scalar field profile ϕ. We intend to extend this work by exploring a more general set of initial perturbations with both non-trivial scalar field ϕ and momentum $\partial_t\phi$, and thus providing more robust conclusions about the precise theory of the Big Bang. This is a highly contentious open problem that has been mostly unexplored due to its computational challenge – one would need to solve for the full set of initial constraint equations.

We will also delve into alternative mechanisms such as the non-perturbative investigation of bouncing cosmologies [307, 306, 119, 215, 470, 280] – which state that the beginning of our universe bounced from another cosmological epoch. This has lately received renewed interest thanks to recent computational studies claiming it to be a more effective cosmological smoother than the inflationary paradigm [162, 278, 281, 279].

Regarding cosmic strings, our ultimate goal is to extend their general relativistic characterisation to other system dynamics and provide the community with accurate gravitational-wave templates to be used in the LVK detector searches. In Chapter 4 we focused on circular cosmic string loops, but it is well known that these are only an example among a plethora of configurations that arise after a phase transition in the early universe. To check whether circular loops are unnatural or the endpoint of more generic loops' lifetime, we will delve into the angular and gravitational radiation of non-circular loops by doing a general relativistic extension of the work done in [349, 414], where their flat space formation and decay was studied. This will allow us to quantify the angular momentum loss rate and thus conclude what number density of circular loops we should expect today.

Another well-motivated and generic signal to look for in the detector data stream is what is known as a cusp – a burst of gravitational waves released when a fragment of a string doubles back on itself and moves at the speed of light. The current waveforms used in the detector analysis pipelines are based on weak-gravity calculations in the Nambu-Goto limit [173]. We will construct their general relativistic waveforms by using field-theory analytical solutions for cosmic string traveling waves [219], which are extremely valuable for the construction of constraint satisfying initial data evolving to a cusp[1].

The PBH formation mechanisms studied in this thesis where most of its mass is gained through post-formation accretion suggests that there might exist a channel to generate PBHs with non-trivial spin. In a future publication, we will investigate the collapse of non-spherically symmetric shells to check whether such configurations can lead to the formation of highly spinning PBHs in a matter dominated era.

In addition, we will use numerical relativity to check whether PBHs can form through the collision of expanding vacuum bubbles, which are expected to arise after a first-order phase transition [158, 159]. As opposed to the literature considering the intersection of multiple null shells [283, 259, 468, 354], we will look into the stability of the post-collision scalar field dynamics.

---

[1] Besides this case, most of the non-trivial systems entail the challenge of solving both the Hamiltonian and momentum constraints, which will be done using the method described in Chapter 2.

In summary, I believe that the research contained in this thesis opens up a new intriguing avenue for the use of numerical relativity in the early universe. In particular, the development of techniques for a general initial condition solver not only allows the extension of the work discussed, but it will also open up an infinite number of opportunities to study a wide range of problems in cosmology.

References

[1] Aasi, J. et al. (2014). Constraints on cosmic strings from the LIGO-Virgo gravitational-wave detectors. *Phys. Rev. Lett.*, 112:131101.

[2] Abadie, J. et al. (2012). All-sky search for gravitational-wave bursts in the second joint LIGO-Virgo run. *Phys. Rev.*, D85:122007.

[3] Abazajian, K. N. et al. (2016). CMB-S4 Science Book, First Edition.

[4] Abbott, B. et al. (2018a). Constraints on cosmic strings using data from the first Advanced LIGO observing run. *Phys. Rev.*, D97(10):102002.

[5] Abbott, B. P. (2016). Observation of gravitational waves from a binary black hole merger. *Phys. Rev. Lett.*, 116:061102.

[6] Abbott, B. P. et al. (2009). First LIGO search for gravitational wave bursts from cosmic (super)strings. *Phys. Rev.*, D80:062002.

[7] Abbott, B. P. et al. (2016a). Binary Black Hole Mergers in the first Advanced LIGO Observing Run. *Phys. Rev. X*, 6(4):041015. [Erratum: Phys.Rev.X 8, 039903 (2018)].

[8] Abbott, B. P. et al. (2016b). Observation of Gravitational Waves from a Binary Black Hole Merger. *Phys. Rev. Lett.*, 116(6):061102.

[9] Abbott, B. P. et al. (2016c). Observing gravitational-wave transient GW150914 with minimal assumptions. *Phys. Rev.*, D93(12):122004. [Addendum: Phys. Rev.D94,no.6,069903(2016)].

[10] Abbott, B. P. et al. (2017). All-sky search for short gravitational-wave bursts in the first Advanced LIGO run. *Phys. Rev.*, D95(4):042003.

[11] Abbott, B. P. et al. (2018b). GWTC-1: A Gravitational-Wave Transient Catalog of Compact Binary Mergers Observed by LIGO and Virgo during the First and Second Observing Runs.

[12] Abbott, B. P. et al. (2018c). Prospects for Observing and Localizing Gravitational-Wave Transients with Advanced LIGO, Advanced Virgo and KAGRA. *Living Rev. Rel.*, 21(1):3.

[13] Abbott, B. P. et al. (2019a). All-Sky Search for Short Gravitational-Wave Bursts in the Second Advanced LIGO and Advanced Virgo Run. *Phys. Rev. D*, 100(2):024017.

[14] Abbott, B. P. et al. (2019b). All-Sky Search for Short Gravitational-Wave Bursts in the Second Advanced LIGO and Advanced Virgo Run. *Phys. Rev.*, D100(2):024017.

[15] Abbott, B. P. et al. (2019c). Search for the isotropic stochastic background using data from Advanced LIGO's second observing run. *Phys. Rev.*, D100(6):061101.

[16] Abbott, R. et al. (2020a). GW190521: A Binary Black Hole Merger with a Total Mass of $150M_{\odot}$. *Phys. Rev. Lett.*, 125(10):101102.

[17] Abbott, R. et al. (2020b). Properties and Astrophysical Implications of the 150 $\mathrm{M}_{\odot}$ Binary Black Hole Merger GW190521. *Astrophys. J. Lett.*, 900(1):L13.

[18] Abbott, R. et al. (2021a). Constraints on Cosmic Strings Using Data from the Third Advanced LIGO–Virgo Observing Run. *Phys. Rev. Lett.*, 126(24):241102.

[19] Abbott, R. et al. (2021b). GWTC-2: Compact Binary Coalescences Observed by LIGO and Virgo During the First Half of the Third Observing Run. *Phys. Rev. X*, 11:021053.

[20] Abbott, R. et al. (2021c). GWTC-2.1: Deep Extended Catalog of Compact Binary Coalescences Observed by LIGO and Virgo During the First Half of the Third Observing Run.

[21] Acharya, B. S., Kumar, P., Bobkov, K., Kane, G., Shao, J., and Watson, S. (2008). Non-thermal Dark Matter and the Moduli Problem in String Frameworks. *JHEP*, 06:064.

[22] Achucarro, A., Kuijken, K., Perivolaropoulos, L., and Vachaspati, T. (1992). Dynamical simulations of semilocal strings. *Nucl. Phys. B*, 388:435–456.

[23] Ade, P. A. R. et al. (2014). Planck 2013 results. XXV. Searches for cosmic strings and other topological defects. *Astron. Astrophys.*, 571:A25.

[24] Afshordi, N., McDonald, P., and Spergel, D. N. (2003). Primordial black holes as dark matter: The Power spectrum and evaporation of early structures. *Astrophys. J. Lett.*, 594:L71–L74.

[25] Akiyama, K. et al. (2019a). First M87 Event Horizon Telescope Results. I. The Shadow of the Supermassive Black Hole. *Astrophys. J. Lett.*, 875:L1.

[26] Akiyama, K. et al. (2019b). First M87 Event Horizon Telescope Results. II. Array and Instrumentation. *Astrophys. J. Lett.*, 875(1):L2.

[27] Akiyama, K. et al. (2019c). First M87 Event Horizon Telescope Results. III. Data Processing and Calibration. *Astrophys. J. Lett.*, 875(1):L3.

[28] Akiyama, K. et al. (2019d). First M87 Event Horizon Telescope Results. IV. Imaging the Central Supermassive Black Hole. *Astrophys. J. Lett.*, 875(1):L4.

[29] Akiyama, K. et al. (2019e). First M87 Event Horizon Telescope Results. V. Physical Origin of the Asymmetric Ring. *Astrophys. J. Lett.*, 875(1):L5.

[30] Akiyama, K. et al. (2019f). First M87 Event Horizon Telescope Results. VI. The Shadow and Mass of the Central Black Hole. *Astrophys. J. Lett.*, 875(1):L6.

[31] Akrami, Y. et al. (2020). Planck 2018 results. X. Constraints on inflation. *Astron. Astrophys.*, 641:A10.

[32] Albrecht, A., Battye, R. A., and Robinson, J. (1999). Detailed study of defect models for cosmic structure formation. *Phys. Rev. D*, 59:023508.

[33] Albrecht, A. and Brandenberger, R. H. (1985). On the Realization of New Inflation. *Phys. Rev.*, D31:1225.

[34] Albrecht, A., Brandenberger, R. H., and Matzner, R. (1985). Numerical Analysis of Inflation. *Phys. Rev.*, D32:1280.

[35] Albrecht, A., Brandenberger, R. H., and Matzner, R. (1987). Inflation With Generalized Initial Conditions. *Phys. Rev.*, D35:429.

[36] Albrecht, A. and Steinhardt, P. J. (1982). Cosmology for Grand Unified Theories with Radiatively Induced Symmetry Breaking. *Phys. Rev. Lett.*, 48:1220–1223.

[37] Albrecht, A. and Turok, N. (1985). Evolution of Cosmic Strings. *Phys. Rev. Lett.*, 54:1868–1871.

[38] Albrecht, A. and Turok, N. (1989). Evolution of Cosmic String Networks. *Phys. Rev. D*, 40:973–1001.

[39] Alcock, C. et al. (2000). The MACHO project: Microlensing results from 5.7 years of LMC observations. *Astrophys. J.*, 542:281–307.

[40] Alcubierre, M. (2008a). *Introduction to 3+1 Numerical Relativity.* International Series of Monographs on Physics. OUP Oxford.

[41] Alcubierre, M. (2008b). *Introduction to 3+1 numerical relativity.* International series of monographs on physics. Oxford Univ. Press, Oxford.

[42] Alcubierre, M. and Bruegmann, B. (2001). Simple excision of a black hole in (3+1)-numerical relativity. *Phys. Rev. D*, 63:104006.

[43] Alcubierre, M., Bruegmann, B., Diener, P., Koppitz, M., Pollney, D., Seidel, E., and Takahashi, R. (2003). Gauge conditions for long term numerical black hole evolutions without excision. *Phys. Rev.*, D67:084023.

[44] Alcubierre, M., Bruegmann, B., Pollney, D., Seidel, E., and Takahashi, R. (2001). Black hole excision for dynamic black holes. *Phys. Rev. D*, 64:061501.

[45] Alexandre, J. and Clough, K. (2018). Black hole interference patterns in flavor oscillations. *Phys. Rev. D*, 98(4):043004.

[46] Alho, A. and Mena, F. C. (2011). Pre-inflationary homogenization of scalar field cosmologies. *Phys. Lett.*, B703:537–542.

[47] Alho, A. and Mena, F. C. (2014). Covariant and gauge-invariant linear scalar perturbations in multiple scalar field cosmologies. *Phys. Rev.*, D90(4):043501.

[48] Alic, D., Bona-Casas, C., Bona, C., Rezzolla, L., and Palenzuela, C. (2012). Conformal and covariant formulation of the z4 system with constraint-violation damping. *Physical Review D*, 85(6).

[49] Allahverdi, R., Amin, M. A., Berlin, A., Bernal, N., Byrnes, C. T., Delos, M. S., Erickcek, A. L., Escudero, M., Figueroa, D. G., Freese, K., and et al. (2021). The first three seconds: a review of possible expansion histories of the early universe. *The Open Journal of Astrophysics*, 4(1).

[50] Allen, B. and Casper, P. (1994). A Closed form expression for the gravitational radiation rate from cosmic strings. *Phys. Rev.*, D50:2496–2518.

[51] Allen, B. and Ottewill, A. C. (2001). Wave forms for gravitational radiation from cosmic string loops. *Phys. Rev.*, D63:063507.

[52] Allen, B. and Shellard, E. P. S. (1990). Cosmic string evolution: a numerical simulation. *Phys. Rev. Lett.*, 64:119–122.

[53] Allen, B. and Shellard, E. P. S. (1992). Gravitational radiation from cosmic strings. *Phys. Rev.*, D45:1898–1912.

[54] an Gu, J. (2007). Oscillating quintessence.

[55] Andrade, T. et al. (2021). GRChombo: An adaptable numerical relativity code for fundamental physics. *J. Open Source Softw.*, 6:3703.

[56] Andrade, T., Figueras, P., and Sperhake, U. (2020). Violations of Weak Cosmic Censorship in Black Hole collisions.

[57] Arnowitt, R., Deser, S., and Misner, C. W. (1959). Dynamical structure and definition of energy in general relativity. *Phys. Rev.*, 116:1322–1330.

[58] Arnowitt, R. L., Deser, S., and Misner, C. W. (2008). The Dynamics of general relativity. *Gen. Rel. Grav.*, 40:1997–2027.

[59] Arzoumanian, Z., Baker, P. T., Blumer, H., Bécsy, B., Brazier, A., Brook, P. R., Burke-Spolaor, S., Chatterjee, S., Chen, S., Cordes, J. M., and et al. (2020). The nanograv 12.5 yr data set: Search for an isotropic stochastic gravitational-wave background. *The Astrophysical Journal Letters*, 905(2):L34.

[60] Auclair, P. et al. (2019). Probing the gravitational wave background from cosmic strings with LISA.

[61] Aurrekoetxea, J. C., Clough, K., Flauger, R., and Lim, E. A. (2020a). The Effects of Potential Shape on Inhomogeneous Inflation. *JCAP*, 05:030.

[62] Aurrekoetxea, J. C., Clough, K., and Lim, E. A. (2022a). CTTK: A new method to solve the initial data constraints in numerical relativity.

[63] Aurrekoetxea, J. C., Ferreira, P. G., Clough, K., Lim, E. A., and Tattersall, O. J. (2022b). Where is the ringdown? Reconstructing quasinormal modes from dispersive waves.

[64] Aurrekoetxea, J. C., Helfer, T., and Lim, E. A. (2020b). Coherent Gravitational Waveforms and Memory from Cosmic String Loops. *Class. Quant. Grav.*, 37(20):204001.

[65] Austin, D., Copeland, E. J., and Kibble, T. W. B. (1993). Evolution of cosmic string configurations. *Phys. Rev. D*, 48:5594–5627.

[66] Baker, J. G., Campanelli, M., and Lousto, C. O. (2002). The Lazarus project: A Pragmatic approach to binary black hole evolutions. *Phys. Rev.*, D65:044001.

[67] Baker, J. G., Centrella, J., Choi, D.-I., Koppitz, M., and van Meter, J. (2006). Gravitational wave extraction from an inspiraling configuration of merging black holes. *Phys. Rev. Lett.*, 96:111102.

[68] Bamber, J., Clough, K., Ferreira, P. G., Hui, L., and Lagos, M. (2021). Growth of accretion driven scalar hair around Kerr black holes. *Phys. Rev. D*, 103(4):044059.

[69] Bantilan, H., Figueras, P., Kunesch, M., and Panosso Macedo, R. (2019). End point of nonaxisymmetric black hole instabilities in higher dimensions. *Phys. Rev. D*, 100(8):086014.

[70] Barrow, J. D. (1986). The Deflationary Universe: An Instability of the De Sitter Universe. *Phys. Lett.*, B180:335–339.

[71] Barrow, J. D. (1987). Cosmic No Hair Theorems and Inflation. *Phys. Lett.*, B187:12–16.

[72] Barrow, J. D. and Goetz, G. (1989). The Asymptotic Approach to De Sitter Space-time. *Phys. Lett.*, B231:228–230.

[73] Barrow, J. D. and Stein-Schabes, J. (1984). Inhomogeneous cosmologies with cosmological constant. *Phys. Lett.*, A103:315.

[74] Barrow, J. D. and Tipler, F. J. (1985). Closed universe - Their future evolution and final state. *MNRAS*, 216:395–402.

[75] Bassett, B. A. and Tsujikawa, S. (2001). Inflationary preheating and primordial black holes. *Physical Review D*, 63(12).

[76] Baumann, D. and McAllister, L. (2007). A Microscopic Limit on Gravitational Waves from D-brane Inflation. *Phys. Rev.*, D75:123508.

[77] Baumgarte, T. and Shapiro, S. (2010). *Numerical Relativity: Solving Einstein's Equations on the Computer*. Cambridge University Press.

[78] Baumgarte, T. W., Murchadha, N. O., and Pfeiffer, H. P. (2007). The Einstein constraints: Uniqueness and non-uniqueness in the conformal thin sandwich approach. *Phys. Rev. D*, 75:044009.

[79] Baumgarte, T. W. and Shapiro, S. L. (1999). On the numerical integration of Einstein's field equations. *Phys. Rev.*, D59:024007.

[80] Bean, R. and Magueijo, J. (2002). Could supermassive black holes be quintessential primordial black holes? *Phys. Rev. D*, 66:063505.

[81] Bentivegna, E. (2014). Solving the Einstein constraints in periodic spaces with a multigrid approach. *Class. Quant. Grav.*, 31:035004.

[82] Berezhiani, L. and Trodden, M. (2015). How Likely are Constituent Quanta to Initiate Inflation? *Phys. Lett.*, B749:425–430.

[83] Berti, E., Cardoso, V., and Will, C. M. (2006). On gravitational-wave spectroscopy of massive black holes with the space interferometer LISA. *Phys. Rev.*, D73:064030.

[84] Bertone, G. et al. (2020). Gravitational wave probes of dark matter: challenges and opportunities. *SciPost Phys. Core*, 3:007.

[85] Bevis, N., Hindmarsh, M., Kunz, M., and Urrestilla, J. (2007). CMB power spectrum contribution from cosmic strings using field-evolution simulations of the Abelian Higgs model. *Phys. Rev. D*, 75:065015.

[86] Bicak, J. and Podolsky, J. (1997). Global structure of Robinson-Trautman radiative space-times with a cosmological constant. *Phys. Rev.*, D55:1985–1993.

[87] Bicknell, G. V. and Henriksen, R. N. (1979). Formation of primordial black holes. *Astrophys. J.*, 232:670–682.

[88] Binetruy, P., Bohe, A., Hertog, T., and Steer, D. A. (2010). Gravitational wave signatures from kink proliferation on cosmic (super-) strings. *Phys. Rev.*, D82:126007.

[89] Blanchet, L. and Damour, T. (1992). Hereditary effects in gravitational radiation. *Phys. Rev.*, D46:4304–4319.

[90] Blanco-Pillado, J. J. and Olum, K. D. (2017). Stochastic gravitational wave background from smoothed cosmic string loops. *Phys. Rev.*, D96(10):104046.

[91] Blanco-Pillado, J. J., Olum, K. D., and Shlaer, B. (2011). Large parallel cosmic string simulations: New results on loop production. *Phys. Rev.*, D83:083514.

[92] Blanco-Pillado, J. J., Olum, K. D., and Shlaer, B. (2014). The number of cosmic string loops. *Phys. Rev.*, D89(2):023512.

[93] Blanco-Pillado, J. J., Olum, K. D., and Siemens, X. (2018a). New limits on cosmic strings from gravitational wave observation. *Phys. Lett.*, B778:392–396.

[94] Blanco-Pillado, J. J., Olum, K. D., and Vilenkin, A. (2021). No black holes from cosmic string cusps.

[95] Blanco-Pillado, J. J., Olum, K. D., and Wachter, J. M. (2018b). Gravitational backreaction near cosmic string kinks and cusps. *Phys. Rev. D*, 98(12):123507.

[96] Blanco-Pillado, J. J., Olum, K. D., and Wachter, J. M. (2019a). Energy-conservation constraints on cosmic string loop production and distribution functions. *Phys. Rev.*, D100(12):123526.

[97] Blanco-Pillado, J. J., Olum, K. D., and Wachter, J. M. (2019b). Gravitational backreaction simulations of simple cosmic string loops. *Phys. Rev. D*, 100(2):023535.

[98] Bloomfield, J. K., Fitzpatrick, P., Hilbert, K., and Kaiser, D. I. (2019). Onset of inflation amid backreaction from inhomogeneities. *Phys. Rev.*, D100(6):063512.

[99] bo Cheng, H. and zhou Li, X. (1996). Primordial black holes and cosmic string loop. *Chinese Physics Letters*, 13(4):317–320.

[100] Boersma, O. M., Nichols, D. A., and Schmidt, P. (2020). Forecasts for detecting the gravitational-wave memory effect with Advanced LIGO and Virgo.

[101] Bogomolny, E. B. (1976). Stability of Classical Solutions. *Sov. J. Nucl. Phys.*, 24:449.

[102] Bona, C., Masso, J., Seidel, E., and Stela, J. (1995). A New formalism for numerical relativity. *Phys. Rev. Lett.*, 75:600–603.

[103] Boucher, W. and Gibbons, G. W. (2011). Cosmic Baldness. In *Nuffield Workshop on the Very Early Universe Cambridge, England, June 21-July 9, 1982*, pages 273–278.

[104] Bouchet, F. R., Peter, P., Riazuelo, A., and Sakellariadou, M. (2002). Is there evidence for topological defects in the BOOMERANG data? *Phys. Rev. D*, 65:021301.

[105] Bowen, J. (1979). General form for the longitudinal momentum of a spherically symmetric source. *General Relativity and Gravitation*, 11:227–231.

[106] Bowen, J. M. and York, J. W. (1980). Time-asymmetric initial data for black holes and black-hole collisions. *Phys. Rev. D*, 21:2047–2056.

[107] Braden, J., Johnson, M. C., Peiris, H. V., and Aguirre, A. (2016). Constraining cosmological ultra-large scale structure using numerical relativity.

[108] Braginsky, V. B. and Thorne, K. S. (1987). Gravitational-wave bursts with memory and experimental prospects. *Nature*, 327(6118):123–125.

[109] Bramberger, S. F., Brandenberger, R. H., Jreidini, P., and Quintin, J. (2015). Cosmic String Loops as the Seeds of Super-Massive Black Holes. *JCAP*, 1506(06):007.

[110] Brandenberger, R. (2016). Initial Conditions for Inflation - A Short Review.

[111] Brandenberger, R., Geshnizjani, G., and Watson, S. (2003). On the initial conditions for brane inflation. *Phys. Rev.*, D67:123510.

[112] Brandenberger, R. H. (1991). Cosmic strings and the large scale structure of the universe. *Phys. Scripta T*, 36:114–126.

[113] Brandenberger, R. H. (2002). Back reaction of cosmological perturbations and the cosmological constant problem. In *18th IAP Colloquium on the Nature of Dark Energy: Observational and Theoretical Results on the Accelerating Universe Paris, France, July 1-5, 2002*.

[114] Brandenberger, R. H., Feldman, H., and Kung, J. (1991). Initial conditions for chaotic inflation. *Phys. Scripta*, T36:64–69.

[115] Brandenberger, R. H. and Feldman, H. A. (1989). Effects of Gravitational Perturbations on the Evolution of Scalar Fields in the Early Universe. *Phys. Lett.*, B220:361–367.

[116] Brandenberger, R. H. and Kung, J. H. (1990). Chaotic Inflation as an Attractor in Initial Condition Space. *Phys. Rev.*, D42:1008–1015.

[117] Bruni, M., Matarrese, S., and Pantano, O. (1995). A Local view of the observable universe. *Phys. Rev. Lett.*, 74:1916–1919.

[118] Bruni, M., Mena, F. C., and Tavakol, R. K. (2002). Cosmic no hair: Nonlinear asymptotic stability of de Sitter universe. *Class. Quant. Grav.*, 19:L23–L29.

[119] Buchbinder, E. I., Khoury, J., and Ovrut, B. A. (2007). On the initial conditions in new ekpyrotic cosmology. *JHEP*, 11:076.

[120] Caldwell, R. and Casper, P. (1996a). Formation of Black Holes from Collapsed Cosmic String Loops. *Phys. Rev.*, D53:3002–3010.

[121] Caldwell, R. R. and Allen, B. (1992). Cosmological constraints on cosmic string gravitational radiation. *Phys. Rev.*, D45:3447–3468.

[122] Caldwell, R. R., Battye, R. A., and Shellard, E. P. S. (1996). Relic gravitational waves from cosmic strings: Updated constraints and opportunities for detection. *Phys. Rev.*, D54:7146–7152.

[123] Caldwell, R. R. and Casper, P. (1996b). Formation of black holes from collapsed cosmic string loops. *Phys. Rev. D*, 53:3002–3010.

[124] Campanelli, M., Lousto, C. O., Marronetti, P., and Zlochower, Y. (2006). Accurate evolutions of orbiting black-hole binaries without excision. *Phys. Rev. Lett.*, 96:111101.

[125] Capozziello, S., de Ritis, R., and Marino, A. A. (1998). Recovering the effective cosmological constant in extended gravity theories. *Gen. Rel. Grav.*, 30:1247–1272.

[126] Carr, B., Dimopoulos, K., Owen, C., and Tenkanen, T. (2018). Primordial black hole formation during slow reheating after inflation. *Physical Review D*, 97(12).

[127] Carr, B., Kohri, K., Sendouda, Y., and Yokoyama, J. (2020). Constraints on Primordial Black Holes.

[128] Carr, B. and Kuhnel, F. (2020). Primordial Black Holes as Dark Matter: Recent Developments. *Ann. Rev. Nucl. Part. Sci.*, 70:355–394.

[129] Carr, B., Kuhnel, F., and Sandstad, M. (2016). Primordial Black Holes as Dark Matter. *Phys. Rev. D*, 94(8):083504.

[130] Carr, B., Tenkanen, T., and Vaskonen, V. (2017). Primordial black holes from inflaton and spectator field perturbations in a matter-dominated era. *Phys. Rev.*, D96(6):063507.

[131] Carr, B. J. (1975). The Primordial black hole mass spectrum. *Astrophys. J.*, 201:1–19.

[132] Carr, B. J. (1975). The primordial black hole mass spectrum. *Astrophys. J.*, 201:1–19.

[133] Carr, B. J. (1976). Some cosmological consequences of primordial black-hole evaporations. *Astrophys. J.*, 206:8–25.

[134] Carr, B. J. (2004). Primordial black holes: Recent developments. *eConf*, C041213:0204.

[135] Carr, B. J., Gilbert, J. H., and Lidsey, J. E. (1994). Black hole relics and inflation: Limits on blue perturbation spectra. *Physical Review D*, 50(8):4853–4867.

[136] Carr, B. J. and Hawking, S. W. (1974). Black Holes in the Early Universe. *Monthly Notices of the Royal Astronomical Society*, 168(2):399–415.

[137] Carr, B. J., Kohri, K., Sendouda, Y., and Yokoyama, J. (2010). New cosmological constraints on primordial black holes. *Phys. Rev.*, D81:104019.

[138] Carr, B. J. and Lidsey, J. E. (1993). Primordial black holes and generalized constraints on chaotic inflation. *Phys. Rev. D*, 48:543–553.

[139] Carr, B. J. and Rees, M. J. (1979). The anthropic principle and the structure of the physical world. *Nature*, 278(5705):605–612.

[140] Carr, B. J. and Rees, M. J. (1984). Can pregalactic objects generate galaxies? *Monthly Notices of the Royal Astronomical Society*, 206(4):801–818.

[141] Carrion, K., Hidalgo, J. C., Montiel, A., and Padilla, L. E. (2021). Complex scalar field reheating and primordial black hole production.

[142] Carroll, S. M. and Tam, H. (2010). Unitary Evolution and Cosmological Fine-Tuning.

[143] Casper, P. and Allen, B. (1995). Gravitational radiation from realistic cosmic string loops. *Phys. Rev.*, D52:4337–4348.

[144] Chapline, G. (1975). Cosmological effects of primordial black holes. *Nature*, 253(5489):251–252.

[145] Chernoff, D. F., Flanagan, E. E., and Wardell, B. (2019). Gravitational backreaction on a cosmic string: Formalism. *Phys. Rev. D*, 99(8):084036.

[146] Choptuik, M. W. (1993). Universality and scaling in gravitational collapse of a massless scalar field. *Phys. Rev. Lett.*, 70:9–12.

[147] Christodoulou, D. (1991). Nonlinear nature of gravitation and gravitational-wave experiments. *Phys. Rev. Lett.*, 67:1486–1489.

[148] Clesse, S. and García-Bellido, J. (2015). Massive primordial black holes from hybrid inflation as dark matter and the seeds of galaxies. *Physical Review D*, 92(2).

[149] Cline, D. B., Sanders, D. A., and Hong, W. (1997). Further evidence for gamma-ray bursts consistent with primordial black hole evaporation. *Astrophys. J.*, 486:169–178.

[150] Clough, K. (2017). *Scalar Fields in Numerical General Relativity: Inhomogeneous inflation and asymmetric bubble collapse.* PhD thesis, King's Coll. London, Cham.

[151] Clough, K. (2021). Continuity equations for general matter: applications in numerical relativity. *Class. Quant. Grav.*, 38(16):167001.

[152] Clough, K., Dietrich, T., and Niemeyer, J. C. (2018a). Axion star collisions with black holes and neutron stars in full 3D numerical relativity. *Phys. Rev. D*, 98(8):083020.

[153] Clough, K., Ferreira, P. G., and Lagos, M. (2019). Growth of massive scalar hair around a Schwarzschild black hole. *Phys. Rev. D*, 100(6):063014.

[154] Clough, K., Figueras, P., Finkel, H., Kunesch, M., Lim, E. A., and Tunyasuvunakool, S. (2015). GRChombo : Numerical Relativity with Adaptive Mesh Refinement. *Class. Quant. Grav.*, 32(24):245011. [Class. Quant. Grav.32,24(2015)].

[155] Clough, K., Flauger, R., and Lim, E. A. (2018b). Robustness of Inflation to Large Tensor Perturbations. *JCAP*, 1805(05):065.

[156] Clough, K. and Lim, E. A. (2016). Critical Phenomena in Non-spherically Symmetric Scalar Bubble Collapse.

[157] Clough, K., Lim, E. A., DiNunno, B. S., Fischler, W., Flauger, R., and Paban, S. (2017). Robustness of inflation to inhomogeneous initial conditions. *Journal of Cosmology and Astroparticle Physics*, 2017(09):025–025.

[158] Coleman, S. R. (1977). The Fate of the False Vacuum. 1. Semiclassical Theory. *Phys. Rev. D*, 15:2929–2936. [Erratum: Phys.Rev.D 16, 1248 (1977)].

[159] Coleman, S. R. and De Luccia, F. (1980). Gravitational Effects on and of Vacuum Decay. *Phys. Rev. D*, 21:3305.

[160] Contaldi, C., Hindmarsh, M., and Magueijo, J. (1999). The Power spectra of CMB and density fluctuations seeded by local cosmic strings. *Phys. Rev. Lett.*, 82:679–682.

[161] Cook, G. B. et al. (1998). Boosted three-dimensional black hole evolutions with singularity excision. *Phys. Rev. Lett.*, 80:2512–2516.

[162] Cook, W. G., Glushchenko, I. A., Ijjas, A., Pretorius, F., and Steinhardt, P. J. (2020). Supersmoothing through Slow Contraction. *Phys. Lett. B*, 808:135690.

[163] Copeland, E. J. and Kibble, T. W. B. (2010). Cosmic Strings and Superstrings. *Proc. Roy. Soc. Lond.*, A466:623–657.

[164] Corichi, A. and Karami, A. (2011). On the measure problem in slow roll inflation and loop quantum cosmology. *Phys. Rev.*, D83:104006.

[165] Corichi, A. and Sloan, D. (2014). Inflationary Attractors and their Measures. *Class. Quant. Grav.*, 31:062001.

[166] Cotner, E. and Kusenko, A. (2017a). Primordial black holes from scalar field evolution in the early universe. *Phys. Rev. D*, 96(10):103002.

[167] Cotner, E. and Kusenko, A. (2017b). Primordial black holes from supersymmetry in the early universe. *Phys. Rev. Lett.*, 119(3):031103.

[168] Cotner, E., Kusenko, A., Sasaki, M., and Takhistov, V. (2019). Analytic Description of Primordial Black Hole Formation from Scalar Field Fragmentation. *JCAP*, 10:077.

[169] Cotner, E., Kusenko, A., and Takhistov, V. (2018). Primordial Black Holes from Inflaton Fragmentation into Oscillons. *Phys. Rev. D*, 98(8):083513.

[170] Crawford, M. and Schramm, D. N. (1982). Spontaneous generation of density perturbations in the early universe. *Nature*, 298(5874):538–540.

[171] Croft, R., Helfer, T., Ge, B.-X., Radia, M., Evstafyeva, T., Lim, E. A., Sperhake, U., and Clough, K. (2022). The Gravitational Afterglow of Boson Stars.

[172] Damour, T. and Vilenkin, A. (2000). Gravitational wave bursts from cosmic strings. *Phys. Rev. Lett.*, 85:3761–3764.

[173] Damour, T. and Vilenkin, A. (2001). Gravitational wave bursts from cusps and kinks on cosmic strings. *Phys. Rev.*, D64:064008.

[174] Damour, T. and Vilenkin, A. (2005). Gravitational radiation from cosmic (super)strings: Bursts, stochastic background, and observational windows. *Phys. Rev.*, D71:063510.

[175] de Bernardis, P. et al. (2000). A Flat universe from high resolution maps of the cosmic microwave background radiation. *Nature*, 404:955–959.

[176] de Jong, E., Aurrekoetxea, J. C., and Lim, E. A. (2022). Primordial black hole formation with full numerical relativity. *JCAP*, 03(03):029.

[177] De Luca, V., Franciolini, G., and Riotto, A. (2021). NANOGrav Data Hints at Primordial Black Holes as Dark Matter. *Phys. Rev. Lett.*, 126(4):041303.

[178] Deng, H., Garriga, J., and Vilenkin, A. (2017). Primordial black hole and wormhole formation by domain walls. *JCAP*, 1704(04):050.

[179] Dietrich, T., Ossokine, S., and Clough, K. (2019). Full 3D numerical relativity simulations of neutron star–boson star collisions with BAM. *Class. Quant. Grav.*, 36(2):025002.

[180] Divakarla, A. K., Thrane, E., Lasky, P. D., and Whiting, B. F. (2019). Memory Effect or Cosmic String? Classifying Gravitational-Wave Bursts with Bayesian Inference.

[181] Dokuchaev, V., Eroshenko, Y., and Rubin, S. (2005). Quasars formation around clusters of primordial black holes. *Grav. Cosmol.*, 11:99–104.

[182] Dolgov, A., Kawasaki, M., and Kevlishvili, N. (2009). Inhomogeneous baryogenesis, cosmic antimatter, and dark matter. *Nuclear Physics B*, 807(1-2):229–250.

[183] Dolgov, A. and Postnov, K. (2020). Why the mean mass of primordial black hole distribution is close to $10M_{\odot}$.

[184] Dolgov, A. and Silk, J. (1993). Baryon isocurvature fluctuations at small scales and baryonic dark matter. *Phys. Rev. D*, 47:4244–4255.

[185] Domènech, G. and Pi, S. (2020). NANOGrav Hints on Planet-Mass Primordial Black Holes.

[186] Drew, A. and Shellard, E. P. S. (2019). Radiation from Global Topological Strings using Adaptive Mesh Refinement: Methodology and Massless Modes.

[187] Drew, A. L. (2021). *Cosmic String Radiation with Adaptive Mesh Refinement*. PhD thesis, Cambridge U.

[188] Durrer, R., Kunz, M., and Melchiorri, A. (1999). Cosmic microwave background anisotropies from scaling seeds: Global defect models. *Phys. Rev. D*, 59:123005.

[189] Dvali, G. R., Shafi, Q., and Solganik, S. (2001). D-brane inflation. In *4th European Meeting From the Planck Scale to the Electroweak Scale (Planck 2001) La Londe les Maures, Toulon, France, May 11-16, 2001*.

[190] East, W. E., Kleban, M., Linde, A., and Senatore, L. (2016). Beginning inflation in an inhomogeneous universe. *JCAP*, 1609(09):010.

[191] East, W. E. and Pretorius, F. (2013). Ultrarelativistic black hole formation. *Phys. Rev. Lett.*, 110(10):101101.

[192] East, W. E., Wojtak, R., and Pretorius, F. (2019). Einstein-Vlasov Calculations of Structure Formation. *Phys. Rev. D*, 100(10):103533.

[193] Easther, R., Price, L. C., and Rasero, J. (2014). Inflating an Inhomogeneous Universe. *JCAP*, 1408:041.

[194] Einstein, A. (1905). Zur elektrodynamik bewegter körper. *Annalen der physik*, 322(10):891–921.

[195] Einstein, A. (1916). Die grundlage der allgemeinen relativitätstheorie. *Annalen der Physik*, 354(7):769–822.

[196] Evans, C. R. and Coleman, J. S. (1994). Critical phenomena and self-similarity in the gravitational collapse of radiation fluid. *Phys. Rev. Lett.*, 72:1782–1785.

[197] Ezquiaga, J. M., Garcia-Bellido, J., and Ruiz Morales, E. (2018). Primordial Black Hole production in Critical Higgs Inflation. *Phys. Lett. B*, 776:345–349.

[198] Favata, M. (2010). The gravitational-wave memory effect. *Class. Quant. Grav.*, 27:084036.

[199] Feldman, H. A. and Brandenberger, R. H. (1989). Chaotic Inflation With Metric and Matter Perturbations. *Phys. Lett.*, B227:359–366.

[200] Figueras, P. and França, T. (2020). Gravitational Collapse in Cubic Horndeski Theories. *Class. Quant. Grav.*, 37(22):225009.

[201] Figueras, P. and França, T. (2021). Black Hole Binaries in Cubic Horndeski Theories.

[202] Figueras, P., Kunesch, M., Lehner, L., and Tunyasuvunakool, S. (2017). End Point of the Ultraspinning Instability and Violation of Cosmic Censorship. *Phys. Rev. Lett.*, 118(15):151103.

[203] Figueras, P., Kunesch, M., and Tunyasuvunakool, S. (2016). End Point of Black Ring Instabilities and the Weak Cosmic Censorship Conjecture. *Phys. Rev. Lett.*, 116(7):071102.

[204] Finn, K. (2020). Initial Conditions of Inflation in a Bianchi I Universe. *Phys. Rev. D*, 101(6):063512.

[205] Finn, K. and Karamitsos, S. (2019). Finite measure for the initial conditions of inflation. *Phys. Rev.*, D99(6):063515. [Erratum: Phys. Rev.D99,no.10,109901(2019)].

[206] Fort, J. and Vachaspati, T. (1993). Do global string loops collapse to form black holes? *Phys. Lett. B*, 311:41–46.

[207] Franche, P., Gwyn, R., Underwood, B., and Wissanji, A. (2010). Initial Conditions for Non-Canonical Inflation. *Phys. Rev.*, D82:063528.

[208] Franciolini, G., Baibhav, V., De Luca, V., Ng, K. K. Y., Wong, K. W. K., Berti, E., Pani, P., Riotto, A., and Vitale, S. (2021). Evidence for primordial black holes in LIGO/Virgo gravitational-wave data.

[209] Frolov, V. P., Israel, W., and Unruh, W. G. (1989). Gravitational fields of straight and circular cosmic strings: Relation between gravitational mass, angular deficit, and internal structure. *Phys. Rev. D*, 39:1084–1096.

[210] García-Bellido, J., Linde, A., and Wands, D. (1996). Density perturbations and black hole formation in hybrid inflation. *Phys. Rev. D*, 54:6040–6058.

[211] Garcia-Bellido, J., Rabadan, R., and Zamora, F. (2002). Inflationary scenarios from branes at angles. *JHEP*, 01:036.

[212] García-Bellido, J. and Ruiz Morales, E. (2017). Primordial black holes from single field models of inflation. *Physics of the Dark Universe*, 18:47–54.

[213] Garfinkle, D. (1985). General relativistic strings. *Phys. Rev. D*, 32:1323–1329.

[214] Garfinkle, D. (1990). Traveling waves in strongly gravitating cosmic strings. *Phys. Rev. D*, 41:1112–1115.

[215] Garfinkle, D., Lim, W. C., Pretorius, F., and Steinhardt, P. J. (2008). Evolution to a smooth universe in an ekpyrotic contracting phase with w $>$ 1. *Phys. Rev. D*, 78:083537.

[216] Garfinkle, D. and Mead, L. (2020). Cosmological initial data for numerical relativity. *Phys. Rev. D*, 102(4):044022.

[217] Garfinkle, D. and Vachaspati, T. (1987). Radiation From Kinky, Cuspless Cosmic Loops. *Phys. Rev.*, D36:2229.

[218] Garfinkle, D. and Vachaspati, T. (1988). FIELDS DUE TO KINKY, CUSPLESS, COSMIC LOOPS. *Phys. Rev.*, D37:257–262.

[219] Garfinkle, D. and Vachaspati, T. (1990). Cosmic string traveling waves. *Phys. Rev. D*, 42:1960–1963.

[220] Garriga, J. and Sakellariadou, M. (1993). Effects of friction on cosmic strings. *Phys. Rev.*, D48:2502–2515.

[221] Garriga, J., Vilenkin, A., and Zhang, J. (2016). Black holes and the multiverse. *JCAP*, 1602(02):064.

[222] Germani, C. and Musco, I. (2019). Abundance of Primordial Black Holes Depends on the Shape of the Inflationary Power Spectrum. *Phys. Rev. Lett.*, 122(14):141302.

[223] Geshnizjani, G. and Brandenberger, R. (2005). Back reaction of perturbations in two scalar field inflationary models. *JCAP*, 0504:006.

[224] Gibbons, G. W. and Hawking, S. W. (1977). Cosmological Event Horizons, Thermodynamics, and Particle Creation. *Phys. Rev.*, D15:2738–2751.

[225] Gibbons, G. W., Hawking, S. W., and Stewart, J. M. (1987). A Natural Measure on the Set of All Universes. *Nucl. Phys.*, B281:736.

[226] Gibbons, G. W. and Turok, N. (2008). The Measure Problem in Cosmology. *Phys. Rev.*, D77:063516.

[227] Goldwirth, D. S. and Piran, T. (1989). Spherical Inhomogeneous Cosmologies and Inflation. 1. Numerical Methods. *Phys. Rev.*, D40:3263.

[228] Goldwirth, D. S. and Piran, T. (1990). Inhomogeneity and the Onset of Inflation. *Phys. Rev. Lett.*, 64:2852–2855.

[229] Goldwirth, D. S. and Piran, T. (1992). Initial conditions for inflation. *Phys. Rept.*, 214:223–291.

[230] Goto, T. (1971). Relativistic quantum mechanics of one-dimensional mechanical continuum and subsidiary condition of dual resonance model. *Prog. Theor. Phys.*, 46:1560–1569.

[231] GRChombo (2018a). Black hole formation - cosmic string loop collapse. https://youtu.be/U5CkThsDU6w.

[232] GRChombo (2018b). Dispersion - cosmic string loop collapse in full gr. https://youtu.be/nHH3gTEjMPo.

[233] GRChombo (2020a). Coherent gravitational waveforms from cosmic string loops: Gw radiation. https://youtu.be/-dhYA2788LA.

[234] GRChombo (2020b). Coherent gravitational waveforms from cosmic string loops: Matter radiation. https://youtu.be/0sSH54gXu4U.

[235] GRChombo (2021a). Primordial black hole formation with full numerical relativity: accretion and direct collapse. https://youtu.be/fqEBlCybF8I.

[236] GRChombo (2021b). Primordial black hole formation with full numerical relativity: expansion and energy density evolution. https://youtu.be/4N5e2RnUkmU.

[237] Green, A. M. (2015). Primordial Black Holes: sirens of the early Universe. *Fundam. Theor. Phys.*, 178:129–149.

[238] Green, A. M. (2016). Microlensing and dynamical constraints on primordial black hole dark matter with an extended mass function. *Physical Review D*, 94(6).

[239] Green, A. M. and Kavanagh, B. J. (2021). Primordial Black Holes as a dark matter candidate. *J. Phys. G*, 48(4):4.

[240] Green, A. M. and Liddle, A. R. (1999). Critical collapse and the primordial black hole initial mass function. *Physical Review D*, 60(6).

[241] Green, A. M., Liddle, A. R., Malik, K. A., and Sasaki, M. (2004). A New calculation of the mass fraction of primordial black holes. *Phys. Rev. D*, 70:041502.

[242] Gregory, R. (1987). Gravitational stability of local strings. *Phys. Rev. Lett.*, 59:740–743.

[243] Gundlach, C. (1999). Critical phenomena in gravitational collapse. *Living Rev. Rel.*, 2:4.

[244] Guth, A. H. (1981). The Inflationary Universe: A Possible Solution to the Horizon and Flatness Problems. *Phys. Rev.*, D23:347–356.

[245] Hansen, R. N., Christensen, M., and Larsen, A. L. (2000). Cosmic string loops collapsing to black holes. *Int. J. Mod. Phys.*, A15:4433–4446.

[246] Harada, T. and Carr, B. J. (2005a). Growth of primordial black holes in a universe containing a massless scalar field. *Phys. Rev. D*, 71:104010.

[247] Harada, T. and Carr, B. J. (2005b). Upper limits on the size of a primordial black hole. *Phys. Rev. D*, 71:104009.

[248] Harada, T., Yoo, C.-M., and Kohri, K. (2013). Threshold of primordial black hole formation. *Phys. Rev. D*, 88(8):084051. [Erratum: Phys.Rev.D 89, 029903 (2014)].

[249] Harada, T., Yoo, C.-M., Kohri, K., and Nakao, K.-I. (2017). Spins of primordial black holes formed in the matter-dominated phase of the Universe. *Phys. Rev. D*, 96(8):083517. [Erratum: Phys.Rev.D 99, 069904 (2019)].

[250] Harada, T., Yoo, C.-M., Kohri, K., Nakao, K.-i., and Jhingan, S. (2016). Primordial black hole formation in the matter-dominated phase of the Universe. *Astrophys. J.*, 833(1):61.

[251] Hawke, I. and Stewart, J. M. (2002). The dynamics of primordial black-hole formation. *Classical and Quantum Gravity*, 19(14):3687–3707.

[252] Hawking, S. (1971). Gravitationally Collapsed Objects of Very Low Mass. *Monthly Notices of the Royal Astronomical Society*, 152(1):75–78.

[253] Hawking, S. (1989). Black Holes From Cosmic Strings. *Phys. Lett. B*, 231:237–239.

[254] Hawking, S. (1990). Gravitational radiation from collapsing cosmic string loops. *Physics Letters B*, 246(1):36 – 38.

[255] Hawking, S. W. (1974). Black hole explosions? *Nature*, 248(5443):30–31.

[256] Hawking, S. W. (1989). Black holes from cosmic strings. *Physics Letters B*, 231:237–239.

[257] Hawking, S. W. and Moss, I. G. (1982). Supercooled Phase Transitions in the Very Early Universe. *Phys. Lett.*, B110:35–38.

[258] Hawking, S. W., Moss, I. G., and Stewart, J. M. (1982a). Bubble collisions in the very early universe. *Phys. Rev. D*, 26:2681–2693.

[259] Hawking, S. W., Moss, I. G., and Stewart, J. M. (1982b). Bubble Collisions in the Very Early Universe. *Phys. Rev. D*, 26:2681.

[260] Hawking, S. W. and Page, D. N. (1988). How probable is inflation? *Nucl. Phys.*, B298:789–809.

[261] Hawkins, M. R. S. (1993). Gravitational microlensing, quasar variability and missing matter. *Nature*, 366(6452):242–245.

[262] Hawkins, M. R. S. (2020). The signature of primordial black holes in the dark matter halos of galaxies. *A&A*, 633:A107.

[263] Helfer, T. (2020). *Exotic Compact Objects in Numerical Relativity.* PhD thesis, King's Coll. London.

[264] Helfer, T., Aurrekoetxea, J. C., and Lim, E. A. (2019a). Cosmic String Loop Collapse in Full General Relativity. *Phys. Rev. D*, 99(10):104028.

[265] Helfer, T., Lim, E. A., Garcia, M. A. G., and Amin, M. A. (2019b). Gravitational Wave Emission from Collisions of Compact Scalar Solitons. *Phys. Rev. D*, 99(4):044046.

[266] Helfer, T., Marsh, D. J. E., Clough, K., Fairbairn, M., Lim, E. A., and Becerril, R. (2017). Black hole formation from axion stars. *JCAP*, 03:055.

[267] Hidalgo, C., De Santiago, J., German, G., Barbosa-Cendejas, N., and Ruiz-Luna, W. (2017). Collapse threshold for a cosmological Klein Gordon field. *Phys. Rev.*, D96(6):063504.

[268] Hilditch, D. (2013). An Introduction to Well-posedness and Free-evolution. *Int. J. Mod. Phys.*, A28:1340015.

[269] Hindmarsh, M. (1990). Gravitational radiation from kinky infinite strings. *Phys. Lett.*, B251:28–33.

[270] Hindmarsh, M., Lizarraga, J., Urrestilla, J., Daverio, D., and Kunz, M. (2017). Scaling from gauge and scalar radiation in Abelian Higgs string networks. *Phys. Rev. D*, 96(2):023525.

[271] Hindmarsh, M. B. and Kibble, T. W. B. (1995). Cosmic strings. *Rept. Prog. Phys.*, 58:477–562.

[272] Hodges, H. M. and Blumenthal, G. R. (1990). Arbitrariness of inflationary fluctuation spectra. *Phys. Rev. D*, 42:3329–3333.

[273] Hogan, C. J. (1984). MASSIVE BLACK HOLES GENERATED BY COSMIC STRINGS. *Phys. Lett.*, 143B:87–91.

[274] Hogan, C. J. and Rees, M. J. (1984). Gravitational interactions of cosmic strings. *Nature*, 311:109–113. [,128(1984)].

[275] Hui, L. (2021). Wave Dark Matter.

[276] Hui, L., Kabat, D., Li, X., Santoni, L., and Wong, S. S. C. (2019). Black Hole Hair from Scalar Dark Matter. *JCAP*, 06:038.

[277] Hübner, M., Talbot, C., Lasky, P. D., and Thrane, E. (2020). Thanks for the memory: measuring gravitational-wave memory in the first LIGO/Virgo gravitational-wave transient catalog. *Phys. Rev.*, D101(2):023011.

[278] Ijjas, A., Cook, W. G., Pretorius, F., Steinhardt, P. J., and Davies, E. Y. (2020). Robustness of slow contraction to cosmic initial conditions. *JCAP*, 08:030.

[279] Ijjas, A., Pretorius, F., Steinhardt, P. J., and Sullivan, A. P. (2021a). The effects of multiple modes and reduced symmetry on the rapidity and robustness of slow contraction. *Phys. Lett. B*, 820:136490.

[280] Ijjas, A. and Steinhardt, P. J. (2018). Bouncing Cosmology made simple. *Class. Quant. Grav.*, 35(13):135004.

[281] Ijjas, A., Sullivan, A. P., Pretorius, F., Steinhardt, P. J., and Cook, W. G. (2021b). Ultralocality and slow contraction. *JCAP*, 06:013.

[282] Inomata, K., Kawasaki, M., Mukaida, K., Tada, Y., and Yanagida, T. T. (2017). Inflationary primordial black holes as all dark matter. *Physical Review D*, 96(4).

[283] Israel, W. (1966). Singular hypersurfaces and thin shells in general relativity. *Nuovo Cim. B*, 44S10:1. [Erratum: Nuovo Cim.B 48, 463 (1967)].

[284] Ivanov, P., Naselsky, P., and Novikov, I. (1994). Inflation and primordial black holes as dark matter. *Phys. Rev. D*, 50:7173–7178.

[285] Jacobs, L. and Rebbi, C. (1979). Interaction Energy of Superconducting Vortices. *Phys. Rev. B*, 19:4486–4494.

[286] James-Turner, C., Weil, D. P. B., Green, A. M., and Copeland, E. J. (2019). Constraints on the cosmic string loop collapse fraction from Primordial Black Holes.

[287] Jeannerot, R., Rocher, J., and Sakellariadou, M. (2003). How generic is cosmic string formation in SUSY GUTs. *Phys. Rev.*, D68:103514.

[288] Jenkins, A. and Sakellariadou, M. (2020). Primordial black holes from cusp collapse on cosmic strings.

[289] Jenkins, A. C. and Sakellariadou, M. (2018). Anisotropies in the stochastic gravitational-wave background: Formalism and the cosmic string case. *Phys. Rev.*, D98(6):063509.

[290] Jenkins, A. C. and Sakellariadou, M. (2021). Nonlinear gravitational-wave memory from cusps and kinks on cosmic strings. *Class. Quant. Grav.*, 38(16):165004.

[291] Jensen, L. G. and Stein-Schabes, J. A. (1987). Is Inflation Natural? *Phys. Rev.*, D35:1146.

[292] Joana, C. (2022). Gravitational dynamics in Higgs inflation: Preinflation and preheating with an auxiliary field.

[293] Joana, C. and Clesse, S. (2021). Inhomogeneous preinflation across Hubble scales in full general relativity. *Phys. Rev. D*, 103(8):083501.

[294] Jones, N. T., Stoica, H., and Tye, S. H. H. (2002). Brane interaction as the origin of inflation. *JHEP*, 07:051.

[295] Jones, N. T., Stoica, H., and Tye, S. H. H. (2003). The Production, spectrum and evolution of cosmic strings in brane inflation. *Phys. Lett.*, B563:6–14.

[296] Kachru, S., Kallosh, R., Linde, A. D., Maldacena, J. M., McAllister, L. P., and Trivedi, S. P. (2003). Towards inflation in string theory. *JCAP*, 0310:013.

[297] Kallosh, R. and Linde, A. (2013). Universality Class in Conformal Inflation. *JCAP*, 1307:002.

[298] Kallosh, R. and Linde, A. (2019). On hilltop and brane inflation after Planck.

[299] Kallosh, R., Linde, A., and Roest, D. (2013). Superconformal Inflationary α-Attractors. *JHEP*, 11:198.

[300] Kannike, K., Marzola, L., Raidal, M., and Veermäe, H. (2017). Single field double inflation and primordial black holes. *Journal of Cosmology and Astroparticle Physics*, 2017(09):020–020.

[301] Khlopov, M., Konoplich, R., Rubin, S. G., and Sakharov, A. S. (1998). Formation of black holes in first order phase transitions.

[302] Khlopov, M., Konoplich, R., Rubin, S. G., and Sakharov, A. S. (1999). First order phase transitions as a source of black holes in the early universe. *Grav. Cosmol.*, 2:S1.

[303] Khlopov, M., Konoplich, R., Rubin, S. G., and Sakharov, A. S. (2000). First-order phase transitions as a source of black holes in the early universe. *Grav. Cosmol.*, 6:153–156.

[304] Khlopov, M. and Polnarev, A. (1980). Primordial Black Holes As A Cosmological Test Of Grand Unification. *Phys. Lett.*, B97:383–387.

[305] Khlopov, M. Y., Malomed, B. A., and Zeldovich, Y. B. (1985). Gravitational instability of scalar fields and formation of primordial black holes. *Monthly Notices of the Royal Astronomical Society*, 215(4):575–589.

[306] Khoury, J., Ovrut, B. A., Seiberg, N., Steinhardt, P. J., and Turok, N. (2002). From big crunch to big bang. *Phys. Rev. D*, 65:086007.

[307] Khoury, J., Ovrut, B. A., Steinhardt, P. J., and Turok, N. (2001). The Ekpyrotic universe: Colliding branes and the origin of the hot big bang. *Phys. Rev. D*, 64:123522.

[308] Kibble, T. W. B. (1976). Topology of Cosmic Domains and Strings. *J. Phys.*, A9:1387–1398.

[309] Kibble, T. W. B. (1985). Evolution of a system of cosmic strings. *Nucl. Phys. B*, 252:227. [Erratum: Nucl.Phys.B 261, 750 (1985)].

[310] Kibble, T. W. B. and Turok, N. (1982). Selfintersection of Cosmic Strings. *Phys. Lett. B*, 116:141–143.

[311] Kiraly, P., Szabelski, J., Wdowczyk, J., and Wolfendale, A. W. (1981a). Antiprotons in the Cosmic Radiation. *Nature*, 293:120–122.

[312] Kiraly, P., Szabelski, J., Wdowczyk, J., and Wolfendale, A. W. (1981b). Antiprotons in the cosmic radiation. *Nature*, 293(5828):120–122.

[313] Kitada, Y. and Maeda, K.-i. (1992). Cosmic no hair theorem in power law inflation. *Phys. Rev.*, D45:1416–1419.

[314] Kitada, Y. and Maeda, K.-i. (1993). Cosmic no hair theorem in homogeneous space-times. 1. Bianchi models. *Class. Quant. Grav.*, 10:703–734.

[315] Kitajima, N. and Takahashi, F. (2020). Primordial Black Holes from QCD Axion Bubbles. *JCAP*, 11:060.

[316] Kleban, M. and Senatore, L. (2016). Inhomogeneous Anisotropic Cosmology.

[317] Kodama, H., Sasaki, M., and Sato, K. (1982). Abundance of Primordial Holes Produced by Cosmological First-Order Phase Transition. *Progress of Theoretical Physics*, 68(6):1979–1998.

[318] Kohri, K. and Terada, T. (2021). Solar-Mass Primordial Black Holes Explain NANOGrav Hint of Gravitational Waves. *Phys. Lett. B*, 813:136040.

[319] Kokkotas, K. D. and Schmidt, B. G. (1999). Quasinormal modes of stars and black holes. *Living Rev. Rel.*, 2:2.

[320] Kokubu, T., Kyutoku, K., Kohri, K., and Harada, T. (2018). Effect of Inhomogeneity on Primordial Black Hole Formation in the Matter Dominated Era. *Phys. Rev. D*, 98(12):123024.

[321] Kolb, E. W. and Turner, M. S. (1990). *The early universe.* Addison-Wesley.

[322] Konoplich, R., Rubin, S. G., Sakharov, A. S., and Khlopov, M. (1999). Formation of black holes in first-order phase transitions as a cosmological test of symmetry-breaking mechanisms. *Phys. atom. Nucl.*, 62:1593–1600.

[323] Kozaczuk, J., Lin, T., and Villarama, E. (2021). Signals of primordial black holes at gravitational wave interferometers.

[324] Kunesch, M. (2018). *Numerical simulations of instabilities in general relativity.* PhD thesis, Cambridge U., DAMTP.

[325] Kurki-Suonio, H., Laguna, P., and Matzner, R. A. (1993). Inhomogeneous inflation: Numerical evolution. *Phys. Rev.*, D48:3611–3624.

[326] Kurki-Suonio, H., Matzner, R. A., Centrella, J., and Wilson, J. R. (1987). Inflation From Inhomogeneous Initial Data in a One-dimensional Back Reacting Cosmology. *Phys. Rev.*, D35:435–448.

[327] Laguna, P., Kurki-Suonio, H., and Matzner, R. A. (1991). Inhomogeneous inflation: The Initial value problem. *Phys. Rev.*, D44:3077–3086.

[328] Laguna, P. and Matzner, R. A. (1989). PEELING U(1) GAUGE COSMIC STRINGS. *Phys. Rev. Lett.*, 62:1948–1951.

[329] Laguna, P. and Matzner, R. A. (1990). Numerical simulation of bosonic superconducting string interactions. *Phys. Rev. D*, 41:1751–1763.

[330] Laguna-Castillo, P. and Matzner, R. A. (1987). Coupled field solutions for u(1)-gauge cosmic strings. *Phys. Rev. D*, 36:3663–3673.

[331] Leach, S. M., Grivell, I. J., and Liddle, A. R. (2000). Black hole constraints on the running mass inflation model. *Phys. Rev. D*, 62:043516.

[332] Lehoucq, R., Casse, M., Casandjian, J. M., and Grenier, I. (2009). New constraints on the primordial black hole number density from Galactic gamma-ray astronomy. *Astron. Astrophys.*, 502:37.

[333] Linde, A. D. (1982). A New Inflationary Universe Scenario: A Possible Solution of the Horizon, Flatness, Homogeneity, Isotropy and Primordial Monopole Problems. *Phys. Lett.*, B108:389–393.

[334] Linet, B. (1987). A vortex-line model for infinite straight cosmic strings. *Physics Letters A*, 124(4):240 – 242.

[335] Liu, J., Guo, Z.-K., and Cai, R.-G. (2020). Primordial Black Holes from Cosmic Domain Walls. *Phys. Rev.*, D101(2):023513.

[336] Lizarraga, J., Urrestilla, J., Daverio, D., Hindmarsh, M., and Kunz, M. (2016). New CMB constraints for Abelian Higgs cosmic strings. *JCAP*, 1610(10):042.

[337] Lorenz, L., Ringeval, C., and Sakellariadou, M. (2010). Cosmic string loop distribution on all length scales and at any redshift. *JCAP*, 1010:003.

[338] MacGibbon, J. H., Brandenberger, R. H., and Wichoski, U. F. (1998). Limits on black hole formation from cosmic string loops. *Phys. Rev.*, D57:2158–2165.

[339] MacGibbon, J. H. and Carr, B. J. (1991). Cosmic rays from primordial black holes. *Astrophys. J.*, 371:447–469.

[340] Maggiore, M. and Press, O. U. (2008). *Gravitational Waves: Volume 1: Theory and Experiments*. Gravitational Waves. OUP Oxford.

[341] Maleknejad, A. and Sheikh-Jabbari, M. M. (2012). Revisiting Cosmic No-Hair Theorem for Inflationary Settings. *Phys. Rev.*, D85:123508.

[342] Marolf, D. and Morrison, I. A. (2011). The IR stability of de Sitter QFT: results at all orders. *Phys. Rev.*, D84:044040.

[343] Marozzi, G., Vacca, G. P., and Brandenberger, R. H. (2013). Cosmological Backreaction for a Test Field Observer in a Chaotic Inflationary Model. *JCAP*, 1302:027.

[344] Marsh, M. C. D., Barrow, J. D., and Ganguly, C. (2018). Inhomogeneous Initial Data and Small-Field Inflation. *JCAP*, 1805(05):026.

[345] Martin, J., Papanikolaou, T., Pinol, L., and Vennin, V. (2020). Metric preheating and radiative decay in single-field inflation. *Journal of Cosmology and Astroparticle Physics*, 2020(05):003–003.

[346] Martin, J., Ringeval, C., and Vennin, V. (2014). Encyclopædia Inflationaris. *Phys. Dark Univ.*, 5-6:75–235.

[347] Martins, C. J. A. P. and Shellard, E. P. S. (1996). Quantitative string evolution. *Phys. Rev. D*, 54:2535–2556.

[348] Martins, C. J. A. P. and Shellard, E. P. S. (2002). Extending the velocity dependent one scale string evolution model. *Phys. Rev. D*, 65:043514.

[349] Matsunami, D., Pogosian, L., Saurabh, A., and Vachaspati, T. (2019). Decay of Cosmic String Loops Due to Particle Radiation. *Phys. Rev. Lett.*, 122(20):201301.

[350] Matzner, R. A. (1988). Interaction of U(1) cosmic strings: Numerical intercommutation. *Comput. Phys.*, 2(5):51–64.

[351] Meszaros, P. (1975). Primeval black holes and galaxy formation. *Astron. Astrophys.*, 38:5–13.

[352] Moore, J. N. and Shellard, E. P. S. (1998). On the evolution of Abelian Higgs string networks.

[353] Moore, J. N., Shellard, E. P. S., and Martins, C. J. A. P. (2002). On the evolution of Abelian-Higgs string networks. *Phys. Rev.*, D65:023503.

[354] Moss, I. G. (1994). Singularity formation from colliding bubbles. *Phys. Rev. D*, 50:676–681.

[355] Muia, F., Cicoli, M., Clough, K., Pedro, F., Quevedo, F., and Vacca, G. P. (2019). The Fate of Dense Scalar Stars. *JCAP*, 07:044.

[356] Mukhanov, V. (2013). Quantum Cosmological Perturbations: Predictions and Observations. *Eur. Phys. J.*, C73:2486.

[357] Mukhanov, V. (2015). Inflation without Selfreproduction. *Fortsch. Phys.*, 63:36–41.

[358] Muller, V., Schmidt, H. J., and Starobinsky, A. A. (1988). The Stability of the De Sitter Space-time in Fourth Order Gravity. *Phys. Lett.*, B202:198–200.

[359] Muller, V., Schmidt, H. J., and Starobinsky, A. A. (1990). Power law inflation as an attractor solution for inhomogeneous cosmological models. *Class. Quant. Grav.*, 7:1163–1168.

[360] Musco, I. (2019a). Threshold for primordial black holes: Dependence on the shape of the cosmological perturbations. *Phys. Rev. D*, 100(12):123524.

[361] Musco, I. (2019b). Threshold for primordial black holes: Dependence on the shape of the cosmological perturbations. *Phys. Rev. D*, 100:123524.

[362] Musco, I., De Luca, V., Franciolini, G., and Riotto, A. (2021). Threshold for primordial black holes. II. A simple analytic prescription. *Phys. Rev. D*, 103(6):063538.

[363] Musco, I. and Miller, J. C. (2013). Primordial black hole formation in the early universe: critical behaviour and self-similarity. *Class. Quant. Grav.*, 30:145009.

[364] Musco, I., Miller, J. C., and Rezzolla, L. (2005). Computations of primordial black hole formation. *Class. Quant. Grav.*, 22:1405–1424.

[365] Nadezhin, D. K., Novikov, I. D., and Polnarev, A. G. (1978). The hydrodynamics of primordial black hole formation. *Soviet Astronomy*, 22:129–138.

[366] Nagasawa, M. (2005). Primordial black hole formation by stabilized embedded strings in the early universe. *General Relativity and Gravitation*, 37(9):1635–1649.

[367] Nagasawa, M. and Yokoyama, J. (1995). Numerical analysis of the dynamics of a cosmic string loop as a vortex. *Phys. Lett.*, B345:416–421.

[368] Nakama, T., Harada, T., Polnarev, A. G., and Yokoyama, J. (2014). Identifying the most crucial parameters of the initial curvature profile for primordial black hole formation. *JCAP*, 01:037.

[369] Nakamura, T. and Oohara, K.-i. (1998). A Way to 3-D numerical relativity: Coalescing binary neutron stars. In *Numerical Astrophysics 1998 (NAP 98)*.

[370] Nambu, Y. (1969). Quark model and the factorization of the Veneziano amplitude.

[371] Nazari, Z., Cicoli, M., Clough, K., and Muia, F. (2021). Oscillon collapse to black holes. *JCAP*, 05:027.

[372] Newman, E. and Penrose, R. (1962). An Approach to gravitational radiation by a method of spin coefficients. *J. Math. Phys.*, 3:566–578.

[373] Ng, K. K. Y., Chen, S., Goncharov, B., Dupletsa, U., Borhanian, S., Branchesi, M., Harms, J., Maggiore, M., Sathyaprakash, B. S., and Vitale, S. (2021). On the single-event-based identification of primordial black hole mergers at cosmological distances.

[374] Niemeyer, J. C. (1998). Numerical investigation of the threshold for primordial black hole formation. In *3rd International Symposium on Sources and Detection of Dark Matter in the Universe (DM 98)*.

[375] Niemeyer, J. C. and Jedamzik, K. (1998). Near-critical gravitational collapse and the initial mass function of primordial black holes. *Phys. Rev. Lett.*, 80:5481–5484.

[376] Niemeyer, J. C. and Jedamzik, K. (1999). Dynamics of primordial black hole formation. *Phys. Rev. D*, 59:124013.

[377] Novikov, I. D. and Polnarev, A. G. (1980). The Hydrodynamics of Primordial Black Hole Formation - Dependence on the Equation of State. *Soviet Astronomy*, 24:147–151.

[378] Olum, K. D. and Blanco-Pillado, J. J. (1999). Field theory simulation of Abelian Higgs cosmic string cusps. *Phys. Rev.*, D60:023503.

[379] Olum, K. D. and Blanco-Pillado, J. J. (2000). Radiation from cosmic string standing waves. *Phys. Rev. Lett.*, 84:4288–4291.

[380] Olum, K. D. and Vanchurin, V. (2007). Cosmic string loops in the expanding Universe. *Phys. Rev. D*, 75:063521.

[381] Ott, C. (2009). The Gravitational Wave Signature of Core-Collapse Supernovae. *Class. Quant. Grav.*, 26:063001.

[382] Page, D. N. and Hawking, S. W. (1976). Gamma rays from primordial black holes. *Astrophys. J.*, 206:1–7.

[383] Palenzuela, C., Lehner, L., and Yoshida, S. (2010). Understanding possible electromagnetic counterparts to loud gravitational wave events: Binary black hole effects on electromagnetic fields. *Phys. Rev.*, D81:084007.

[384] Pen, U.-L., Seljak, U., and Turok, N. (1997). Power spectra in global defect theories of cosmic structure formation. *Phys. Rev. Lett.*, 79:1611–1614.

[385] Pen, U.-L., Spergel, D. N., and Turok, N. (1994). Cosmic structure formation and microwave anisotropies from global field ordering. *Phys. Rev. D*, 49:692–729.

[386] Penrose, R. (1989). Difficulties with inflationary cosmology. *Annals N. Y. Acad. Sci.*, 571:249–264.

[387] Pfeiffer, H. P. and York, Jr., J. W. (2005). Uniqueness and non-uniqueness in the Einstein constraints. *Phys. Rev. Lett.*, 95:091101.

[388] Pogosian, L., Tye, S. H. H., Wasserman, I., and Wyman, M. (2003). Observational constraints on cosmic string production during brane inflation. *Phys. Rev.*, D68:023506. [Erratum: Phys. Rev.D73,089904(2006)].

[389] Pogosian, L. and Vachaspati, T. (1999). Cosmic microwave background anisotropy from wiggly strings. *Phys. Rev. D*, 60:083504.

[390] Pogosian, L. and Wyman, M. (2008). B-modes from cosmic strings. *Phys. Rev. D*, 77:083509.

[391] Pogosian, L., Wyman, M. C., and Wasserman, I. (2004). Observational constraints on cosmic strings: Bayesian analysis in a three dimensional parameter space. *JCAP*, 09:008.

[392] Polchinski, J. (2004). Introduction to cosmic F- and D-strings. pages 229–253.

[393] Polnarev, A. and Zembowicz, R. (1991). Formation of Primordial Black Holes by Cosmic Strings. *Phys. Rev. D*, 43:1106–1109.

[394] Polnarev, A. G. and Musco, I. (2007). Curvature profiles as initial conditions for primordial black hole formation. *Class. Quant. Grav.*, 24:1405–1432.

[395] Polyakov, A. M. (2010). Decay of Vacuum Energy. *Nucl. Phys.*, B834:316–329.

[396] Pretorius, F. (2005a). Evolution of binary black hole spacetimes. *Phys. Rev. Lett.*, 95:121101.

[397] Pretorius, F. (2005b). Evolution of binary black-hole spacetimes. *Phys. Rev. Lett.*, 95:121101.

[398] Quashnock, J. M. and Spergel, D. N. (1990). Gravitational Selfinteractions of Cosmic Strings. *Phys. Rev.*, D42:2505–2520.

[399] Radia, M., Sperhake, U., Berti, E., and Croft, R. (2021a). Anomalies in the gravitational recoil of eccentric black-hole mergers with unequal mass ratios. *Phys. Rev. D*, 103(10):104006.

[400] Radia, M., Sperhake, U., Drew, A., Clough, K., Figueras, P., Lim, E. A., Ripley, J. L., Aurrekoetxea, J. C., França, T., and Helfer, T. (2021b). Lessons for adaptive mesh refinement in numerical relativity.

[401] Randall, L., Soljačić, M., and Guth, A. H. (1996). Supernatural inflation: inflation from supersymmetry with no (very) small parameters. *Nuclear Physics B*, 472(1):377–405.

[402] Remmen, G. N. and Carroll, S. M. (2013). Attractor Solutions in Scalar-Field Cosmology. *Phys. Rev.*, D88:083518.

[403] Remmen, G. N. and Carroll, S. M. (2014). How Many e-Folds Should We Expect from High-Scale Inflation? *Phys. Rev.*, D90(6):063517.

[404] Ricotti, M., Ostriker, J. P., and Mack, K. J. (2008). Effect of Primordial Black Holes on the Cosmic Microwave Background and Cosmological Parameter Estimates. *Astrophys. J.*, 680:829.

[405] Ringeval, C., Sakellariadou, M., and Bouchet, F. (2007). Cosmological evolution of cosmic string loops. *JCAP*, 0702:023.

[406] Ringeval, C. and Suyama, T. (2017). Stochastic gravitational waves from cosmic string loops in scaling. *JCAP*, 1712:027.

[407] Robbins, K. W. and Olum, K. D. (2019). Backreaction on an infinite helical cosmic string. *Phys. Rev. D*, 100(10):103512.

[408] Roest, D. (2014). Universality classes of inflation. *JCAP*, 1401:007.

[409] Rubin, S., Khlopov, M., and Sakharov, A. (2000). Primordial black holes from nonequilibrium second order phase transition. *Grav. Cosmol.*, 6:51–58.

[410] Rubin, S., Sakharov, A., and Khlopov, M. (2001). The formation of primary galactic nuclei during phase transitions in the early universe. *J. Exp. Theor. Phys.*, 91:921–929.

[411] Saini, A. and Stojkovic, D. (2018). Modified hoop conjecture in expanding spacetimes and primordial black hole production in FRW universe. *JCAP*, 05:071.

[412] Saito, R., Yokoyama, J., and Nagata, R. (2008). Single-field inflation, anomalous enhancement of superhorizon fluctuations, and non-Gaussianity in primordial black hole formation. *JCAP*, 06:024.

[413] Sakellariadou, M. (1990). Gravitational waves emitted from infinite strings. *Phys. Rev.*, D42:354–360. [Erratum: Phys. Rev.D43,4150(1991)].

[414] Saurabh, A., Vachaspati, T., and Pogosian, L. (2020). Decay of Cosmic Global String Loops. *Phys. Rev. D*, 101(8):083522.

[415] Schiffrin, J. S. and Wald, R. M. (2012). Measure and Probability in Cosmology. *Phys. Rev.*, D86:023521.

[416] Schwarzschild, K. (1916). Über das Gravitationsfeld eines Massenpunktes nach der Einsteinschen Theorie. *Sitzungsberichte der Königlich Preußischen Akademie der Wissenschaften (Berlin*, pages 189–196.

[417] Seidel, E. and Suen, W.-M. (1992). Towards a singularity proof scheme in numerical relativity. *Phys. Rev. Lett.*, 69:1845–1848.

[418] Shellard, E. P. S. (1987). Cosmic String Interactions. *Nucl. Phys. B*, 283:624–656.

[419] Shellard, E. P. S. (1992). The numerical study of topological defects. In D'Inverno, R., editor, *Approaches to Numerical Relativity*, pages 308–334.

[420] Shibata, M. (1999). Fully general relativistic simulation of merging binary clusters: Spatial gauge condition. *Prog. Theor. Phys.*, 101:1199–1233.

[421] Shibata, M. and Nakamura, T. (1995). Evolution of three-dimensional gravitational waves: Harmonic slicing case. *Phys.Rev.*, D52:5428–5444.

[422] Shibata, M. and Sasaki, M. (1999). Black hole formation in the friedmann universe: Formulation and computation in numerical relativity. *Physical Review D*, 60:084002.

[423] Siemens, X., Creighton, J., Maor, I., Ray Majumder, S., Cannon, K., and Read, J. (2006). Gravitational wave bursts from cosmic (super)strings: Quantitative analysis and constraints. *Phys. Rev.*, D73:105001.

[424] Silverstein, E. and Westphal, A. (2008). Monodromy in the CMB: Gravity Waves and String Inflation. *Phys. Rev.*, D78:106003.

[425] Smarr, L. L., Epstein, R., and Clark, J. P. A. (1979). *Sources of gravitational radiation. Proceedings of the Battelle Seattle workshop, July 24 - August 4, 1978.*

[426] Sperhake, U., Cardoso, V., Ott, C. D., Schnetter, E., and Witek, H. (2011). Collisions of unequal mass black holes and the point particle limit. *Phys. Rev. D*, 84:084038.

[427] Sperhake, U., Cardoso, V., Pretorius, F., Berti, E., and Gonzalez, J. A. (2008). The High-energy collision of two black holes. *Phys. Rev. Lett.*, 101:161101.

[428] Starobinsky, A. (1982). Dynamics of phase transition in the new inflationary universe scenario and generation of perturbations. *Physics Letters B*, 117(3):175 – 178.

[429] Starobinsky, A. A. (1980). A New Type of Isotropic Cosmological Models Without Singularity. *Phys. Lett.*, B91:99–102.

[430] Starobinsky, A. A. (1983). Isotropization of arbitrary cosmological expansion given an effective cosmological constant. *JETP Lett.*, 37:66–69.

[431] Taruya, A. (1999). Parametric amplification of density perturbations in the oscillating inflation model. *Physical Review D*, 59(10).

[432] Thornburg, J. (1987). Coordinates and boundary conditions for the general relativistic initial data problem. *Classical and Quantum Gravity*, 4(5):1119–1131.

[433] Thornburg, J. (2004). A Fast apparent horizon finder for three-dimensional Cartesian grids in numerical relativity. *Class. Quant. Grav.*, 21:743–766.

[434] Thorne, K. S. (1992). Gravitational-wave bursts with memory: The christodoulou effect. *Phys. Rev. D*, 45:520–524.

[435] Traykova, D., Clough, K., Helfer, T., Ferreira, P. G., Berti, E., and Hui, L. (2021). Dynamical friction from scalar dark matter in the relativistic regime.

[436] Tsamis, N. C. and Woodard, R. P. (1993). Relaxing the cosmological constant. *Phys. Lett.*, B301:351–357.

[437] Tunyasuvunakool, S. (2017). *Applications of Numerical Relativity Beyond Astrophysics*. PhD thesis, Cambridge U.

[438] Turok, N. and Brandenberger, R. H. (1986). Cosmic Strings and the Formation of Galaxies and Clusters of Galaxies. *Phys. Rev. D*, 33:2175.

[439] Vachaspati, T. (1986). Cosmic Strings and the Large-Scale Structure of the Universe. *Phys. Rev. Lett.*, 57:1655–1657.

[440] Vachaspati, T. (1987). Gravity of Cosmic Loops. *Phys. Rev.*, D35:1767–1775.

[441] Vachaspati, T. and Trodden, M. (1999). Causality and cosmic inflation. *Phys. Rev.*, D61:023502.

[442] Vachaspati, T. and Vilenkin, A. (1984). Formation and Evolution of Cosmic Strings. *Phys. Rev. D*, 30:2036.

[443] Vachaspati, T. and Vilenkin, A. (1985). Gravitational Radiation from Cosmic Strings. *Phys. Rev.*, D31:3052.

[444] Vachaspati, T. and Vilenkin, A. (1991). Large scale structure from wiggly cosmic strings. *Phys. Rev. Lett.*, 67:1057–1061.

[445] van Meter, J. R., Baker, J. G., Koppitz, M., and Choi, D.-I. (2006). How to move a black hole without excision: Gauge conditions for the numerical evolution of a moving puncture. *Phys. Rev.*, D73:124011.

[446] Vanchurin, V., Olum, K. D., and Vilenkin, A. (2006). Scaling of cosmic string loops. *Phys. Rev. D*, 74:063527.

[447] Vaskonen, V. and Veermäe, H. (2021). Did NANOGrav see a signal from primordial black hole formation? *Phys. Rev. Lett.*, 126(5):051303.

[448] Vilenkin, A. (1981a). Cosmic Strings. *Phys. Rev.*, D24:2082–2089.

[449] Vilenkin, A. (1981b). Cosmological Density Fluctuations Produced by Vacuum Strings. *Phys. Rev. Lett.*, 46:1169–1172. [Erratum: Phys.Rev.Lett. 46, 1496 (1981)].

[450] Vilenkin, A. (1981c). Gravitational Field of Vacuum Domain Walls and Strings. *Phys. Rev. D*, 23:852–857.

[451] Vilenkin, A. (1981d). Gravitational radiation from cosmic strings. *Phys. Lett.*, 107B:47–50.

[452] Vilenkin, A. (1984). Cosmic strings as gravitational lenses. *Astrophys. J.*, 282:L51–L53.

[453] Vilenkin, A. (1985). Cosmic Strings and Domain Walls. *Phys. Rept.*, 121:263–315.

[454] Vilenkin, A. and Shellard, E. P. S. (2000). *Cosmic Strings and Other Topological Defects*. Cambridge University Press.

[455] Vincent, G., Antunes, N. D., and Hindmarsh, M. (1998). Numerical simulations of string networks in the Abelian Higgs model. *Phys. Rev. Lett.*, 80:2277–2280.

[456] Vincent, G. R., Hindmarsh, M., and Sakellariadou, M. (1997). Scaling and small scale structure in cosmic string networks. *Phys. Rev. D*, 56:637–646.

[457] Wachter, J. M. and Olum, K. D. (2017a). Gravitational backreaction on piecewise linear cosmic string loops. *Phys. Rev. D*, 95(2):023519.

[458] Wachter, J. M. and Olum, K. D. (2017b). Gravitational smoothing of kinks on cosmic string loops. *Phys. Rev. Lett.*, 118(5):051301. [Erratum: Phys.Rev.Lett. 121, 149901 (2018)].

[459] Wald, R. M. (1983). Asymptotic behavior of homogeneous cosmological models in the presence of a positive cosmological constant. *Phys. Rev.*, D28:2118–2120.

[460] Walsh, D. M. (2007). Non-uniqueness in conformal formulations of the Einstein constraints. *Class. Quant. Grav.*, 24:1911–1926.

[461] Wang, Z., Helfer, T., Clough, K., and Berti, E. (2022). Superradiance in massive vector fields with spatially varying mass.

[462] Wichoski, U. F., MacGibbon, J. H., and Brandenberger, R. H. (1998). Astrophysical constraints on primordial black hole formation from collapsing cosmic strings. *Phys. Rept.*, 307:191–196.

[463] Widdicombe, J. (2020). *Numerical General Relativity and Beyond: Formation of Relativistic Axion Stars, Boosting and Colliding Oscillotons, and Gravitational Collapse in Khronometric Theory*. PhD thesis, King's Coll. London.

[464] Widdicombe, J. Y., Helfer, T., and Lim, E. A. (2020). Black hole formation in relativistic Oscillaton collisions. *JCAP*, 01:027.

[465] Widdicombe, J. Y., Helfer, T., Marsh, D. J. E., and Lim, E. A. (2018). Formation of Relativistic Axion Stars. *JCAP*, 10:005.

[466] Witten, E. (1985). Cosmic Superstrings. *Phys. Lett.*, 153B:243–246.

[467] Wright, E. L. (1996). On the density of pbh's in the galactic halo. *Astrophys. J.*, 459:487.

[468] Wu, Z.-C. (1983). GRAVITATIONAL EFFECTS IN BUBBLE COLLISIONS. *Phys. Rev. D*, 28:1898–1906.

[469] Wyman, M., Pogosian, L., and Wasserman, I. (2005). Bounds on cosmic strings from WMAP and SDSS. *Phys. Rev. D*, 72:023513. [Erratum: Phys.Rev.D 73, 089905 (2006)].

[470] Xue, B., Garfinkle, D., Pretorius, F., and Steinhardt, P. J. (2013). Nonperturbative analysis of the evolution of cosmological perturbations through a nonsingular bounce. *Phys. Rev. D*, 88:083509.

[471] Yoo, C.-M., Harada, T., and Okawa, H. (2020). Threshold of Primordial Black Hole Formation in Nonspherical Collapse. *Phys. Rev. D*, 102(4):043526.

[472] Yoo, C.-M., Ikeda, T., and Okawa, H. (2019). Gravitational Collapse of a Massless Scalar Field in a Periodic Box. *Class. Quant. Grav.*, 36(7):075004.

[473] York, Jr., J. W. (1978). Kinematics and Dynamics of General Relativity. In *Workshop on Sources of Gravitational Radiation*.

[474] Zel'dovich, Y. B. and Novikov, I. D. (1967). The Hypothesis of Cores Retarded during Expansion and the Hot Cosmological Model. *Soviet Astronomy*, 10:602.

[475] Zel'dovich, Y. B. and Polnarev, A. G. (1974). Radiation of gravitational waves by a cluster of superdense stars. *Sov. Astron.*, 18:17.

[476] Zilhão, M., Witek, H., and Cardoso, V. (2015). Nonlinear interactions between black holes and Proca fields. *Class. Quant. Grav.*, 32:234003.

Part III

Extra material

Appendix A

Foliation of Einstein's equations

A.1 ADM decomposition

Obtaining *Gauss-Codazzi* equation:

$$\begin{aligned} D_j V^k = P^q_j P^k_r \nabla_q V^r &= P^q_j \nabla_q V^k + P^q_j n^k n_r \nabla_q V^r = P^q_j \nabla_q V^k - P^q_j n^k V^r \nabla_q n_r \\ &= P^q_j \nabla_q V^k - P^q_j n^k V^r K_{qr} = P^q_j \nabla_q V^k - n^k V^r K_{jr} \end{aligned} \tag{A.1}$$

Now, $D_i D_j V^k = D_i \left(P^q_j\right) \nabla_q V^k + P^q_j D_i \left(\nabla_q V^k\right) - D_i \left(n^k V^r K_{jr}\right)$

$$\begin{aligned} D_i \left(P^q_j\right) \nabla_q V^k &= D_i \left(n^q n_j\right) \nabla_q V^k = P^s_i P^t_j \nabla_s \left(n^q n_t\right) \nabla_q V^k \\ &= P^s_i P^t_j n^q \nabla_s \left(n_t\right) \nabla_q V^k + P^s_i P^t_j n_t \nabla_s \left(n^q n_t\right) \nabla_q V^k = -K_{ij} n^q \nabla_q V^k \end{aligned} \tag{A.2}$$

$$P^q_j D_i \left(\nabla_q V^k\right) = P^q_j P^s_i P^k_t \nabla_s \nabla_q V^t \tag{A.3}$$

$$\begin{aligned} D_i \left(n^k V^r K_{qr}\right) &= P^s_i P^k_t P^u_q \nabla_s \left(n^t V^r K_{ur}\right) \\ &= P^s_i P^k_t P^u_j (\nabla_s n^t) V^r K_{ur} + P^s_i P^k_t P^u_j \nabla_s n^t \left(V^r K_{ur}\right) = -V^r K^k_i K_{jr} \end{aligned} \tag{A.4}$$

since $P^k_t n^t = 0$ and $K^k_i = -D_i n^k$. Therefore,

$$\begin{aligned} {}^{(3)}R^{\alpha}_{\beta\mu\nu} = D_{[a} D_{b]} V^c &= -K_{[ab]} n^q \nabla_q V^c + P^s_{[a} P^p_{b]} P^c_t \nabla_s \nabla_q V^t - V^r K^c_{[a} K_{b]r} \\ &= P^s_a P^p_b P^c_t \nabla_{[s} \nabla_{q]} V^t - V^r K^c_{[a} K_{b]r} \end{aligned} \tag{A.5}$$

since $K_{\mu\nu}$ is symmetric. Noting the definition of the 4-dimensional Riemannian curvature tensor $R_{\alpha\beta\mu\nu}V^{\beta} = 2\nabla_{[\mu}\nabla_{\nu]}V_{\alpha}$, the *Gauss-Codazzi* equation is obtained

$$P^{\delta}_{\alpha}P^{\kappa}_{\beta}P^{\lambda}_{\mu}P^{\sigma}_{\nu}R_{\delta\kappa\lambda\sigma} = {}^{(3)}R_{\alpha\beta\mu\nu} + K_{\alpha\mu}K_{\beta\nu} - K_{\alpha\nu}K_{\beta\mu}. \tag{A.6}$$

Similarly for the *Codazzi-Mainardi* equation, defining $a_a \equiv n^b\nabla_b n_a$,

$$K_{ab} = -P^p_a P^q_b \nabla_p n_q = -(\delta^p_a + n^p n_a)(\delta^p_a + n^p n_a)\nabla_p n_q = -\nabla_a n_b - n_a a_b \tag{A.7}$$

so that

$$\begin{aligned} D_a K_{bc} &= P^p_a P^q_b P^r_c \nabla_p K_{qr} = -P^p_a P^q_b P^r_c \nabla_p(\nabla_q n_r - n_q a_r) \\ &= -P^p_a P^q_b P^r_c \nabla_p \nabla_q n_r - P^p_a P^q_b P^r_c \nabla_p(n_q a_r) = -P^p_a P^q_b P^r_c \nabla_p \nabla_q n_r + K_{ab}a_c \end{aligned} \tag{A.8}$$

and hence

$$D_{[a}K_{b]c} = -P^p_a P^q_b P^r_c \nabla_{[p}\nabla_{q]}n_r + K_{[ab]}a_c = -P^p_a P^q_b P^r_c R_{pqrs}n^s \tag{A.9}$$

which is the *Codazzi-Mainardi equation*

$$D_b K_{ac} - D_a K_{bc} = P^p_a P^q_b P^r_c n^s R_{pqrs} \tag{A.10}$$

The evolution equation for the extrinsic curvature tensor $K_{\mu\nu}$ is obtained following the definition of the Lie derivative

$$\begin{aligned} \pounds_{\vec{n}}K_{ab} &= n^c\nabla_c K_{ab} + K_{ca}\nabla_b n^c + K_{cb}\nabla_a n^c \\ &= -n^c\nabla_c\nabla_a\nabla_b - n^c\nabla_c(n_a a_b) - K_{ca}K^c_b - K_{ca}n_b a^c - K_{cb}n_a a^c \\ &= -n^c R_{acbd}n^d - n^c\nabla_a\nabla_c n_b -^c a_b\nabla_c n_a + n^c n_a\nabla_c a_b - 2K^c_{(a}K_{b)c} - 2K_{c(a}n_{b)}a^c \end{aligned} \tag{A.11}$$

and as $\nabla_a a_b = n^c\nabla_a\nabla_c n_b + \nabla_a n^c\nabla_c n_b$,

$$\pounds_{\vec{n}}K_{ab} = -n^d n^c R_{dbac} - \nabla_a a_b - n^c n_a \nabla_c a_b - a_a a_b - K^c_b K_{ac} - K_{ca}n_b a^c \tag{A.12}$$

It can be easily shown that $\pounds_{\vec{n}}K_{ab}$ is purely spatial since

$$\begin{aligned} n^a\pounds_{\vec{n}}K_{ab} &= n^a n^c\nabla_c K_{ab} + n^a K_{ac}\nabla_b n^c + n^a K_{bc}\nabla_a n^c \\ n^c\nabla_c(n^a K_{ab}) - K_{ab}n^c\nabla_c n^a + &= n^a K_{bc}\nabla_a n^c = 0 \end{aligned} \tag{A.13}$$

because K_{ab} is purely spatial, which implies $n^a K_{ab}$ and also $\nabla_c(n_a K_{ab}) = n^a \nabla_c K_{ab} + K_{ab}\nabla_c n^a = 0$. Therefore, projecting two indices in LHS of (A.12) will give the same result but with a simplified version of RHS.

$$\pounds_{\vec{n}} K_{ab} = -n^d n^c P^p_a P^q_b R_{dqpc} - a_a a_b - K^c_b K_{ac} \tag{A.14}$$

since $P^p_a n_p = 0$. In addition,

$$n^d n^c P^p_a P^q_b R_{dqpc} = (\gamma^{dc} - g^{dc}) P^p_a P^q_b R_{dqpc} = \gamma^{dc} P^p_a P^q_b R_{dqpc} - P^p_a P^q_b R_{qp}. \tag{A.15}$$

and replacing the first term by the *Gauss-Codazzi* equation and the second term by Einstein's equations

$$\begin{aligned} n^d n^c P^p_a P^q_b R_{dqpc} &= {}^{(3)}R_{ab} + K K_{ab} - K_{ac} K^c_b - 8\pi P^p_a P^q_b \left(T_{pq} - \frac{1}{2} g_{pq} T\right) \\ &= {}^{(3)}R_{ab} + K K_{ab} - K_{ac} K^c_b - 8\pi \left(S_{ab} - \frac{1}{2}\gamma_{ab}(S - \rho)\right) \end{aligned} \tag{A.16}$$

where $S_{ab} \equiv P^p_a P^q_b S_{ab}$ and $P^p_a P^q_b g_{pq} g^{rs} T_{rs} = \gamma_{ab}(\gamma^{rs} - n^r n^s) T_{rs} = \gamma_{ab}(S - \rho)$. Now as $a_a = D_a \ln \alpha$ and using the Gauss-Codazzi equation for the first and Einstein's equations for the second term on RHS,

$$D_a a_b = D_a D_b \ln \alpha = D_a \left(\frac{1}{\alpha} D_b \alpha\right) = -\frac{1}{\alpha^2} D_a \alpha D_b \alpha + \frac{1}{\alpha} D_a D_b \alpha = -a_a a_b + \frac{1}{\alpha} D_a D_b \alpha \tag{A.17}$$

so that finally the evolution equation for K_{ab} is

$$\pounds_{\vec{t}} K_{ab} - \pounds_{\vec{\beta}} K_{ab} = -D_a D_b \alpha + \alpha \left({}^{(3)}R_{ab} - 2K_{ac}K^c_b + K K_{ab}\right) + 4\pi\alpha \left(\gamma_{ab}(S - \rho) - 2S_{ab}\right) \tag{A.18}$$

where the last part comes from the matter content.

A.2 BSSN reformulation

Starting from the evolution equation for the spatial metric

$$\frac{d}{dt}(\gamma_{ij}) = -2\alpha \left(A_{ij} + \frac{1}{3}\gamma_{ij} K\right) \tag{A.19}$$

and doing the conformal transformation,

$$\frac{d}{dt}\left(\chi^{-1}\bar{\gamma}_{ij}\right) = \chi^{-1}\frac{d}{dt}\left(\bar{\gamma}_{ij}\right) - \chi^{-2}\bar{\gamma}_{ij}\frac{d}{dt}\left(\chi\right) = -2\alpha\chi^{-1}\left(\tilde{A}_{ij} + \frac{1}{3}\bar{\gamma}_{ij}K\right) \tag{A.20}$$

which splits into

$$\frac{d}{dt}\chi = \frac{2}{3}\chi\alpha K \tag{A.21}$$

$$\frac{d}{dt}\bar{\gamma}_{ij} = -2\alpha\tilde{A}_{ij}. \tag{A.22}$$

Similarly for the evolution equation of the extrinsic curvature tensor

$$\frac{d}{dt}\left(K_{ij}\right) = -D_iD_j\alpha + \alpha\left({}^{(3)}R_{ij} - 2K_{ik}K^k_j + KK_{ij}\right) + 4\pi\alpha\left(\gamma_{ij}(S-\rho) - 2S_{ij}\right). \tag{A.23}$$

Expanding

$$K_{ik}K^k_j = \frac{1}{\chi}\left(\tilde{A}_{ik} + \frac{1}{3}\bar{\gamma}_{ik}K\right)\left(\tilde{A}^k_j + \frac{1}{3}\delta^k_jK\right) = \frac{1}{\chi}\left(\tilde{A}_{ik}\tilde{A}^k_j + \frac{2}{3}\tilde{A}_{ij}K + \frac{1}{9}\bar{\gamma}_{ij}K^2\right) \tag{A.24}$$

$$KK_{ij} = \frac{K}{\chi}\left(\tilde{A}_{ij} + \frac{1}{3}\bar{\gamma}_{ij}K\right) = \frac{1}{\chi}\left(\tilde{A}_{ij}K + \frac{1}{3}\bar{\gamma}_{ij}K^2\right) \tag{A.25}$$

so that equation (A.23) can be rewritten

$$\begin{aligned}\frac{d}{dt}\left(K_{ij}\right) =& - D_iD_j\alpha + \alpha\left({}^{(3)}R_{ij} + \frac{1}{\chi}\left(-2\tilde{A}_{ik}\tilde{A}^k_j - \frac{1}{3}\tilde{A}_{ij}K + \frac{1}{9}\bar{\gamma}_{ij}K^2\right)\right)\\ &+ 4\pi\alpha\left(\gamma_{ij}(S-\rho) - 2S_{ij}\right)\end{aligned} \tag{A.26}$$

and expanding LHS

$$\frac{d}{dt}\left(K_{ij}\right) = \frac{d}{dt}\left(\frac{1}{\chi}\left(\tilde{A}_{ij} + \frac{1}{3}\bar{\gamma}_{ij}K\right)\right) = \frac{1}{\chi}\frac{d}{dt}\tilde{A}_{ij} + \frac{1}{3\chi}\bar{\gamma}_{ij}\frac{d}{dt}K - \frac{4\alpha}{3\chi}\tilde{A}_{ij}K - \frac{2\alpha}{9\chi}\bar{\gamma}_{ij}K^2. \tag{A.27}$$

Equation (A.26) can be rewritten as

$$\frac{1}{\chi}\frac{d}{dt}\tilde{A}_{ij} + \frac{1}{3\chi}\bar{\gamma}_{ij}\frac{d}{dt}K = - D_iD_j\alpha + \alpha\left({}^{(3)}R_{ij} + \frac{1}{\chi}\left(-2\tilde{A}_{ik}\tilde{A}^k_j + \tilde{A}_{ij}K + \frac{1}{3}\bar{\gamma}_{ij}K^2\right)\right) \tag{A.28}$$

$$+ 4\pi\alpha\left(\gamma_{ij}(S-\rho) - 2S_{ij}\right) \tag{A.29}$$

which can be splitted into a traceless and a trace part

$$\frac{d}{dt}\tilde{A}_{ij} = \chi\left\{-D_iD_j\alpha + \alpha\left({}^{(3)}R_{ij} - 8\pi\alpha S_{ij}\right)\right\}^{TF} + \alpha\left(\tilde{A}_{ij}K - 2\tilde{A}_{ik}\tilde{A}^k_j\right) \tag{A.30}$$

$$\frac{d}{dt}K = -\gamma^{ij}D_iD_j\alpha + \alpha\left({}^{(3)}R + K^2\right) + 4\pi\alpha(S - 3\rho). \tag{A.31}$$

Now inserting the Hamiltonian constraint,

$${}^{(3)}R = K_{ij}K^{ij} - K^2 + 16\pi\rho = A_{ij}A^{ij} - \frac{2}{3}K^2 + 16\pi\rho \tag{A.32}$$

a final evolution equation can be obtained for K

$$\frac{d}{dt}K = -\gamma^{ij}D_iD_j\alpha + \alpha\left(\tilde{A}_{ij}\tilde{A}^{ij} + \frac{1}{3}K^2\right) + 4\pi\alpha(\rho + S). \tag{A.33}$$

For the conformal connection functions, first note that

$$\frac{d}{dt}\bar{\gamma}^{ij} = 2\alpha\tilde{A}^{ij} \tag{A.34}$$

and therefore

$$\begin{aligned}\partial_t\bar{\Gamma}^i &= -\,\partial_j\left(\partial_t\bar{\gamma}^{ij}\right) = -\partial_j\left(\pounds_{\vec{\beta}}\bar{\gamma}^{ij} + 2\alpha\tilde{A}^{ij}\right)\\ &= -\,\partial_j\left(\pounds_{\vec{\beta}}\bar{\gamma}^{ij}\right) - 2\left(\alpha\partial_j\tilde{A}^{ij} + \tilde{A}^{ij}\partial_j\alpha\right)\end{aligned} \tag{A.35}$$

Expanding the Lie derivative,

$$\begin{aligned}-\partial_j\left(\pounds_{\vec{\beta}}\bar{\gamma}^{ij}\right) &= -\partial_j\left(\beta^k\partial_k\bar{\gamma}^{ij} - \bar{\gamma}^{ik}\partial_k\beta^j - \bar{\gamma}^{kj}\partial_k\beta^i + \frac{2}{3}\bar{\gamma}^{ij}\partial_k\beta^k\right)\\ &= \bar{\gamma}^{jk}\partial_j\partial_k\beta^i + \frac{1}{3}\bar{\gamma}^{ij}\partial_j\partial_k\beta^k + \beta^j\partial_j\bar{\Gamma}^i - \bar{\Gamma}^j\partial_j\beta^i + \frac{2}{3}\bar{\Gamma}^i\partial_j\beta^j\end{aligned} \tag{A.36}$$

where the rule of taking Lie derivative of tensor densities has been used. Using the momentum constraints

$$\begin{aligned}&D_jA^{ij} - \frac{2}{3}D_j\left(\gamma^{ij}K\right) = 8\pi S^i \longrightarrow\\ &\qquad\longrightarrow \partial_j\tilde{A}^{ij} = -\bar{\Gamma}^i_{jk}\tilde{A}^{jk} - \frac{3}{2}\tilde{A}^{ij}\partial_j\chi + \frac{2}{3}\bar{\gamma}^{ij}\partial_jK + 8\pi\bar{S}^i\end{aligned} \tag{A.37}$$

where $\bar{S}^i = \chi S^i$, we can rewrite the evolution equation into its final form

$$\begin{aligned}\partial_t \bar{\Gamma}^i = \bar{\gamma}^{jk}\partial_j\partial_k\beta^i + \frac{1}{3}\bar{\gamma}^{ij}\partial_j\partial_k\beta^k + \beta^j\partial_j\bar{\Gamma}^i - \bar{\Gamma}^j\partial_j\beta^i + \frac{2}{3}\bar{\Gamma}^i\partial_j\beta^j - 2\tilde{A}^{ij}\partial_j\alpha \\ +2\alpha\left(\bar{\Gamma}^i_{jk}\tilde{A}^{jk} + \frac{3}{2}\tilde{A}^{ij}\partial_j\chi - \frac{2}{3}\bar{\gamma}^{ij}\partial_j K - 8\pi\bar{S}^i\right). \qquad \text{(A.38)}\end{aligned}$$

Appendix B

The effects of potential shape on inhomogeneous inflation

B.1 Evolution equations

In this work, we use GRCHOMBO, a multipurpose numerical relativity code [55, 154] which solves the BSSN [79, 421] formulation of the Einstein equation and the *moving-puncture gauge* [102, 67, 124, 445], which helps us control constraint violation growth and evolve black hole spacetimes. The matter part of the Lagrangian is

$$\mathcal{L}_\phi = -\frac{1}{2}g^{\mu\nu}\partial_\mu\phi\partial_\nu\phi - V(\phi) \ , \tag{B.1}$$

which gives the evolution equations

$$-\nabla_\mu\nabla^\mu\phi + \frac{dV(\phi)}{d\phi} = 0 \ , \tag{B.2}$$

and decomposing the equation into two first order equations, with BSSN variables it becomes

$$\partial_t\phi = \alpha\Pi + \beta^i\partial_i\phi \ , \tag{B.3}$$

$$\begin{aligned}\partial_t\Pi = {} & \beta^i\partial_i\Pi + \alpha\partial^i\partial_i\phi + \partial_i\phi\partial^i\alpha \\ & + \alpha\left(K\Pi - \gamma^{ij}\Gamma^k_{ij}\partial_k\phi - \frac{dV}{d\phi}\right) \ .\end{aligned} \tag{B.4}$$

The stress energy tensor is

$$T_{ab} = \nabla_a \phi \nabla_b \phi - \frac{1}{2} g_{ab} \left(\nabla_c \phi \nabla^c \phi + 2V \right) , \tag{B.5}$$

and its various components are defined as

$$\begin{aligned} &\rho = n_a \, n_b \, T^{ab} \, , \quad S_i = -\gamma_{ia} \, n_b \, T^{ab} \, , \\ &S_{ij} = \gamma_{ia} \, \gamma_{jb} \, T^{ab} \, , \quad S = \gamma^{ij} \, S_{ij} \ . \end{aligned} \tag{B.6}$$

The Hamiltonian and momentum constraints are monitored throughout the evolution to check the quality of our simulations, see Fig. B.1a. We use periodic boundary conditions in all directions.

B.2 Initial data

We have defined the conformal metric $\tilde{\gamma}_{ij} = \chi \gamma_{ij}$ where χ is the conformal factor, a scalar density. We make the simplifying assumption that $A_{ij} = 0$ and that the induced metric is conformally flat $\tilde{\gamma}_{ij} = \delta_{ij}$. We solve the Hamiltonian constraint for χ using a multigrid solver. As explained in Sec. 3.2, the momentum constraints are trivially satisfied, and the constant value of K is set by imposing an integrability condition on the periodic domain.

B.3 Measurement of e-folds

The number of e-folds informs by how much the universe has expanded from a reference time t_0. In an inflationary spacetime the scale factor grows as $a(t) \propto e^{Ht}$ and the number of e-folds $\mathcal{N}$ with respect to t_0 is then defined as

$$\mathcal{N} = \ln \left(\frac{a(t)}{a(t_0)} \right) \tag{B.7}$$

In our code, the conformal factor is related to the scale factor in a FLRW spacetime as $\chi = a(t)^{-2}$ so that the local number of e-folds can be obtained by evaluating

$$\mathcal{N} = -\frac{1}{2} \ln \chi \ . \tag{B.8}$$

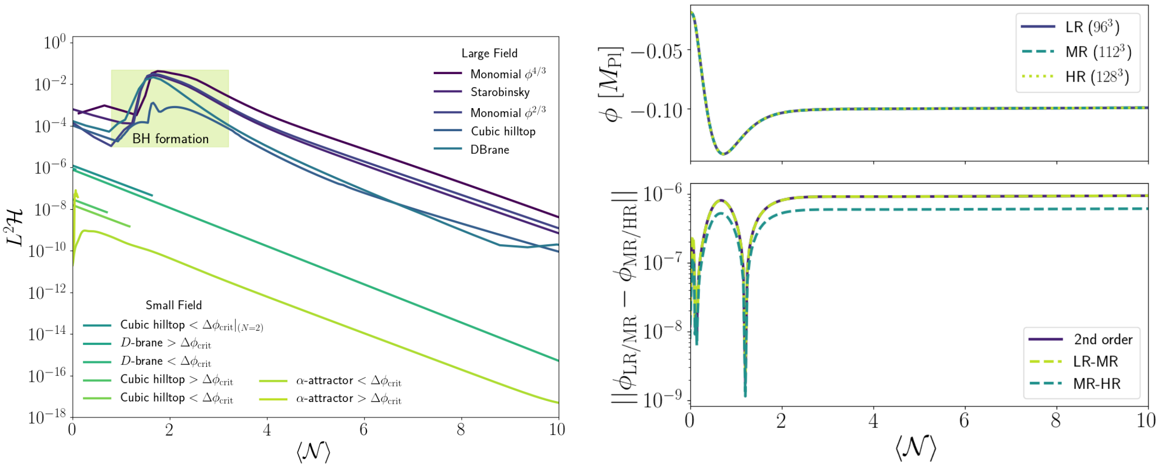

(a) **(b)**

Fig. B.1 (a): **$L^2\mathcal{H}$ constraint** remains stable throughout the evolution for all runs. Dark colours correspond to large field models, for which black holes form at $\mathcal{N} \approx 2$ (yellow-coloured region). Lighter colours represent the Hamiltonian constraint violation for small field cases, in which the gradient energy density is not enough to form singularities. For these cases the $L^2\mathcal{H}$ analysis is stopped when the field first reaches the minimum. **(b):** **Convergence test** for small field D-brane inflation model is consistent with a 2nd order convergence. Top panel: Evolution of $\phi_{\rm max}$ for low (LR: 96^3), mid (MR: 112^3) and high (HR: 128^3) resolutions. Bottom panel: LR-MR and MR-HR errors and the LR-MR values expected at 2nd order convergence.

In this work we track the average number of e-folds over the simulation box with coordinate volume $V = dxdydz$ by averaging χ, so that

$$\langle\mathcal{N}\rangle = -\frac{1}{2}\ln\langle\chi\rangle \tag{B.9}$$

where

$$\langle\chi\rangle = \frac{1}{V}\int_V \chi\, dV\ . \tag{B.10}$$

B.4 Constraint violation

In Fig. B.1a, we show that the volume-averaged Hamiltonian constraint violation

$$L^2\mathcal{H} = \sqrt{\frac{1}{V}\int_V |\mathcal{H}^2| dV}\ , \tag{B.11}$$

where V is the box volume, is under control throughout the simulations studied in this paper.

We use the gradient conditions on ϕ and χ to tag cells for regridding, although in many of our simulations a single level is sufficient. It is only for the large field cases in which $\Delta\phi > M_{\text{Pl}}$, where large gradient energies are present, that we need to use AMR to resolve any collapse to black holes. As we do not excise the interior of the black holes, an increase in $L^2\mathcal{H}$ can be seen in the yellow-coloured region until the black holes are inflated out due to the expanding spacetime. In addition, cases in which the field initially rolls-down to the reheating minimum and drags-down the rest of the field, sharp gradients have to be resolved by using multiple levels of AMR which is challenging numerically due to the two different scales that need to be tracked.

B.5 Convergence testing

We tested the convergence of our simulations using a box of size $L = 32M = H^{-1}$ with low (LR: 96^3), mid (MR: 112^3) and high (HR: 128^3) resolutions. We extract the value of the field at the center of the grid, which corresponds to ϕ_{max} and track its evolution. In particular we look at the case of $\Delta\phi < \Delta\phi_{\text{crit}}$ for the small field D-brane model 3.4b. The evolution of the field with respect to the average number of e-folds is shown in the top panel of Fig. B.1b, together with the relative errors for different resolutions in dashed lines $||\phi_{\text{LR}} - \phi_{\text{MR}}||$ and $||\phi_{\text{MR}} - \phi_{\text{HR}}||$. The evolution is consistent with 2nd order convergence (solid line).

Model $V(\phi)$	μ $[M_{\rm Pl}]$	$\lambda \mid \Lambda^4$ $[M_{\rm Pl}^4]$	ϕ_0 $[M_{\rm Pl}]$	$H_{\rm inf}$ $[M_{\rm Pl}]$	$\Delta\phi_{\rm e}$ $[M_{\rm Pl}]$	$\Delta\phi_{\rm crit}$ $[M_{\rm Pl}]$	$\Delta\phi_1$ $[M_{\rm Pl}]$	$\Delta\phi_2$ $[M_{\rm Pl}]$
$\lambda M_{\rm Pl}^{8/3}(-\phi)^{4/3}$	$---$	2.57×10^{-14}	-3.26	1.02×10^{-6}	3.07	$---$	3.26	$---$
$\lambda M_{\rm Pl}^{10/3}(-\phi)^{2/3}$	$---$	3.58×10^{-14}	-2.31	7.23×10^{-7}	2.21	$---$	2.31	$---$
$\Lambda^4\left(1-\left(\frac{\phi}{\mu_3}\right)^3\right)$	1	2.05×10^{-16}	7.43×10^{-2}	4.14×10^{-8}	8.03×10^{-1}	$---$	9.40×10^{-1}	$---$
	5×10^{-2}	5.15×10^{-24}	1.05×10^{-5}	6.57×10^{-12}	1.68×10^{-2}	1.38×10^{-2}	1.10×10^{-2}	1.50×10^{-2}
$\Lambda^4\left(1-\left(\frac{\phi}{\mu_4}\right)^{-4}\right)$	1	5.58×10^{-15}	-2.18	2.11×10^{-7}	1.07	$---$	1.25	$---$
	1×10^{-2}	1.29×10^{-17}	-9.92×10^{-2}	1.04×10^{-8}	7.67×10^{-2}	8.21×10^{-2}	8.10×10^{-2}	8.40×10^{-2}
$\Lambda^4\left(1-\exp\left[\phi/\mu\right]\right)^2$	$\sqrt{3/16\pi}$	2.11×10^{-14}	-2.19	3.97×10^{-7}	1.95	$---$	2.19	$---$
	5×10^{-3}	1.18×10^{-18}	-6.33×10^{-2}	3.14×10^{-9}	4.31×10^{-2}	4.74×10^{-2}	4.50×10^{-2}	5.10×10^{-2}

Table B.1 Overview of runs: (i) Convex monomial. (ii) Concave monomial. (iii) Cubic hilltop. (iv) *D*-brane. (v) α-attractor model. In these cases Λ^4 is chosen such that it is compatible with scalar index measurements from the Planck 2018 observations. In addition, ϕ_0 is the initial field value that would correspond to 100 *e*-folds in the absence of inhomogeneities $\Delta\phi = 0$. $\Delta\phi_{\rm e}$ corresponds to the value where $\epsilon_V(\phi_{\rm e}) = 1$ with $\phi_{\rm e} = \phi_0 + \Delta\phi_{\rm e}$. $\Delta\phi_{\rm crit}$ is the value for which $f(\phi_0, \Delta\phi_{\rm crit}) = 0$ and $\Delta\phi_1$ and $\Delta\phi_2$ are different amplitudes used in simulations.

Appendix C

Abelian Higgs cosmic strings with full numerical relativity

C.1 Evolution equations

In this work, we use GRCHOMBO, a multipurpose numerical relativity code [55, 154] which solves the BSSN [79, 421] formulation of the Einstein equation and the *moving-puncture gauge* [102, 67, 124, 445], which helps us control constraint violation growth and evolve black hole spacetimes. The matter part of the Lagrangian is

$$\mathcal{L}_m = -(D_\mu\phi)^*(D^\mu\phi) - \frac{1}{4}F_{\mu\nu}F^{\mu\nu} - V(\phi) \ , \tag{C.1}$$

which gives the evolution equations

$$-D_\mu D^\mu\phi + \frac{\partial V(\phi)}{\partial\bar{\phi}} = 0 \ , \tag{C.2}$$

$$\nabla_\mu F^{\mu\nu} = -eJ^\nu \ , \tag{C.3}$$

with

$$J^\nu = 2\mathrm{Im}(\phi^* D^\nu\phi) \ , \ F_{\mu\nu} = \partial_\mu A_\nu - \partial_\nu A_\mu \ . \tag{C.4}$$

We decompose these equations in 3+1 coordinates, following [476]. Furthermore, we impose the Lorenz condition

$$\nabla^\mu A_\mu = 0 \ . \tag{C.5}$$

Using the projector

$$P^\nu_\mu = \delta^\nu_\mu + n_\mu n^\nu \ , \tag{C.6}$$

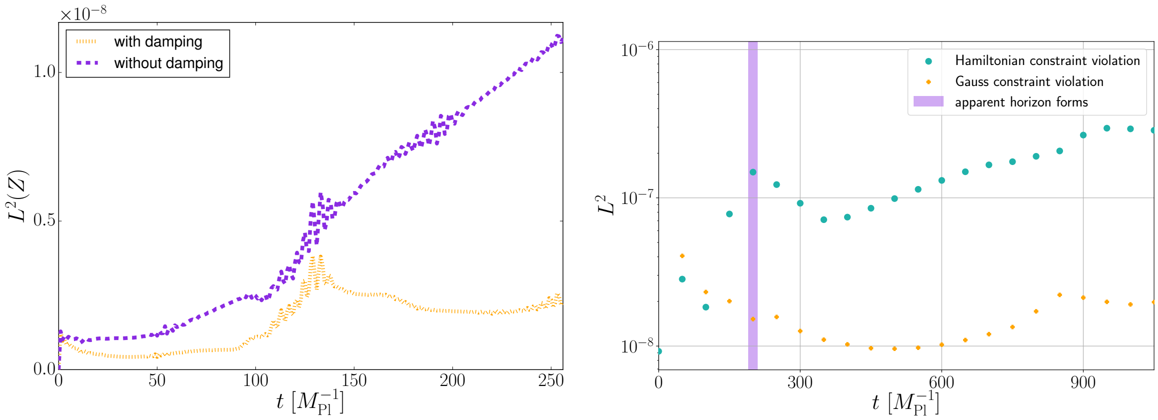

(a) **(b)**

Fig. C.1 (a): Gauss constraint for static string: We run the same simulation for an infinite static string with $G\mu = 1.6 \times 10^{-2}$ ($\eta = 0.05 M_{\rm Pl}$) with and without damping. We find that the damping stabilises the linear growth in violation. **(b): L^2 norm of constraints:** Loop with $G\mu = 1.6 \times 10^{-2}$ and $R = 100\ M_{\rm Pl}^{-1}$ remains stable throughout evolution, even after black hole formation. The initial Hamiltonian constraint is smaller than it can be maintained by the evolution scheme. The momentum constraints violation are negligible throughout.

where n^μ is the normal to the hypersurface, the gauge field and current can further be decomposed into traverse and longitudinal components via

$$\begin{aligned} A_\mu &= \mathcal{A}_\mu + n_\mu \mathcal{A}\ , \\ J_\mu &= \mathcal{J}_\mu + n_\mu \mathcal{J}\ , \end{aligned} \tag{C.7}$$

such that

$$\begin{aligned} \mathcal{A}_\mu &= P^\nu_\mu A_\nu \quad \text{and} \quad \mathcal{A} = -n^\nu A_\nu\ , \\ \mathcal{J}_\mu &= P^\nu_\mu J_\nu \quad \text{and} \quad \mathcal{J} = -n^\nu J_\nu\ . \end{aligned} \tag{C.8}$$

The electric and magnetic fields are defined as

$$E_\mu = P^\nu_\mu n^\rho F_{\nu\rho}\ , \tag{C.9}$$

$$B_\mu = P^\nu_\mu n^\rho (\star F_{\nu\rho})\ , \tag{C.10}$$

where $(\star F_{\nu\rho})$ is the dual Maxwell tensor. Using the previous decomposition we rewrite the Maxwell tensor as

$$F_{\mu\nu} = n_\mu E_\nu - n_\nu E_\mu + \partial_\mu \mathcal{A}_\nu - \partial_\nu \mathcal{A}_\mu \ . \tag{C.11}$$

In addition, Eqn. (C.3) gives the Gauss constraint

$$\tilde{\nabla}_i E^i = e\mathcal{J} \ , \tag{C.12}$$

where $\tilde{\nabla} = P^\nu_\mu \nabla_\nu$.

To ensure that numerical violation of Eqn. (C.12) is kept to a minimum, we stabilise it by introducing an auxiliary damping variable Z [476, 268, 383], resulting in the following modified evolution equations

$$\begin{aligned}
\partial_t E^i &= \alpha(KE^i + \tilde{\nabla}^i Z - e\mathcal{J}^i + \tilde{\nabla}^i \mathcal{A}) - \mathcal{A}\tilde{\nabla}^i\alpha + \beta^j\partial_j E^i \\
&\quad - E^j\partial_j\beta^i \ , && \text{(C.13)}\\
\partial_t \mathcal{A} &= -\mathcal{A}^i\tilde{\nabla}_i\alpha + \alpha(K\mathcal{A} - \tilde{\nabla}_i\mathcal{A}^i - Z) + \beta^j\partial_j\mathcal{A} \ , && \text{(C.14)}\\
\partial_t \mathcal{A}_i &= -\alpha(E_i + \tilde{\nabla}_i\mathcal{A}) - \mathcal{A}\tilde{\nabla}_i\alpha + \beta^j\partial_j\mathcal{A}_i \\
&\quad + \partial_i\beta^j\mathcal{A}_j \ , && \text{(C.15)}\\
\partial_t Z &= \alpha(\tilde{\nabla}_i E^i - e\mathcal{J} - \kappa Z) + \beta^j\partial_j Z \ . && \text{(C.16)}
\end{aligned}$$

From fig. C.1a we see the scheme is effective at stopping the growth of constraint violations.

Finally, we decompose the complex scalar field

$$\phi = \frac{1}{\sqrt{2}}(\phi_1 + i\phi_2) \ , \tag{C.17}$$

and rewriting the matter equations with BSSN variables,

$$
\begin{aligned}
\partial_t\phi_a &= \alpha\Pi_a + \beta^i\partial_i\phi_a \ , && \text{(C.18)}\\
\partial_t\Pi_a &= \beta^i\partial_i\Pi_a + \alpha\partial^i\partial_i\phi_a + \partial_i\phi_a\partial^i\alpha \\
&\quad + \alpha\left(K\Pi_a - \gamma^{ij}\Gamma^k_{ij}\partial_k\phi_a + \frac{dV}{d\phi_a}\right) \\
&\quad + \alpha(-e^2A_\mu A^\mu\phi_a \pm e\phi_{a+1}\nabla_\mu A^\mu \\
&\quad \pm 2eA^\mu\partial_\mu\phi_{a+1}) \ , && \text{(C.19)}\\
\partial_t E^i &= \alpha K E^i - e\alpha\chi\tilde{\gamma}^{ij}\mathcal{J}_j + \alpha\chi\tilde{\gamma}^{ij}\partial_j Z \\
&\quad + \chi^2\tilde{\gamma}^{ij}\tilde{\gamma}^{kl}\partial_l\alpha(\partial_j\mathcal{A}_k - \partial_k\mathcal{A}_j) \\
&\quad + \alpha\chi^2\tilde{\gamma}^{ij}\tilde{\gamma}^{kl}(\tilde{D}_k\partial_j\mathcal{A}_l - \tilde{D}_k\partial_l\mathcal{A}_j) \\
&\quad + \frac{\alpha}{2}\chi\tilde{\gamma}^{ij}\tilde{\gamma}^{kl}(\partial_j\mathcal{A}_l\partial_k\chi - \partial_k\mathcal{A}_j\partial_l\chi) \\
&\quad + \beta^j\partial_j E^i - E^j\partial_j\beta^i \ , && \text{(C.20)}\\
\partial_t\mathcal{A} &= \alpha K\mathcal{A} - \alpha\chi\tilde{\gamma}^{ij}\partial_j\mathcal{A}_i + \alpha\chi\mathcal{A}_i\tilde{\Gamma}^i - \alpha Z \\
&\quad + \frac{\alpha}{2}\mathcal{A}_i\tilde{\gamma}^{ij}\partial_j\chi - \chi\tilde{\gamma}^{ij}\mathcal{A}_i\partial_j\alpha + \beta^j\partial_j\mathcal{A} \ , && \text{(C.21)}\\
\partial_t\mathcal{A}_i &= -\alpha\chi^{-1}\tilde{\gamma}_{ij}E^j - \alpha\partial_i\mathcal{A} - \mathcal{A}\partial_i\alpha \\
&\quad + \beta^j\partial_j\mathcal{A}_i + \partial_i\beta^j\mathcal{A}_j \ , && \text{(C.22)}\\
\partial_t Z &= \alpha\tilde{\nabla}_i E^i - \frac{3}{2}\frac{\alpha}{\chi}E^i\partial_i\chi - \alpha e\mathcal{J} - \alpha\kappa Z + \beta^j\partial_j Z \ , && \text{(C.23)}
\end{aligned}
$$

where $a \in \{1, 2\}$ and the second order Klein Gordon equation has been decomposed into two first order equations as usual. The stress energy tensor for Abelian Higgs is[1]

$$
T_{\mu\nu} = D_{(\mu}\phi^* D_{\nu)}\phi + F_{\mu\alpha}F^{\alpha}_{\nu} + g_{\mu\nu}\mathcal{L}_m, \tag{C.24}
$$

and its various components are defined as

$$
\begin{aligned}
\rho &= n_a\, n_b\, T^{ab}\,, \quad S_i = -\gamma_{ia}\, n_b\, T^{ab}\,, \\
S_{ij} &= \gamma_{ia}\, \gamma_{jb}\, T^{ab}\,, \quad S = \gamma^{ij}\, S_{ij} \ .
\end{aligned} \tag{C.25}
$$

The Hamiltonian constraint

$$
\mathcal{H} = R + K^2 - K_{ij}K^{ij} - 16\pi\rho \ , \tag{C.26}
$$

---

[1] We define the symmetrisation as $D_{(\mu}\phi^* D_{\nu)}\phi \equiv D_\mu\phi^* D_\nu\phi + D_\mu\phi D_\nu\phi^*$.

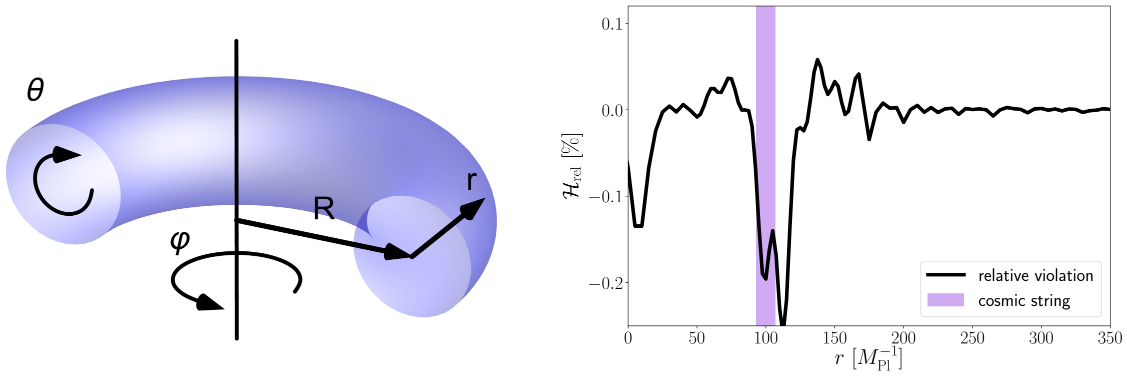

(a) **(b)**

Fig. C.2 **(a): Toroidal coordinates** encode the symmetry of our cosmic string loops. They are used to generate the initial field configuration, where R defines the radius of the loop. **(b): Initial relative violation**: Slice through initial data for loop from center through string with $G\mu = 1.6 \times 10^{-2}$ and initial radius $R = 100\ M_{\rm Pl}^{-1}$. The green region indicates where the string is located. We find that there is an error of at most 0.3%.

the momentum constraint

$$\mathcal{M}_i = D^j(K_{ij} - \gamma_{ij}K) - 8\pi S_i \ , \tag{C.27}$$

and the Gauss constraint

$$\mathcal{Z} = \tilde{\nabla}_i E^i + e\mathcal{J}^\nu n_\nu \ , \tag{C.28}$$

are monitored throughout the evolution to check the quality of our simulations (see Fig. C.1b). Our boundary conditions are Dirichlet.

C.2 Initial data

We set up the field as mentioned in the main text using toroidal coordinates (see Fig. C.2a). Time symmetry is assumed for our initial data,

$$K = 0 \ , \qquad A_{ij} = 0 \ , \tag{C.29}$$

which automatically fulfils the momentum contraint (eq. C.27). In addition, we make a conformally flat[2] ansatz $\tilde{\gamma}_{ij}$,

$$\tilde{\gamma}_{ij} = \delta_{ij} \ , \tag{C.30}$$

and impose the metric to be identity in the center of the string, similar as the static string (see eq. C.36). We find that doing so reduces possible excitations of the string. For the gravitational wave extraction, we impose the condition

$$\lim_{r\to\infty} \chi = 1 \ . \tag{C.31}$$

We solve for χ using the Hamiltonian constraint Eqn. (C.26). We reduce the spatial dimension of the problem by using its cylindrical symmetry. This solution is then further relaxed to obtain the final solution, which is that of an excited cosmic string loop.

As shown in Fig. C.2b, the relative Hamiltonian violation from our prescription is

$$\mathcal{H}_{\text{rel}} = \frac{\mathcal{H}}{16\pi\rho_{\text{max}}} < 1\% \ .$$

C.3 Abelian Higgs code test

To test the code, we compare the evolution of a simulation with a known semi-analytic case of the infinite static string [454]. Given the symmetry of the problem we use polar coordinates

$$\begin{aligned} x &= r\cos(\theta) \ , \\ y &= r\sin(\theta) \ , \\ z &= z \ . \end{aligned} \tag{C.32}$$

and choose cylindrically symmetric ansatz for the scalar and gauge fields ϕ and A_μ

$$\begin{aligned} \phi &= f(r)e^{in\theta} \ , \\ A_\theta &= \frac{n\alpha(r)}{e} \ , \end{aligned} \tag{C.33}$$

---

[2] This is not the unique solution to the constraint equations given the initial field configuration. However, it is the most easily implemented, as more general initial conditions require much greater computational resources to find. Conformal flatness is also consistent with the fact that the spacetime is asymptotically Schwarzschild.

and all other components are set to zero. We impose the boundary conditions

$$\begin{aligned} f(0) &= 0 \ , \qquad & f(\infty) &= 1 \ , \\ \alpha(0) &= 0 \ , \qquad & \alpha(\infty) &= 1 \ . \end{aligned} \tag{C.34}$$

For the metric, the following ansatz is chosen

$$ds^2 = -e^{A(r)}dt^2 + e^{B(r)}(dr^2 + r^2 d\theta^2) + e^{A(r)}dz^2 \ , \tag{C.35}$$

where $A(r)$ and $B(r)$ are radial functions numerically determined. We impose the metric and its derivatives to be locally flat

$$\begin{aligned} A(0) &= 0 \ , \qquad & A'(0) &= 0 \ , \\ B(0) &= 0 \ , \qquad & B'(0) &= 0 \ . \end{aligned} \tag{C.36}$$

We solve Einstein's and the corresponding matter evolution equations

$$G_{\mu\nu} = 8\pi T_{\mu\nu} \ , \tag{C.37}$$

$$D_\mu D^\mu \phi = \frac{dV}{d\bar{\phi}} \ , \tag{C.38}$$

iteratively as follows. We solve the Klein-Gordon equation (eq. C.38) for fixed flat background, then use this solution to calculate the stress-energy tensor and retrieve the values of $A(r)$ and $B(r)$ via (C.37) to build a new metric. Plugging this back into the Klein-Gordon equation we find new profiles for the fields using the new metric as background. The solution converges quickly (within ~ 5 iterations), see Fig. C.3a for the obtained profiles of f and α.

C.4 Comparison with Nambu-Goto

Previous work showed that without gravity [367] the Nambu-Goto (NG) action is still valid at relativistic speeds. However, a comparison between the two approaches, leads to consistent results with NG up to roughly the point when the string radius is close to the string thickness (see fig. C.3b). To reduce gauge effects we use the time of static observer at the position of the string,

$$\tau = \int \alpha|_{\rho=\max(\rho)} \, dt \ . \tag{C.39}$$

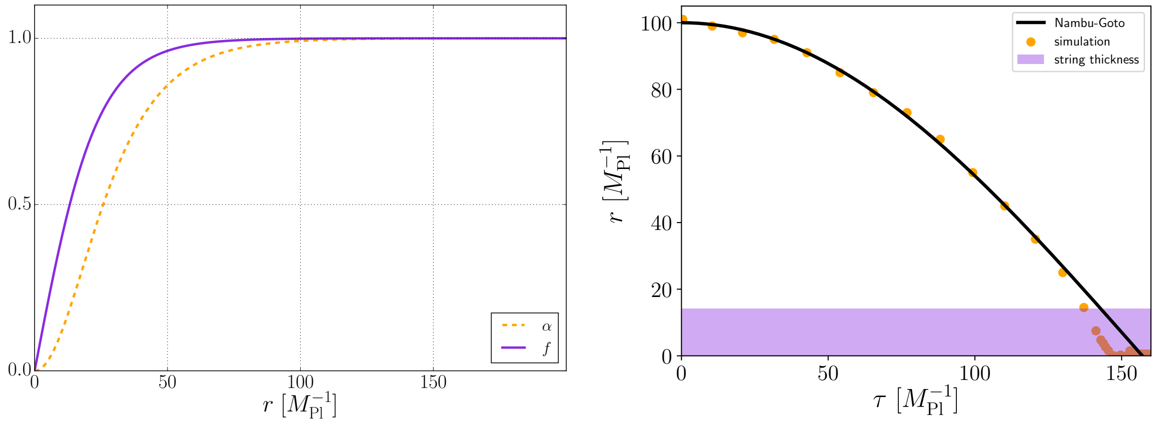

(a) **(b)**

Fig. C.3 (a): Radial profile of α **and** f for an infinite static string with gravity in the critical coupling limit ($e = 1,\ \lambda = 2$) and $\eta = 0.05\ M_{\rm Pl}$ ($G\mu = 1.6 \times 10^{-2}$). **(b): Comparison with Nambu-Goto** for loop with $G\mu = 1.6 \times 10^{-2}$ and initial radius $R_0 = 100\ M_{\rm Pl}^{-1}$ shows agreement.

Having shown that NG is a good approximation, we use it to estimate the velocity before unwinding, which we define as the point where the radius of the loop R is equal to the thickness of the string δ. We find

$$v_\delta = \sqrt{1 - \left(\frac{\delta}{R_0}\right)^2}\ , \tag{C.40}$$

which, for our simulations, gives results ranging from 0.97 c to 0.99 c. In the case for which we extract the gravitational wave signal ($G\mu = 1.6 \times 10^{-2}$, $R_0 = 100\ M_{\rm Pl}^{-1}$) we estimate a velocity of 0.99 c before collision.

C.5 Convergence testing

In Fig. (C.4a), we show that the volume-averaged Hamiltonian constraint violation

$$L^2(H) = \sqrt{\frac{1}{V}\int_V |\mathcal{H}^2| dV}\ , \tag{C.41}$$

where V is the simulation box coordinate volume with the interior of the apparent horizon excised, is under control throughout the simulation.

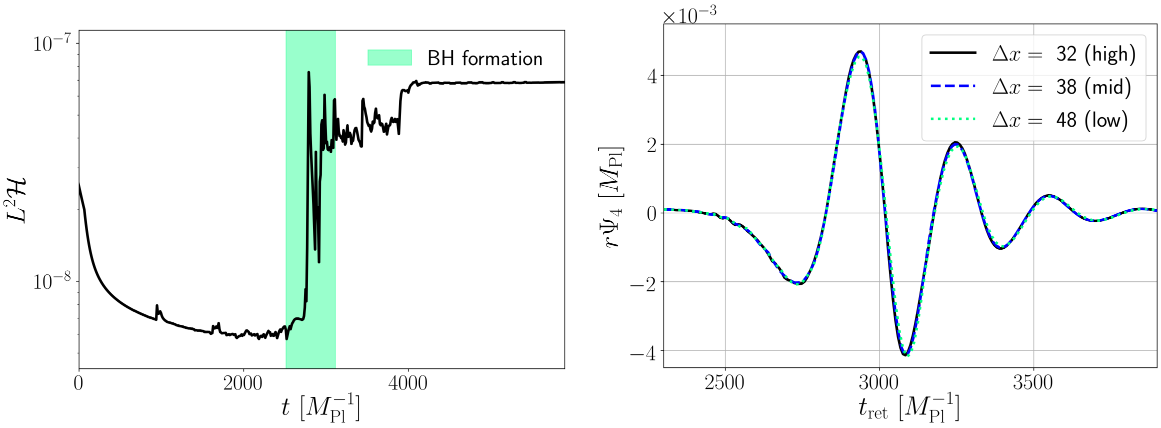

(a) **(b)**

Fig. C.4 (a): **L^2 norm of constraints:** We test the Hamiltonian constraint evolution for a loop with $G\mu = 2 \times 10^{-3}$ and $R_0 = 1600 M_{\rm Pl}^{-1}$. It collapses and forms a black hole at $t \approx 2500 M_{\rm Pl}^{-1}$. After that, the Hamiltonian constraint remains stable at $L^2\mathcal{H} < 10^{-7}$. This plot shows that we have very good numerical control over our simulations. **(b):** **Convergence in $r\Psi_4$** for $G\mu = 2 \times 10^{-3}$ and $R_0 = 1600 M_{\rm Pl}^{-1}$ between different coarse grid resolutions: low ($\Delta x = 48 M_{\rm Pl}^{-1}$), mid ($\Delta x = 38 M_{\rm Pl}^{-1}$) and high ($\Delta x = 32 M_{\rm Pl}^{-1}$) resolutions, in addition to 6 refinement levels.

We use the gradient conditions on ϕ and χ to tag cells for regridding. The precise criteria is chosen depending on the symmetry breaking scale η and the total mass of the system. We use the symmetry of the system to only simulate one quarter of the system, which reduces the computational cost of the problem.

We cut off our signal after some time t when the black hole has formed (and hence the QNM signal is completely determined analytically), and fit QNM modes for the $l = 2$ $m = 0$ mode [319] in Fig. C.7b). We test the precision of the simulation by comparing the radiated energies with the initial mass. We find that these number for the simulations in table (C.1) are consistent within the 1-5 % range.

We tested the convergence of our simulations with a cosmic string loop of $G\mu = 2 \times 10^{-3}$ and $R_0 = 1600 M_{\rm Pl}^{-1}$ by using a box of size $L = 3072 M_{\rm Pl}^{-1}$ in which we improved by a factor of 1.2 between the medium and highest resolution and 1.25 between the lowest and medium resolution. The convergence of $r\Psi_4$ is shown in Fig. C.4b, for different coarse grid resolutions: low ($\Delta x = 32 M_{\rm Pl}^{-1}$), medium ($\Delta x = 38.4 M_{\rm Pl}^{-1}$) and high ($\Delta x = 48 M_{\rm Pl}^{-1}$), in addition to 6 refinement levels.

C.6 Constructing the strain waveform

We extract the Newman-Penrose scalar Ψ_4 [372] with tetrads proposed by [66]. We compute it in the numerical grid using the BSSN variables, and extract its real and imaginary components at a certain distance from the source, which we then decompose into spin-2 spherical harmonics. Similarly as in black hole binaries, there is some non-physical radiation associated with the initial data, which in our case consists of a toroidal shell of artificial radiation resulting in two GW peaks before the physical signal. While such stray-GW can often be ignored as they quickly radiate away at light speed, due to the rapid collapse of the cosmic string loops at ultrarelativistic speeds, they cannot be ignored.

Nevertheless, these artefacts can be separated by simulating larger loops. The time for the stray radiation moving at the speed of light is $R_0 + r_{\mathrm{ext}}$, while the signal of the collapsing loop arrives around $R_0\pi/2 + r_{\mathrm{ext}}$. This implies that we can separate the artificial radiation from the real signal by increasing the radius of the loop, which is computationally expensive. This is especially visible in Fig. 4.2, where we increased the radius of the loop for smaller $G\mu$ to guarantee black hole formation. The initial peak, which is the artificial, becomes more and more separated with the signal for larger R_0. To calculate the total emitted GW energy we use the usual equation

$$\frac{dE_{\mathrm{GW}}}{dt} = \frac{r^2}{16\pi G}\int_{\mathcal{S}_r}\left|\int_{t_0}^{t}\Psi_4 dt'\right|^2 d\Omega \ , \tag{C.42}$$

where $\mathcal{S}_r$ is a sphere of radius r.

C.6.1 Integrating the $r\Psi_4$

The GW strain can be obtained directly from integrating the numerically obtained Weyl scalar Ψ_4,

$$\ddot{h} = \ddot{h}_+ + i\ddot{h}_\times = \Psi_4, \tag{C.43}$$

with the boundary conditions that the emission in gravitational wave power stops at large times and $P_{GW} \propto \dot{h}$

$$\lim_{t\to\infty}\dot{h} = 0 \ . \tag{C.44}$$

We hence have the freedom to shift h

$$h = h_{\mathrm{num}} + \Delta h \ , \tag{C.45}$$

where $h_{\rm num}$ is the gravitational wave strain calculated using a numerical integration technique from Ψ_4. However, we found in the simulations that the quasi-normal modes become unreliable after a certain time due to numerical resolution (see Fig. C.7b for $t \gtrsim 4500$), which causes substantial errors in the integration. To deal with this, this we substitute the signal with analytical QNMs [83] for the corresponding $l = 2$ mode. We performed convergence checks in resolution, courant-factor, box-radius and extraction radius, to ensure that all our numerical integrations are converged.

C.6.2 Weak-field gravity extension

To construct the infall signal, we will calculate ithe strain of a collapsing circular and planar cosmic string loop with energy momentum tensor given by

$$T^{\alpha\beta}(t,\mathbf{x}) = \mu v^{\alpha} v^{\beta} \gamma \; \delta(r - R(t))\delta(z) \tag{C.46}$$

where we define $r = \sqrt{x^2 + y^2}$ and the behaviour of the pre-merger collapse in the weak-field limit is well described by

$$R(t) = R_0 \left[\Theta(t_0 - t) + \cos\left(\frac{t}{R_0}\right) \Theta(t - t_0) \right] . \tag{C.47}$$

so that $v^{\alpha} = (1,\; v_R \sin(\phi),\; v_R \cos(\phi),\; 0)$ with

$$v_R(t) = \frac{dR}{dt} = \sin(t/R_0)\Theta(t - t_0) \; . \tag{C.48}$$

where $\delta(t - t_0)$ is the Dirac delta and we set the starting time $t_0 = 0$ to be consistent with the simulations. Note that we have use the Heaviside Theta functions to impose the initial of the cosmic loop such that it is infinitely static from $t < t_0$, consistent with the initial conditions of our numerical simulations. This is important as the Nambu-Goto loop is oscillating, and hence will contribute GW in the regime $t < t_0$, in contradiction to our numerical simulations (see Figs. C.6 and C.5b).

The effective GW generated for sources that are relativistic is given by [340]

$$r h_{ij}^{TT}(t) = 4G\Lambda_{ij,kl}(\mathbf{n}) \int_{-\infty}^{\infty} \frac{d\omega}{2\pi} \tilde{T}_{kl}(\omega, \omega\mathbf{n}/c) e^{-i\omega(t - r/c)} \; , \tag{C.49}$$

where $\mathbf{n}$ is the direction of the observer

$$\mathbf{n} = (\sin\theta \sin\phi, \sin\theta\cos\phi, \cos\theta) \;\; , \tag{C.50}$$

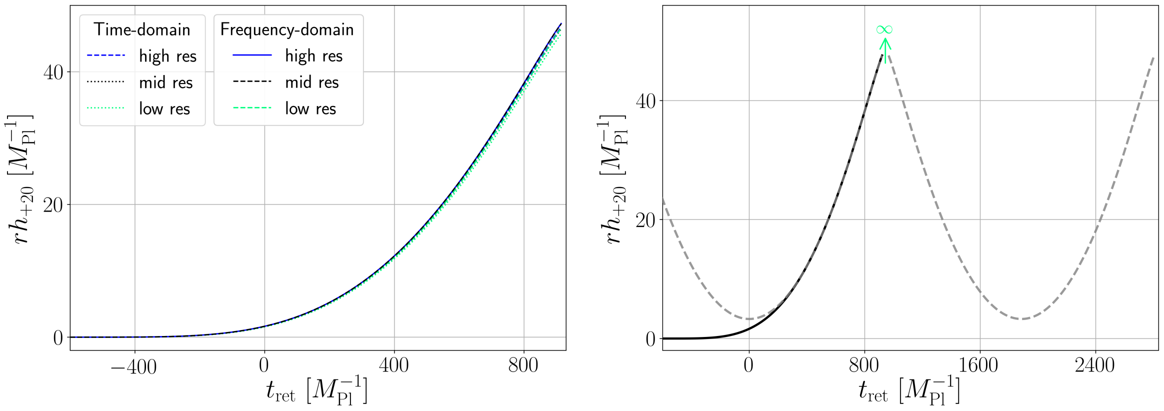

(a) **(b)**

Fig. C.5 (a): Consistency test between the frequency-domain and time-domain methods for $G\mu = 4 \times 10^{-3}$ and $R_0 = 600 M_{\rm Pl}^{-1}$. We run both methods with three resolutions, which we refer as low, mid and high. The difference between them becomes smaller as the resolution is increased, indicating that our integration has converged. Both methods recover the same signal. **(b): GW signal from weak field gravity** for the infall of a loop simulated in this paper (solid black line) and an oscillatory Nambu-Goto loop (dashed grey line). The signal of the former starts at $rh = 0$ while for the latter, the observer gets contribution from the expanding regime ($t < 0$) of the Nambu-Goto loop. The weak gravity calculation breaks down when the loop collapses to a point.

and $\Lambda_{ij,kl}(\mathbf{n})$ is the projector to the TT gauge,

$$\Lambda_{ij,kl}(\mathbf{n}) = P_{ik}P_{jl} - \frac{1}{2}P_{ij}P_{kl} \ , \tag{C.51}$$

where

$$P(\mathbf{n}) = \delta_{ij} - n_i n_j \ . \tag{C.52}$$

We define the fourier transform as

$$\tilde{T}_{kl}(\omega, \mathbf{k}) = \int d^4x \ T_{kl}(t, \mathbf{x}) e^{i\omega t - i\mathbf{k}\cdot\mathbf{x}} \ . \tag{C.53}$$

To check the calculation we also calculate the same expression in the time-domain,

$$rh_{ij}^{TT}(t) = 4G\Lambda_{ij,kl}(\mathbf{n}) \int_{-\infty}^{\infty} d^3x \ T_{kl}\left(t - \frac{r}{c} + \mathbf{x}\cdot\mathbf{n}, \mathbf{x}\right) \ , \tag{C.54}$$

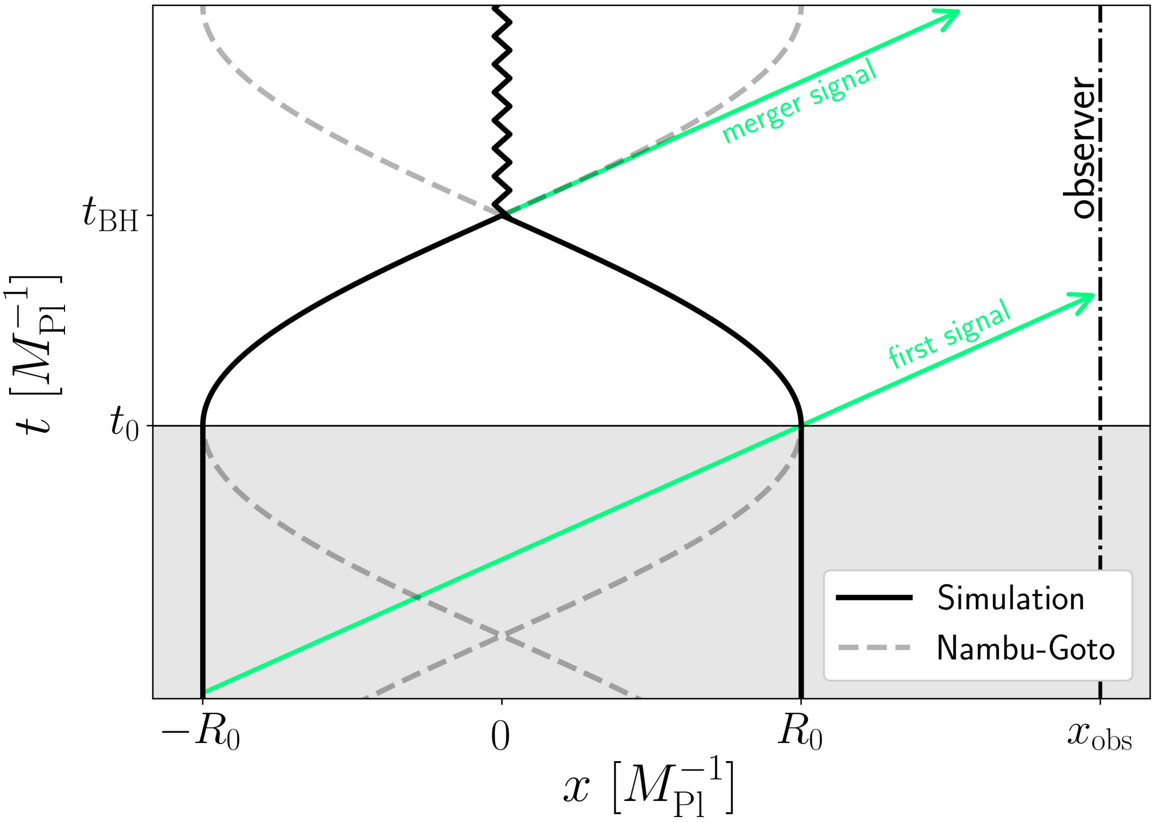

Fig. C.6 Spacetime diagram of loop evolution: The solid black line represents the loop evolution of our simulations. The loop is initially at rest with radius R_0, then starts to collapse at t_0 and forms a black hole at t_{BH}. The dashed grey is the solution of an oscillating loop following the Nambu-Goto action. As shown in Fig. C.5b, the first signal an observer at x_{obs} receives depends on the past history of the loop (grey shaded area). For the Nambu-Goto case, one would get gravitational radiation coming from the expansion phase of the loop (after it has shrunk to a point in the previous cycle). We cut this spurious signal off by imposing a Heaviside function in (4.19).

we indeed find that both formulations converge to the same result (see Fig. C.5a).

Frequency-domain

We simplify (C.49) into

$$\begin{aligned} rh_+(t,\theta,\phi) &= \frac{1}{2}\Big(I_2(t,\theta) - \cos^2(\theta)(I_1(t,\theta) - I_2(t,\theta))\Big)\,, \\ rh_\times &= 0 \end{aligned} \tag{C.55}$$

where the two integrals are

$$I_1(t,\theta) = 8G\mu R_0 \int_{t_1}^{t_2} \frac{\sin(t'/R_0)^2\Theta(t')}{\sqrt{A^2-(t'-t_{\rm ret})^2}}dt' \ , \tag{C.56}$$

and

$$I_2(t,\theta) = 8G\mu R_0 \int_{t_1}^{t_2} \frac{\sin(t'/R_0)^2\sqrt{A^2-(t'-t_{\rm ret})^2}\Theta(t')}{A^2}dt' \tag{C.57}$$

with $A = R_0\left[\Theta(-t') + \cos\left(t'/R_0\right)\Theta(t')\right]\sin(\theta)$ and $t_{\rm ret} = t - r/c$ the retarded time. These are integrated numerically from $t_1(t,\theta)$ to $t_2(t,\theta)$, defined so that the square root above is well defined. To find these two points, one has to find the roots in t' of $R_0^2\left[\Theta(-t') + \cos\left(t'/R_0\right)\Theta(t')\right]^2\sin(\theta)^2 - (t'-t_{\rm ret})^2 = 0$, which we did using a non-linear numerical solver for every t and θ.

Time-domain

Similarly as in (C.55), we can simplify (C.54) into

$$\begin{aligned} rh_+(t,\theta,\phi) &= \frac{1}{2}\left(rI_{xx}(t,\theta) - \cos^2(\theta) rI_{yy}(t,\theta)\right) \ , \text{ and } , \\ rh_\times &= 0 \end{aligned} \tag{C.58}$$

where the integrals are

$$I_{xx}(t,\theta) = 4G\mu R_0 \int_0^{2\pi} d\phi' \ \frac{B^2\sin^2(\phi')}{1+\cos(\phi')\sin(\theta)B}, \tag{C.59}$$

and

$$I_{yy}(t,\theta) = 4G\mu R_0 \int_0^{2\pi} d\phi' \ \frac{B^2\cos^2(\phi')}{1+\cos(\phi')\sin(\theta)B} \tag{C.60}$$

with

$$\begin{aligned} B = \sin&\left(\frac{t_{\rm ret} + r(\phi',\theta,t)\cos(\phi')\sin(\theta)}{R_0}\right) \\ &\times \Theta(t_{\rm ret} + r(\phi',\theta,t)\cos(\phi')\sin(\theta)) \ , \end{aligned} \tag{C.61}$$

where one has to first obtain $r(\phi',\theta,t)$ by solving

$$\begin{aligned} r - R_0\cos&\left(\frac{t_{\rm ret} + r(\phi',\theta,t)\cos(\phi')\sin(\theta)}{R_0}\right) \\ &\times\Theta(t_{\rm ret} + r(\phi',\theta,t)\cos(\phi')\sin(\theta)) = 0, \end{aligned} \tag{C.62}$$

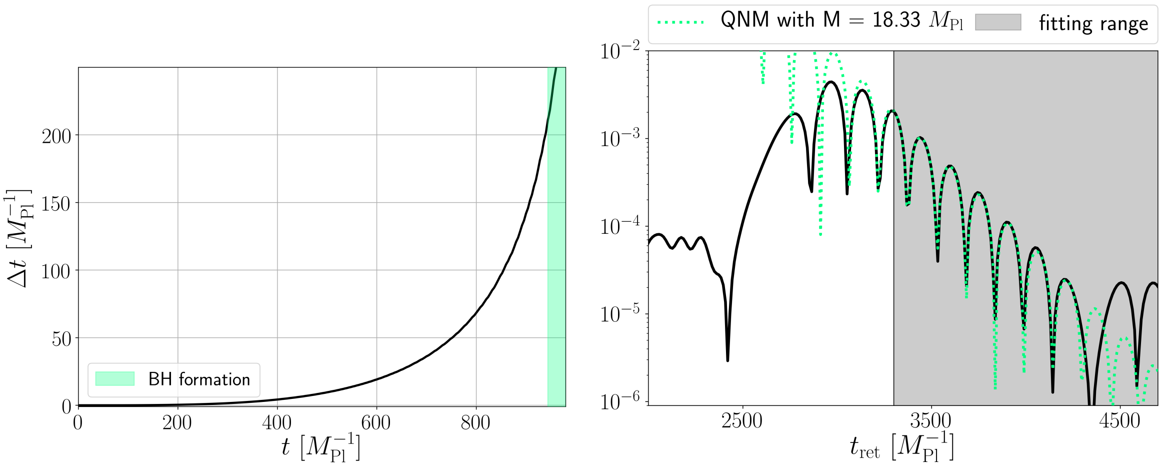

(a) **(b)**

Fig. C.7 (a): Time delay ((C.63)) caused by the dynamical gauge for the case $G\mu = 4\times10^{-3}$, $R_0 = 600M_{\rm Pl}^{-1}$. We estimate GWs emitted near BH formation to be reaching our extraction radius with $\Delta t \approx 200M_{\rm Pl}^{-1}$ delay in simulation time. **(b): Fitting** $l = 2$ $m = 0$ **Quasinormal mode:** We cut off the numerical signal at $t = 3300M_{\rm Pl}^{-1}$ and search for the mass that best fits the analytic quasi-normal mode with the signal. We find a good fit with the mass $18.33M_{\rm Pl}$ for $G\mu = 2\times10^{-3}$ and $R_0 = 1600M_{\rm Pl}^{-1}$.

using a non-linear solver similarly to the frequency approach for $t_1(t,\theta)$ and $t_2(t,\theta)$. However, we need to solve for an additional variable this method, it is numerically much more expensive but we use it to check consistency between both methods, Fig. C.5a.

C.6.3 Fitting to the NR signal

We first correct a time delay Δt of the signal caused by a redshift, which we estimate as

$$\Delta t = \int_{R(t)}^{r_{\rm ext}} dr \left(\frac{1}{\alpha(t,r)} - 1\right) \tag{C.63}$$

where $\alpha(t,r)$ is the lapse function and $\int_{R(t)}^{r_{\rm ext}} dr = r_{\rm ext} - R(t)$ is the distance from the string center to the extraction radius as the loop collapses, which we track throughout the simulation. The delay Δt encodes the difference between the simulation time and the real time it takes a gravitational wave to propagate from the string center to the detector. The delay over time is shown in Fig. C.7a and for near black hole formation, we estimate it to be $\Delta t \approx 200M_{\rm Pl}^{-1}$ for $G\mu = 4\times10^{-3}$ and $R_0 = 600M_{\rm Pl}^{-1}$ case.

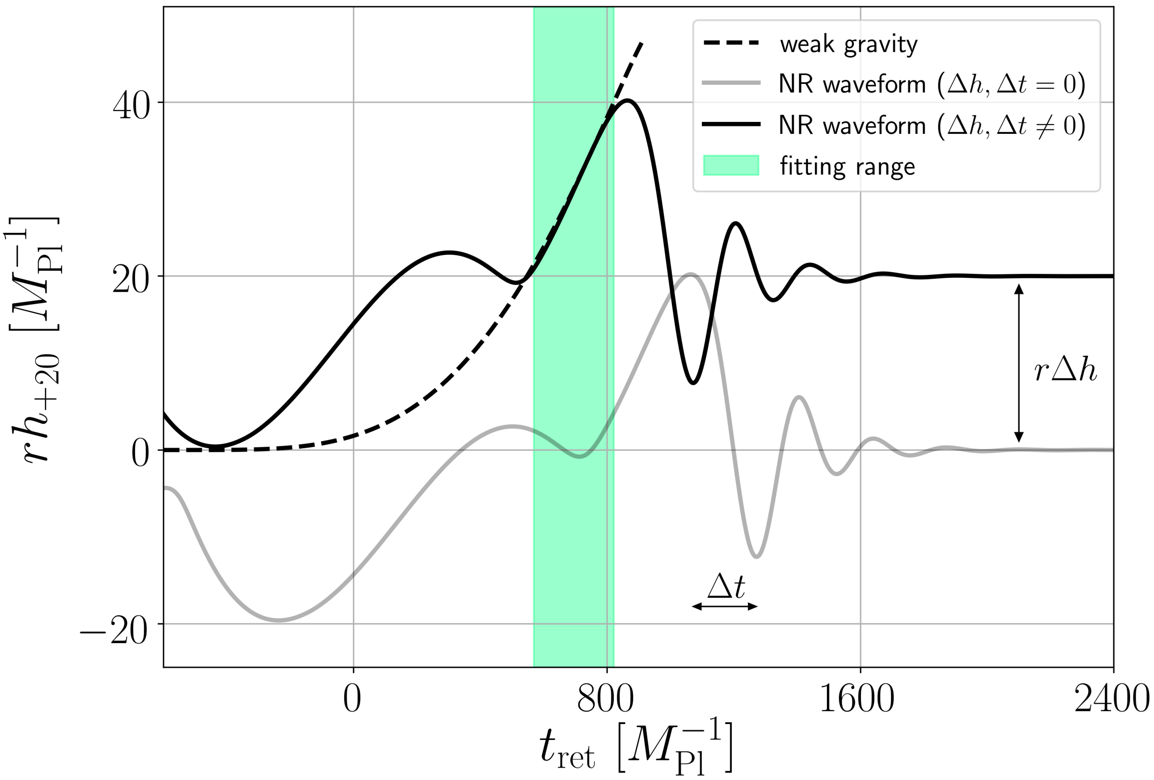

Fig. C.8 Matching the numerical and analytical signals for the $G\mu = 4 \times 10^{-3}$, $R_0 = 600 M_{\rm Pl}^{-1}$ case. As estimated in Fig. C.7a, we correct the time delay by shifting the numerical signal by $-\Delta t = -200 M_{\rm Pl}^{-1}$. The shaded region indicates where the best fit is being calculated to determine the free shift $r\Delta h$, which is found to be $r\Delta h \approx 20 M_{\rm Pl}$.

We then match the strain from our numerical relativity simulations $rh_{\rm num}$ with the weak gravity calculation $rh_{\rm weak}$ of the previous section as follows

$$rh = \begin{cases} rh_{\rm weak}, & t < t_{cut} \\ rh_{\rm num} + r\Delta h & t > t_{cut} \end{cases} . \tag{C.64}$$

The free shift $r\Delta h$ is chosen by finding the best fit value over a region where both signals are valid (shaded region in Fig. C.8). We define this region of validity as, that when $GM/R(t_f) \approx 0.25$, such that $t_f = R_0 \cos^{-1}(4GM/R_0)$. In addition, we define the starting point as the time when most of the initial data artefacts have passed the detector (we can read this value from the $r\Psi_4$ plot). The best fit is shown in Fig. C.8.

A similar analysis can be done for other $(G\mu, R_0)$ cases, which we compare in Fig. C.9. The larger the initial radius R_0 of the loop, the longer the infall. In addition,

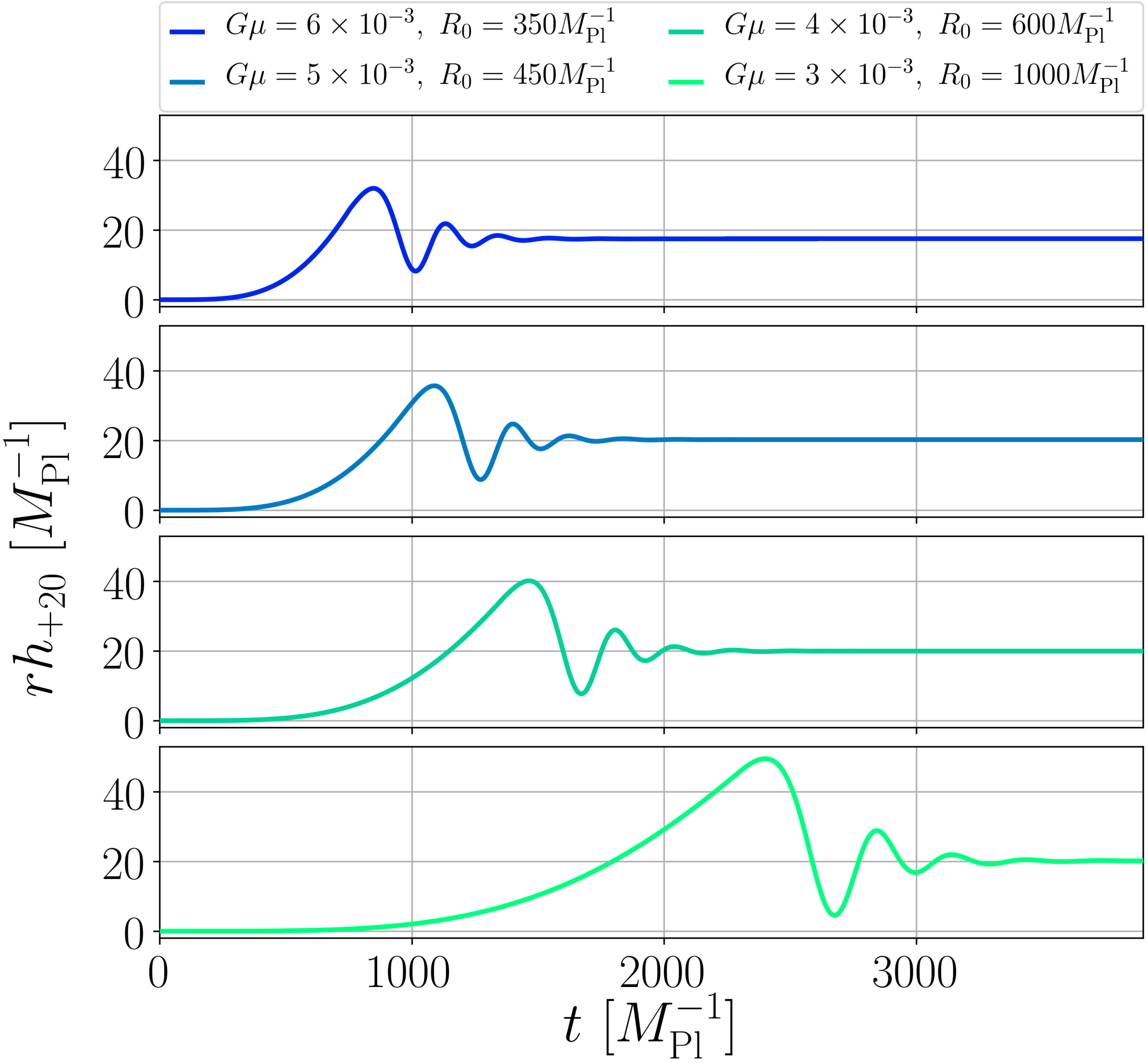

Fig. C.9 Gravitational waveforms for $(G\mu, R_0) = \{(6 \times 10^{-3}, 350M_{\rm Pl}^{-1}), (5 \times 10^{-3}, 450M_{\rm Pl}^{-1}), (4 \times 10^{-3}, 600M_{\rm Pl}^{-1}), (3 \times 10^{-3}, 1000M_{\rm Pl}^{-1})\}$. The numerical signals have been corrected the delays $\Delta t = \{160M_{\rm Pl}^{-1},\ 180M_{\rm Pl}^{-1},\ 200M_{\rm Pl}^{-1},\ 300M_{\rm Pl}^{-1}\}$ respectively, estimated via (C.63). The figure shows how larger loops have a longer infall and the memory is about the same for the last three cases, which is expected since the total radiation in GWs and matter is very similar $M_0 - M_{\rm BH} \approx 1.25M_{\rm Pl}$, while for $(G\mu, R_0) = (6 \times 10^{-3}, 350M_{\rm Pl}^{-1})$ the memory is smaller as $M_0 - M_{\rm BH} \approx 1.05M_{\rm Pl}$, see Tab. C.1.

more energetic events (larger $E_{\rm GW}$) have larger amplitude rh whereas we see that the last three waveforms show a similar amount of memory $r\Delta h$, which is expected as the total energy emitted is $M_0 - M_{\rm BH} \approx 1.25M_{\rm Pl}$, and for $(G\mu, R_0) = (6 \times 10^{-3}, 350M_{\rm Pl}^{-1})$

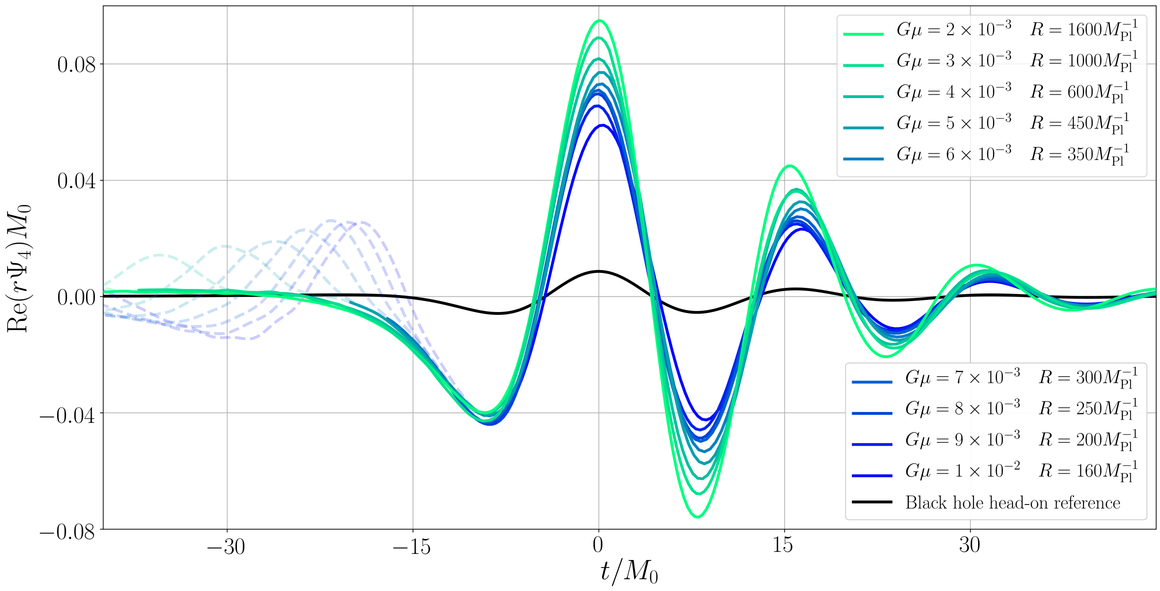

Fig. C.10 Gravitational wave signal for different string tension $G\mu$ and black hole head-on reference [154]: The signal is normalised with the initial mass of the system and shifted such that the maximum of $r\Psi_4$ coincides at time $t = 0$, for all cases in table (C.1). Unphysical parts of the signal are de-emphasised using dashed lines. A summary of the parameters used for these runs is shown below in table (C.1).

less energy is radiated to infinity $M_0 - M_{\rm BH} \approx 1.05 M_{\rm Pl}$, resulting in smaller memory, see Tab. C.1.

C.7 Summary of simulations

Here we show the summary of the results for the different $G\mu$ runs. The first three columns correspond to the parameter space studied. The next four columns include information of data extracted from the simulations together with the corresponding error bars. Lastly, we compute the length contraction before black hole formation using the velocity given by the Nambu-Goto approximation ((4.20)).

To get an approximate estimate of the numerical precision of the signal in Figs. (4.2), (4.6a) and (4.6b), we performed two simulations with two different resolutions. Conservatively we can assume our simulations possess 2nd order convergence (see section C.5 below) and used the difference between the two runs to get an estimate for the error. We then chose the maximum value of the error (excluding the non-physical signal from the initial data) as the value for all points.

Furthermore, in Fig. (4.5) we calculated errors for all measured quantities. We estimated the error of M_0 by calculating the difference between the theoretical value and the integrated energy of the first frame. The errors for M_{BH} are obtained by performing a best fit using QNMs after some different time. To calculate E_{matter} we integrated over the grid, excluding a region close to the black hole. Lastly, the error of E_{GW} is estimated by the energy in initial data artefacts mixed with the physical signal, ie. the energy between $t = R_0 + r_{\text{ext}}$ and when the artefacts have passed the detectors.

$G\mu$	R_0 $[M_{\mathrm{Pl}}^{-1}]$	λ	M_0 $[M_{\mathrm{Pl}}]$	M_{BH} $[M_{\mathrm{Pl}}]$	E_{matter} $[M_{\mathrm{Pl}}]$	E_{GW} $[M_{\mathrm{Pl}}]$	$\gamma(t_{\mathrm{BH}})$
1×10^{-2}	160	2	10.05 ± 0.07	9.21 ± 0.18	0.41 ± 0.10	0.07 ± 0.02	7.96
9×10^{-3}	200	2	11.31 ± 0.07	10.27 ± 0.05	0.31 ± 0.08	0.09 ± 0.02	8.84
8×10^{-3}	250	2	12.57 ± 0.07	11.59 ± 0.08	0.26 ± 0.07	0.11 ± 0.02	9.95
7×10^{-3}	300	2	13.19 ± 0.07	12.23 ± 0.01	0.29 ± 0.07	0.13 ± 0.03	11.37
6×10^{-3}	350	2	13.19 ± 0.07	12.14 ± 0.06	0.46 ± 0.12	0.15 ± 0.02	13.26
5×10^{-3}	450	2	14.14 ± 0.06	12.97 ± 0.02	0.56 ± 0.14	0.19 ± 0.02	15.92
4×10^{-3}	600	2	15.08 ± 0.05	13.76 ± 0.04	0.75 ± 0.19	0.25 ± 0.02	19.89
3×10^{-3}	1000	2	18.85 ± 0.04	17.58 ± 0.12	0.62 ± 0.16	0.38 ± 0.02	26.53
2×10^{-3}	1600	2	20.11 ± 0.03	18.33 ± 0.06	1.38 ± 0.35	0.44 ± 0.02	39.79

Table C.1 Overview of simulations with different $G\mu$ and R_0: In this table, we list all the simulations we have done for this work. The initial mass M_0 is obtained using (4.8) and the error calculated with the difference to the integrated mass of the numerical initial data. To extract the energy in gravitational waves E_{GW} we integrated over the $r\Psi_4$ at different radii. The radiated energy in matter components E_{matter} is estimated by integrating it after black hole formation over the numerical grid excluding the interior of the BH.

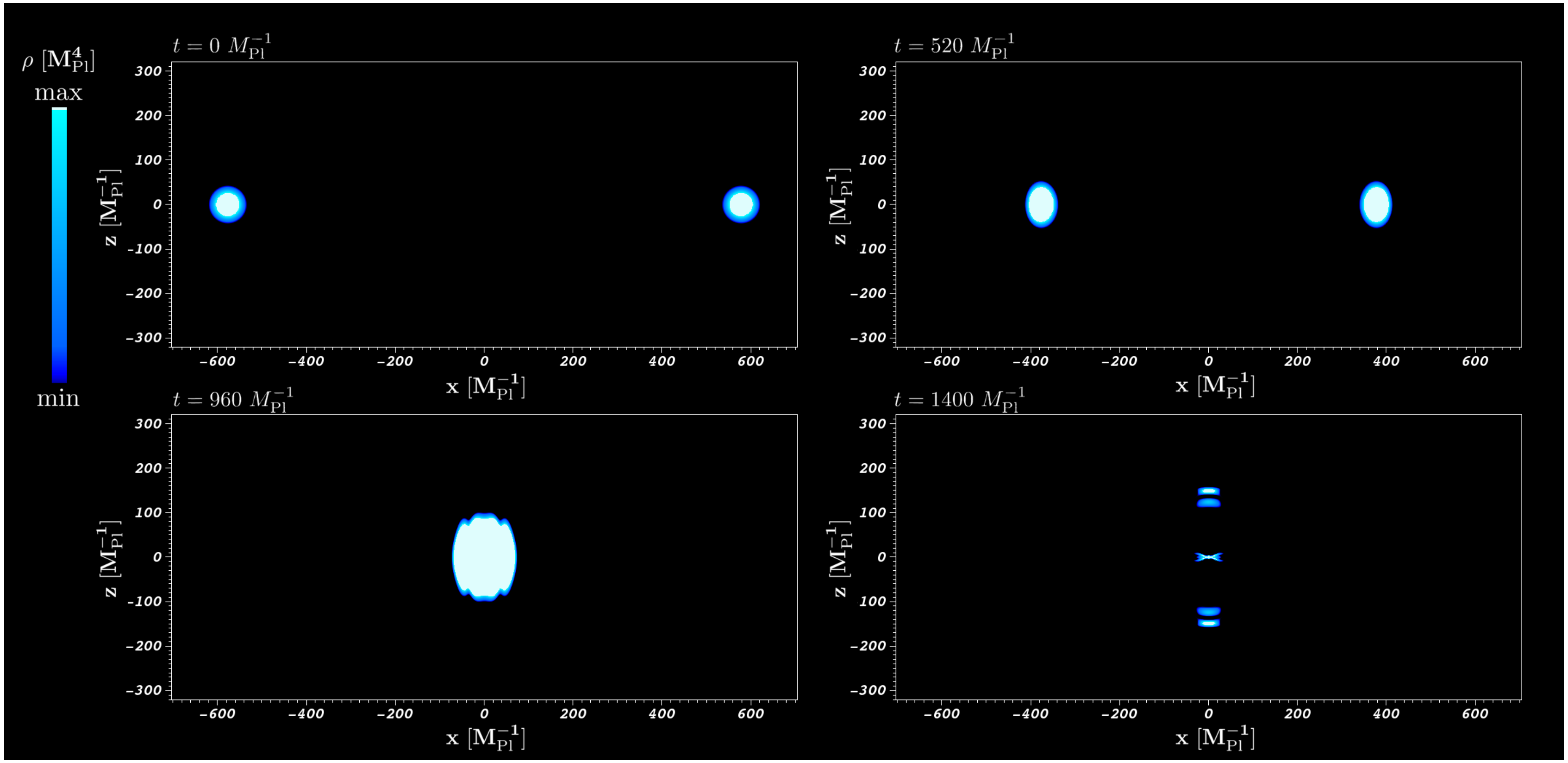

Fig. C.11 2D slice of the collapse of a cosmic string loop using 3+1D numerical relativity.: Figures in the panel above show the evolution of the system from left to right and top to bottom. In colour we plot the energy density. Initially, the loop starts to collapse from rest (upper left); The energy density of the loop increases as its radius becomes shorter and accelerates to ultra-relativistic speeds, when Lorentz contraction effects emerge in the direction of the collapse (upper right). When the radius of the loop is of the same order as the width of the string, the collision happens, where high curvature effects appear (lower left). If the system is massive and thin enough, part of the initial mass of the system collapses to a black hole and high-relativistic jets are emitted axially as a result of the ultra-relativistic collision (lower right). This aspherical ejection of matter is responsible for a constant shift in the gravitational waveform known as gravitational wave memory. The full movie can be found here [234].

Appendix D

Primordial black hole formation with full numerical relativity

D.1 Evolution equations

This work was written based on simulations run using GRCHOMBO [55, 154], with the CCZ4 formulation of the Einstein equations [48] and the *moving-puncture gauge* [102, 67, 124, 445]. The matter part of the Lagrangian is

$$\mathcal{L} = \frac{1}{2} g^{\mu\nu} \partial_\mu \phi \partial_\nu \phi + V_\phi(\phi) + \frac{1}{2} g^{\mu\nu} \partial_\mu \xi \partial_\nu \xi + V_\xi(\xi) \ , \tag{D.1}$$

which gives the evolution equations

$$\nabla_\mu \nabla^\mu \phi - \frac{dV_\phi(\phi)}{d\phi} = 0 \ , \qquad \nabla_\mu \nabla^\mu \xi - \frac{dV_\xi(\xi)}{d\xi} = 0 \ , \tag{D.2}$$

and decomposing them into first order equations, with BSSN variables

$$\partial_t \phi = \alpha \Pi_\phi + \beta^i \partial_i \phi \ , \tag{D.3}$$

$$\begin{aligned} \partial_t \Pi_\phi = {} & \beta^i \partial_i \Pi_\phi + \alpha \partial^i \partial_i \phi + \partial_i \phi \partial^i \alpha \\ & + \alpha \left(K \Pi_\phi - \gamma^{ij} \Gamma^k_{ij} \partial_k \phi - \frac{dV_\phi}{d\phi} \right) \ , \end{aligned} \tag{D.4}$$

$$\partial_t \xi = \alpha \Pi_\xi + \beta^i \partial_i \xi \ , \tag{D.5}$$

$$\begin{aligned} \partial_t \Pi_\xi = {} & \beta^i \partial_i \Pi_\xi + \alpha \partial^i \partial_i \xi + \partial_i \xi \partial^i \alpha \\ & + \alpha \left(K \Pi_\xi - \gamma^{ij} \Gamma^k_{ij} \partial_k \xi - \frac{dV_\xi}{d\xi} \right) \ , \end{aligned} \tag{D.6}$$

D.2 Initial data

The matter content of this work is comprised by a massive ϕ field that dominates the background dynamics, and an inhomogeneous massless ξ field which provides the local overdensity through its gradients. We choose potentials

$$V_\phi(\phi) = \frac{1}{2}m^2\phi^2, \qquad V_\xi(\xi) = 0\,, \tag{D.7}$$

and spherically symmetric initial field configurations

$$\begin{aligned} \phi(t=0,x^i) &= \phi_0\,, \\ \xi(t=0,x^i) &= \Delta\xi\,\tanh\left[\frac{r-R_0}{\sigma_0}\right], \\ \frac{\partial\phi(t=0,x^i)}{\partial t} &= \frac{\partial\xi(t=0,x^i)}{\partial t} = 0\,. \end{aligned} \tag{D.8}$$

In our simulations, $mH_0^{-1} = 62.6$. We also choose a conformally flat metric $\bar{\gamma}_{ij} = \delta_{ij}$, so the energy density on the initial hyperslice is given by

$$\rho(t=0,x^i) = \frac{\psi^{-4}}{2}\delta^{ij}\partial_i\xi\partial_j\xi + \frac{1}{2}m^2\phi_0^2\,, \tag{D.9}$$

which corresponds to a shell-like overdensity in a dark matter environment. This setup is spherically symmetric and we reduce the computational cost of evolution by simulating one eighth of the system using symmetric boundary conditions. A schematic depiction of the initial setup is given in Fig. D.1a.

The equation of motion for a massive homogeneous field ϕ is given by the Klein-Gordon equation

$$\ddot{\phi} + 3H\dot{\phi} + \frac{\partial V(\phi)}{\partial\phi} = 0\,, \tag{D.10}$$

where $H \equiv \dot{a}/a$ is the Hubble function defined with the scale factor of the universe $a(t)$. For the universe to stay matter dominated for an extended period of time, we require the solution of Eqn. (D.10) to be an undamped oscillation. This constrains the initial value of ϕ to

$$\phi_0 < \frac{1}{\sqrt{3\pi}}M_{\mathrm{Pl}}\,, \tag{D.11}$$

and we use $\phi_0 = 7.8\times10^{-3}M_{\mathrm{Pl}}$ for all our simulations. Momentum constraints are trivially satisfied, and we solve the Hamiltonian constraint (5.14) numerically to find the conformal factor ψ.

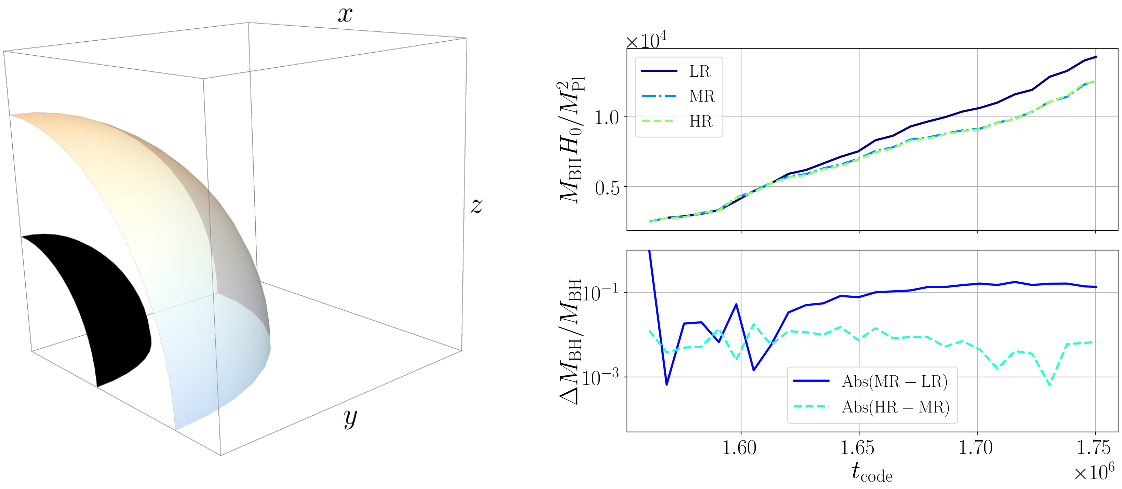

(a) **(b)**

Fig. D.1 (a): Initial setup of collapsing superhorizon overdensity (transparent shell) and inner initial Hubble horizon depicted in black. Using symmetric (reflective) boundary conditions we simulate an eighth of the system. **(b): Convergence test** of the black hole mass formed from an initial perturbation of $R_0 = 1.6H_0^{-1}$ and $\Delta\xi M_{\rm Pl}^{-1} = 0.075$. Top panel shows the estimated mass for three base grid resolutions $N_{\rm LR} = 80$, $N_{\rm MR} = 96$, $N_{\rm HR} = 128$. Bottom panel shows errors in mass measurements between high-middle and middle-low resolutions showing convergence to 1%.

D.3 Convergence testing

We test the robustness of our numerical results by finding the mass of the black hole formed from an initial perturbation of radius $R_0 = 1.6H_0^{-1}$ and $\Delta\xi = 0.15H_0^{-1}$, using three different base grid resolutions, namely $N_{\rm LR} = 80$, $N_{\rm MR} = 96$, $N_{\rm HR} = 128$. Fig. D.1b shows the mass obtained with an apparent horizon finder [433] for these three runs, indicating that convergence is achieved.

Additionally, we made sure the code reproduces the FLRW limit for appropriate initial conditions. If one uses the same initial setup as described in appendix D.2, but gives the field ξ a uniform value throughout the simulation box, evolution should proceed in an FLRW manner, as the simulated universe is now completely homogeneous. We checked this by averaging the values of the energy density ρ and the scale factor a over the box, and tracking these throughout the evolution. We satisfactorily find that the scaling between these two quantities is then $\rho \sim a^{-3}$, as expected for a matter-dominated FLRW universe.